N84-31344

NASA Technical Memorandum 83738

Overlay Coating Degradation by Simultaneous Oxidation and Coating/Substrate Interdiffusion

James A. Nesbitt
Lewis Research Center
Cleveland, Ohio

August 1984

NASA

TABLE OF CONTENTS

APPENDICES

Introduction

(Ni-Co)CrAl overlay coatings are finding increased use for oxidation and corrosion protection in high-temperature turbine applications (1-9). The coatings provide high-temperature protection by the formation of an adherent Al_2O_3 scale (1, 10-12). For many applications, overlay coatings possess several desirable advantages over the more common aluminide coatings (1,10,12). One of the main advantages of overlay coatings is the inherent compositional flexibility which permits tailoring of the coating for both optimal oxidation resistance and coating/substrate compatibility (1,4,10). With regard to the oxidation resistance, the compositional flexibility allows addition of active elements, as Y or Zr, to the coating which greatly increases the adherence of the oxide scale during thermal cycling (13-18). Similarly, the coating composition can be varied for specific applications, such as increasing the Cr content of the coating for use in corrosive environments. The purpose of improving coating/substrate compatibility is to reduce degradation of critical substrate properties (such as creep resistance and fatigue life) caused by the presence of the coating (1,4,10). Coating/substrate interdiffusion may have a detrimental effect on both the environmental resistance of the coating and also on the mechanical properties of the substrate (10). Not only does interdiffusion dilute the Al concentration in the coating, but diffusion of alloying elements from the substrate into the coating may degrade the mechanical properties of the substrate (4) and have an adverse effect on the oxidation resistance.

The compositional flexibility of overlay coatings also permits increased coating ductility (1,10,19) to minimize coating/substrate thermal-expansion mismatch and reduce the possibility of premature thermal fatigue cracking. The ductility of the overlay coatings results from the two-phase structure where the high-Al, brittle, β phase (NiAl-type structure) is imbedded in a Y (FCC) Ni solid-solution matrix (1,2).

Currently two techniques are typically employed for applying overlay coatings, physical vapor deposition (PVD) (6,10,19) and low-pressure plasma spray (LPPS) (2). Both techniques require sophisticated apparatus for applying a coating, usually coating only a relatively few components in a single operating cycle (2,6). As a result, overlay coatings are more costly to apply than simple aluminide coatings. One advantage of LPPS over PVD is that complex compositions virtually impossible to apply by PVD can easily be applied by LPPS deposition (1,2,4). To summarize, the compositional flexibility of LPPS overlay coatings permits tailoring of the coating to select superalloy substrates for specific environmental applications.

Diffusional Degradation of Coatings

Two mechanisms of coating degradation which occur by diffusional transport are loss of Al to the Al_2O_3 scale (1,19-21), and loss of Al by coating/substrate interdiffusion (1,20-23). During high-temperature oxidation, Al is transported by diffusion to the oxide/metal interface where it is selectively oxidized (11). At the same time, Al also diffuses from the high-Al coating into the substrate while Ni and other alloying elements from the substrate diffuse into the coating (22,24). Both types of coating degredation reduce the Al content of the coating,

thereby reducing the ability of the coating to supply Al to the oxide/metal interface. Loss of the oxide scale by cracking and spalling during thermal cycling significantly accelerates the **loss** of Al due to oxidation (12,19,25). Oxide spallation has previously been shown to depend on the thermal cycle frequency (14,261, the concentration of active element additions (13-18), the cooling rate (27), and the temperature differential between the heating and cooling portion of each cycle (28). The loss of Al by oxidation also increases with increasing oxidation temperature (13,141.

Coating/substrate interdiffusion is critically dependent on the oxidation temperature (22). The diffusivities which govern diffusion processes generally increase exponentially with increasing temperature (29). The composition of the coating and substrate, and especially the Al content of both, also affects the rate of coating/substrate interdiffusion (22). The greater the difference in chemical potential between the coating and substrate, the greater the "driving force" for coating/substrate interdiffusion. Reducing the difference in Al content between the coating and substrate will generally reduce the difference in the chemical potential and Consequently lower the rate of Al loss from the coating by coating/substrate interdiffusion. Unfortunately, superalloys are compositionally complex, multiphase alloys and may easily contain over a dozen elements (30,311. Ternary or higher diffusional interactions can complicate and hinder a complete understanding of coating degradation by coating/substrate interdiffusion.

Continued degradation of overlay coatings results in failure of the coating to provide the protective Al_2O_3 scale (10,21,25). Once the

coating becomes sufficiently depleted of Al, it can no longer supply Al to the oxide/metal interface at the rate necessary to continue growth of the Al_2O_3 scale. Less protective oxides of Ni and Cr will form as a result of the lack of Al flux to the oxide/metal interface (10,32,33). The failure of the coating to supply sufficient Al resulting in formation of the less protective oxides is commonly referred to as breakaway oxidation (34,35).

The transport of Al in the coating to the growing oxide scale depends on both the concentration gradients (Al and Cr) and the ternary interdiffusion coefficients (36) in the coating near the oxide/metal interface. The maximum flux of Al to the oxide/metal interface occurs when the Al concentration at the interface is zero (37,381. This maximum flux condition has previously been used to predict the bulk solute concentration in binary alloys which is necessary to supply sufficient solute to form a continuous, external oxide scale during isothermal oxidation (39,40). Insufficient solute transport to the oxide/metal interface generally results in internal oxidation of the solute (37,38). The necessary solute flux is directly related to the growth rate of the oxide. The greater the growth rate of the oxide, the greater the requisite solute flux, and the higher the bulk solute concentration necessary to supply the solute flux (37,38). During isothermal oxidation, as the thickness of the oxide scale increases, the growth rate of the scale decreases (34,371. Similarly, the solute flux in the alloy at the oxide/metal interface will also decrease so as to always supply the necessary solute to the growing oxide scale (38). The oxide growth rate during isothermal oxidation decreases inversely with the square root of time as the oxide scale thickness increases

parabolically with time (37). Since the growth rate of oxide scale controls the rate of solute consumption at the oxide/metal interface, the solute flux in the alloy at the oxide/metal interface also decreases inversely with the square root of time. The alloy can supply solute to the oxide scale at the required rate during isothermal oxidation by maintaining a constant solute concentration at the oxide/metal interface (38,41).

Thermal cycling resulting in scale spallation continually reduces the thickness of the oxide scale. As a result, the growth rate of the oxide scale will be higher than if the scale were growing under isothermal conditions (25,38). The main consequence of the higher growth rate of the oxide scale is a higher requisite solute flux in the alloy. A higher solute flux in the alloy can be maintained by reducing the solute concentration at the oxide/metal interface (25,38). Therefore, following each thermal cycle where the oxide layer has spalled (either partially or completely), the solute concentration at the oxide/metal interface would be expected to decrease. As the oxide scale thickens during the high-temperature period of a cycle, the solute concentration at the oxide/metal interface would be expected to remain essentially constant until the next thermal cycle. The effect of oxide spallation on the thickness of the oxide, the growth rate of the oxide (which is proportional to the rate of solute consumption), the solute concentration at the oxide/metal interface and the solute concentration in the alloy are shown schematically in Figure 1. Figure la shows the increase in the thickness of the oxide scale during oxidation (0-2, 2-4 hours, etc.) and the decrease in the thickness of the oxide scale due to oxide spallation upon cooling (after 2 and 4 hours). Figure 1b shows a

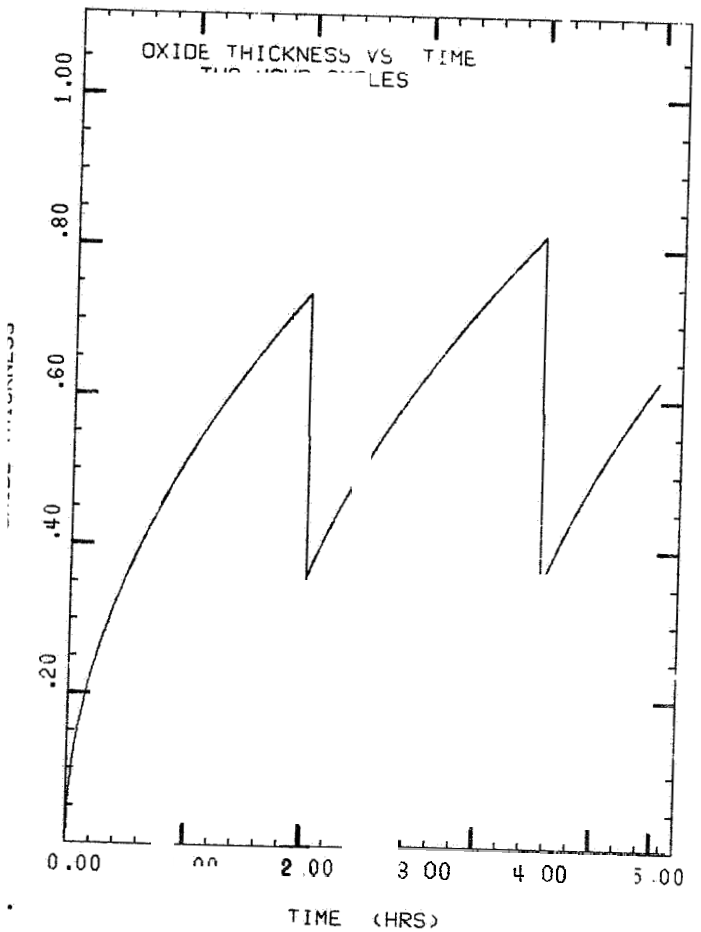

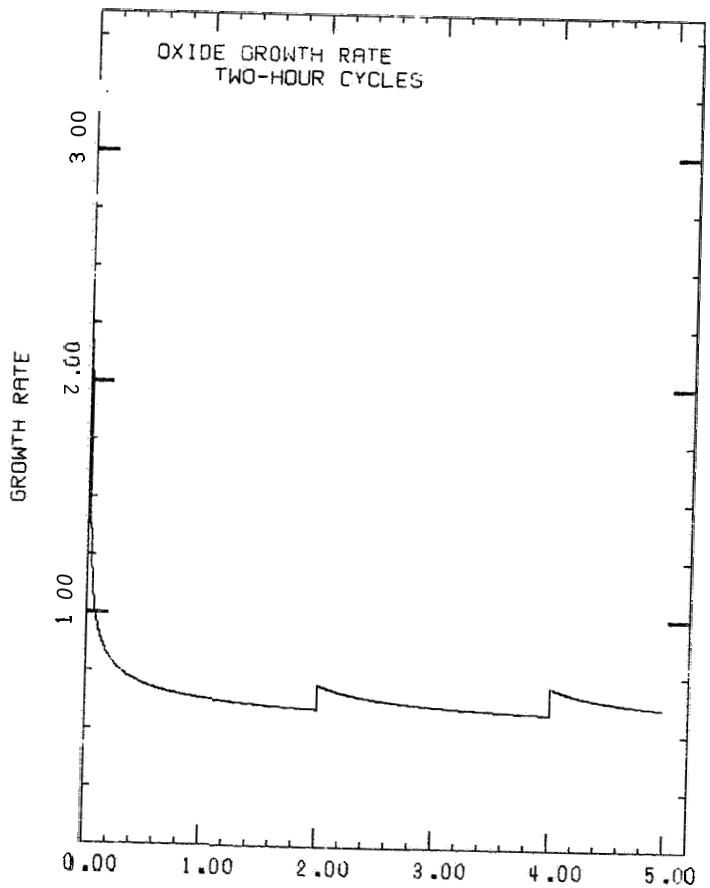

Figure 1 Schematic plot of the effect of oxide spallation on the:
a. oxide thickness, b. oxide growth rate (cooling occurs after 2 hours, 4 hours, etc.)

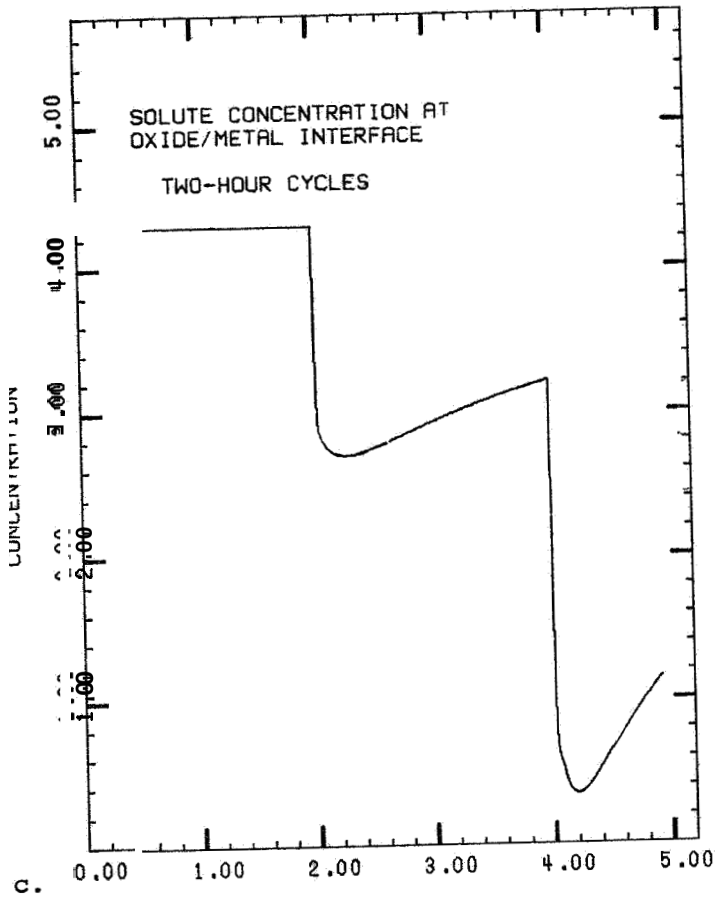

c.

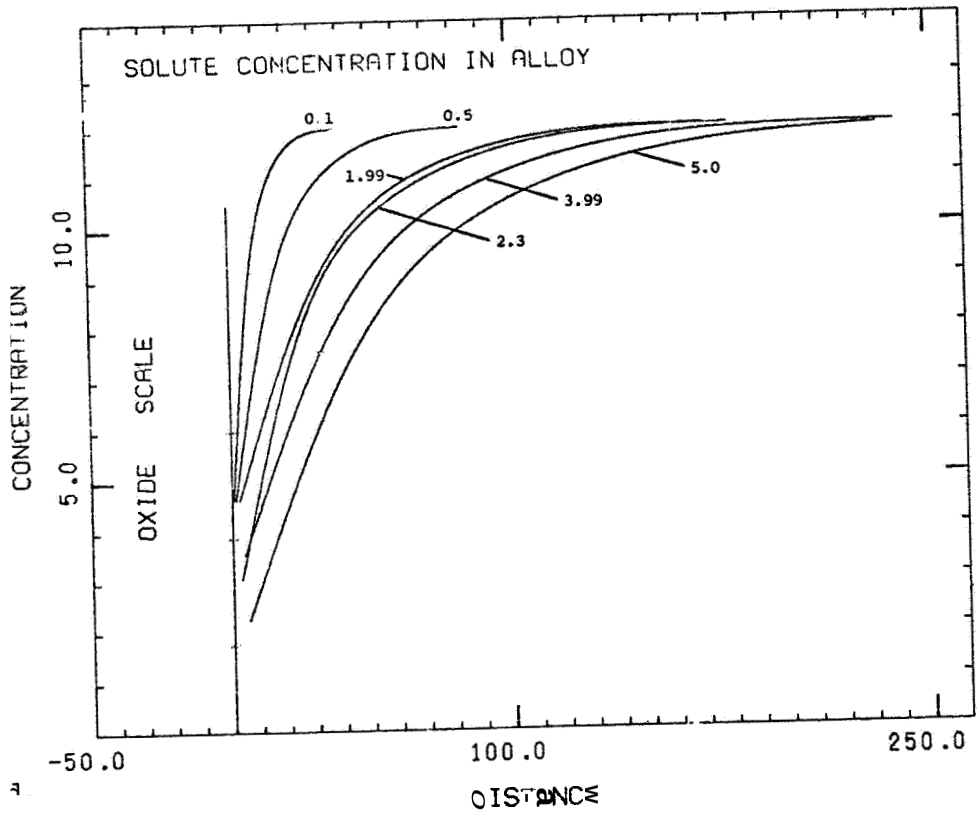

Schematic plot of the effect of oxide spallation on the:
c. solute concentration at the oxide/metal interface
d. solute concentration/distance profiles (cooling occurs after 2 hours, 4 hours, etc.).

decrease in the oxide growth rate as the oxide scale thickens (0–2 and 2–4 hours) and an increase when the thickness of the oxide scale decreases after spallation (after 2 and 4 hours). Figure 1c shows the solute concentration at the oxide/metal interface as independent of time for the first two hours of isothermal oxidation, followed by a sharp decrease (and slight increase) after partial oxide spallation (after 2 and 4 hours). The effect of the changing rate of solute consumption is illustrated in Figure 1d where the solute concentration/distance profiles are shown before and after the thermal cycles. The solute concentration gradient decreases as the growth rate of the oxide scale decreases (the rate of solute consumption decreases as the oxide scale thickens between 0–2 and 2–4 hours). When the growth rate of the oxide increases due to oxide spallation (after 2 hours), the solute concentration at the oxide/metal interface decreases, increasing the solute concentration gradient so as to supply solute at an inceased rate. If the solute concentration at the interface is depressed to zero the solute concentration gradient will thereafter decrease, and the alloy will be unable to supply sufficient solute at the rate required for the growth of the oxide scale.

Less protective oxides form when an alloy is incapable of supplying solute at the rate required for the growing solute scale (32,35). The continued presence of the less protective oxides permit an influx of oxygen into the alloy which results in internal oxidation of the solute (11,32,35). Either the solute flux in the alloy will reestablish a continuous solute oxide layer (25,35), or the less protective oxides will continue to grow and the internal oxidation will totally deplete the alloy of solute (32). Figure 2 shows regions near the surface of a

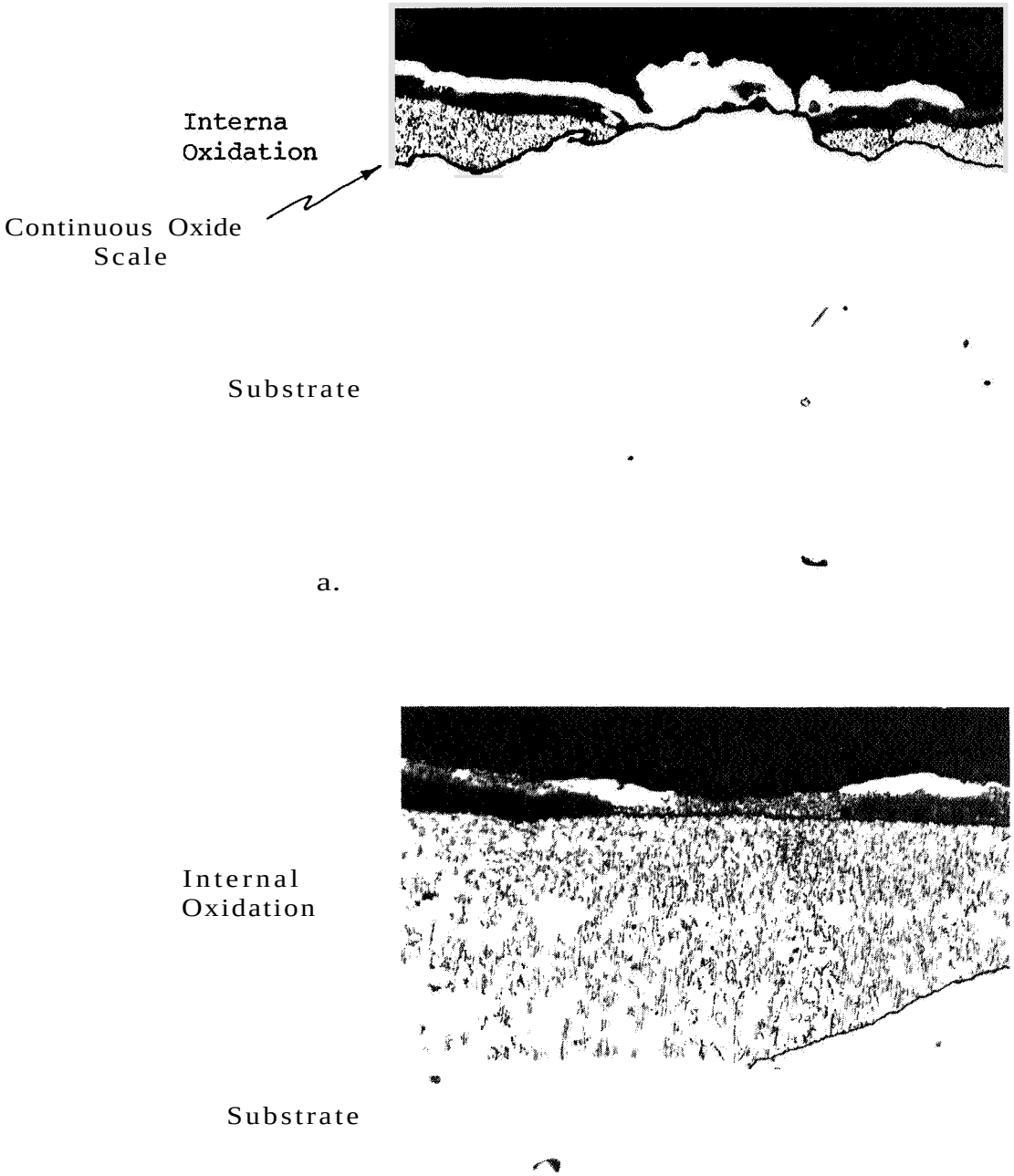

Figure 2. Oxidation of Ni-6.7 at.%Al Alloy
a. Region of external scale formation (center) and a continuous oxide layer below a region of internal oxidation. b. band of internal oxidation (left) and formation of continuous oxide layer (right).

Ni-6.7Al alloy after isothermal oxidation where the solute flux was just sufficient to form an external oxide scale (Figure 2a), where the solute flux was able to form a continuous internal oxide scale only after a time of internal oxidation (Figures 2a and b), and where the solute flux was incapable of supplying sufficient solute to form a continuous oxide scale resulting in unrestrained internal oxidation (Figure 2b).

The above discussion regarding the transition from a protective solute oxide scale to formation of less protective oxides has been simplistic in several respects. First, oxide spallation during thermal cycling is a very random, non-uniform process (25). The oxide typically does not spall to bare metal. Therefore, the rate of solute consumption, and the flux of solute to the oxide/metal interface would vary at different locations on a sample surface. A non-uniform solute flux as well as a physically irregular oxide/metal interface would result in non-planar diffusion with solute at areas of high solute concentration flowing to areas of low solute concentration parallel to the oxide/metal interface. In addition, the above discussion has not considered the possible formation of such oxides as spinels which may form by a transference reaction between the less protective oxides and solute (42).

In summary, any reduction in the Al content of an overlay coating will reduce the ability of the coating to supply sufficient solute to the growing oxide. Both oxidation and coating/substrate interdiffusion degrade the coating by reducing the Al content *of* the coating. As a result, both forms of degradation hasten failure of the protective Al_2O_3 scale.

Finally, it is essential to understand the coupled nature of the two forms of coating degradation. All coatings are of a finite thickness. The ability of a coating to continually supply Al to the oxide depends entirely on the transport of Al to the oxide/metal interface. It is not so much the Al content in the coating which determines coating failure as it is the maximum possible flux of Al towards the oxide scale. It is possible for alloys with very high Al contents to undergo breakaway oxidation (25). It is also not sufficient to state that Al which has diffused from the coating due to coating/substrate interdiffusion is completely lost with regard to oxidation protection. There is no reason why Al which has diffused into the substrate cannot at a later time reverse its direction and flow back through the coating to support the growing oxide scale. Finally, there have been many discussions (10,19,20) in the past as to which effect, oxidation or coating/substrate interdiffusion, is more important regarding coating degradation. Most of the studies examining this question have been on different coating/substrate systems oxidized under different conditions. It is generally recognized that increasing the coating thickness, or increasing the Al content of the coating prolongs coating life. It is also quite obvious that increasing the rate of Al consumption, by increasing the oxidizing temperature or increasing the cycle frequency, generally shortens the life of the coating. But even a qualitative prediction of the coating life when two parameters are varied, such as thicker coatings and a higher cycle frequency, is not easily made. There has been no clear theoretical basis for establishing guidelines as to when one form of degradation might dominate over

another for various coating/substrate systems under different oxidizing conditions. The present study makes an attempt in this direction.

Purpose of this Study

The purpose of the present study was two-fold:

1. To examine the coupled nature of the diffusional degradation of $\gamma + \beta$ overlay coatings on various Ni-base γ alloys and,
2. To identify the critical coating/substrate system parameters having the most significant effect on coating life.

To accomplish this purpose, several γ -phase, Ni-base alloys were coated with a $\gamma + \beta$, NiCrAlZr overlay coating and cyclically oxidized. Subsequent analysis including microstructural investigation and determination of concentration/distance profiles provided insight into the two forms of diffusional degradation. A diffusion model was developed to simulate the diffusional interactions in overlay-coating/substrate systems undergoing oxidation accompanied by thermal cycling. The necessary experimental work was undertaken to provide the required input to the diffusion model. The cyclically oxidized coated alloys were used to provide verification of the diffusion model. Following verification, the diffusion model was utilized to further understand the coupled nature of diffusional degradation and to identify the most critical parameters affecting coating life.

Experimental Procedure

Four NiCrAl y-phase substrates spanning the Al and Cr concentration range of most current Ni-base superalloys (30,31) were chosen for use in this study. Substrate designations and compositions are given in Table 1. The substrate alloys were fabricated by repeated arc melting (of pressed elemental powders) into approximately 1 cm diameter bars 7.5 cm in length. The bars were machined into pins 0.635 cm (0.25 in.) in diameter with V shaped notches cut to a depth of 0.16 cm approximately every 2.5 cm (1 in.) along the length of the pin.

A $\gamma + \beta$, NiCrAlZr coating composition (43) was chosen for application on the four substrate alloys. An overlay coating was applied by a low-pressure plasma spray (2) process at the General Electric Research and Development Center, Schenectady, N.Y. The cylindrical surface of each pin was sprayed individually followed by spraying of the ends after the pins had been sectioned at the notches. The coating thickness on the cylindrical surface of each pin was uniform while the coating on the end was usually slightly thicker. The coating thickness varied between pins generally in the range 50-100 microns (measured after oxidation). Following the low-pressure plasma spray the pins were annealed for two hours at 1150°C in flowing Ar to increase the diffusion bond between the substrate and coating. The microstructure of the coating (as sprayed and after a short anneal) is shown in Appendix D.

The coated pins were cyclically oxidized at the NASA-Lewis Research Center, Cleveland, OH (13,14). One thermal cycle consisted of oxidation at 1150°C in still air for one hour followed by a minimum cooling period of 20 minutes at near room temperature. (A heating/cooling cycle is

Table 1

Substrate and Coating Compositions*

Substrate Designation	Cr (at.%)	Al (at.%)
Ni-10Cr	11.7	-
Ni-10Al	-	6.7
Ni-20Cr	22.6	-
Ni-10Cr-10Al	11.5	7.0
Coating Composition	13.5	24.85 (0.05Zr)

* Compositon determined by electron microprobe analysis (see Appendix A).

hereafter referred to simply as one cycle.) The pins were periodically removed from the cyclic oxidation furnace and the weight of the pin measured. The pins were oxidized for either 50, 100, 200, 250 or 350 cycles.

Following oxidation, the retained surface oxides were identified by x-ray diffractometry. Quantitative determination of the amount of each oxide phase was not possible. The oxide morphology was also examined by scanning electron microscopy. Oxide phase identification was aided by energy dispersive spectroscopy (EDS). The oxidized pins were then Cu and Ni plated to aid in retention of the oxide scale and edge retention of the the metal near the oxide/metal interface during polishing. The Cu and Ni plated pins were sectioned, mounted and polished by standard metallographic techniques in preparation for quantitative electron microscopy.

Concentration/distance profiles for each oxidized pin were measured with an electron microprobe. The Al and Cr concentrations were measured from the oxide/metal interface across the coating and into the substrate. Two to four concentration profiles were measured on each pin. Details of the concentration measurements and subsequent correction procedure are given in Appendix A. All concentration measurements were in the γ phase; the γ' and @ phases were not detected in the coating or substrate. (The results of Appendix D indicate that only the γ phase would be present in the coating after 5-15 one-hour cycles at 1150°C.) Occasionally a very high Al concentration was measured in the coating and could often be visually associated with an oxide inclusion. These questionable concentrations were removed from the concentration profiles. In addition, unusual concentrations

typically associated with porosity in the coating or substrate were also removed.

Experimental Results and Discussion

Weight Change and Oxide Formation

Each of the four coated substrates exhibited varying resistance to oxide spallation. The Ni-10Cr and Ni-10Al pins* exhibited the best cyclic oxidation behavior, whereas the Ni-10Cr-10Al pins exhibited the poorest. The weight-change data for each of the coated substrates are shown in Figures 3a-d. Each of the coated substrates suffered some form of coating loss near the end of the pin usually after 200-300 cycles. The Ni-10Cr pins exhibited a continuous weight increase through 190 cycles. The large weight loss after 200 cycles was due to loss of large pieces of coating from one end of the pin. The smooth area on the side and at the end of the pin where macro-spallation of the coating occurred is shown in Figure 4a. The spalled coating, in the shape of a disk, was recovered with the collected oxide spall. The large weight loss from the Ni-10Al pin after 300 cycles was also due to partial loss of the coating near the end of the pin. Negligible oxide spall was collected during cyclic oxidation of either the Ni-10Cr or Ni-10Al pins. X-ray diffraction showed that Al_2O_3 and $NiAl_2O_4$ were the main oxides formed on these coated substrates. Both oxides have previously been shown to exhibit the best resistance to spallation during thermal cycling (44). The morphologies of the retained surface oxides were very similar for the coated Ni-10Cr and Ni-10Al pins. The Al-rich oxides (presumably Al_2O_3) are shown in Figure 5a and the Ni and Al-rich oxides ($NiAl_2O_4$)

---

* The coating/substrate composite will simply be referred to as a pin designated with the substrate composition.

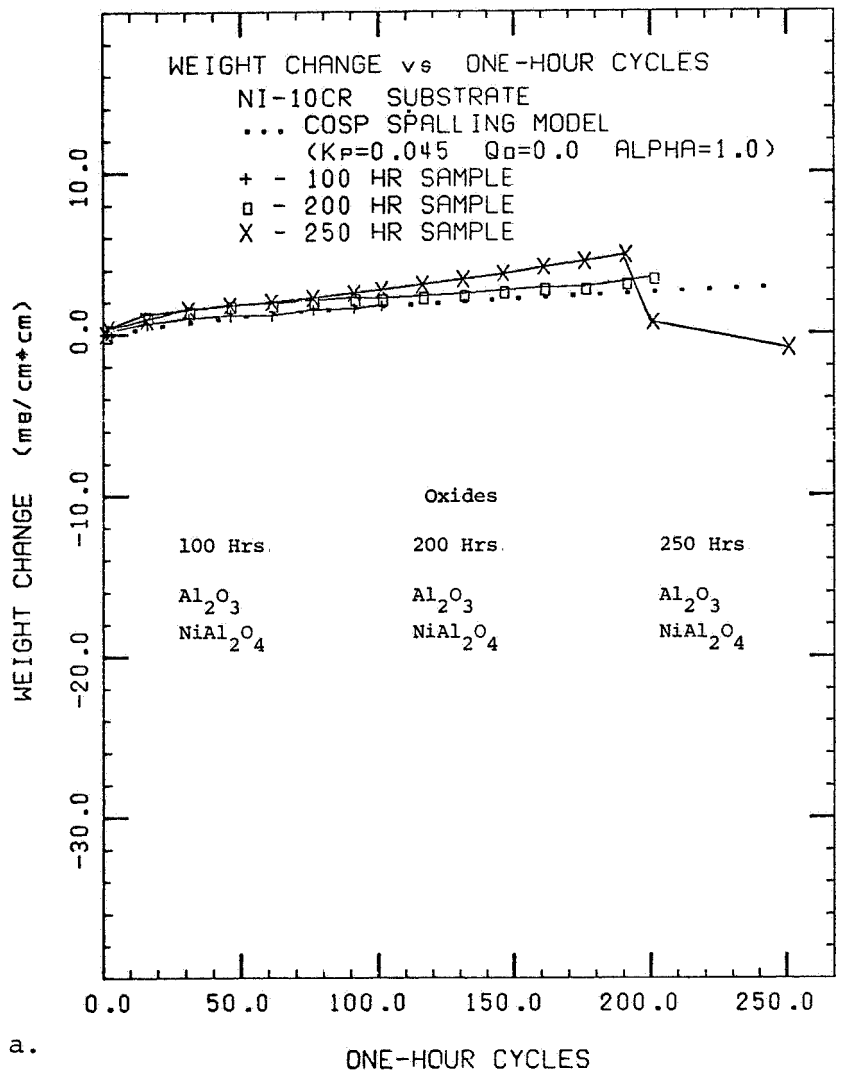

a.

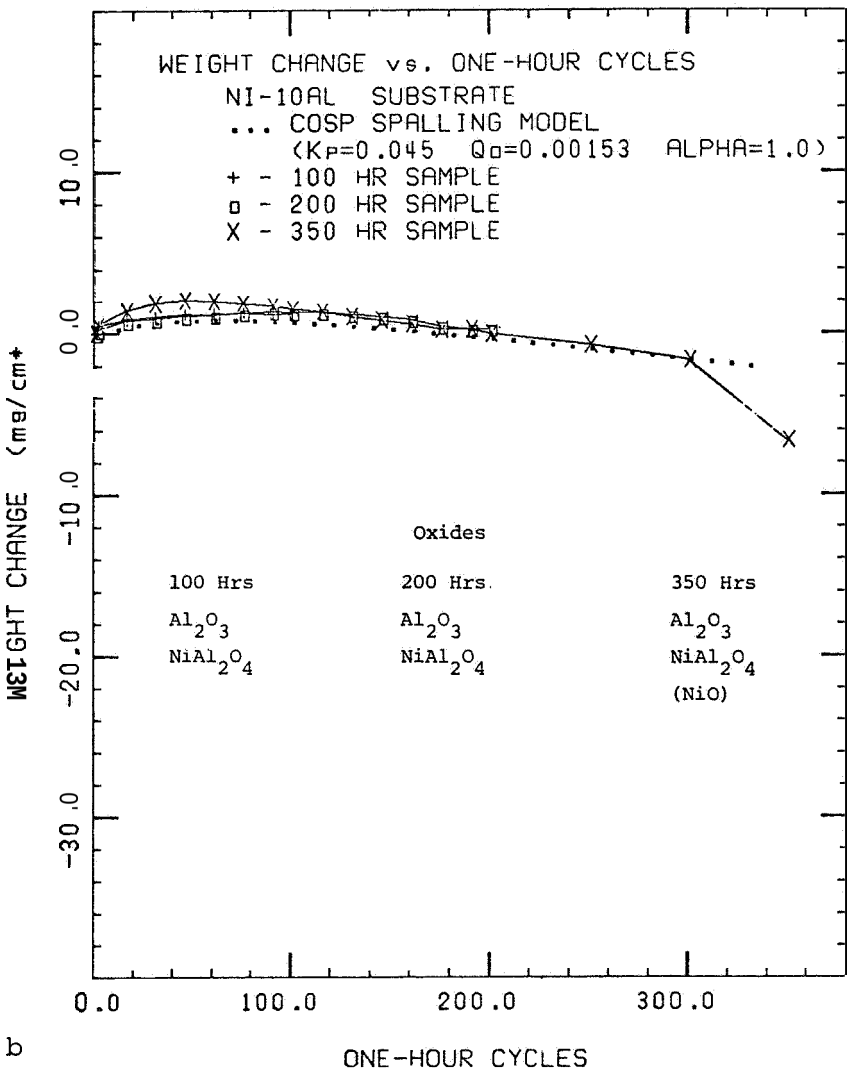

b

Figure 3 Weight Change During Cyclic Oxidation
a Ni-10Cr substrate b Ni-10Al substrate.

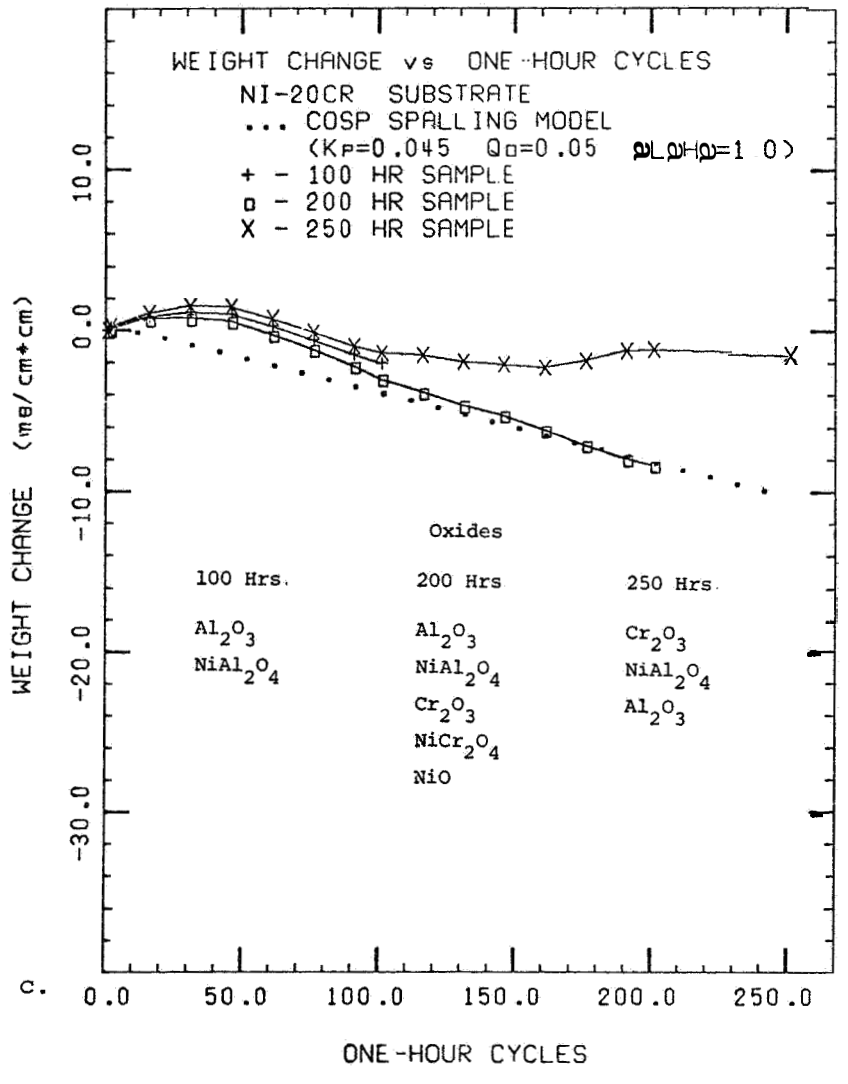

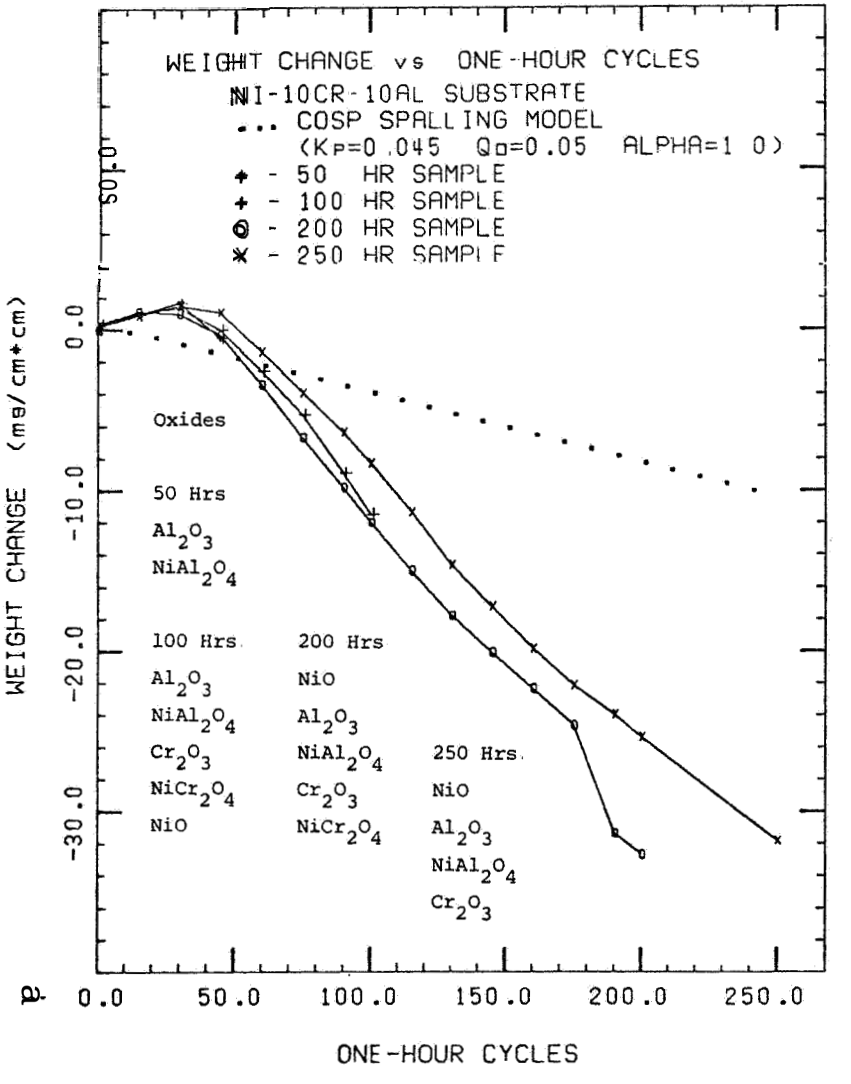

Figure 3 (con't.) Weight Change During Cyclic Oxidation
c. Ni-20Cr substrate d Ni-10Cr-10Al substrate.

Ni-10Cr 250 Cycles

a.

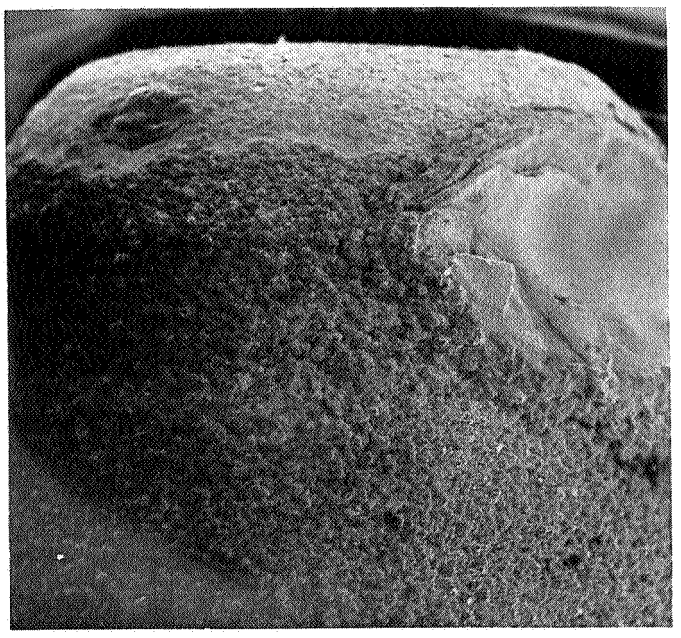

Ni-20Cr 250 Cycles

b.

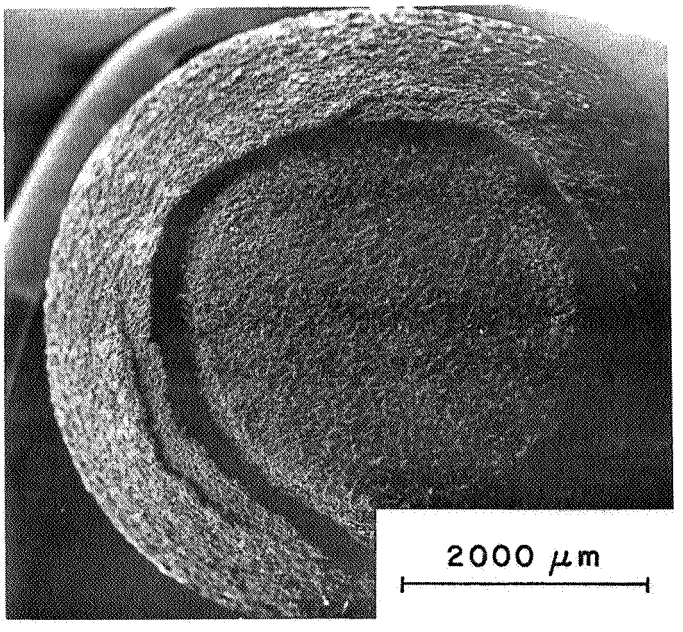

Figure 4 Coating Spallation Near the End of the Pins

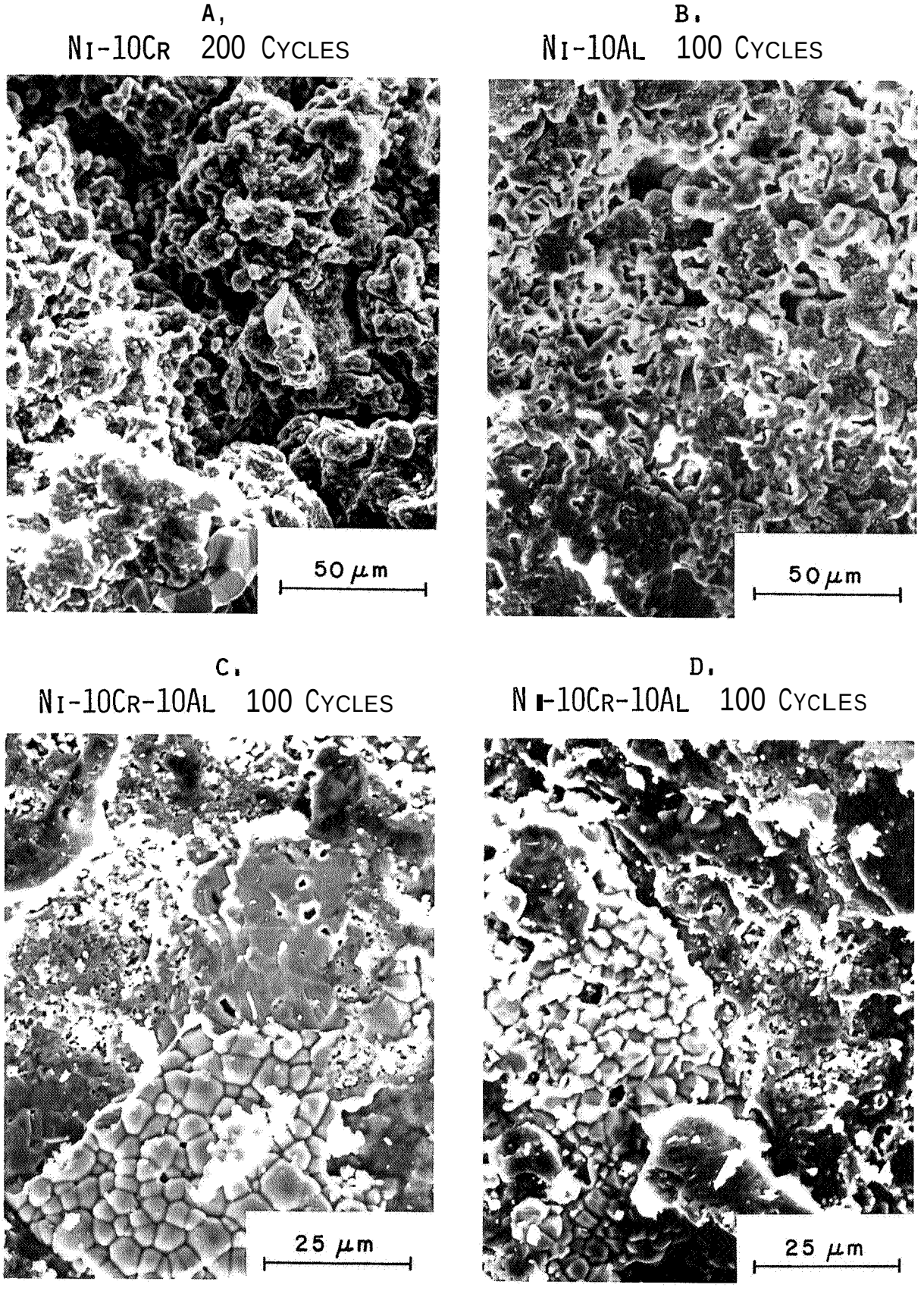

Figure 5 Surface Oxide Morphology After Cyclic Oxidation.

are shown in Figure 5b. Both oxide morphologies are very similar to $Al_2O_3/NiAl_2O_4$ scales previously observed on cyclically oxidized, cast NiCrAlZr alloys (45). A small amount of smooth Ni-rich oxide crystals (NiO) are also shown in Figure 5a.

The oxide formed on the Ni-20Cr pins was less resistant to spalling than that on the Ni-10Cr or Ni-10Al pins. The weight change data for the Ni-20Cr pins are shown in Figure 3c. The pin oxidized for 250 cycles suffered macro-spallation of the coating from the end of the pin (Figure 4b). Examination of the exposed coating revealed mainly Ni and Cr-rich oxides. As expected, a Cr-rich oxide had formed on the exposed substrate where the coating had spalled. Sectioning the pin after 250 cycles revealed almost complete loss of contact between the coating and substrate. Considerable oxide formation was observed in both the coating and substrate where the contact was lost. The low weight loss for this pin (Figure 3c, 250 cycles) was attributed to the oxide formation which occurred between the coating and substrate.

The coating on the Ni-10Cr-10Al pins exhibited the poorest resistance to oxide spallation. The weight change data for the Ni-10Cr-10Al pins are shown in Figure 3d. Poorly protective oxides of Ni and Cr were present on the surface of the coating after only 100 cycles. The high weight loss from the Ni-10Cr-10Al pins was reflected by a large amount of oxide spall collected after only 100 cycles. The coating spalled from both ends of the pin before 200 cycles.

The morphology of the surface oxides on the Ni-20Cr and Ni-10Cr-10Al pins was very similar. Typical oxide morphologies are shown in Figures 5c and d. NiO crystals were usually smooth with irregular shapes (Figure 5c) but were sometimes faceted (Figure 5d).

The Ni-10Cr-10Al pins contained mainly NiO after 200 cycles, whereas the Ni-20Cr pins contained significant amounts of Cr_2O_3 after 200 cycles. The Cr_2O_3 crystals on the Ni-20Cr pins were usually faceted and indistinguishable from the NiO crystals without the use of EDS.

Microstructural Changes

Many of the microstructural changes which occurred in the coating or substrate during cyclic oxidation were similar for each of the four pin compositions. Kirkendall porosity typically formed in the coating, substrate or both. After short exposures (10-50 cycles), most of the observed porosity was located in the coating (Figures 6a and b). In the thicker coatings ($\sim$100 μm), the porosity appeared to be greater in the inner half of the coating (nearest the substrate). Porosity appeared to form preferentially at the coating/substrate interface in the Ni-10Cr and Ni-20Cr pins (Figure 6a). Varying amounts of porosity were observed within the four substrates after equal oxidation exposures. The Ni-10Al and Ni-10Cr substrates contained the least amount of porosity (Figure 6c and d). The Ni-10Cr-10Al and Ni-20Cr substrates contained significant amounts of porosity (Figure 6e) with the Ni-20Cr substrate containing more porosity than the coating.

Several different types of oxide formation were observed in the coating and substrate. Large oxide "stringers" grew inward from the outer oxide scale (Figure 6d and f). This type of oxide formation was observed after 10-50 cycles but was more obvious at longer times. The formation of the oxide in the coating may result from oxidation of cavities or crevices in the as-sprayed coating. Expansion and contraction of the metal surrounding the oxide stringers during heating

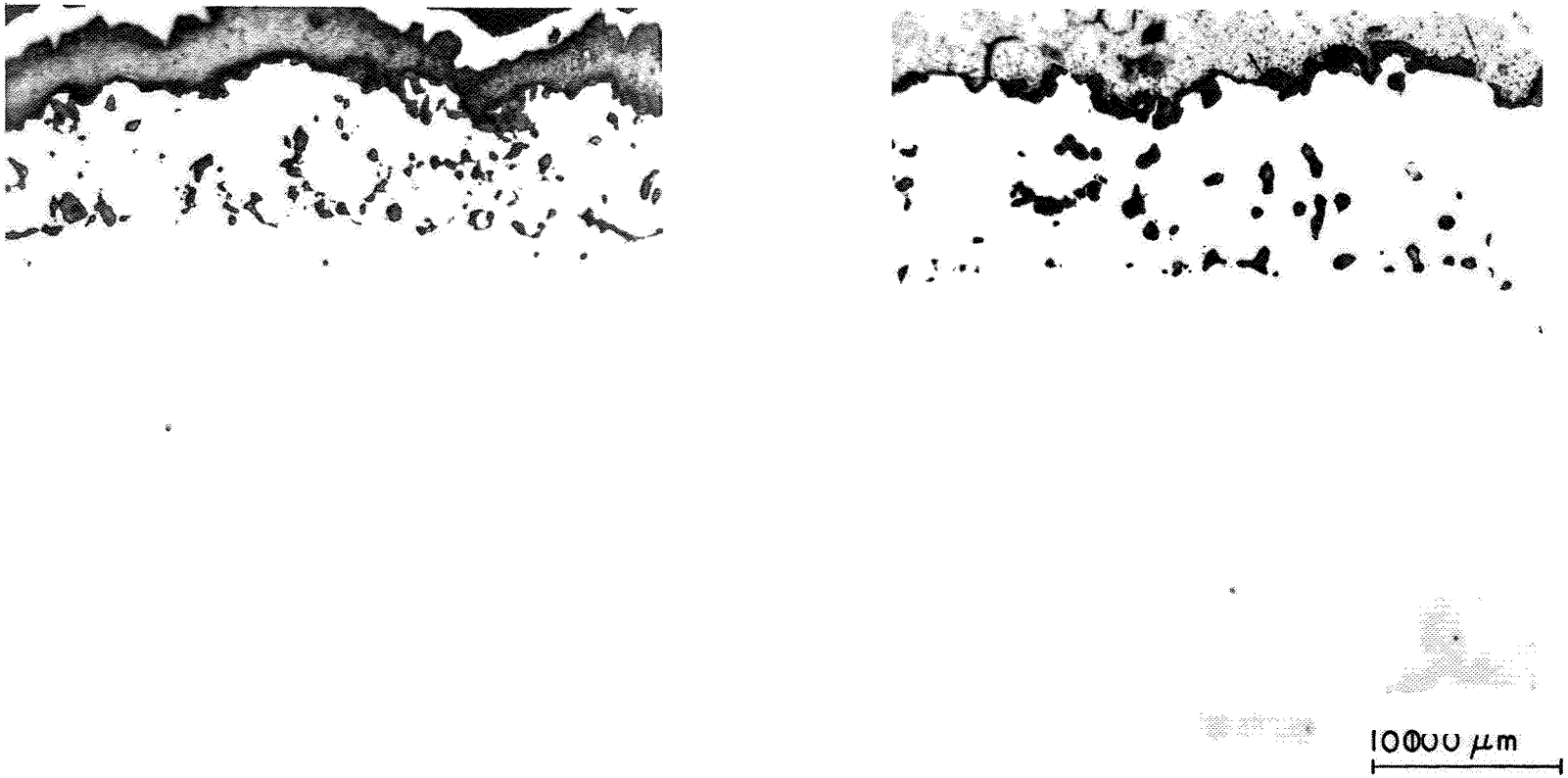

a. Ni-10Cr 10 Cycles

b. Ni-10Cr-10Al 50 Cycles

Figure 6 Microstructures of the Coating and Substrate.

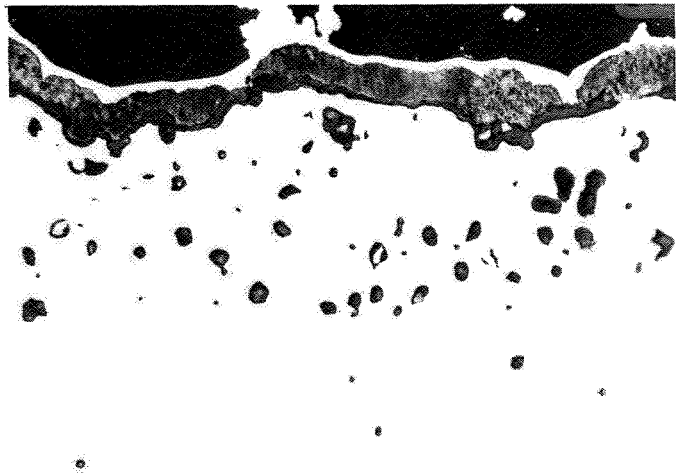

c

Ni-10Al 250 Cycles

a

Ni-10Cr 250 Cycles

Figure 6 (con't.) Microstructures of the Coating / Substrate

a

Ni-10Cr-10Al 200 Cycles

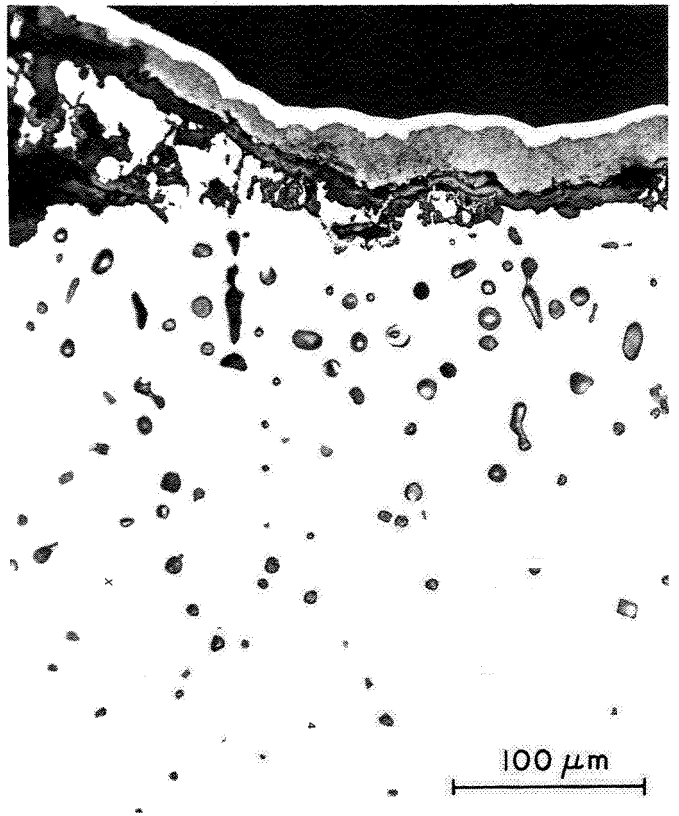

f.

Ni-20Cr 200 Cycles

Fig. 6 (con't.) Microstructures of the Coating and Substrate.

g. Ni-20Cr 250 Cycles

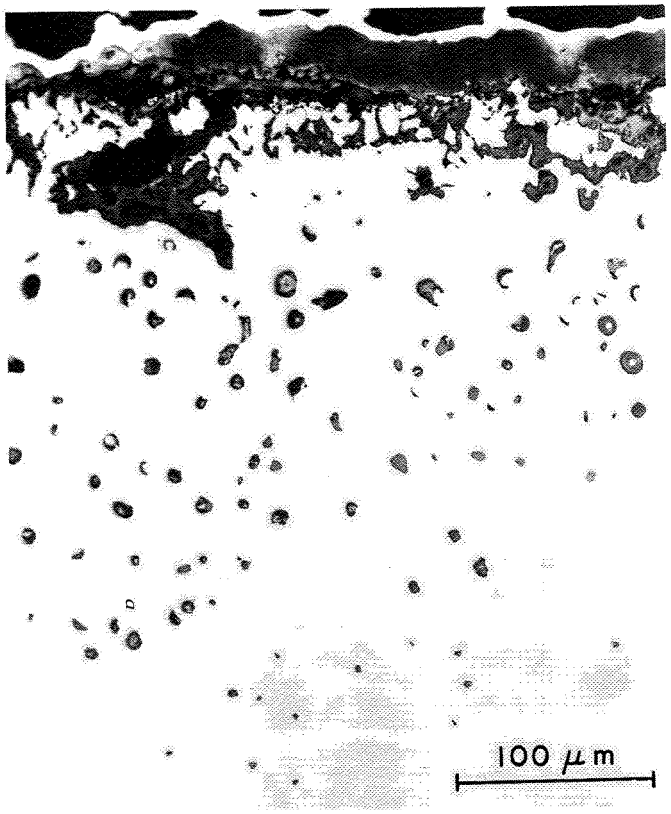

h. Ni-10Cr-10Al 200 Cycles

Figure 6 (con't.) Microstructures of the Coating and Substrate.

and cooling of the pins could permit the oxidizing gas to penetrate into the coating to continue growth of the stringers.

Al_2O_3 precipitates were observed in both the coating and substrate (Figure 6g and h). The Al_2O_3 precipitates were usually discernible from the Kirkendall porosity by their faceted geometry. Many of the precipitates were in regions of relatively high Al concentrations (4-6 at.%). Very fine dispersions of Al_2O_3 precipitates (see Figure 2b) were observed near the end of the pins where complete coating spallation had occurred. Internal oxidation of Al would be expected below surface oxide scales of NiO or Cr_2O_3 (11,32). Link-up of internal oxides resulting in a continuous oxide layer (see Figure 2a) was observed in the Ni-10Al substrate near the end of the pin where complete coating spallation had occurred.

Considerable oxide formation was observed at the coating/substrate interface of the Ni-10Cr and Ni-20Cr pins oxidized for 250 cycles (Figures 6d and g). As previously mentioned, large portions of the coating were not in contact with the Ni-10Cr and Ni-20Cr substrates after 200 cycles. The oxidizing gas could easily travel along the coating/substrate interface after the coating had spalled from the end of the pin. Presence of the oxidizing gas at the coating/substrate interface would also account for the formation of Al_2O_3 precipitates in the Ni-20Cr substrate (Figure 6g).

Small oxide stringers growing in from the oxide scale were observed in the coating on the Ni-10Cr-10Al pins (Figure 6h) and on the Ni-20Cr pins (Figure 6f). Formation of the Al_2O_3 stringers probably resulted from an influx of oxygen into the coating associated with the onset of localized breakaway oxidation. (NiO and/or Cr_2O_3 were detected on both

coated substrates after 200 cycles). At one location link-up of the oxide stringers resulted in reforming a continuous Al_2O_3 layer (Figure 6f).

Concentration/Distance Profiles

Diffusion behavior associated with a finite coating thickness was reflected in many of the changes in the concentration/distance profiles which occurred with increasing cyclic oxidation exposure. Select concentration/distance profiles measured across the coating and into each of the substrates after various oxidation exposures are shown in Figures 7a-d. As expected, the Al content in the coating decreased rapidly due to coating/substrate interdiffusion (Figures 7a-d). The Cr concentration in the coating decreased when Cr diffused from the coating into the substrate (Figure 7b), increased when Cr diffused into the coating (Figure 7c), or underwent little change when the Cr content in the substrate and coating were similar (Figure 7a and d). The effect of the coating thickness is apparent in Figure 7b where the Al concentration in the 50 micron thick coating was 6-7 at.% after 100 cycles but was still 9-10 at.% after 200 cycles in the 100 micron thick coating. The maximum in the Cr concentration profile in the Ni-10Cr substrate (10 cycles, Figure 7a), the Ni-20Cr substrate (100 cycles, Figure 7c), and the Ni-10Cr-10Al substrate (50 cycles, Figure 7d) is indicative of the effect of the Al concentration gradient on the diffusion of Cr. A steep Al gradient decreasing from the coating to the substrate causes Cr to diffuse from the coating and to the substrate (see Appendix C). Apparently the presence of oxygen between the coating and Ni-10Cr substrate after 250 cycles depleted the Al in the coating

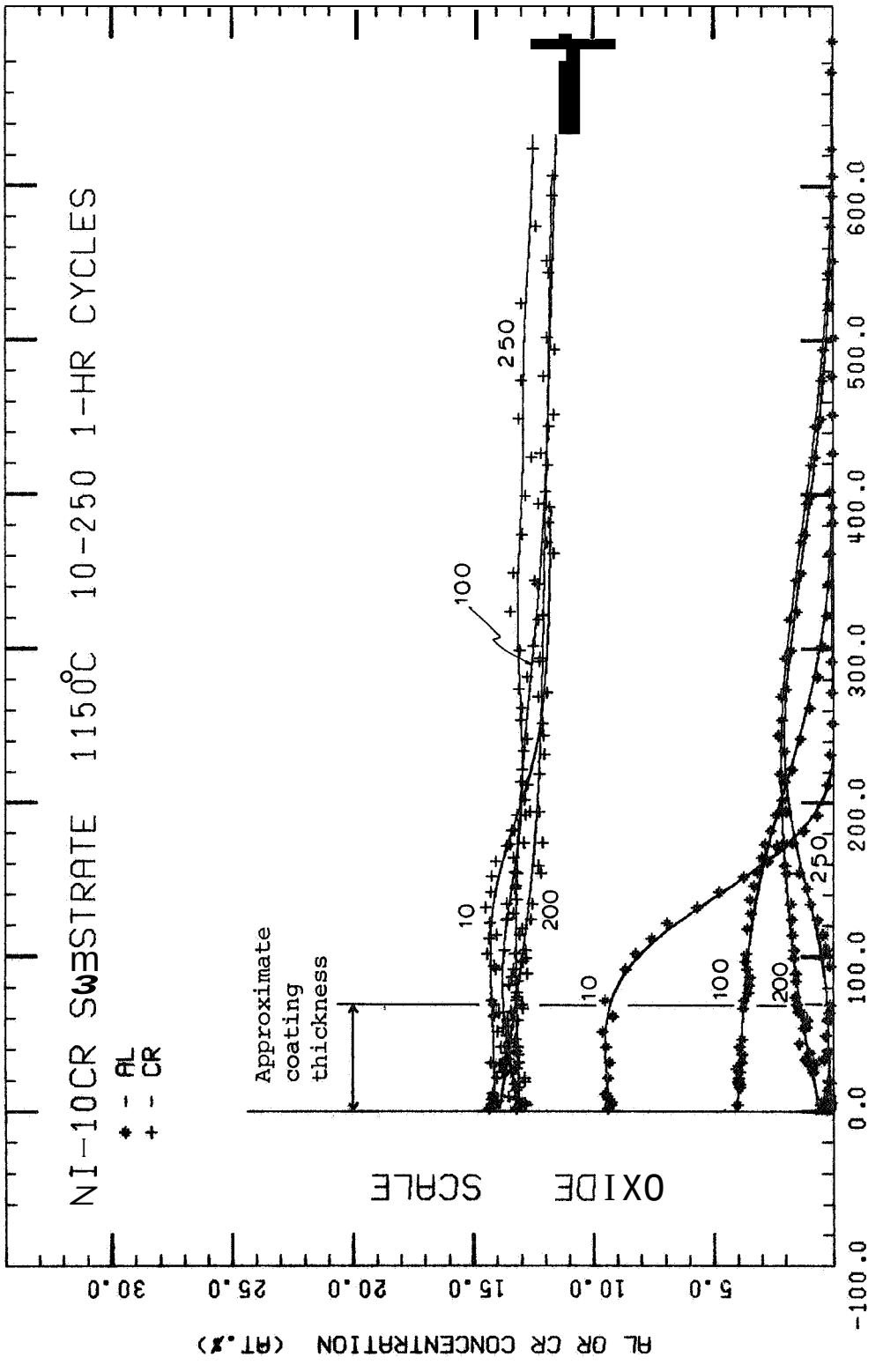

a.

Figure 7 Concentration/Distance Profiles in the Coating and Substrate
a. Ni-10Cr

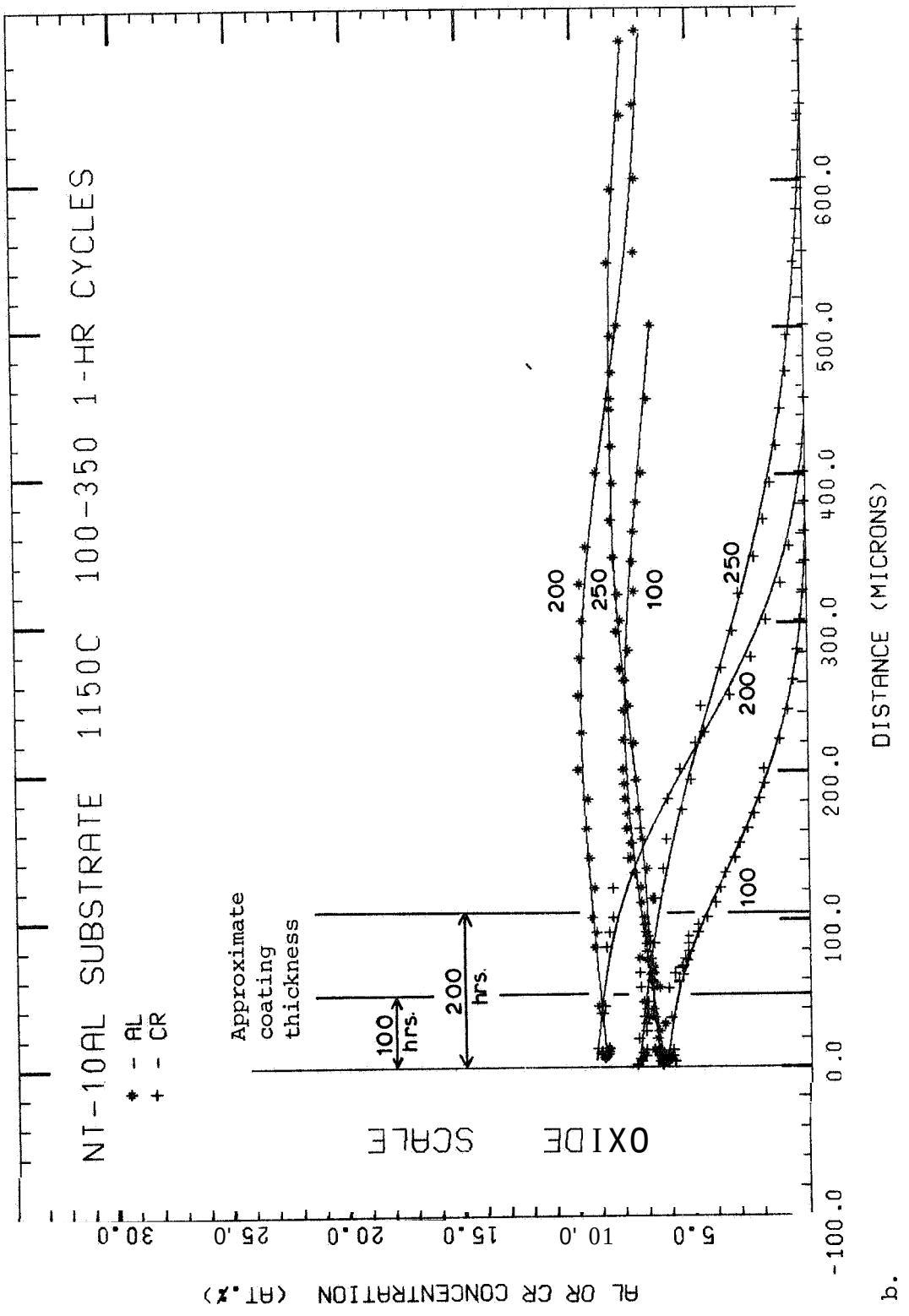

b.

Figure 7 (con't.) Concentration/Distance Profiles in the Coating and Substrate
b. Ni-10Al (The coating thickness for the pins oxidized for 100 and 200 cycles is indicated.)

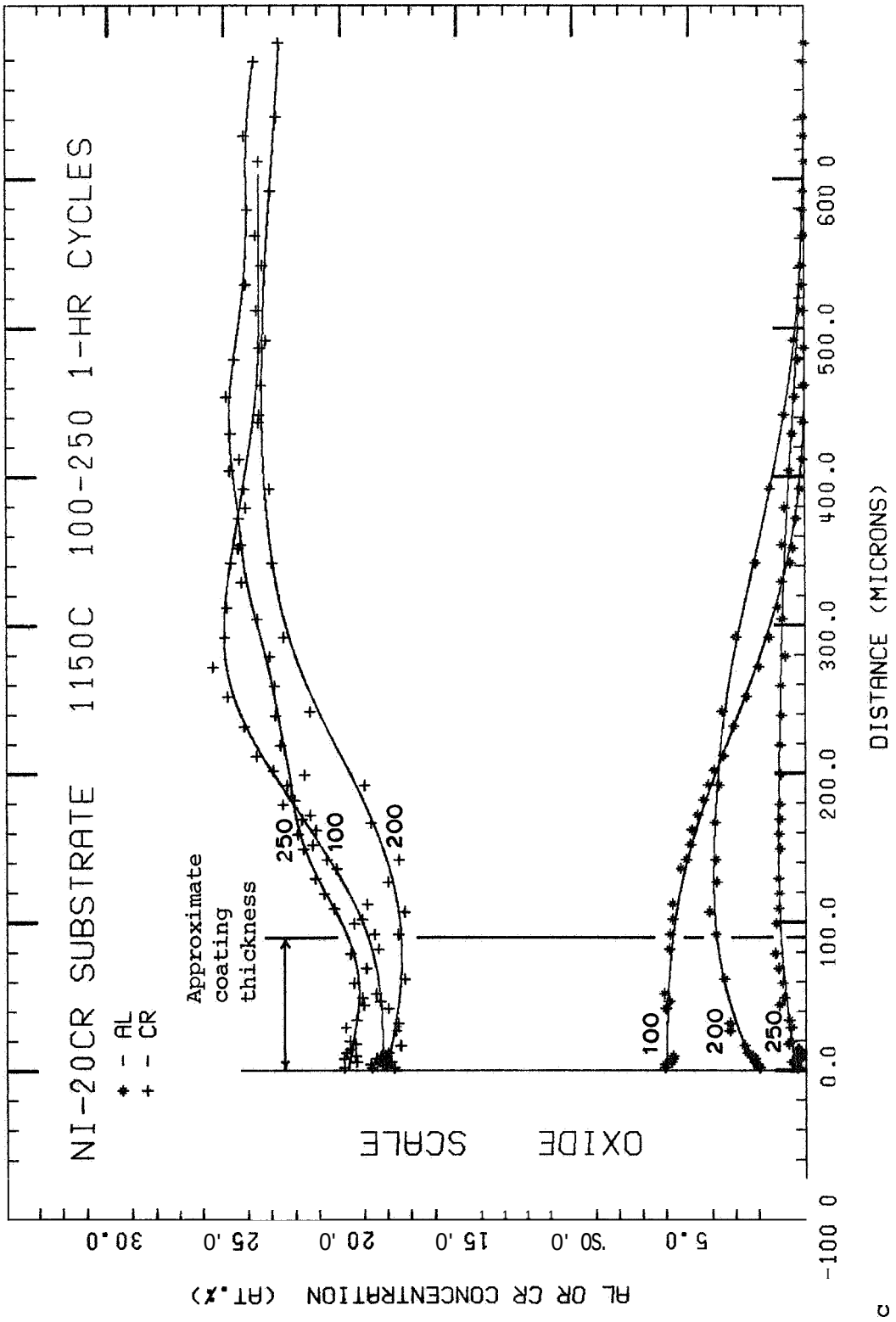

Figure 7 (con't.) Concentration/Distance Profiles in the Coating and Substrate
c. Ni-20Cr

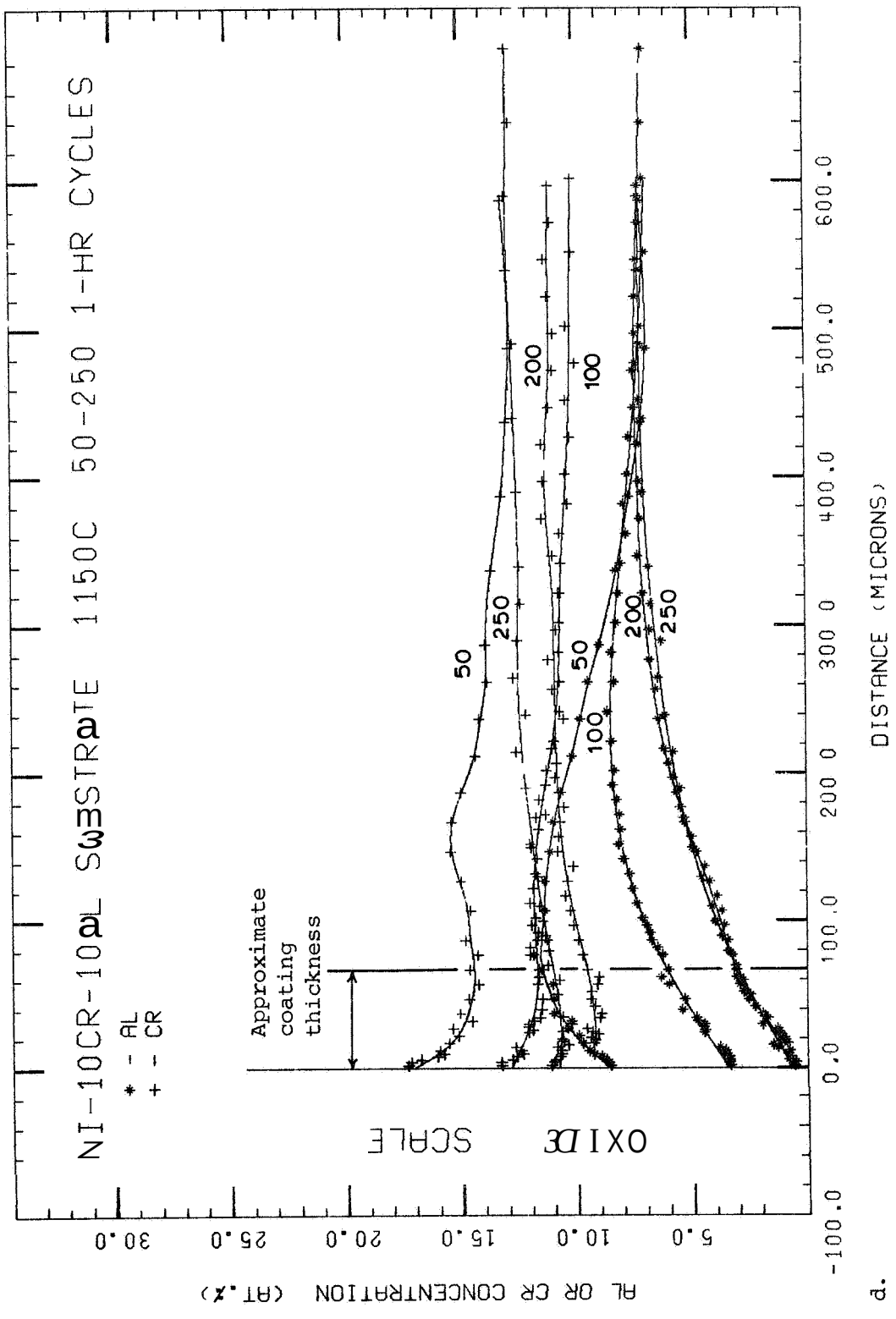

Figure 7 (con't.) Concentration/Distance Profiles in the Coating and Substrate
d. Ni-10Cr-10Al

(Figure 7a). Both the coating and Ni-20Cr substrate are almost depleted of Al after 250 cycles (Figure 7c).

The rate of Al consumption for each coating/substrate was reflected in the Al concentration profiles in the coating. It is obvious that the higher the rate of Al consumption, the steeper the Al gradient towards the oxide scale. The coating on the Ni-10Cr-10Al substrate, which exhibited the poorest resistance to oxide spallation (Figure 3d), contained the steepest Al concentration gradients. The Al gradients in the coatings on the Ni-10Cr and Ni-10Al substrates, which exhibited the best resistance to oxide spallation, were much less steep. Clearly, the oxide scale places a lower demand on the transport of Al in the coating for the pins which exhibit good oxide spalling resistance.

Each of the four coated substrates exhibit unnaturally high weight gains for oxidation at 1150°C. The maximum weight gain during cyclic oxidation should ideally be no greater than that which occurs during isothermal oxidation assuming formation of the same oxide scale. The Ni-20Cr and Ni-10Cr-10Al pins reach a maximum weight gain of 1-2 mg/cm^2 after approximately 30 cycles (Figures 3c and d). The weight of the Ni-10Cr pins increased to 3.2-4.9 mg/cm^2 after 190 cycles (Figure 3a). For isothermal oxidation at 1150°C, the parabolic growth constants reported in the literature for $Al_2O_3/NiAl_2O_4$ scales are in the range of 0.002-0.015 mg^2/cm^4 (11,17,32,44,46). The growth constant is reported as high as 0.025 mg^2/cm^4 for isothermal oxidation of commercial superalloys where oxide doping effects may be significant (44). Taking 0.025 mg^2/cm^4 as the growth constant, the weight gain for isothermal oxidation after 30 hours is less than 1 mg/cm^2, while the weight gain after 190 hours is only 2.2 mg/cm^2. External oxide formation on a very

irregular, non-planar surface could account for much of the large weight gains observed with each of the coated substrates (Figure 3). Sprayed overlay coatings typically possess rough external surfaces (2,47). An irregular, non-planar oxide/metal interface is apparent in many of the micrographs presented in Figure 6. The oxide formation growing in from the external scale could also partially account for the large weight gains observed after only 30 cycles.

The presence of Kirkendall porosity in the coating and substrate can be directly attributed to an intrinsic flux imbalance. The occurrence of porosity has previously been reported for the NiCrAl system during oxidation (45) and interdiffusion (22, see also Appendix C). An intrinsic flux imbalance will occur whenever the number of atoms diffusing in one direction is greater than the number diffusing in the reverse direction. Consequently, a net flux of vacancies equal to, and opposite to the intrinsic flux imbalance must exist. Vacancy coalescence resulting in porosity may occur if sufficient lattice imperfections are not available to absorb and equilibrate the vacancy flux. Appendix C has suggested a qualitative ranking of the intrinsic diffusivities as:

$$D_{AlAl} > D_{CrCr} > D_{NiNi}$$

Therefore, a high intrinsic Al flux from the coating towards the substrate would produce a vacancy flux in the reverse direction from the substrate towards the coating. Vacancy coalescence would most likely occur in the coating or at the coating/substrate interface (see Figures 6a and b). The vacancy flux toward the coating would diminish after coating/substrate interdiffusion reduced the large Al concentration difference between the coating and substrate. The

concentration/distance profiles shown in Figures 7a-d indicate that the Al content of the coating is significantly reduced after only 10-50 cycles. A high rate of Al consumption at the oxide/metal interface resulting from poor oxide scale adherence may cause a significant Al flux in the coating and substrate towards the oxide scale (Figure 7d). In this case, the vacancy flux would be away from the oxide and into the substrate. Vacancy coalescence would now be expected to occur in either the coating or the substrate. Therefore, the porosity observed in the Ni-10Cr-10Al substrate after 200 cycles (Figures 6c and h) is not surprising considering the high rate of Al consumption at the oxide/coating interface. Figure 6c indicates that some of the porosity may be interconnected. Oxygen transport via interconnected porosity would explain the formation of Al_2O_3 precipitates where the Al content in the surrounding matrix is unacceptably high (4-6 at.%) for the occurrence of classical internal oxidation (48,49).

The concentration/distance profiles (Figures 7a-d) permit determination of the weight of Al consumed by oxidation. The weight of Al consumed can be calculated from the difference between the initial mass of Al in the coating and substrate, and the mass of Al which is present after oxidation. The initial mass of Al present can be calculated from the Al concentration of the substrate and coating, and the coating thickness. The mass of Al present after oxidation can be determined after measuring the area under the Al concentration/distance profile. The initial coating thickness has been approximated as the coating thickness measured after oxidation. (Surface recession due to loss of Al only was calculated to be approximately 5 microns after 200 cycles for the Ni-10Cr and Ni-10Al substrates.) The weight of Al

consumed for each of the oxidized pins is shown in Figure 8. The uncertainty in the weight of Al consumed shown in Figure 8 is the result of the uncertainty in the measurement of the thickness of the coating after oxidation. The Ni-10Cr and Ni-10Al pins exhibit the lowest loss of Al as expected from the weight change data and the concentration/distance profiles. The Ni-10Cr-10Al pins exhibit the highest Al loss through 200 cycles. Even so, the Al losses after 100 and 200 cycles for the Ni-10Cr-10Al pins is probably underestimated. The large amount of oxide spall would indicate that considerable surface recession had occurred (due to rapid growth of NiO and Cr_2O_3 oxides). There was so little coating left after 250 cycles that it was impossible to determine the initial coating thickness, Calculating the loss of Al based on a thinner coating than was actually present would produce a lower weight of Al consumed.

The Cr concentration/distance profiles can be used to estimate the original Cr content of the coating. Following a similar procedure as that outlined above for Al, and assuming negligible loss of Cr to the oxide scale allows the initial Cr concentration in the coating to be estimated. The assumption of negligible loss of Cr to the scale is a good approximation for the Ni-10Cr and Ni-10Al pins on which Cr_2O_3 was not detected. Calculations of the initial Cr content of the coating indicate an approximate concentration of 16 at.%, slightly higher than the Cr content of the starting powder (13.5 at.%) sprayed onto the substrate pins. Quantitative electron microscopy of the as sprayed, two-phase coating could reveal the exact composition of the coating after application.

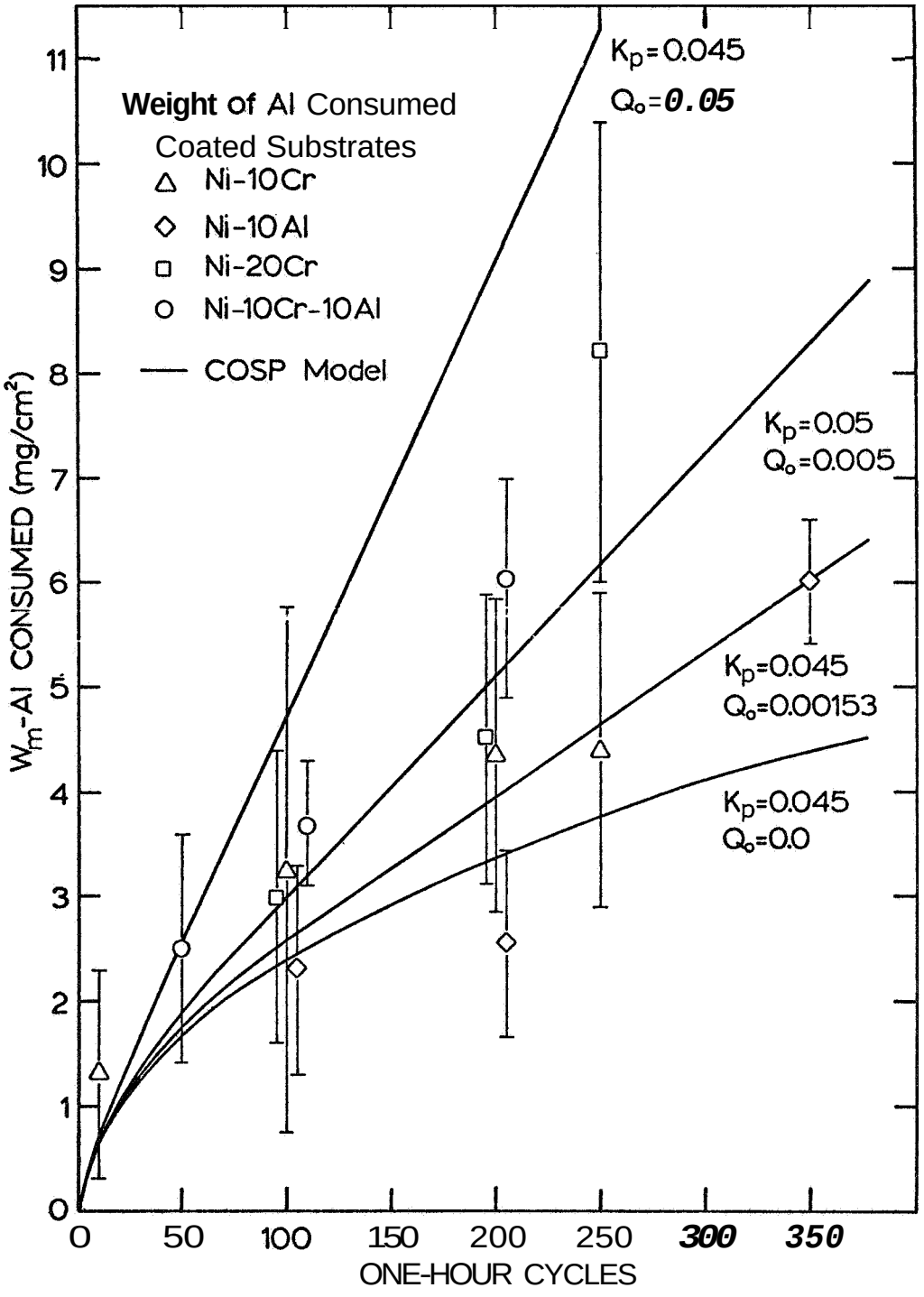

Figure 8 Weight of Al Consumed During Cyclic Oxidation.

Before concluding this section it is interesting to examine the cyclic oxidation behavior of the four coated substrates as reflected by the weight change data, the concentration profiles, and the weight of Al consumed. A wide spectrum of oxidation behavior was observed (Figures 3a-d) from excellent resistance to spallation (Ni-10Cr pins) to very poor resistance to spallation (Ni-10Cr-10Al). It is curious as to why the Ni-10Cr-10Al pin, with the same initial coating, exhibited the poorest oxidation resistance. Intuitively it would be expected that the Ni-10Cr-10Al pins would exhibit oxidation behavior very similar to either the Ni-10Cr or Ni-10Al pins. The oxidation behavior of the Ni-10Cr-10Al pins demonstrates the need for a better understanding of stress-induced scale spallation during cyclic oxidation. Several studies have already been accomplished towards this purpose (50,51). It is unknown what characteristic of the Ni-10Cr-10Al substrate consistently caused the poor cyclic oxidation behavior. It was noted that the room-temperature hardness of the four substrates were ranked in the same order as the resistance to oxide spallation as reflected by the weight change data. The Ni-10Cr-10Al substrate had twice the hardness of the Ni-10Cr and Ni-10Al substrates.

In summary, there was considerable variation in the oxidation behavior of the four coated substrates. The concentration/distance profiles, and particularly the Al concentration profiles and gradients, reflected the resistance to oxide spallation exhibited by the weight change of each pin during cyclic oxidation. The occurrence of Kirkendall porosity in the coating and substrates was generally explainable in terms of the intrinsic fluxes. The poor spalling

resistance of the coated Ni-10Cr-10Al substrate again points out the need for further study towards the cause of oxide scale spallation.

Numerical Modeling

Simulating complex diffusion phenomena typically requires the use of numerical techniques. The basic equation governing diffusion in alloys is Fick's second law, which for NiCrAl alloys can be stated as *(36)*:

$$\frac{\partial C_{Al}}{\partial t} = \frac{\partial}{\partial X}\left(D_{AlAl}\frac{\partial C_{Al}}{\partial X}\right) + \frac{\partial}{\partial X}\left(D_{AlCr}\frac{\partial C_{Cr}}{\partial X}\right)$$

$$\frac{\partial C_{Cr}}{\partial t} = \frac{\partial}{\partial X}\left(D_{CrAl}\frac{\partial C_{Al}}{\partial X}\right) + \frac{\partial}{\partial X}\left(D_{CrCr}\frac{\partial C_{Cr}}{\partial X}\right)$$

Analytical, closed-form solutions to Equation [1] are available if certain simplifications can be made. For instance, an analytical solution has been derived for semi-infinite γ/γ and γ/β diffusion couples (36,52-55) when the diffusion coefficients are assumed to be independent of concentration. Solutions have also been derived for γ/γ and γ/β interdiffusion in the dilute solution range (55-58) where the diffusivities were described as:

$$\frac{D_{12}}{D_{11}} = \varepsilon_{12}$$

$$\frac{D_{21}}{D_{22}} = \varepsilon_{21} C_2$$

where D_{11} and D_{22} are assumed independent of concentration.

Numerical techniques are required when the diffusivities are not independent of concentration or when complex boundary conditions exist. Examples of complex boundary conditions are time-dependent surface

concentrations as might occur during carburization (59) or, during homogenization after aluminization or carburization (59-61). In addition, complex boundary conditions result when diffusion fields overlap as during the latter stages of precipitation (62), or when diffusion occurs in a slab of finite width (63). Numerical techniques are also required when diffusion occurs under non-isothermal conditions (59,64). In this case, the diffusivities vary not only with concentration but also as a function of time.

A numerical model, entitled COSIM, was developed to simulate overlay coating degradation by simultaneous oxidation and coating/substrate interdiffusion. A numerical model was necessary to account for the concentration dependence of the four diffusivities in the γ phase of the NiCrAl system (see Appendix C). In addition to a finite coating width, a complex boundary condition exists at the oxide/metal interface. This boundary condition was supplied as the rate of Al consumption predicted by the COSP spalling model (65). The COSP spalling model, developed at NASA-Lewis Research Center, simulates oxide growth and spallation during cyclic oxidation. Finite-difference techniques were utilized in the COSIM model to simulate diffusional transport of both Al and Cr in the coating and substrate. Finite-difference techniques have previously been used successfully to simulate diffusion in binary systems (59,60,63) and in ternary alloys (59,62,64). Typically some simplifying assumptions are made concerning the concentration dependence of ternary diffusivities (59,62,63) to reduce the necessary computation time. No simplifications regarding the ternary diffusivities were made in the numerical model developed in this

study. The basic operation of the COSIM model is discussed in Appendix E.

Several assumptions were required in the development of the numerical model. These assumptions were:

1. The oxide/metal interface was planar.
2. The partial molar volumes of Al and Cr were concentration independent.
3. Diffusion occurred only at the oxidizing temperature (i.e., sample heat-up and cool-down was rapid).
4. Only Al_2O_3 was formed.
5. The two-phase coating could be approximated as a single phase of equivalent Al and Cr content.
6. The ternary diffusivities appropriate for the γ phase could be extrapolated to the high Al concentration in the assumed, single-phase coating.

Each of the above assumptions are discussed shortly.

Parameters input to the COSIM model consisted of the Al and Cr content of the coating and substrate, as well as the coating thickness. The model also required the concentration dependence of the ternary diffusion coefficients appropriate for the oxidation temperature. The concentration dependence of the diffusivities is given in Table 2. The Zr initially present in the coating (0.05 at.%) has previously been shown to have a negligible effect on interdiffusion in NiCrAl(Zr) alloys (66). The COSP spalling model requires input of a parabolic oxide growth constant, k_p, and two spalling parameters, Q_Θ and Alpha (Appendix E). The growth constant, k_p, can be determined from an isothermal oxidation test. The parameters Q_Θ and Alpha are determined by best fit

Table 2

Concentration Dependence of the
Ternary Diffusion Coefficients
Ni Solid Solution: 1150°C

$D\ (cm^2/s) \times 10^{10}$

$$D_{AlAl} = 1.81 \pm 0.39 \times Al + 0.030 \times Cr + 0.013 \times Al^2 - 0.0005 \times Cr^2$$

$$D_{AlCr} = 0.024 + 0.18 \times Al - 0.0043 \times Cr + 0.0067 \times Al^2 + 0.0001 \times Cr^3$$

$$D_{CrAl} = -0.24 + 0.055 \times Al + 0.20 \times Cr - 0.0023 \times Al^2 - 0.0035 \times Cr^2$$

$$D_{CrCr} = 1.53 - 0.11 \times Al + 0.071 \times Cr + 0.013 \times Al^2 - 0.0015 \times Cr^2$$

Al and Cr concentrations in atom per cent.

of the COSP-predicted weight change and experimental weight change measured during cyclic oxidation (see Figure 3 and Appendix E).

The COSIM model predicts the Al and Cr concentration/distance profiles in the coating and in the substrate after a set number of oxidation cycles. More importantly, the COSIM model predicts the time variation of the Al concentration at the oxide/metal interface. Consequently, the COSIM model is able to predict the time at which the coating is unable to supply sufficient Al to the oxide scale resulting in formation of less protective oxides.

Results and Discussion

The COSIM model has been utilized to simulate coating degradation for each of the four coated substrates discussed in the experimental section of this report. The measured and predicted concentration/distance profiles were compared to establish the predictive capability of the model.

Input to COSIM

The composition of the substrates input to the COSIM model were measured in the substrates after oxidation at locations where negligible diffusion had occurred (right-most concentrations, Figures 7a-d). The Al concentration of the coating was assumed equal to the Al concentration of the starting powder. The Cr concentration of the coating was increased to 16 at.% based on the results discussed in the experimental section of this report. The average coating thickness (X_o) measured on each pin after oxidation was also input to the COSIM model.

Input to COSP

The same parabolic oxide growth constant (k_P) was input to the COSP model for each of the coated substrates. An oxide growth constant of 0.045 mg^2/cm^4 was chosen to account for the observed weight gain during cyclic oxidation (Figure 3a). This oxide growth constant was approximately three times greater than the highest growth constant for isothermal growth of $Al_2O_3/NiAl_2O_4$ scales found in the literature (44). Since each of the coated substrates exhibited large weight gains after short cyclic oxidation exposures (Figure 3), the large value for k_P appeared reasonable considering the weight change data. The spalling parameter Q_o was determined for each of the coated substrates by comparing the weight change predicted by the COSP model with the weight change measured during cyclic oxidation (Figure 3). The spalling parameter Alpha was set equal to one for all substrates. There was good agreement between the measured and predicted weight change for the Ni-10Cr and Ni-10Al substrates as shown in Figures 3a and b. There was reasonable agreement between the measured and predicted weight change for the Ni-20Cr substrate (Figure 3c). An even larger value of k_P would be required to account for the weight increase of the Ni-20Cr pins between 0-50 cycles. There was not good agreement between the measured and predicted weight change for the Ni-10Cr-10Al pins (Figure 3d). The rapid weight gain (0- 50 cycles) followed by the accelerated weight loss could not be matched with reasonable combinations of k_P and Q_o. The failure to predict the weight change for this substrate was not unexpected. The COSP model assumes exclusive formation of an Al_2O_3 scale. After 100 cycles, five oxide phases were detected on the surface of the pin. After 200 hours, NiO was the dominate oxide phase present.

Comparing the weight of Al consumed measured on each of the substrates after cyclic oxidation with the weight of Al consumed predicted by the COSP model shows good agreement for the Ni-10Cr and Ni-10Al substrates (Figure 8). The COSP prediction is slightly high for the Ni-20Cr and Ni-10Cr-10Al substrates. Since the COSP model assumes only Al_2O_3 formation, spallation of less protective oxides as NiO or Cr_2O_3 will exaggerate the predicted consumption of Al. In addition, as previously mentioned in the experimental section, significant surface recession of the coating would also result in a low determination of the weight of Al consumed.

Concentration/Distance Profiles

Ni-10Cr Substrate. Very good agreement was found between the COSIM-predicted and measured Al and Cr concentration profiles for the Ni-10Cr pins. The concentration/distance profiles after 10-250 cycles are shown in Figure 9. Three points can be noted regarding the measured and predicted concentration/distance profiles after 10 cycles (Figure 9a). First, the area under the measured and predicted Al concentration profiles are obviously not equal. Either more Al is being consumed in the first 10 cycles than predicted, or there is less Al initially in the coating. The detection of small Al-rich (Al_2O_3) oxide particles in the coating indicates that some Al is oxidized during the low-pressure plasma spray process. Second, the measured Al content in the coating has decreased to less than 10 at.%, whereas the predicted Al content is 12-13 at.%. Reducing the initial Al content in the coating so that the areas under the measured and predicted Al profiles are equal still results in a higher predicted Al profile in the coating (but less in the

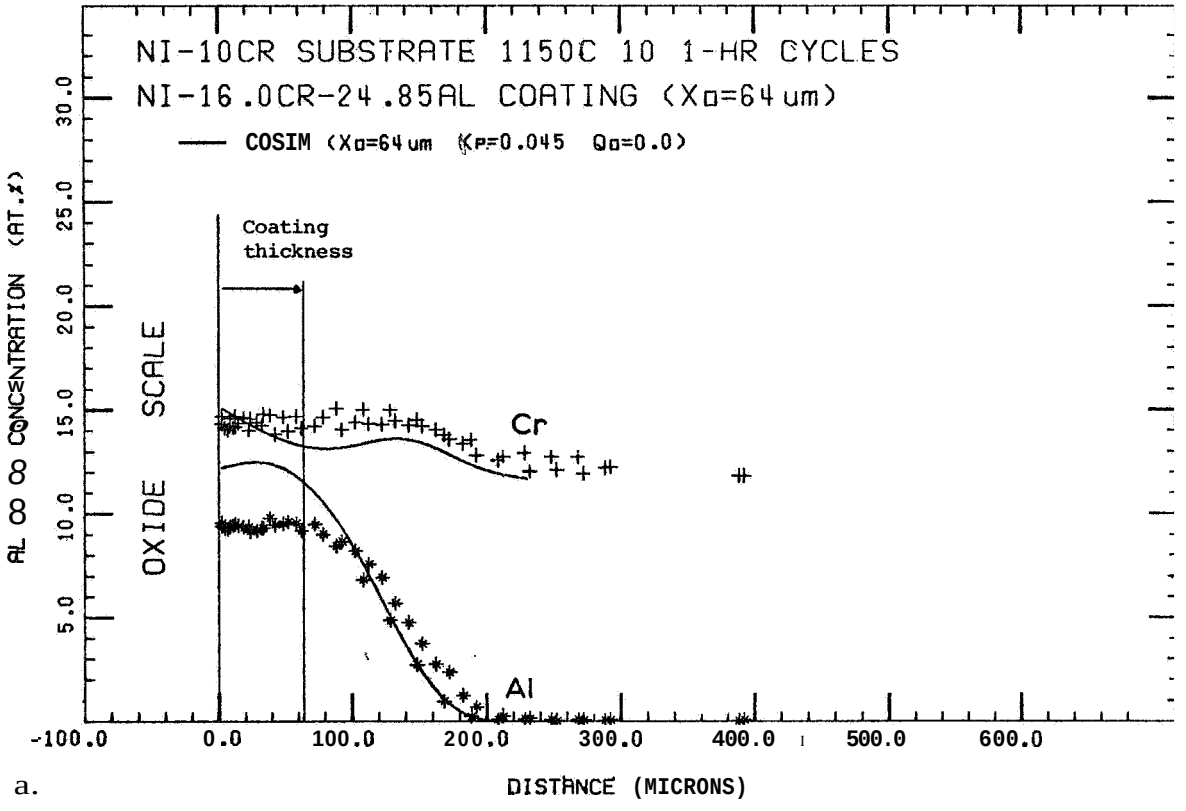

a.

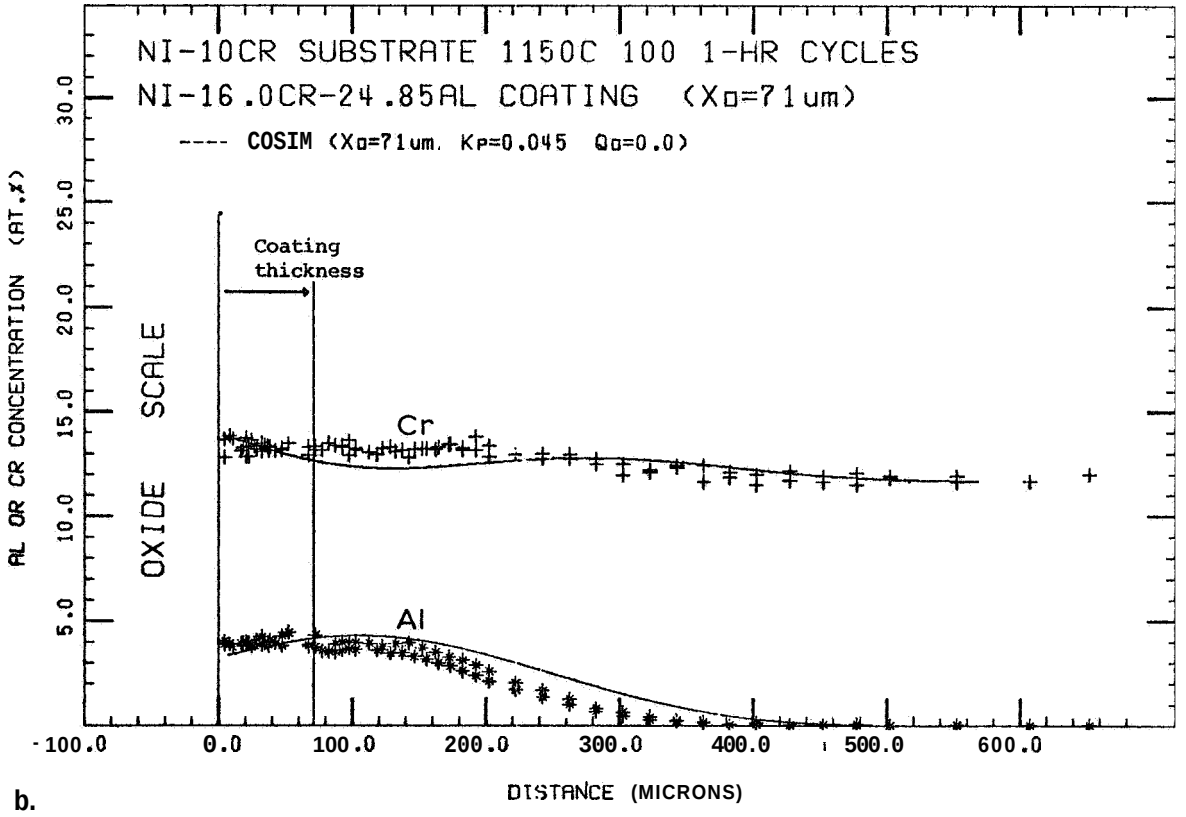

b.

Figure 9 Predicted and measured concentration/distance profiles for the Ni-10Cr pins a. after 10 cycles b. after 100 cycles.

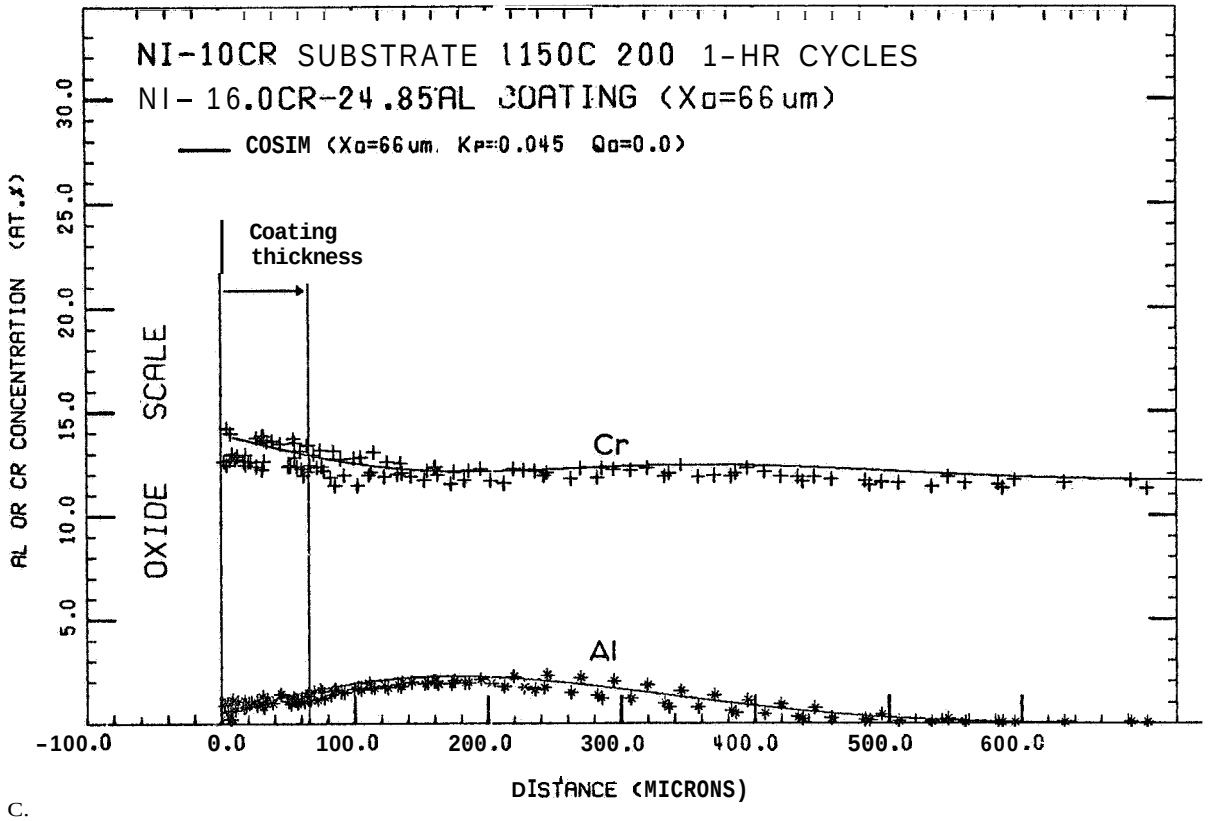

c.

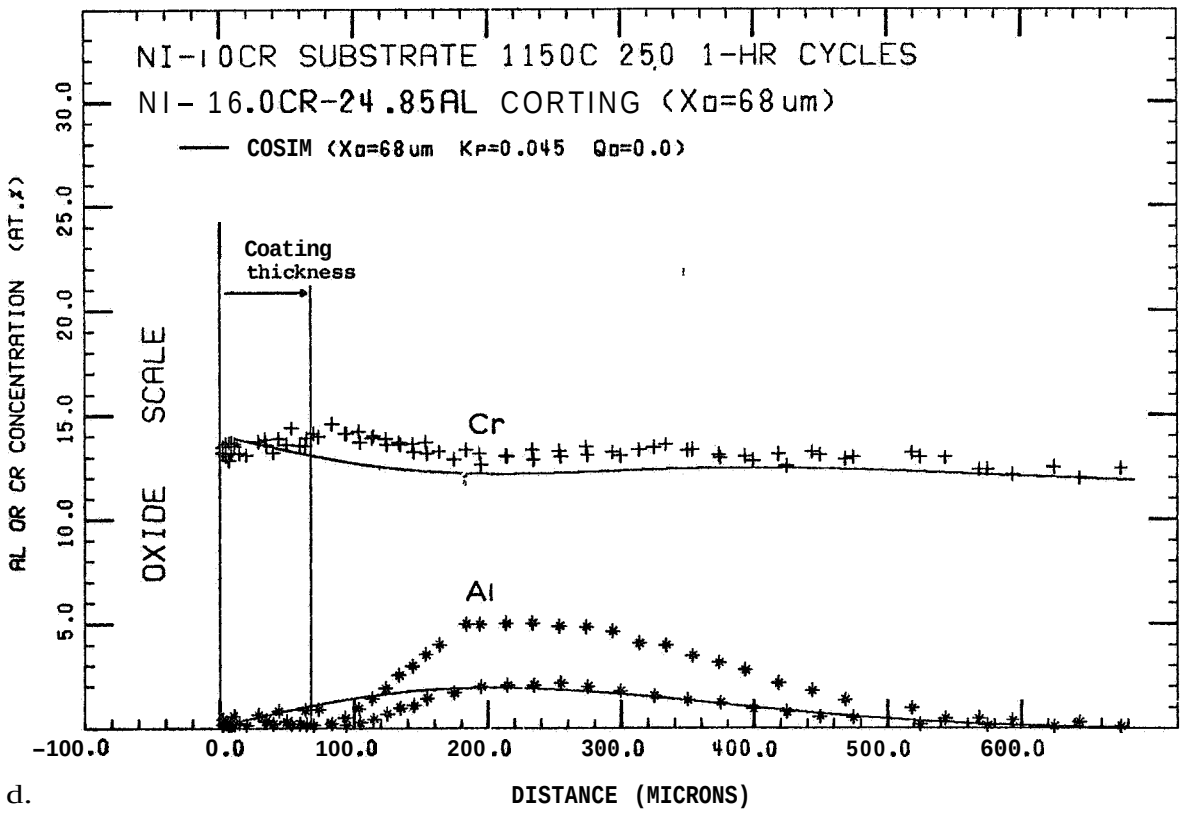

d.

Figure 9 (con't.) Predicted and measured concentration/distance profiles for the Ni-10Cr pins **c.** after 200 cycles d. after 250 cycles.

substrate). This result would indicate that diffusion of Al from the coating into the substrate occurs at a greater rate than that predicted by the COSIM model. The difference in the predicted and measured rate of interdiffusion after a short number of cycles could be due to the assumption that the two-phase coating could be approximated as a single phase, but would seem more likely to be the result of an unusually high Al flux from the coating to the substrate. A large initial Al flux was suggested in Appendix D. The third point to note is that the predicted Cr concentration profile is generally less than the measured Cr profile. This observation illustrates the increased Cr concentration in the coating above that reported for the starting powder (13.5 at.%). (The Predicted Cr concentration profiles shown in Figure 9 were based on 16 at.%Cr in the coating). The predicted profile exhibits the same general shape as the measured profile even though the predicted Cr concentration profile is less than that measured.

The maximum in the Cr concentration profiles (Figures 9a-c) is due to the ternary cross-term effect in which the Al concentration gradient has affected the diffusion of Cr. Maxima in the Cr concentration profiles were common in γ/γ diffusion couples where it was shown that $D_{CrAl} \simeq D_{CrCr}$. The effect of the Al concentration gradient in Figure 9 is to drive Cr out of the coating and into the substrate.

A high Al concentration profile was measured in the Ni-10Cr substrate (Figure 9d) where the coating and substrate had become detached. The high Al profile indicates that significant Al had diffused from the coating into the substrate after a short number of cycles and had been unable to diffuse back into the coating after the coating had become detached from the substrate. The almost continuous

oxide layer which formed at the coating/substrate interface after oxygen had been permitted entry beneath the coating (Figure 6d) would have also limited Al diffusion back into the coating. The COSIM prediction agrees very well with the lower Al profile (Figure 9d).

Ni-10Al Substrate. The COSIM predictions show reasonable agreement with the measured concentrations in the coating and in the Ni-10Al substrate (Figure 10). The fact that both the Al and Cr profiles predicted by COSIM are almost always less than the measured profiles indicates that a thicker coating may have been present where the concentration profiles were measured. Increasing the coating thickness by an amount equal to the uncertainty in the measurement of the coating ($\sim$13 microns) would account for much of the difference in the concentration profiles.

Ni-20Cr substrate. The concentration profiles predicted by the COSIM model show excellent agreement with the profiles measured for the Ni-20Cr pins (Figure 11a) after 100 cycles. Reasonable agreement is shown after 200 cycles but relatively poor agreement after 250 cycles (Figure 11b and c). The observed agreement is not surprising. After 100 cycles, only Al_2O_3 and $NiAl_2O_4$ oxide phases were detected on the surface of the oxidized pins. After 200 cycles, five oxide phases were detected, and after 250 cycles Cr_2O_3 was the dominant oxide phase retained on the pin surface. In addition, the coating and substrate were almost completely detached and considerable oxide formation had occurred at the coating/substrate interface after 250 cycles (Figure 6g). It appears again that detachment of the coating from the substrate has limited interdiffusion, the Cr concentration being very low in the coating where the coating and substrate were detached after 250 cycles

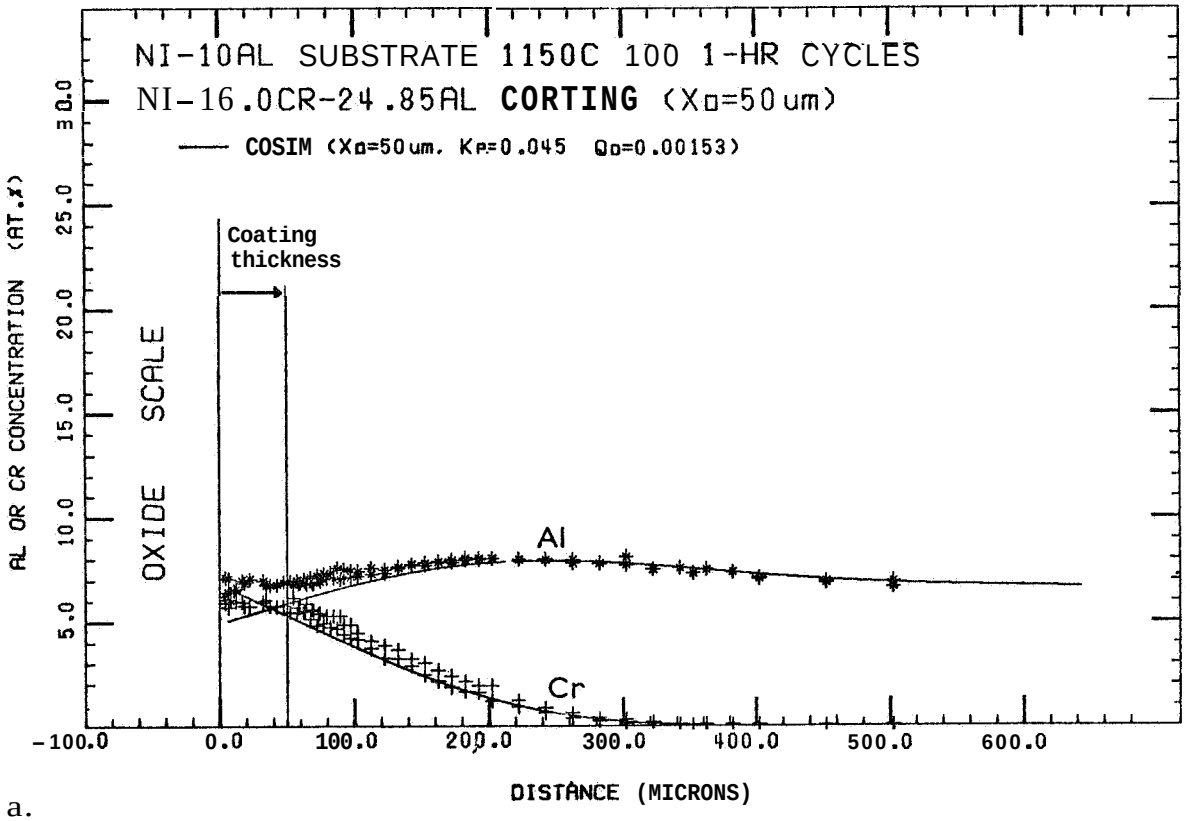

a.

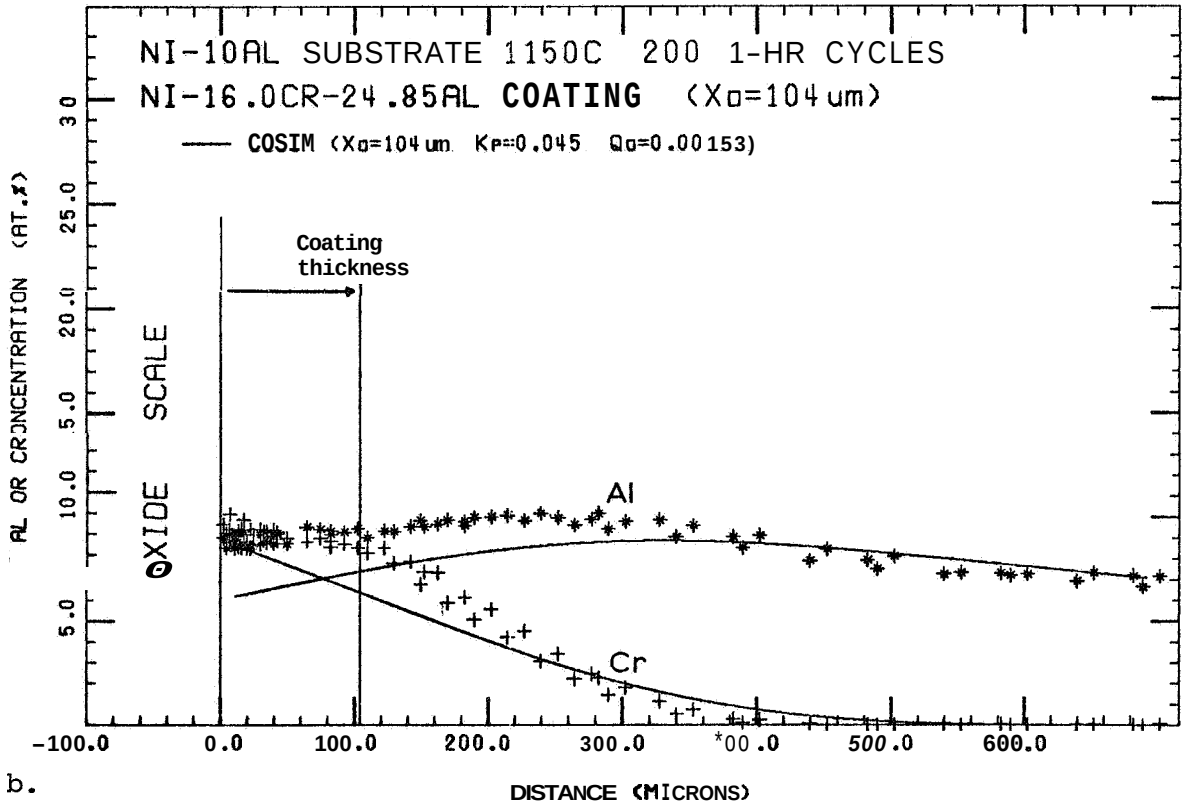

b.

Figure 10 Predicted and measured concentration/distance profiles for the Ni-10Al pins **a.** after 100 cycles b. after 200 cycles.

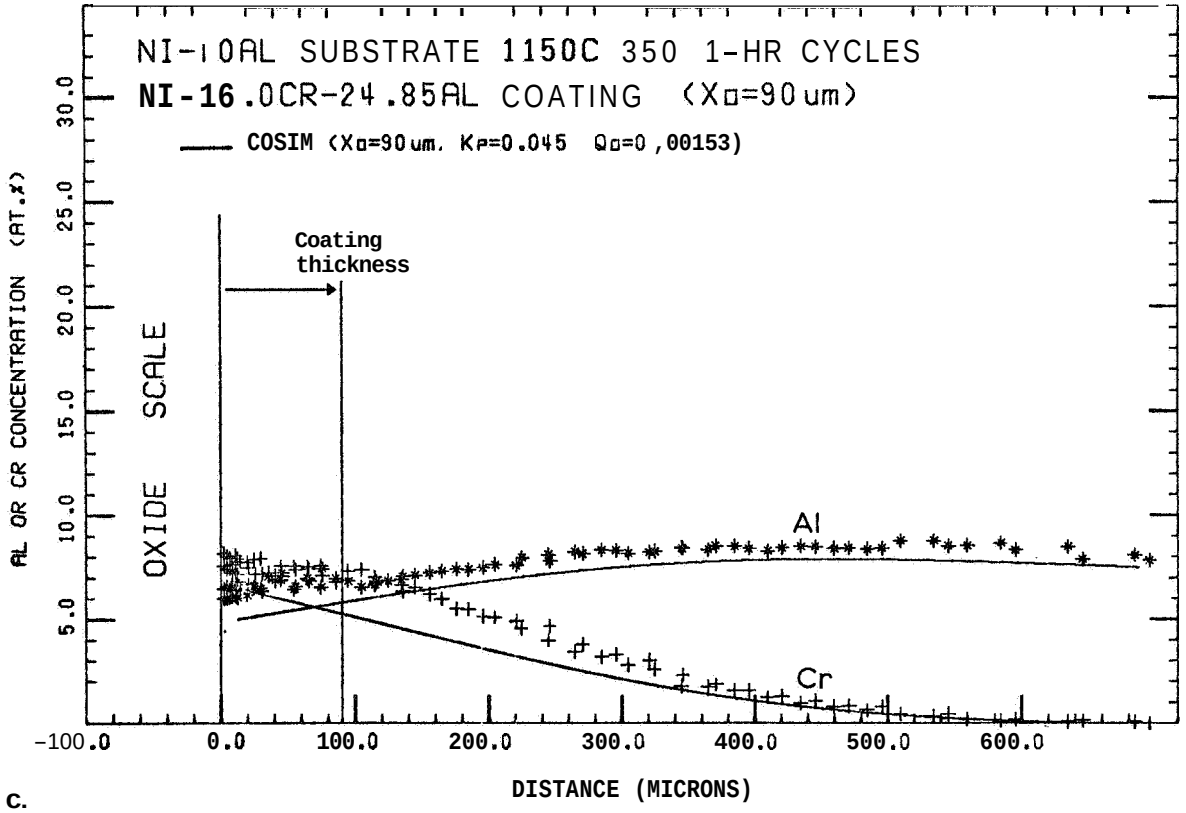

c.

Figure 10 (con't.) Predicted and measured concentration/distance profiles for the Ni-10Al pins c. after 359 cycles.

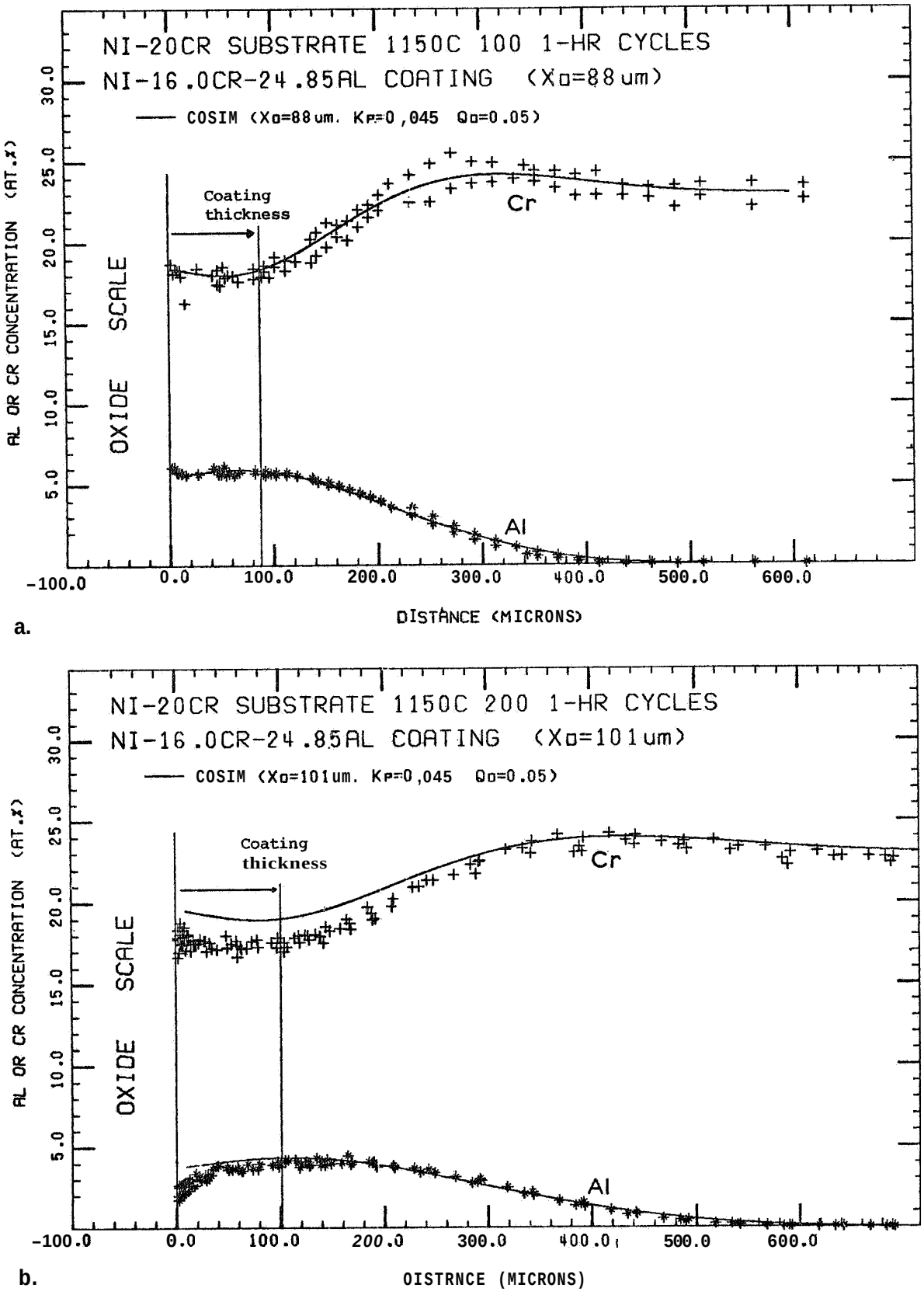

Figure 11 Predicted and measured concentration/distance profiles for the Ni-20Cr pins a. after 100 cycles b. after 200 cycles.

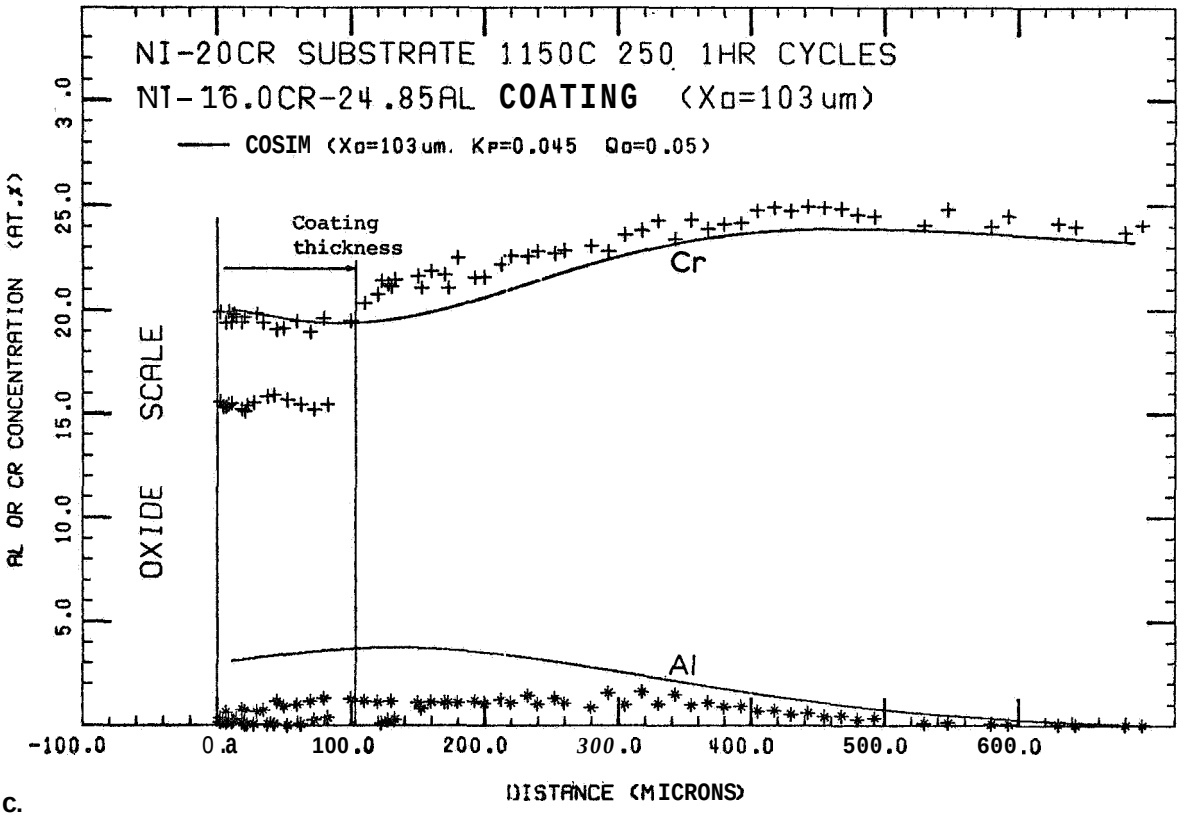

c.

Figure 11 (con't.) Predicted and measured concentration/distance profiles for the Ni-20Cr pins c. after 250 cycles. (Low Cr concentrations in coating were measured where the coating had become detached from the substrate.)

(Figure 11c). The Al content in the coating was almost completely depleted after the coating had become detached from both the Ni-10Cr (FIgure 9d) and Ni-20Cr (Figure 11c) substrates.

Ni-10Cr-10Al Substrate. There was good agreement between the measured and predicted concentration profile after 50 cycles, but less agreement after 100 cycles for the coating and Ni-10Cr-10Al substrate (Figure 12). The poor spalling resistance and high weight loss (Figure 3) exhibited by this alloy is the obvious cause of the poor fit. The formation of less-protective oxides between 50 and 100 cycles has increased the rate of Al consumption above that predicted by the COSP model as indicated by the Al concentration gradient near the oxide/metal interface. Simulating oxide spallation where several oxides have formed is beyond the predictive capability of the COSP or COSIM models.

The assumptions made in the development of the COSIM model can be reexamined to identify possible sources of inaccuracy introduced into the numerical model. The assumption of a planar oxide/metal interface is obviously only an approximation (see Figure 6). The reasonable agreement between the measured and predicted Al concentration profiles near the oxide/metal interface would indicate that this is not a critical approximation. The concentration dependence of the partial molar volumes of Al and Cr are not known. It has been previously shown that variation in the partial molar volume of Al has little effect on the overall diffusion behavior (45). The assumption that negligible diffusion occurred during heating and cooling of the pins appears justified considering the rapid heating and cooling rates (13) and the exponential relationship of the diffusion coefficients with temperature (29). The assumption that only Al_2O_3 has formed is obviously a better

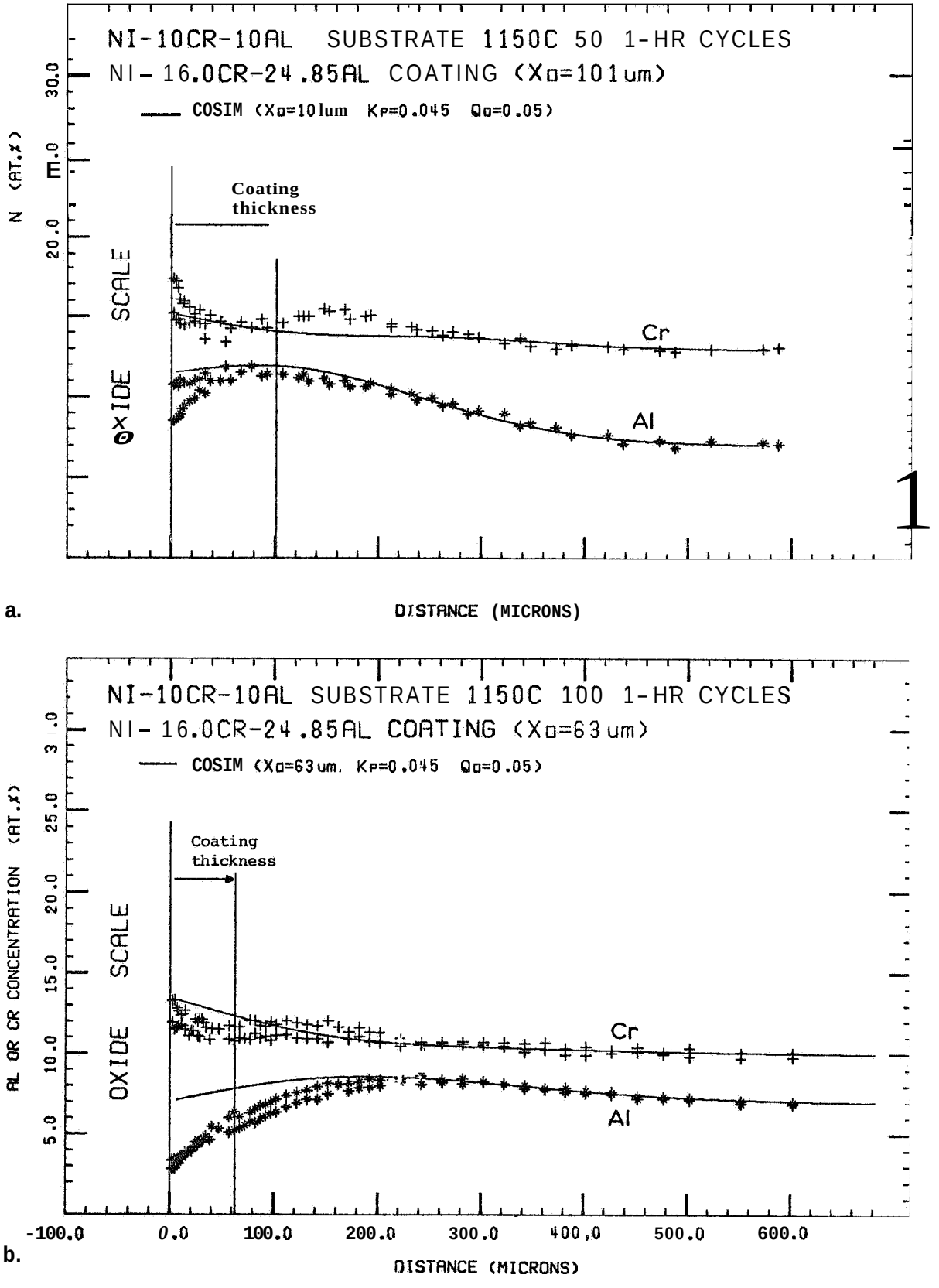

Figure 12 Predicted and measured concentration/distance profiles for the Ni-10Cr-10Al pins a. after 50 cycles b. after 100 cycles.

approximation for the Ni-10Cr and Ni-10Al pins than for the Ni-20Cr pins after 200 cycles or the Ni-10Cr-10Al pins after 50 cycles. As shown, the results indicate that the closer this approximation is to the actual case, the more accurate the prediction by the COSIM model. Approximating the two-phase coating as a single phase appears justified considering the relatively short time ($\sim$ 5-15 hours) that the β phase exists in the coating undergoing cyclic oxidation at 1150°C. The extrapolation of the ternary diffusivities to high Al concentrations in the coating also appears justified since the Al concentration in the coating decreases very rapidly to concentrations representative of the phase ($\sim$ 15 at.% Al).

In summary, the COSIM model has been shown to predict coating degradation by simultaneous oxidation and coating/substrate interdiffusion with reasonable success. As expected, the COSIM model. shows the best agreement with the measured profiles when Al_2O_3 is the main oxide formed on the pin surface. Many of the discrepancies between the measured and predicted profiles could be accounted for by the uncertainty in the initial coating thickness. Based on the agreement between the measured and predicted profiles, the COSIM model is considered as a reasonable and valid model to simulate diffusional degradation of overlay coatings.

Critical Parameters

The COSIM model was utilized to identify the most critical parameters in coating/substrate systems which influence coating life. To accomplish this task each of the main parameter input to the COSIM model were varied individually. The effect of each parameter on the time dependence of the Al concentration at the oxide/metal interface was

examined since a decrease in the Al concentration at this interface to approximately zero signals the onset of breakaway oxidation and coating failure.

The Al content of the substrate has a greater effect on the coating life than the Al content of the coating. The effect of the Al content in the coating and substrate is shown in Figure 13a. It is obvious that a 4 at.% increase in the Al content of the substrate has a much greater effect on coating life than a 5 at.% increase in the Al content of the coating. In addition, it was found that the total mass of Al in the coating is a more important parameter than the coating thickness or Al content of the coating taken separately. It makes little difference to the coating life when equivalent amounts of Al are in the coating. Increasing the coating thickness and decreasing the Al content, or decreasing the coating thickness and increasing the Al content changes the coating life very little.

The Cr content of either the coating or substrate has very little effect on the coating life as shown in Figure 13b. This result is a consequence of the limited effect of the Cr concentration gradient on the diffusion of Al ($D_{AlAl} >> D_{AlCr}$; Appendix C) and the limited dependence of D_{AlAl} on the Cr concentration (Appendix C).

Not surprisingly, the rate of Al consumption ($\dot{W}_m$) has a considerable effect on the coating life. The effect of the rate of Al consumption is illustrated in Figure 13c where the Al concentration at the oxide/metal interface is shown for three different rates of Al consumption. The rate of Al consumption $\dot{W}_m$ has been predicted by the COSP model for the input parameters k_P=0.05, Q_O=0.005 and Alpha=1.0. The weight of Al consumed predicted by the COSP model for this choice of

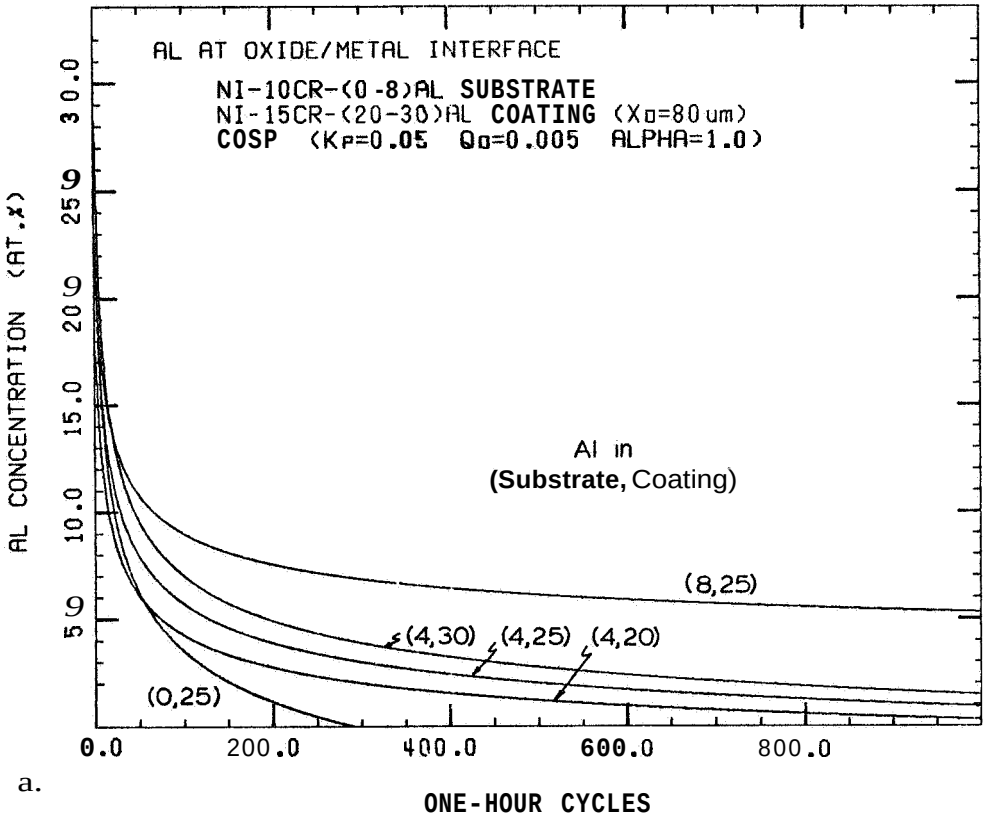

a.

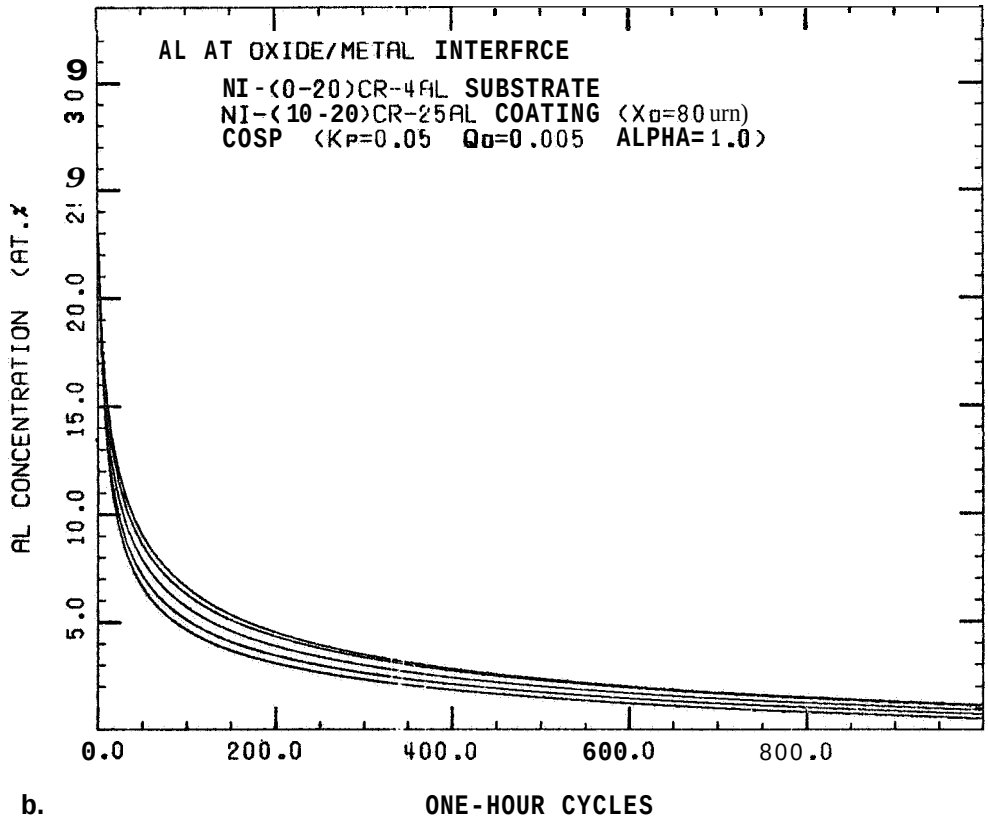

b.

Figure 13 **Effect of** coating composition, substrate composition and rate **of** Al consumption on coating life.

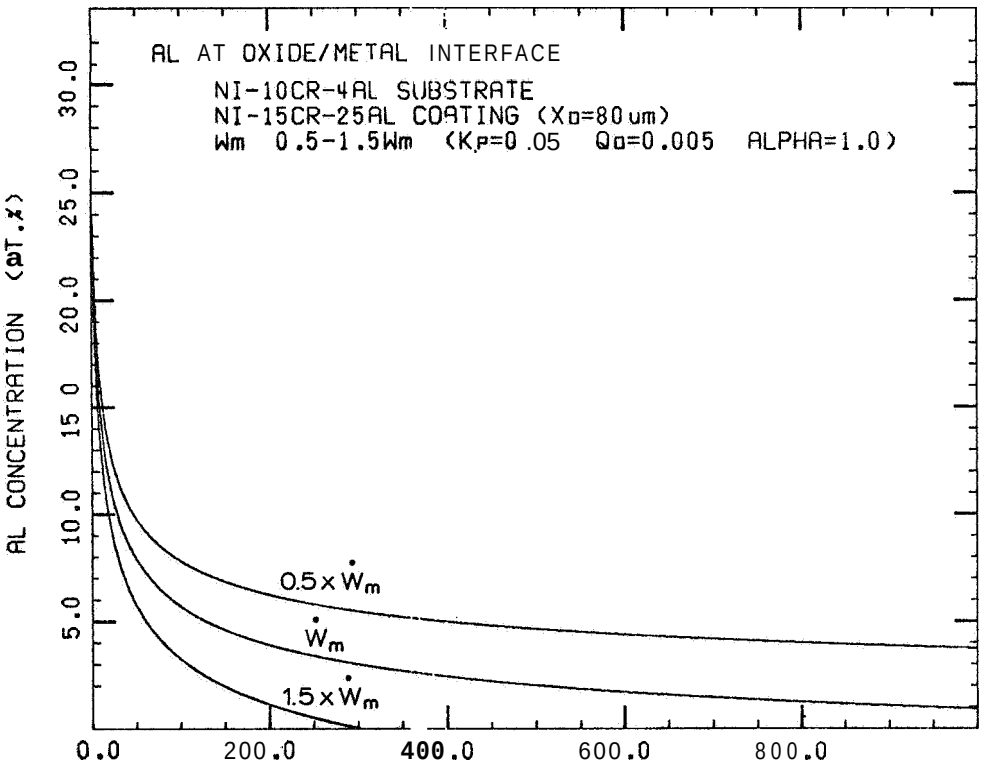

c.

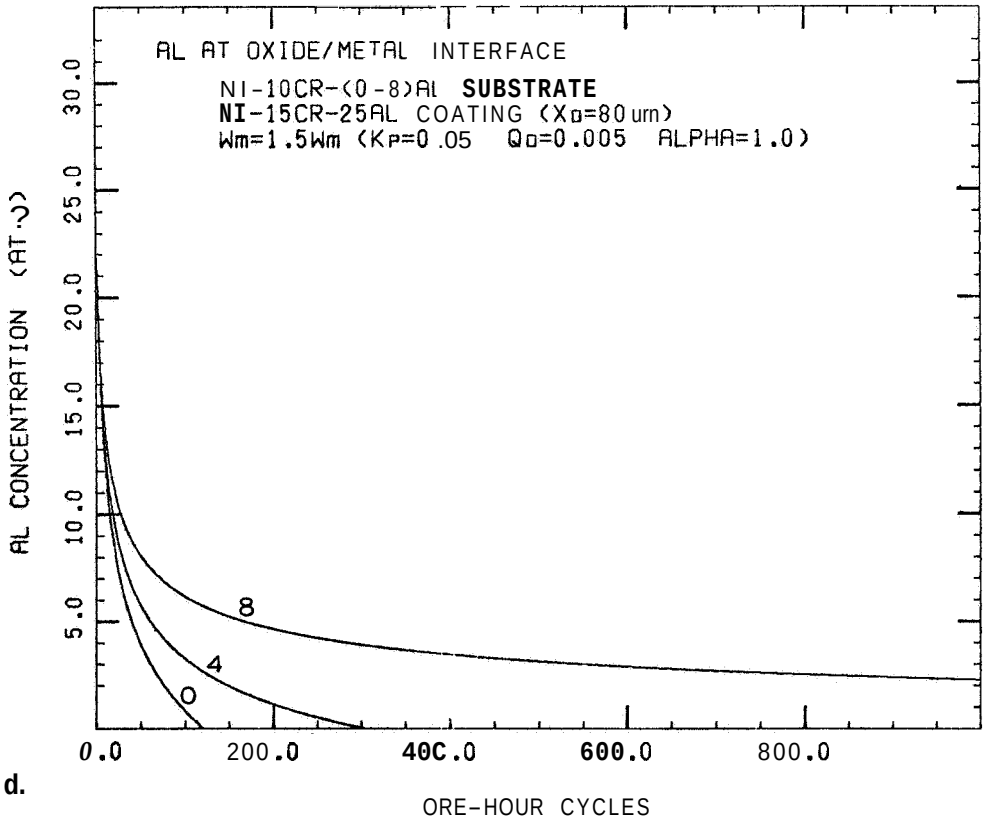

d.

Figure 13 (con't.) Effect of coating composition, substrate composition and rate of Al consumption on coating life.

input parameters is in the range of values determined from the four coated substrates previously discussed and was shown in Figure 8.

The value of the COSIM model can now be illustrated. It was previously shown that increasing the Al concentration of the substrate increased the coating life, whereas increasing the rate of Al consumption decreased the coating life. The effect on the coating life of the Al content of the substrate for a higher rate of Al consumption is shown in Figure 13d. The results of Figures 13a and d can be combined to show the weight of Al consumed and the time to coating failure for various substrate compositions and rates of Al consumption (Figure 14). The locations of the symbols for each substrate shown in Figure 14 indicate both the weight of Al consumed from the coating (and substrate) and the time of coating failure for various rates of Al consumption. As shown, for any one substrate the time to coating failure decreases as the rate of Al consumption increases, but also the total weight of Al consumed is greater at coating failure for the lower the rate of Al consumption (or for the longer the time to coating failure). Stated otherwise, the lower the rate of Al consumption, the greater the amount of Al which is consumed before coating failure (i.e. the more efficient the use of Al in the coating and substrate). Therefore, identical coatings on the same substrate do not fail after a fixed amount of Al has been consumed. Figure 14 also demonstrates the importance of Al in the substrate. The amount of Al in a Ni-15Cr-25Al coating 80 microns thick ($\sim$ 7.7 mg/cm^2) is also shown in Figure 14. When the weight of Al consumed at coating failure is less than the weight of Al initially in the coating (i.e. for the Ni-10Cr substrates, $\dot{W}_m$ and $2\dot{W}_m$), Al initially in the coating remains in either the coating

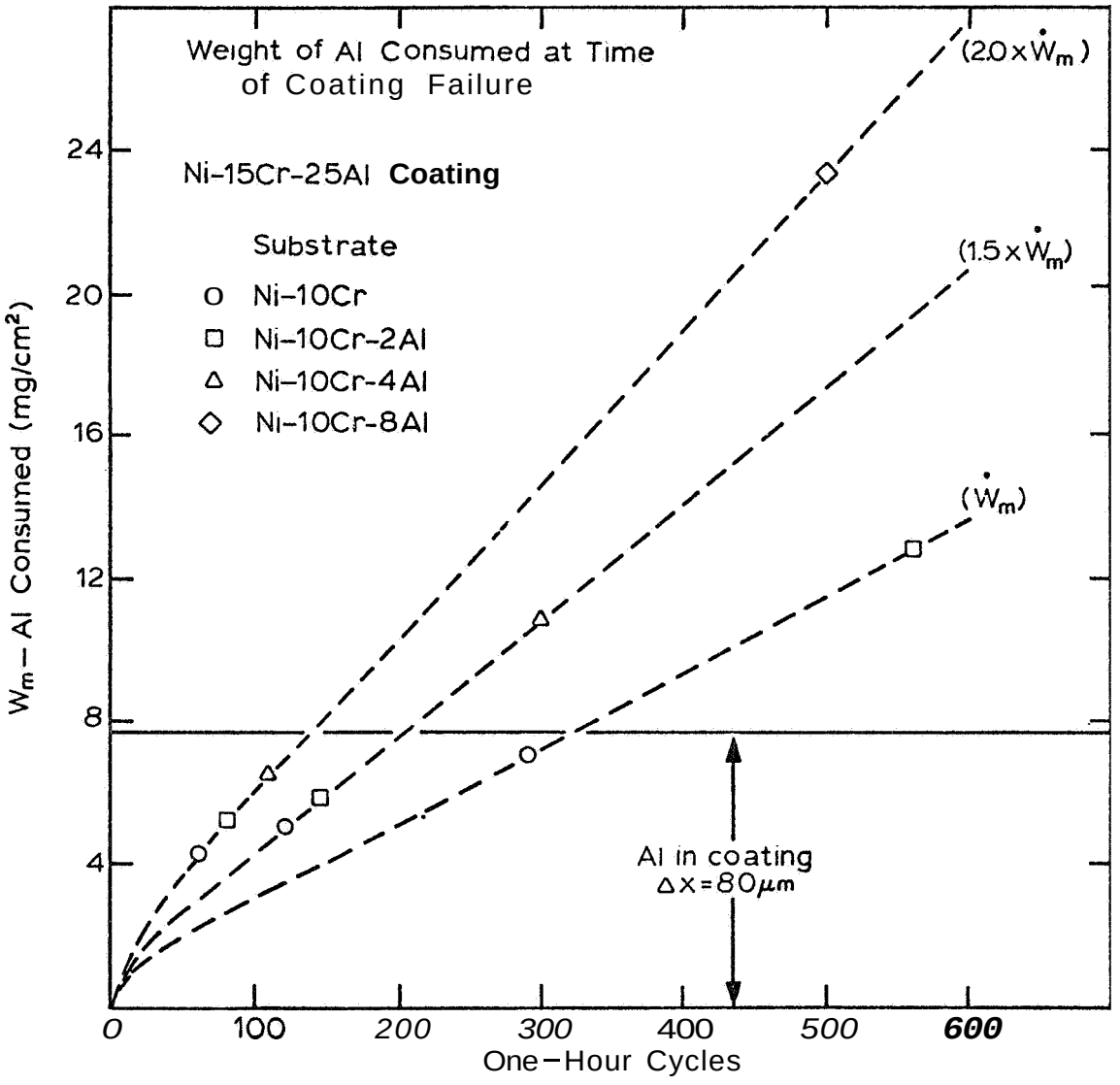

Figure 14 Weight of Al consumed at time of coating failure for various rates of Al consumption.

or substrate and has not been used for oxidation protection. In contrast, when the weight of Al consumed at coating failure is greater than the weight of Al initially in the coating (i.e. for the Ni-10Cr-2Al substrate, $\dot{W}_m$), the additional Al consumed in the formation of Al_2O_3 has obviously been supplied from the Al in the substrate. Therefore, for the Ni-10Cr-2Al substrate, coating failure occurs after 560 cycles with a total weight of Al consumed of approximately 13 mg/cm^2. But since there was only 7.7 mg/cm^2 Al initially in the coating, approximately 5.3 mg/cm^2 of Al has been consumed from the substrate. For this case, one might make the claim that coating/substrate interdiffusion is actually beneficial! (Obviously the mechanical properties of a superalloy substrate will decrease if Al is extracted.)

The effect of coating/substrate interdiffusion might best be understood by considering the fraction of Al from the coating which has diffused into the substrate after a certain oxidation exposure. For instance, the amount of Al initially in the coating but which has diffused into the substrate after 100 cycles is shown as the cross-hatched areas in Figure 15 for three different substrate compositions. Quite apparent is that more Al has diffused into the substrate containing no Al than the substrate containing 8 at.%Al. Therefore an obvious effect of Al in the substrate is to reduce the diffusion of Al from the coating to the substrate. This point can be made more obvious by considering the fraction of Al which had diffused into the substrate (W_I [Figure 15] divided by the initial amount of Al in the coating-W_C) for various substrate compositions and rates of Al consumption as shown in Figure 16. Several points from Figure 16 deserve attention. First, a very large amount (30-40%) of the Al

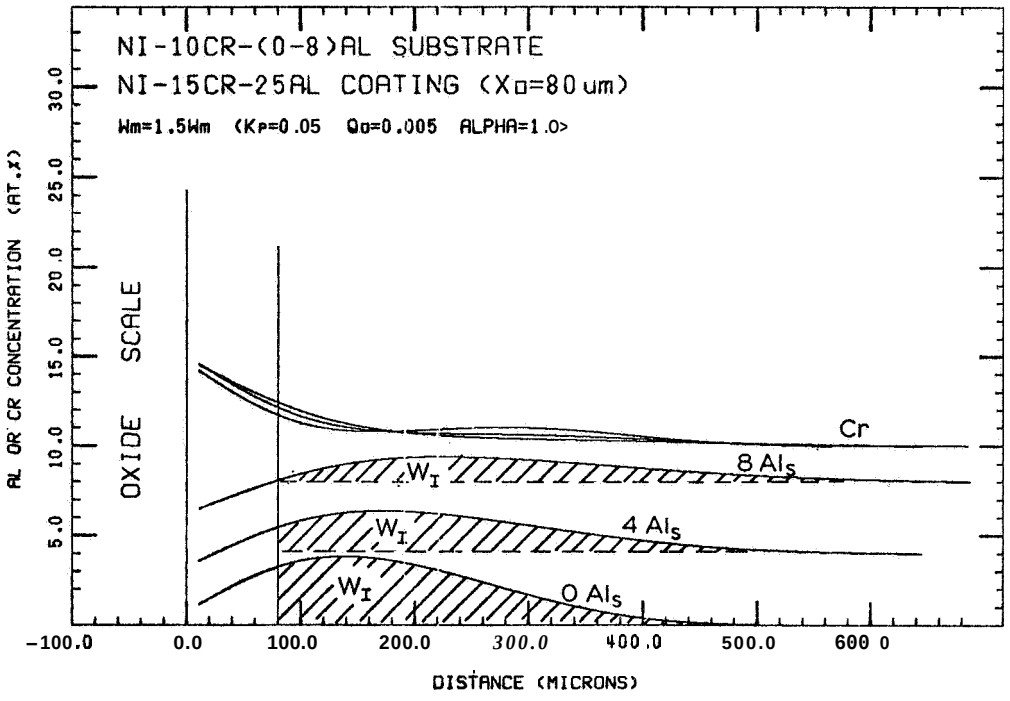

Figure 15 Al and Cr concentration profiles for 0–8 at.% Al in substrate after 100 cycles.

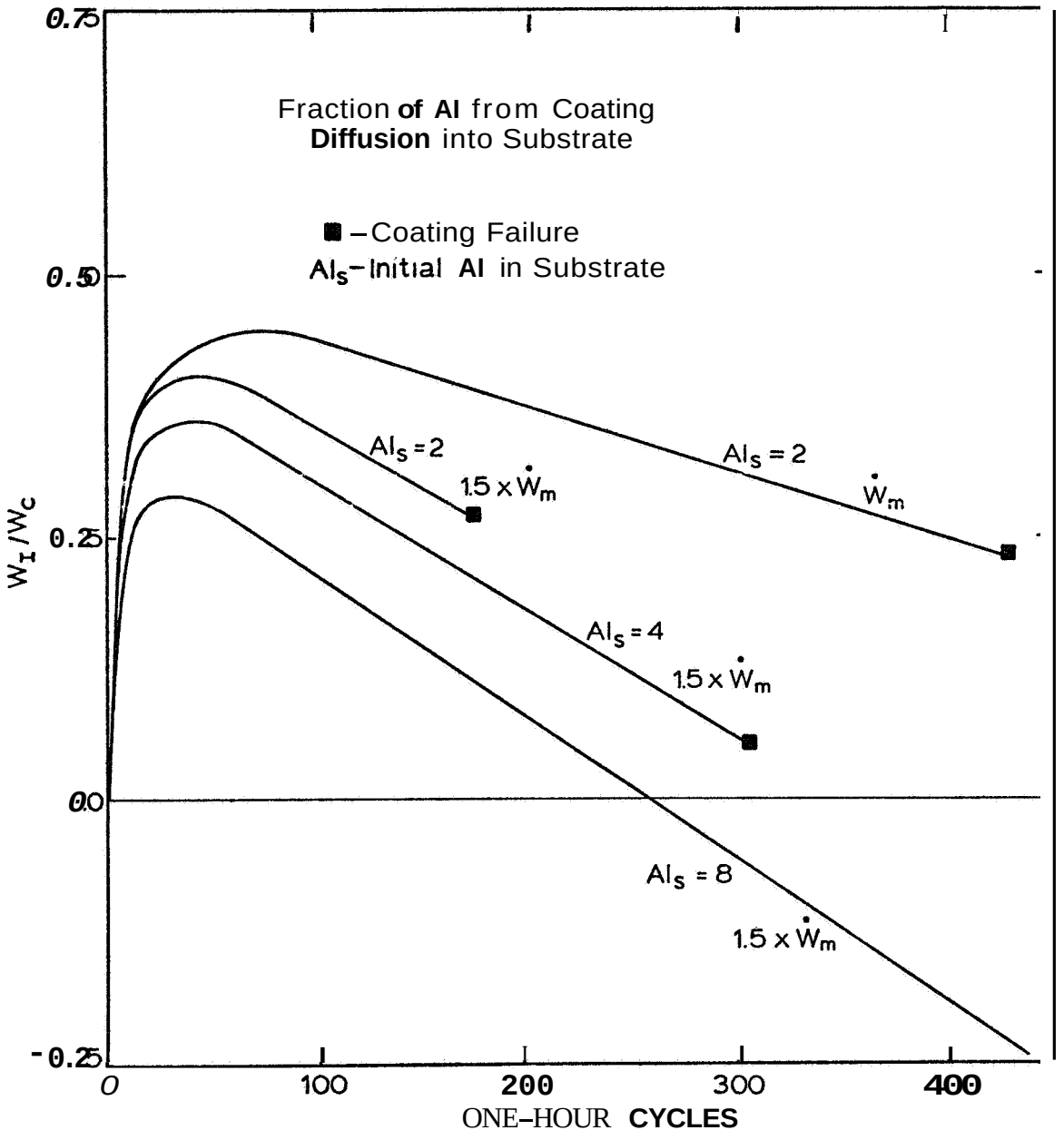

Figure 16 Fraction of Al from the coating which has diffused into the substrate.

initially in the coating diffuses into the substrate after only 10-25 cycles. Second, increasing the Al content of the substrate decreases the amount of Al which diffuses into the coating (compare Al_s=2 to Al_s=8). Closely related is that reducing the coating/substrate interdiffusion also permits a greater fraction of the Al initially in the coating to be consumed before coating failure. Third, and quite important, after an initial "surge", the Al begins to diffuse back out of the substrate(W_I/W_c decreases). Fourth, for the same substrate, the lower the rate of Al consumption, the greater the amount of Al which diffuses into the substrate, but interestingly, a larger portion of the Al is also able to diffuse back out of the substrate before the coating fails.

In summary, some of the more important points illustrated by the COSIM model can be reviewed.

1. The Al content of the substrate has a major effect on coating life, while the Al content of the coating has somewhat less effect.
2. The Cr content of the coating and substrate has only a limited effect on the coating life.
3. The rate of Al consumption has a major effect on coating life.
4. Decreasing the rate of metal consumption allows more coating/substrate interdiffusion, but also permits more of the Al to diffuse back out of the substrate before coating failure. Conversely, increasing the rate of Al consumption results in a greater amount of Al from the coating to be left in the substrate at coating failure (i.e. the greater the rate of Al

consumption, the greater the loss of Al due to coating/substrate interdiffusion.

5. Identical coatings on the same substrate do not fail after a fixed amount of Al has been consumed.
6. Increasing the Al content of the substrate reduces coating/substrate interdiffusion and permits more efficient use of the Al in the coating.

Conclusions

Several conclusions can be stated from the results of this study.

1. A wide range in the cyclic oxidation behavior was observed for the same overlay coating applied to various substrates.
2. The concentration/distance profiles and microstructural changes generally reflected the resistance to oxide spallation of each coated substrate.
3. Kirkendall porosity was observed in the coating, the substrate and particularly at the coating/substrate interface. The location of the porosity could be explained with reference to the intrinsic diffusion fluxes.
4. A numerical model was developed and shown to predict coating degradation by simultaneous oxidation and coating/substrate interdiffusion with reasonable success.
5. The numerical model has been utilized to identify the critical parameters in coating/substrate systems. The most important parameters affecting coating life are the rate of Al consumption and the Al content of the substrate. The Al

content of the coating has a lesser effect on the coating life while the Cr content of the coating or substrate have very little impact on the coating life.

6. The numerical model has been utilized to provide insight into the coupled nature of oxidation and coating/substrate interdiffusion. In brief, as the rate of Al consumption increases, the loss of Al due to coating/substrate interdiffusion also increases. As the rate of Al consumption decreases, the amount of coating/substrate interdiffusion increases, but a larger fraction of the Al is able to diffuse back out of the substrate before coating failure. Increasing the Al content of the substrate reduces coating/substrate interdiffusion.

References

1. G. W. Goward, Source Book on Materials for Elevated Temperature Applications, pp. 369–386, ASM, 1979.

2. S. Shankar, D. E. Koning and L. E. Dardi, J. Met., 33, 13 (1981).

3. M. R. Jackson and J. R. Rairden, "Protective Coatings for Superalloys and the Use of Phase Diagrams" Applications of Phase Diagrams in Metallurgy and Ceramics, G. C. Carter, Editor, NBS Sp–496, p. 423, 1977.

4. J. R. Rairden, M. R. Jackson, M. F. X. Gigliotti, M. E. Henry, J. R. Ross, W. A. Seaman, D. A. Woodford, and S. W. Yamg, "Coatings for Balanced Environmental/Mechanical Behavior" General Electric Corporate Research and Development, Rept. No. 81CRD075, 1981.

5. J. R. Rairden and M. R. Jackson, "Coatings for Protecting Ni–Base TaC Eutectics Against Oxidation", General Electric Corporate Research and Development Rept. No. 76CRD274, 1976.

6. W. K. Halnan and D. Lee, High Temperature Protective Coatings, S. C. Singhal, Editor, AIME, p. 3, 1982.

7. M. Nakamori, Y. Harada, and I. Hukua, High Temperature Protective Coatings, S. C. Singhal, Editor, AIME, p. 175, 1982.

8. C. J. Spengler, S. T. Scheirer, and D. C. Barksdale, High Temperature Protective Coating, S. C. Singhal, Editor, AIME, p. 189, 1982.

9. D. G. Capelli, High Temperature Alloys for Gas Turbines, D. Coutsouradis, P. Felix, H. Fischmeister, L. Habraken, Y. Lindblom, and M. O. Speidel, Editors, Applied Science Publishers, London, p. 177, 1978.

10. S. J. Grisaffe, The Superalloys, John Wiley and Sons, N.Y., p. 341, 1972.

11. C. S. Giggins and F. S. Pettit, J. Electrochem. Soc., 118, 1782 (1971).

12. G. W. Goward, J. Metals, 22, 31 (1970).

13. C. A. Barrett and C. E. Lowell, Oxid. of Met., 11, 199 (1977).

14. C. A. Barrett and C. E. Lowell, Oxid. of Met., 12, 293 (1978).

15. C. A. Barrett, A. S. Khan, and C. E. Lowell, J. Electrochem. Soc., 128, 25 (1981).

16. I. M. Allam, D. P. Whittle, and S. Stringer, Oxid. of Met., 13, 381 (1979).

17. A. Kumar, M. Nasrallah, and D. L. Douglass, Oxid. of Met., 8, 227 (1974).

18. I. A. Kvernes, Oxid. of Met., 6, 45 (1973).

19. R. G. Ubank, Rev. Int. Htes. Temp. et Retract. 14, 21 (1977).

20. G. W. Goward, D. H. Boone, and C. S. Giggins, Trans. ASM, 60, 228 (1967).

21. J. Stringer and D. P. Whittle, "High Temperature Corrosion and Coating of Superalloys", High Temperature Materials in Gas Turbines, P. R. Sahm and M. O. Speidel, Editors, Elserier Scientific Publishing Company, N.Y. p. 283, 1974.

22. S. R. Levine, Met. Trans., 9A, 1237 (1978).

23. J. L. Smialek and C. E. Lowell, J. Electrochem. Soc. 121, 800 (1974).

24. D. P. Whittle, Acta Met. 17, 1247 (1969).

25. J. A. Nesbitt and R. W. Heckel, High Temperature Protective Coatings, S. C. Singhal, Editor, TMS-AIME, p. 75, 1982.

26. C. A. Barrett, J. R. Johnson, and W. A. Sanders, Oxid. of Met., 12, 343 (1978).

27. C. E. Lowell and D. L. Deadmore, "The Role of Thermal Shock on Cyclic Oxidation", NASA TM-78876 (1978).

28. D. L. Deadmore and C. E. Lowell, Oxid. of Met. 11, 91 (1977).

29. P. G. Shewmon, Diffusion in Solids, McGraw-Hill Book Co. Inc., N.Y., 1963.

30. W. F. Smith, Structures and Properties of Engineering Alloys, McGraw-Hill, 1981.

31. The Superalloys, C. T. Sims and W. C. Hagel, Editors, John Wiley and Sons, N.Y., 1972.

32. F. S. Pettit, Trans. TMS-AIME, 239, 1296 (1967).

33. C. S. Giggins, E. J. Felten, and F. S. Pettit, Stress Effects and the Oxidation of Metals, J. V. Cathcart, Editor, pp. 245-260, TMS-AIME, N.Y., 1975.

34. P. Kofstad, High-Temperature Oxidation of Metals, pp. 112-146, John Wiley and Sons, N.Y., 1966.

35. J. Stringer and D. P. Whittle, Rev. Int. Htes. Temp. et. Retract. 14, 6 (1977).

36. J. S. Kirkaldy, Advances in Materials Research, 4, 55 (1970).

37. C. Wagner, J. Electrochem. Soc., 99, 369 (1952).

38. B. D. Bastow, D. P. Whittle, and G. C. Wood, Oxid. of Met., 12, 413 (1978).

39. R. A. Rapp, Acta Met. 9, 730 (1961).

40. P. Moulin, A. M. Huntz, and P. Lacombe, Acta Met. 28,745 (1980).

41. H. Y. Ku, J. Appl. Phys., 35, 3391 (1964).

42. R. A. Rapp, A. Ezis, and G. J. Yurek, Met. Trans., 4, 1283 (1973).

43. Alloy Metals, Inc., Troy, MI.

44. C. A. Barrett and C. E. Lowell, Oxid. of Met. 9, 307 (1975).

45. J. A. Nesbitt, M.S. Thesis, MTU Houghton, MI 1981, also published as NASA Contractor Report 165544, May, 1982.

46. A. S. Kahn, C. E. Lowell, and C. A. Barrett, J. Electrochem. Soc., 127, 670 (1980).

47. H.Bhat, H. Herman, and R. J. Coyle, High Temperature Protective Coatings, S. C. Singhal, Editor, TMS-AIME, p. 37, 1982.

48. R. A. Rapp, Corrosion, 21, 382 (1965).

49. J. H. Swisher, Oxidation of Metals and Alloys, p. 235, ASM, Ohio, 1971.

50. C. E. Lowell, R. G. Garlick, and B. Henry, Met. Trans. 7A, 655 (1976).

51. Stress Effects and the Oxidation of Metals, J. V. Cathcart, Editor, TMS-AIME, N.Y., 1975.

52. J. S. Kirkaldy, Can. J. Physics, 36, 907 (1958).

53. J. S. Kirkaldy, Can. J. Physics, 36, 917 (1958).

54. G. R. Purdy, D. H. Weichert and J. S. Kirkaldy, Trans. AIME, 230, 1025 (1964).

55. J. S. Kirkaldy, Zia-UI-Hag and L. C. Brown, Trans. ASM, 56, 835 (1963).

56. G. Bolze, D. E. Coates and J. S. Kirkaldy, Trans. ASM, 62, 795 (1969).

57. J. S. Kirkaldy and G. R. Purdy, Can. J. Physics, 40, 208 (1962).

58. J. S. Kirkaldy and L. C. Brown, Can. Met. Quart. 2, 89 (1963).

59. J. I. Goldstein and A. E. Moren, Met. Trans., 9A, 1515 (1978).

60. A. J. Hickl and R. W. Heckel, Met. Trans. 6A, 431 (1975).

61. A. K. Sarkel, Ph.D. Dissertation, SUNY–Stoneybrook, N.Y., 1979.

62. J. I. Goldstein and E. Randich, Met. Trans., 8A, 105 (1977).

63. J. A. Nesbitt and R. W. Heckel, Met. Trans., 12A, 1548 (1981).

64. E. Randich and J. I. Goldstein, Met. Trans., 6A, 1553 (1975).

65. C. E. Lowell, C. A. Barrett, and R. W. Palmer "Development of a Cyclic Oxidation Spall Model", Presented at the Oxidation, Deposition and Hot Corrosion in Combustion Turbine Engines Conference, NASA–Lewis Research Center, Cleveland, OH, April 27–28, 1983.

66. J. A. Nesbitt, A. E. Zyskowski, S. R. Levine, and R. W. Heckel, "Interdiffusion and Interface Motion in Y/Y + β Ni-Cr-Al Diffusion Couples", presented at the Fall Meeting of TMS–AIME, St. Louis, MO. 1982.

Appendix A

Concentration Measurement

Concentrations in the γ and γ' phases were determined by use of an electron microprobe (EM) and subsequent ZAF correction scheme (ZAF). The accuracy of the EM/ZAF procedure was established by measuring the Ni, Cr and Al concentrations of several γ -phase alloys of known compositition. After establishment of the accuracy of the EM/ZAF procedure, only the Cr and Al concentrations were measured.

y-phase standards. The Ni, Cr and Al concentrations of seven γ -phase alloys of known composition were determined by use of the EM/ZAF procedure. The seven alloys were repeatedly arc melted (from pressed, elemental powders), annealed for a week at 1240°C, sectioned, mounted and polished through 0.25 micron diamond polish. The two available crystal spectrometers were set to collect first the Cr and Al x-rays at numerous locations on each of the seven alloys. The Ni and Al x-rays were measured similarly. At the start, finish, and at various intervals during the measurement procedure the pure element (Ni, Cr and Al) x-ray intensities were measured. The sample current was also measured by use of a Faraday cup on the sample holder. The x-rays were counted for six ten-second periods at each site where x-rays were collected. The background was measured for each of the alloys and pure elements. The six x-ray counts for each site were averaged and corrected for background and deadtime. The pure element intensities were also corrected for background and deadtime. The corrected x-ray intensities

for the alloys were divided by the corrected pure element intensities to produce k ratios for Ni, Cr and Al. The k ratios were input to the ZAF correction program.

The ZAF correction program "MULTI8" (1)* was used to calculate the Ni, Cr and Al weight fractions from the three k ratios. The MULTI8 correction program accounts for the variation in the generation of x-rays due to changes in the matrix composition and the incident electron energy (atomic number effect - Z), the absorption of characteristic x-rays of one element by the other elements in the matrix (absorption - A), and the secondary fluorescence of x-rays generated by one element when it absorbs the primary x-rays generated by a second element (fluorescence - F). In addition to the k ratios, parameters input to MULTI8 included: the x-ray emergence angle, the atomic numbers and atomic weight of the elements being measured, the operating kV, the excitation potential and fluorescence yield of each element, and the appropriate mass absorption coefficients (i.e. mass absorption coefficient for Al K_{α} x-rays in pure Al, pure Cr, and pure Ni, etc.). For each of the parameters input to MULTI8, excluding the k ratios, the mass absorption and fluoresence yield coefficients contain the greatest uncertainty. Variation of the fluoresence yield has only a very small effect on the final concentration predicted by MULTI8, whereas variation of the mass absorption coefficients has a significant effect on the final concentration. The mass absorption and fluoresence yield coefficients used in this study are listed in Table A-1. The concentrations (wt.%) of the seven γ -phase standards were also

---

* The references for this appendix are listed on page A8.

Table A-1

Mass Absorption and Fluorescence Yield Coefficients

Used in the MULTI8 ZAF Correction Program

Mass Absorption Coefficients

Emitter

Absorber	Al	Cr	Ni	Ref.
Al	502.5	**173.6**	**65.2**	2
Cr	**2470.0**	90.0	**316.0**	**3**
Ni	**3140.0**	**146.0**	**61.0**	**3**

Fluorescence Yield Coefficients (2)

Al - 0.026

Cr - 0.258

Ni - 0.392

Table A-2

Comparison of the Concentrations* of the y-phase Standards as Measured by Atomic Absorption and the EM/ZAF Procedure.

Standard	Atomic Absorption		EM/ZAF		ΔC	% Relative Error
s-1	62.57	(±0.28) **Ni**	61.87	(±o.35)	-0.70	-1.1
	34.34	(±0.10) **Cr**	34.95	(±0.32)	0.61	1.8
	3.09	(±0.18) **Al**	3.09	(±0.05)	0.0	0.0
s-2	66.54	(±0.15) **Ni**	64.75	(±0.50)	-1.79	-2.7
	29.50	(k0.03) **Cr**	29.61	(k0.30)	0.11	0.4
	3.96	(k0.12) Al	3.92	(k0.04)	-0.04	1.0
s-3	70.28	(k0.08) **Ni**	68.48	(k0.38)	**-1.80**	-2.6
	24.74	(50.00) **Cr**	25.22	(k0.33)	0.48	1.9
	4.98	(50.07) **Al**	5.05	(k0.04)	0.07	1.4
s-4	76.41	(±0.11) **Ni**	75.34	(-10.48)	-1.07	-1.4
	17.95	(±0.02) **Cr**	17.95	(k0.22)	0.0	0.0
	5.64	(±0.13) Al	5.76	(50.05)	0.12	2.1
s-5	73.40	(±0.16) **Ni**	72.53	(±0.39)	-0.87	-1.2
	24.26	(k0.05) **Cr**	24.40	(k0.21)	0.14	0.6
	2.43	(k0.12) **Al**	2.26	(k0.02)	-0.08	-3.4
S-6	79.83	(k0.03) **Ni**	79.96	(±0.40)	-0.13	-0.2
	17.88	(±0.00) **Cr**	18.53	(k0.26)	0.65	3.6
	2.29	(50.03) **Al**	2.27	(50.04)	-0.02	-0.9
S-7	90.34	(k0.14) **Ni**	90.08	(±0.43)	-0.26	0.3
	7.10	(±0.02) **Cr**	7.41	(±0.27)	0.31	4.4
	2.56	(k0.12) **Al**	2.36	(±0.06)	-0.20	-7.8

* **All concentrations in weight** %.

measured by atomic absorption. Two pieces of each standard were measured and the average and range of the two measurements are shown in Table A-2. The concentrations measured using the EM/ZAF procedure for each of the seven alloys are compared with the concentrations measured by atomic absorption in Table A-2. The maximum absolute difference between the EM/ZAF measurement and the average atomic absorption measurement for the seven Y-phase standards is only 0.2 wt.% Al, (7.8% relative difference); 0.65 wt.% Cr (3.6% relative difference) and, 1.8 wt.% Ni (2.6% relative difference). Therefore, the accuracy of the EM/ZAF procedure is estimated at f0.2 wt.%Al, k0.6 wt.%Cr and ±2.0 wt.%Ni. The precision of the EM/ZAF procedure is indicated by the range shown in the EM/ZAF measurement in Table A-2. The ideal standard deviation associated with x-ray production assuming a Gaussian distribution is equal to the square root of the mean of the counts collected at a single point (std. dev. = $\bar{N}^{\frac{1}{2}}$). The variation in percent is given as (std. dev.)x100/$\bar{N}$. In addition, an actual standard deviation can be calculated from the six counts made at a single site in the alloy. The actual standard deviation is typically twice that of the ideal standard deviation (2). Both the actual and ideal standard deviations were calculated when measuring the concentrations using the EM/ZAF procedure. The range in concentrations shown in Table A-2 is associated with the maximum of the two standard deviations. The variation in compositions at random locations across the same alloy sample surface was typically within the range shown in Table A-2.

β -phase Alloys. An attempt was made to utilize four β -phase alloys to verify the accuracy of the EM/ZAF procedure for high Al, NiCrAl alloys. The alloys were fabricated as previously described for

the Y-phase alloys but suffered oxidation within cracks in the sample buttons during the homogenization treatment. The cracks formed in the hard, brittle phase during cooling in the arc melter. Portions of the melted buttons were analyzed by wet chemistry. The EM/ZAF measurement procedure consistently yielded Al concentrations significantly lower than those measured by wet chemistry. The EM/ZAF values for Ni were consistently high while those for Cr did not show a consistent deviation from the wet chemistry measurement. It was not certain if the large concentration discrepancies was due to the EM/ZAF procedure or to the quality of the β -phase alloys. Therefore, concentrations of the β phase in this report are only presented qualitatively.

No standards were used for the γ' phase. Use of the EM/ZAF procedure was considered acceptable due to the similarity in composition and structure of the γ and γ' phases.

Concentration/Distance Profiles and Phase Compositions. Cr and Al x-rays were counted for determination of the concentration/distance profiles and the concentrations in the two and three phase regions. The procedure for measuring the Cr and Al content of the individual phases in the multiphase regions was identical to that for the Y-phase standards. Concentration/distance profiles were measured by counting the Cr and Al x-rays at regular steps across a diffusion-affected zone. The sample current and time were also recorded at each point of the traverse. The pure element intensities and sample current were measured at the beginning and end of most traverses. The time of each measurement was used to correct for any drift in the electron current between the start and finish of a traverse.

The MULTI8 correction program calculated the Cr and Al concentrations from the Cr and Al k ratios and determined the Ni concentration by difference. Each iteration of the MULTI8 program normalizes the Ni, Cr, and Al concentrations to 100%, thereby including the effect of Ni on the ZAF correction for Cr and Al. All other input to the MULTI8 program is identical to that for the γ-phase standards described previously. The output differs only in that the concentrations in weight % always equal 100.

References

1. K.E. Heinrich, R.L. Myklebust, H. Yakowitz and S.D. Rasberry, "A Simple Correction Procedure €or Quantitative Electron Probe Microanalysis", NBS Technical Note 719, 1972.

2. **H.A.** Liebhafsky, H.G. Pfeiffer, E.H. Winslow, P.D. Zemay and S.S. Liebhafsky, X–Rays, Electrons and Anaylical Chemistry, Wiley Interscience, N.Y., 1972.

3. R. Jenkins and **J.L.** DeVeries, Work Examples in X–ray Anaylsis, 2nd Edition, Springer–Verlag, N.Y., 1978.

4. **J.I.** Goldstein and **J.W.** Colby, Practical Scanning Electron Microscopy, **J.I.** Goldstein and H. Yakowitz, Editors, Plenum Press, N.Y., 1975.

Appendix B

Partial NiCrAl Phase Diagrams at 1150° and 1200°C

Concentrations of the γ and γ' phases in two and three phase regions were measured to determine portions of the NiCrAl phase diagram at 1150° and 1200°C. The concentrations of the phases were measured in $\gamma + \beta$ and $\gamma + \gamma' + \beta$ diffusion couples after 500 hour anneals at 1150°C and in $\gamma + \beta$ and $\gamma + \beta + \alpha$ diffusion couples after 100-500 hour anneals at 1200°C. The phase concentrations were measured in multiphase regions of the diffusion couples well removed from the diffusion-affected area (1150° and 1200°C) and in the $\gamma + \beta$ region near the $\gamma / \gamma + \beta$ interface (1200°C). The accuracy and precision of the measurement technique were discussed in Appendix A.

1150°C Compositions of the γ and γ' phases measured in this study, as well as phase boundaries, interface concentrations, and bulk alloy compositions from two previous studies (1,2)* are shown in Figure B1. Limited phase concentrations measured after isothermal oxidation are included. The bulk compositions of the three alloys used in the phase diagram measurements are also shown. The dark lines of the phase diagram are drawn roughly as a best fit through the data of this study and that of Tu (2). The data of Tu were taken from multiphase concentration profiles which only permitted an estimated accuracy of 1-2 at.%. The γ and γ' concentrations of Tu and this study compare

---

* The references for this appendix are listed on page B6.

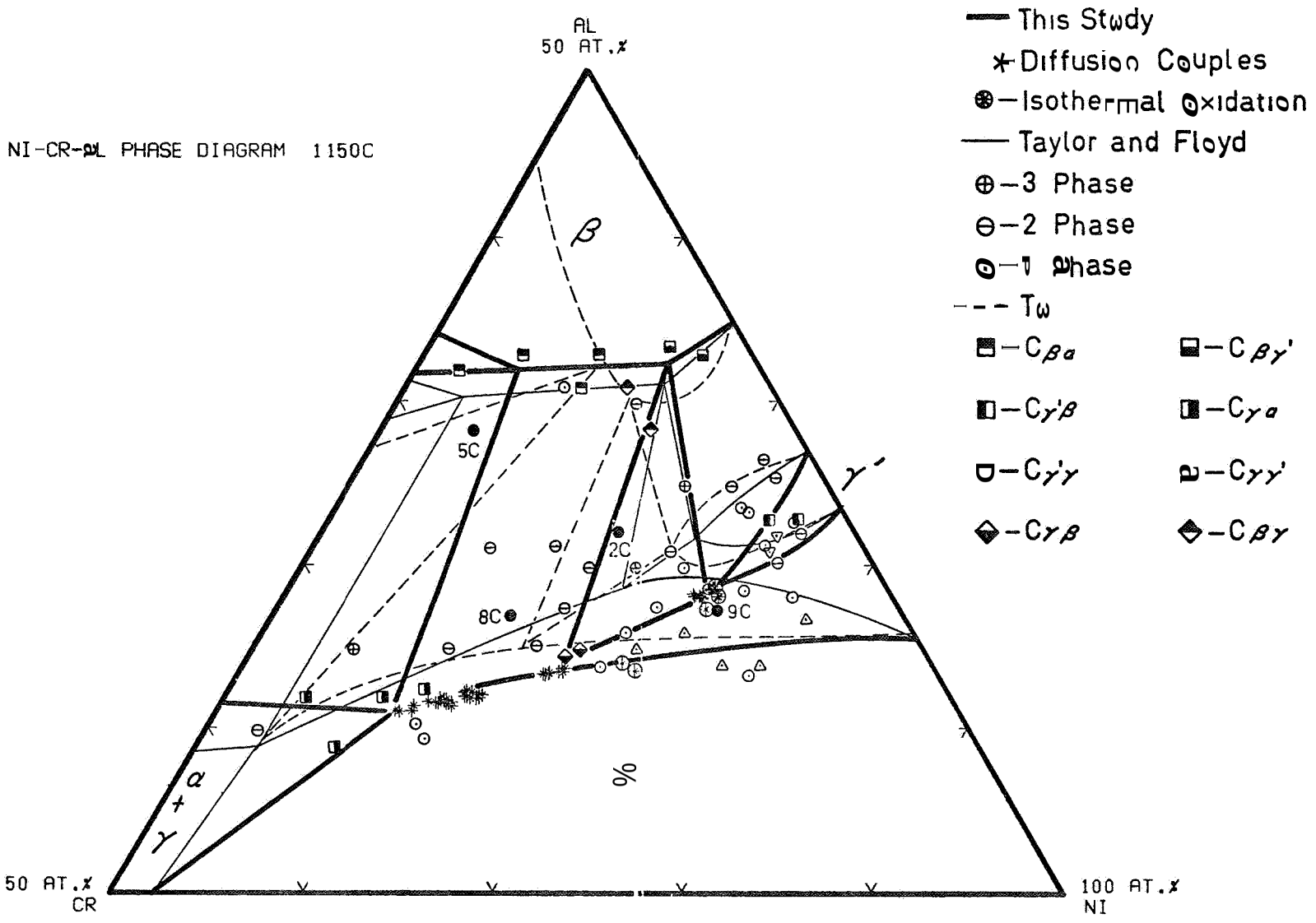

Figure B.1 NiCrAl phase diagram at 1150°C

reasonably well. Taylor and Floyd (1), Tu and this study (Appendix C) have each recorded the appearance of the α-Cr phase at concentrations which could not be accounted for by the phase diagram shown. Taylor and Floyd show a much higher Al content of the γ and y'phases than that of this study. The difference is much greater than the uncertainty in the concentrations due to the measurement technique used in this study. The phase diagram of Taylor and Floyd places alloy 9C (Ref. 3) in the γ phase region, and alloy 2C (Ref. 3) in the $\gamma + \beta$ region. Optical examination of the two alloys clearly reveals $\gamma + \gamma'$ and $\gamma + \gamma' + \beta$ phases, respectively. A possible error in the identification of the γ and γ' phases, which have very similar compositions and almost identical lattice parameters (1), could be one explanation for the large discrepancy. Additional electron microscopy (4) should be utilized to resolve this discrepancy.

1200°C. Compositions of the γ phase measured on numerous $\gamma / \gamma + \beta$ diffusion couples and one $\gamma / \gamma + \beta + \alpha$ diffusion couple are shown in Figure B2. The concentrations were measured in the $\gamma + \beta$ region of the couple to the $\gamma / \gamma + \beta$ interface. Even though considerable diffusion occurred in the $\gamma + \beta$ region, the γ-phase concentrations can be described by a single line (within the accuracy of the measurements). This result would indicate that the γ phase maintains local equilibrium as described by the phase diagram even though the diffusion path is obviously cutting tie lines in the $\gamma + \beta$ region (Appendix C). There was no measurable difference in the concentrations of the γ phase after increasing the annealing time from 100 to 500 hours. Comparison of the 1150° and 1200°C phase boundaries shows little change in the concentration of the $\gamma / \gamma + \beta$ phase boundary, but a shift of the $\gamma + \gamma'$

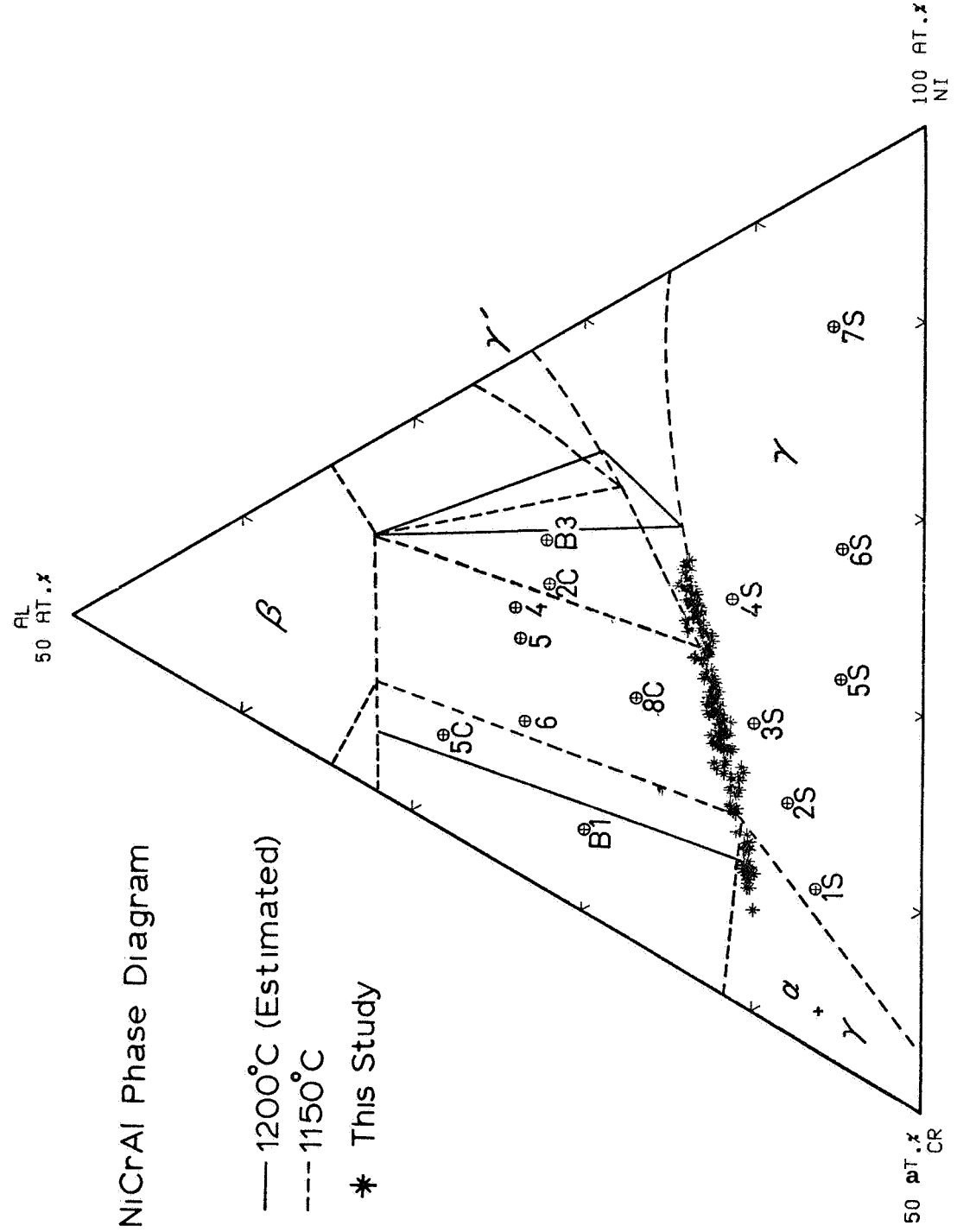

Figure B.2 NiCrAl phase diagram at 1200°C.

$+\beta$ phase triangle to higher Cr concentrations at lower temperatures, in agreement with the findings of Taylor and Floyd (1). The position of the $\gamma / \gamma + \beta$ phase boundary is in excellent agreement with the boundary position previously measured on both diffusion couples and $\gamma+\beta$ alloys oxidized at 1200°C (5).

References

1. A. Taylor and R.W. Floyd, J. Inst. Metals, 81, 451 (1952).

2. D. Tu, 'Diffusion and Pack Aluminizing Study in the Ni-Cr-Al System', Ph.D. Dissertation, SUNY, Stoney Brook, N.Y., 1982.

3. S.R. Levine, Met. Trans., 9A, 1237 (1978).

4. A.D. Romig and J.I. Goldstein, Applications of Phase Diagrams in Metallurgy and Ceramics, G.C. Carter, Editor, NBS Sp-496 (1977) p. 462.

5. J.A. Nesbitt, 'Solute Transport During the Cyclic Oxidation of Ni-Cr-Al Alloys', M.S. Thesis, MTU, Houghton, MI, 1981. Also published as NASA Contractor Report 165544, May, 1982.

Appendix C

Interdiffusion in Ni-Rich, Ni-Cr-Al Alloys at 1100° and 1200°C

I. Determining the Interdiffusion Coefficients

Introduction

(Ni-Co)CrAl overlay coatings are finding increased use for oxidation protection in high-temperature turbine applications (1-6)*. Typical overlay coatings contain the high-Al β (NiAl-type structure) phase imbedded in a ductile γ (FCC) Ni solid-solution matrix. Typical substrates are γ+γ' (Ni_3Al-type structure) Ni or Co based superalloys (7). Overlay coatings are applied to provide oxidation protection by the selective oxidation of Al. Small additions (< 1.0 wt.%) of reactive elements such as Y (2,4-6) or Zr (8-10) are usually added to increase the oxide scale adherence during thermal cycling.

Two mechanisms of coating degradation by diffusional transport are loss of Al to the Al_2O_3 scale (1,11), and loss of Al by coating/substrate interdiffusion (1,12,13). Understanding diffusional degradation of coatings requires knowledge of the diffusional processes in γ + β coating/substrate systems which occur under service conditions. Understanding, and ultimately predicting, the diffusional transport in even simple coating/substrate systems requires knowledge of the concentration and temperature dependence of the ternary diffusion coefficients, phase boundaries of the γ and β phases at the

---

* The references for this appendix are listed on pages C65-68.

temperature of interest, and the rate of Al loss (as Al_2O_3) at the oxide/metal interface.

At present, there is limited ternary diffusion data available for the NiCrAl or CoCrAl systems. Roper and Whittle (14) measured the ternary interdiffusion coefficients for the Co-rich solid-solution phase in the CoCrAl system at 1100°C. More recently, Tu (15) has measured the ternary interdiffusion coefficients for the Ni-rich γ phase in NiCrAl alloys at 1025°C. The lower temperature studied by Tu is representative of the temperature for the aluminization process. The results of Tu alone are not amenable to extrapolation to higher temperatures. The lack of available ternary diffusion data is easily understood considering the relative unproductivity (16) of ternary diffusion experiments in comparison to binary diffusion experiments. In ternary alloys, two intersecting diffusion paths are required to measure the four ternary interdiffusion coefficients for one concentration (17). In contrast, a single binary diffusion couple yields diffusion coefficients for all concentrations between the bulk concentration of the alloys making up the couple (18). While there is a considerable lack of ternary diffusion coefficients for the NiCrAl system, there is ample data for the binary systems (15,19-26).

The purpose of the present study was to determine ternary diffusion coefficients in the γ phase of the NiCrAl system. Most of the coefficients were determined at 1200°C, with a small number being determined at 1100°C. It was also the purpose of this study to examine and gain a better understanding of the γ / $\gamma + \beta$ interface motion which occurs in γ / $\gamma + \beta$ diffusion couples. Recession of the β phase

occurs in $\gamma + \beta$ overlay coatings as a result of both oxidation and coating/substrate interdiffusion.

Procedure

Diffusion Couple Fabrication

Various NiCrAl alloys were fabricated by repeated arc melting (of pressed elemental powders) on a water-cooled copper hearth. The Y-phase alloys also used as microprobe standards were annealed for one week at 1240°C. Several alloys were supplied in the as-cast condition by the NASA-Lewis Research Center. Details of the NASA casting procedure are given elsewhere (8). Each of the samples were sectioned into approximately 1 cm x 0.2 cm disks. Alloy designation and compositions are given in Table C-1. The flat disks were polished on each surface through 600 grit SiC paper. The disks were cleaned in acetone and methanol and placed side by side in a molybdenum canister. The molybdemum canisters containing the disks were annealed for 100 hours at either 1100° or 1200°C ± 4°C. Following the anneal, the diffusion couples were sectioned, mounted, and polished by standard metallographic techniques.

Many γ / γ , $\gamma / \gamma + \gamma'$ and $\gamma / \gamma + \beta$ diffusion couples previously fabricated and studied (12) at the NASA-Lewis Research Center were examined in the present study with the electron microprobe. Details of the couple fabrication are given elsewhere (12). The couples were annealed at 1095° and 1205°C for times of 100, 300, and 500 hours. The alloy designations and compositions are also given in Table C-1. The

Table C-1

Alloy **Compositions**

Alloy **Designation**	**Ni**	**Cr**	**Al**	**Phases Present**	
				1100°C	**1200°C**
1s	57.90	35.88	6.22	**NE**	γ(+α)
2s	61.35	30.71	7.94	γ+α	γ
3s	64.45	25.61	9.94	NE	γ
4s	70.13	18.60	11.26	γ	γ
6S	76.03	19.22	4.74	**NE**	γ
7s	86.93	7.71	5.36	**NE**	γ
B69*	78.80	8.60	12.60	**NE**	γ
5SB*	79.35	10.95	9.70	γ	**NE**
Bl2*	88.80	0.0	11.20	**NE**	γ
Ni-10Al*	93.30	0.0	6.70	**NE**	γ
Ni-10-10*	78.10	15.20	6.70	γ	**NE**
Ni	100.00	0.0	*0.0*	γ	γ
W*	88.00	12.00	*0.0*	γ	γ
X*	75.00	25.00	*0.0*	γ	γ
Y*	64.80	35.20	*0.0*	γ	γ
Z*	54.5	45.5	*0.0*	γ	γ
4	63.30	12.70	24.00	NE	γ+β
6	57.90	19.00	23.60	NE	γ+B
8	62.70	20.80	16.50	**NE**	γ+B
Bl	54.10	26.10	19.90	**NE**	γ+β+α

Table C-1 (con't.)

Alloy Designation	Ni	Cr	Al	Phase Present 1100°C	Phase Present 1200°C
B3	67.50	10.20	22.20	NE	$\gamma+\beta$
From Reference (12)					
3SL	74.70	13.20	12.10	$\gamma+\gamma'$	γ
4SL	70.50	18.40	11.10	γ	γ
1C	61.90	14.40	23.70	NE	$\gamma+\beta$
2C	65.40	12.50	22.00	NE	$\gamma+\beta$
5C	54.60	17.10	28.20	NE	$\gamma+\beta$
6C	57.90	18.80	23.40	NE	$\gamma+\beta$
8C	62.30	20.80	16.90	NE	$\gamma+\beta$
9C	73.10	9.70	17.20	NE	$\gamma+\gamma'$

NE - Not examined at the indicated temperature.

* - Composition determined by electron microprobe analysis.

** - Used in couples of Reference 12 and also cast for additional couples fabricated in this study.

diffusion couples were repolished with 0.25 micron diamond polish before examination with the electron microprobe.

Concentration Measurements

An electron microprobe (EMP) was used to measure the Cr and Al concentration/distance profiles across the diffusion-affected zone of each couple. A ZAF correction program (27) was used to convert the measured x-ray intensities to weight fractions. The accuracy of the EMF/ZAF measurement technique for the γ and γ' phases is estimated at ±0.25 wt.% Al and 0.70 wt.% Cr based on measurements of seven Y-phase standards of known composition (Appendix A). Uncertainty in the composition of several β -phase alloys prohibited verification of the EMP/ZAF measurement procedure for high Al, low Cr alloys. As a result, concentrations of the β phase will only be discussed qualitatively in this paper. Further details of the use of the EMP and ZAF correction program are given in Appendix A.

Results

Microstructures and Concentration/Distance Profiles

1100°C Couples

Most of the diffusion couples annealed at 1100°C revealed limited microstructural change as a result of interdiffusion. The diffusion paths have been plotted on the ternary phase diagrams in Figures C.1a and b. The a (BCC, Cr solid-solution) phase present in alloy 2S ($<$ 2 vol.%) receded ($\sim$ 250 μm) from the original 2S/W couple interface. Small pores were observed in the *a* -depleted layer. Couple 4S/Y contained a very small amount of *a* stringers which grew on the high-Cr (Y) side of the couple. The appearance of the α stringers indicates that the diffusion path had looped into the a+y phase field (28,29).

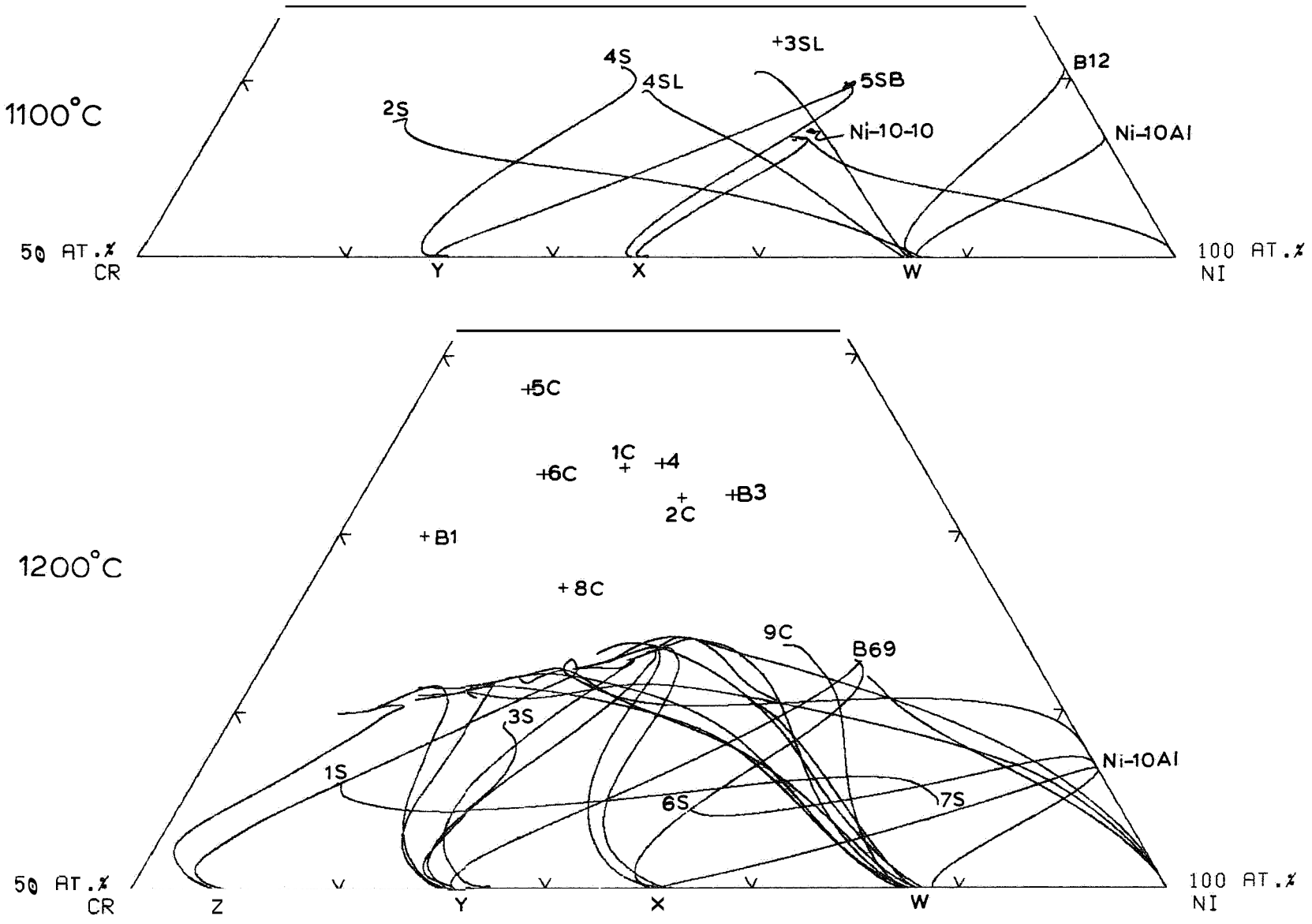

Figure C.1a Diffusion paths in the NiCrAl system at 1100° and 1200°C

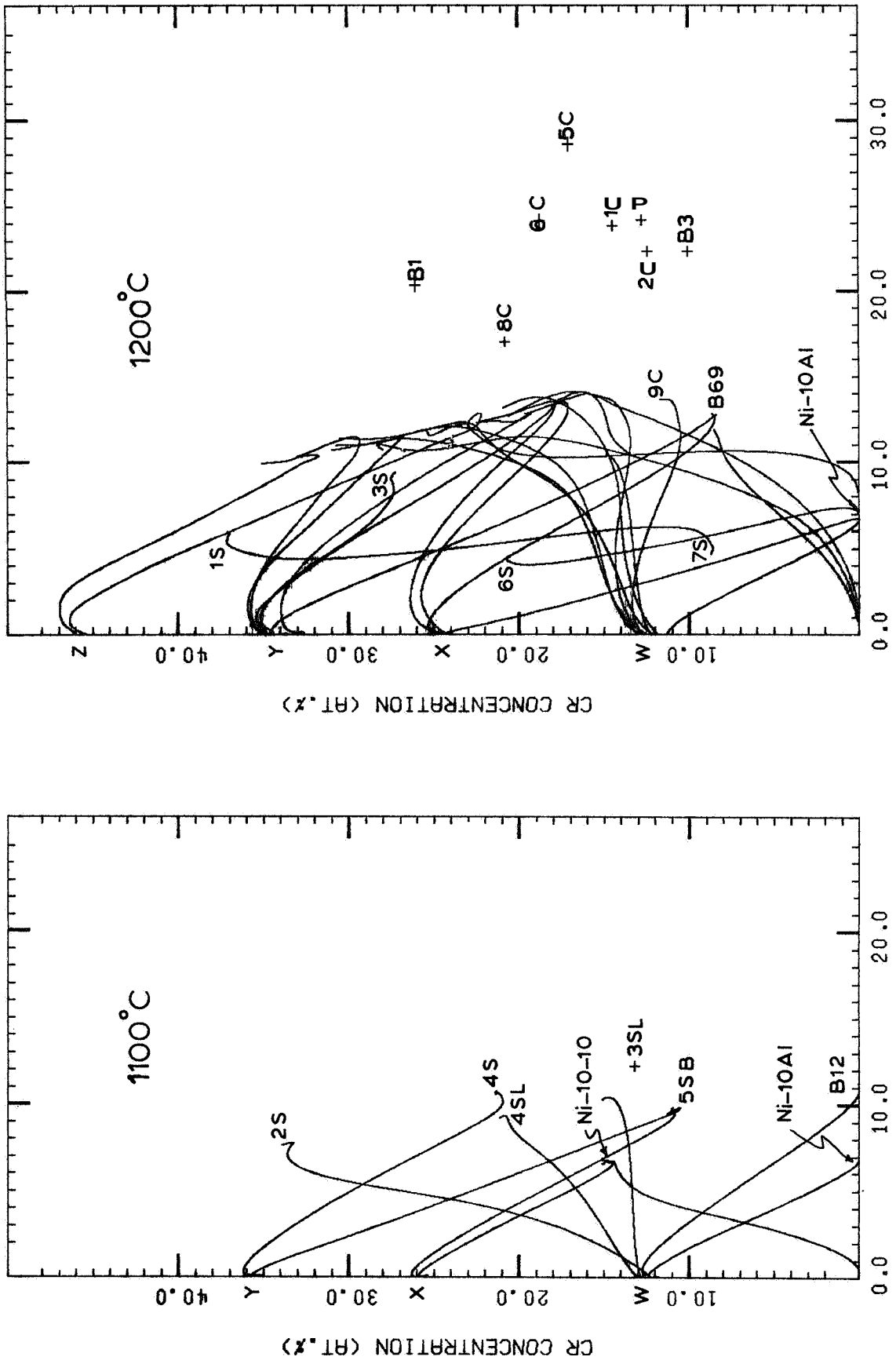

Figure C.1b Diffusion paths in the NiCrAl system at 1100° and 1200°C.

The Ni-10-10/Ni couple contained a very small amount of porosity on the Ni-10-10 side of the original couple interface. The γ' phase present in alloy 3SL receded from the original 3SL/W couple interface. The microstructures of the remaining γ/γ couples annealed at 1100°C exhibited no microstructural change as a result of interdiffusion. A representative concentration/distance profile is shown in Figure C.2. Concentration/distance profiles for the remaining γ/γ couples annealed at 1100°C are shown in Appendix C.2. The zero distance coordinate of each plot has been aligned with the location of small particles originally at the initial couple interface. Small shifts in the particle position may have occurred during annealing due to the Kirdendall effect (30). The concentrations of the alloys shown in the upper left of each plot were taken from the end points of the cubic spline curve (solid line) used to represent the experimental data during analysis of the diffusion couples.

1200°C Couples

γ/γ Couples. The amount and location of Kirdendall porosity was the only distinguishable microstructural difference between the γ/γ couples. The porosity was usually located on only one side of the original couple interface and is discussed in a later section. Some couples showed little or no porosity (Ni-10Al/W, B69/Y, Ni-10Al/X) while others showed a large amount (up to 12 vol. %) of porosity (7S/1S, Ni-10Al/6S, 3S/Y). In many of the 1200°C diffusion couples containing porosity, the concentration measured at a specific point was significantly different from that in the surrounding area. In most cases, the questionable concentration could be visibly associated with a pore. Questionable concentrations were removed from the

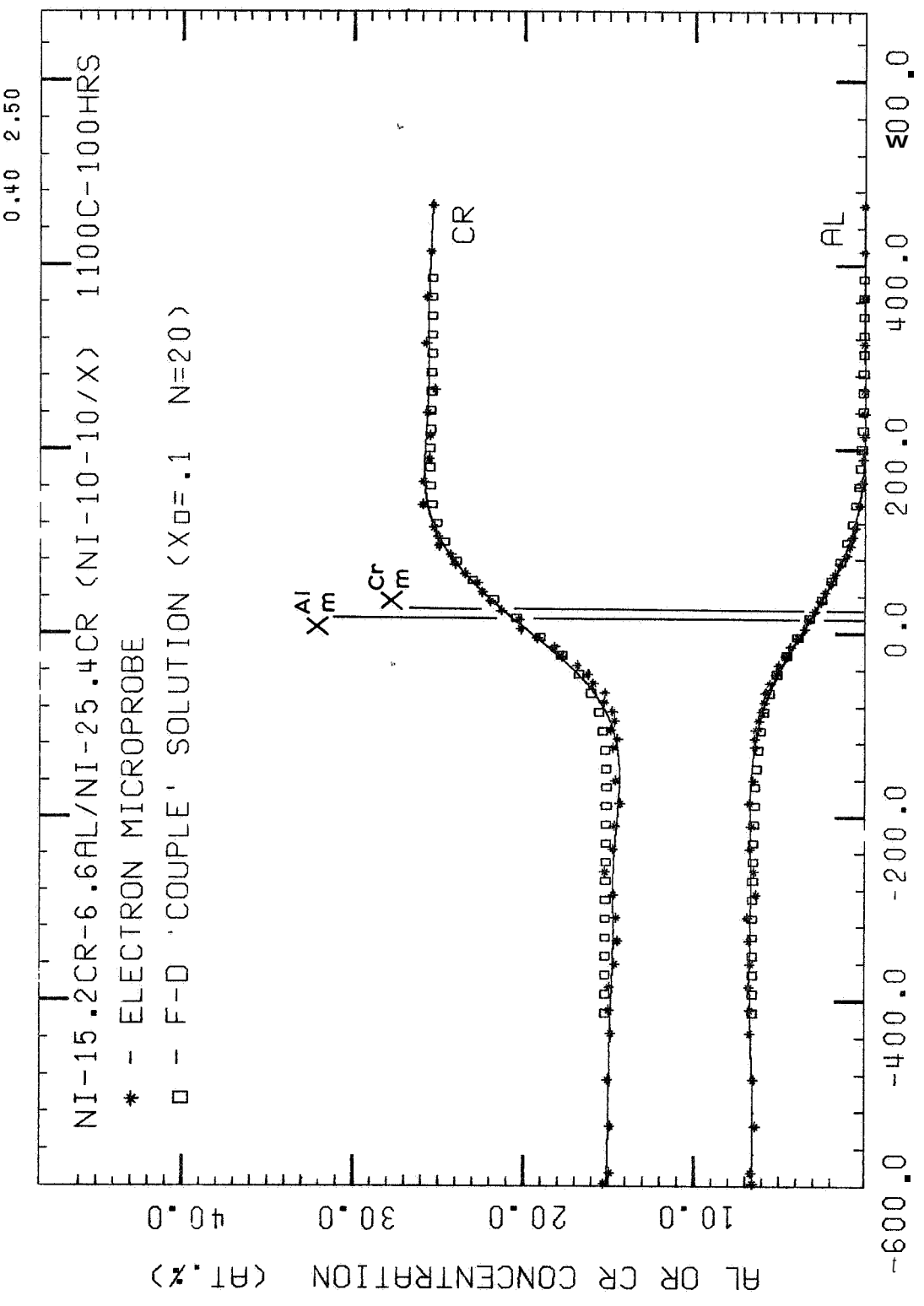

Figure 2 Predicted and measured concentration/distance profile for Ni-15.2Cr-6 6Al/ Ni-25.4Cr (Ni-10-10/X) couple after 100 hours at 1200°C.

concentration/distance profiles *so* as not to affect the smoothing routines used in the analysis of the diffusion couples.

Many of the couples exhibited a maximum in the Cr concentration profile, while two of the couples exhibited maxima and minima in the Al concentration profiles (Ni-10Al/6S, 7S/1S). A representative concentration/distance profile for one of the γ/γ couples annealed at 1200°C is shown in Figure C.3. Concentration/distance profiles for the remaining γ/γ couples and the γ/γ + γ' couple (3SL/W) are shown in Appendix C.2. The distance coordinate is shifted as previously described for the 1100°C couples. The diffusion paths for the γ/γ couples annealed at 1200°C are shown in Figures C.1a and b.

γ/γ + β and γ/γ + γ' Couples. The γ/γ + β couples exhibited complex diffusion behavior associated with recession of the β phase and diffusion in the γ + β region. Many of the couples contained porosity which varied in amount and location. For all γ/γ + β couples, the β phase receded from the original couple interface For the same γ + β alloy, the β recession decreased with increasing Cr in the Ni-Cr, γ-phase alloy. For example, in the alloy 4 couple series, the 8 recession was greatest in couple 4/Ni (317 μm), followed by 4/X (205 μm), 4/Y (143 μm) and 4/Z (123 μm). In addition, diffusion in the γ + β region of the alloy always shifted the concentration of the γ and β phase near the γ/γ + β interface from the equilibrium tie-line (ETL) to higher Al, lower Cr concentrations (Figure C.4). Stated otherwise, the diffusion path cut across tie-lines in the γ + β region, exiting the γ + β region at a higher Al, lower Cr concentration than that given by the ETL for the bulk γ + β alloy. The greater the Ni content of the γ-phase alloy, the greater the shift in concentration from that given by

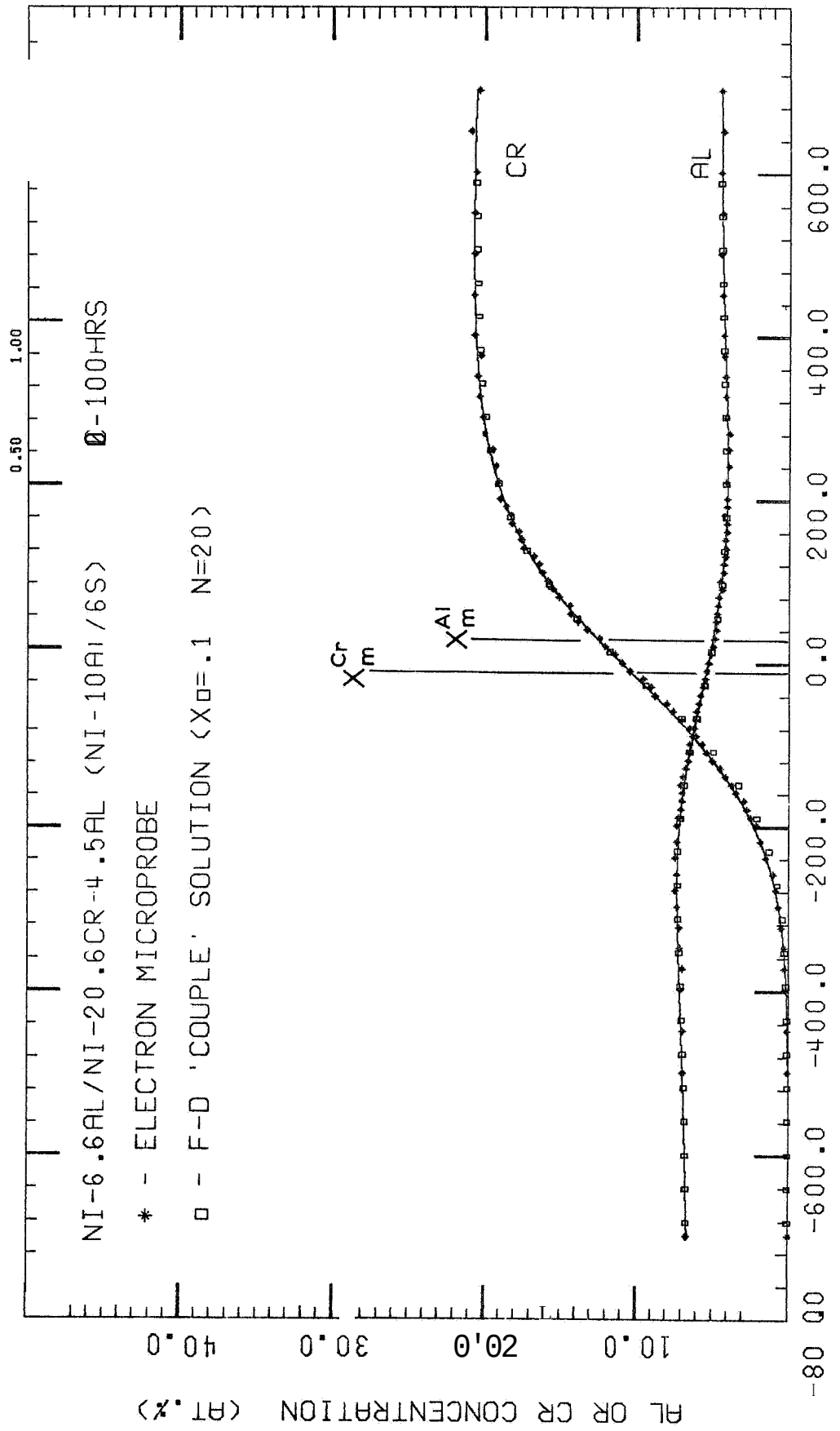

Figure C.3 Predicted and measured concentration/distance profile for Ni-6.6Al/Ni-20.6Cr-4.5Al (Ni-10Al/6S) couple after 100 hours at 1200°C.

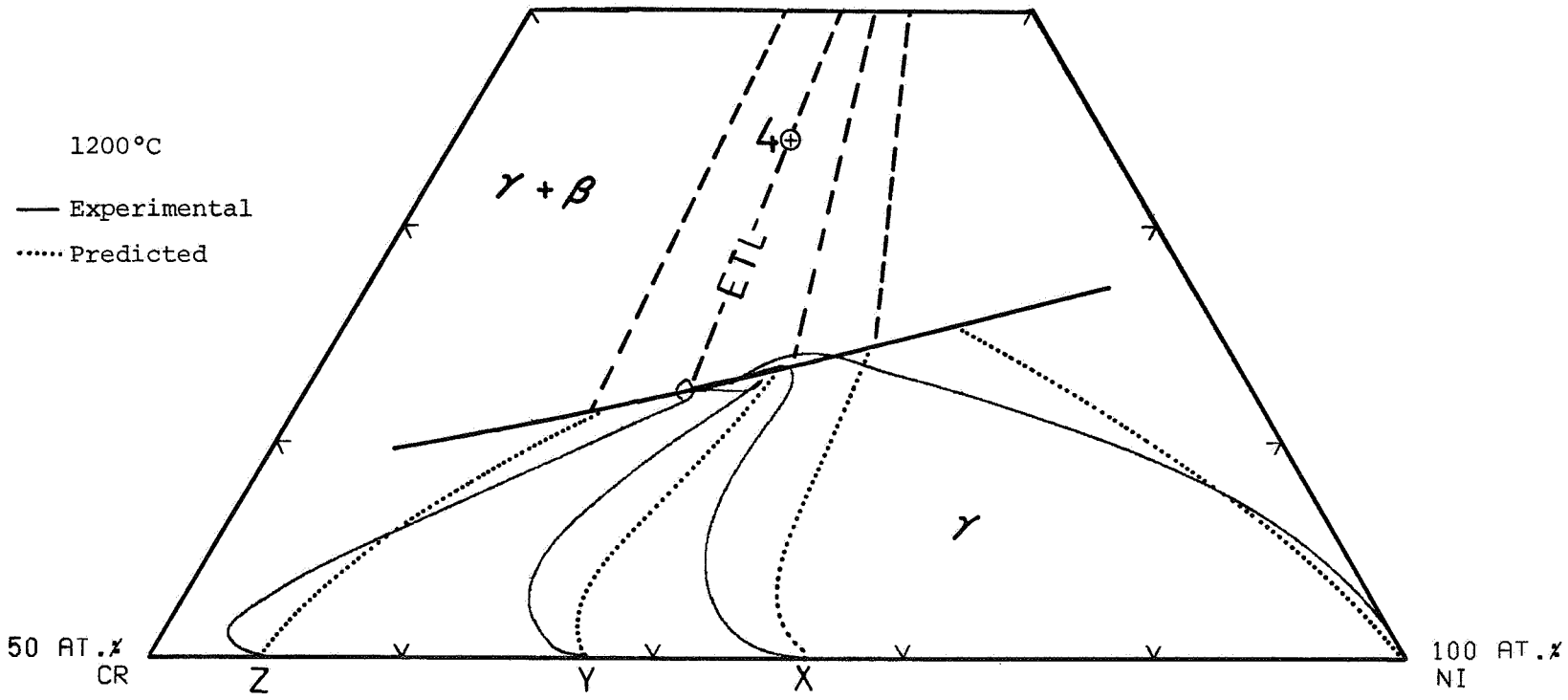

Figure C.4 Measured and predicted diffusion paths for the 4/Ni, 4/X, 4/Y and 4/Z γ/γ+β couples at 1200°C.

the ETL. Even though the concentrations in the $\gamma + \beta$ region shifted from that given by the ETL, the concentration of the γ phase was consistent with the $\gamma / \gamma + \beta$ phase boundary of the NiCrAl phase diagram at 1200°C (Appendix B). This observation implies the existence of local equilibrium between the γ and β phases in the $\gamma + \beta$ region (31).

A representative concentration/distance profile for one of the $\gamma / \gamma + \beta$ couples is shown in Figure C.5. The distance coordinate has been shifted so that the zero position corresponds to the $\gamma / \gamma + \beta$ interface. Many of the couples exhibited a maximum in the Cr concentration profile (Figure C.5) typically associated with a steep Al concentration gradient (4/X, 4/Y, 4/Z, B1/Z, B3/Y, 2C/W, B3/X, 6/Y, 9C/W and B1/Y). The $\gamma / \gamma + \beta$ diffusion paths are plotted on the ternary phase diagrams in Figures C.1a and b. The recession of the β phase (and γ' phase for couple 9C/W) after 100 hours at 1200°C is given in Table C-2. Representative microstructures of three of the $\gamma / \gamma + \beta$ couples are shown in Figure C.6. A significant difference in the amount of porosity between the couples of Levine (12) (Figure C.6c) and those fabricated in this study (Figure C.6a,b) is evident in the microstructures of Figure C 6

Analysis

γ / γ Couples (1100° and 1200°C).

Two techniques are commonly employed to determine concentration-dependent interdiffusion coefficients in ternary alloys. The first technique requires positioning of the Matano plane while the second technique does not. For simplicity, the two techniques will be simply referred to as KBM (Kirkaldy E171 and Boltzman/Matano [18]) and

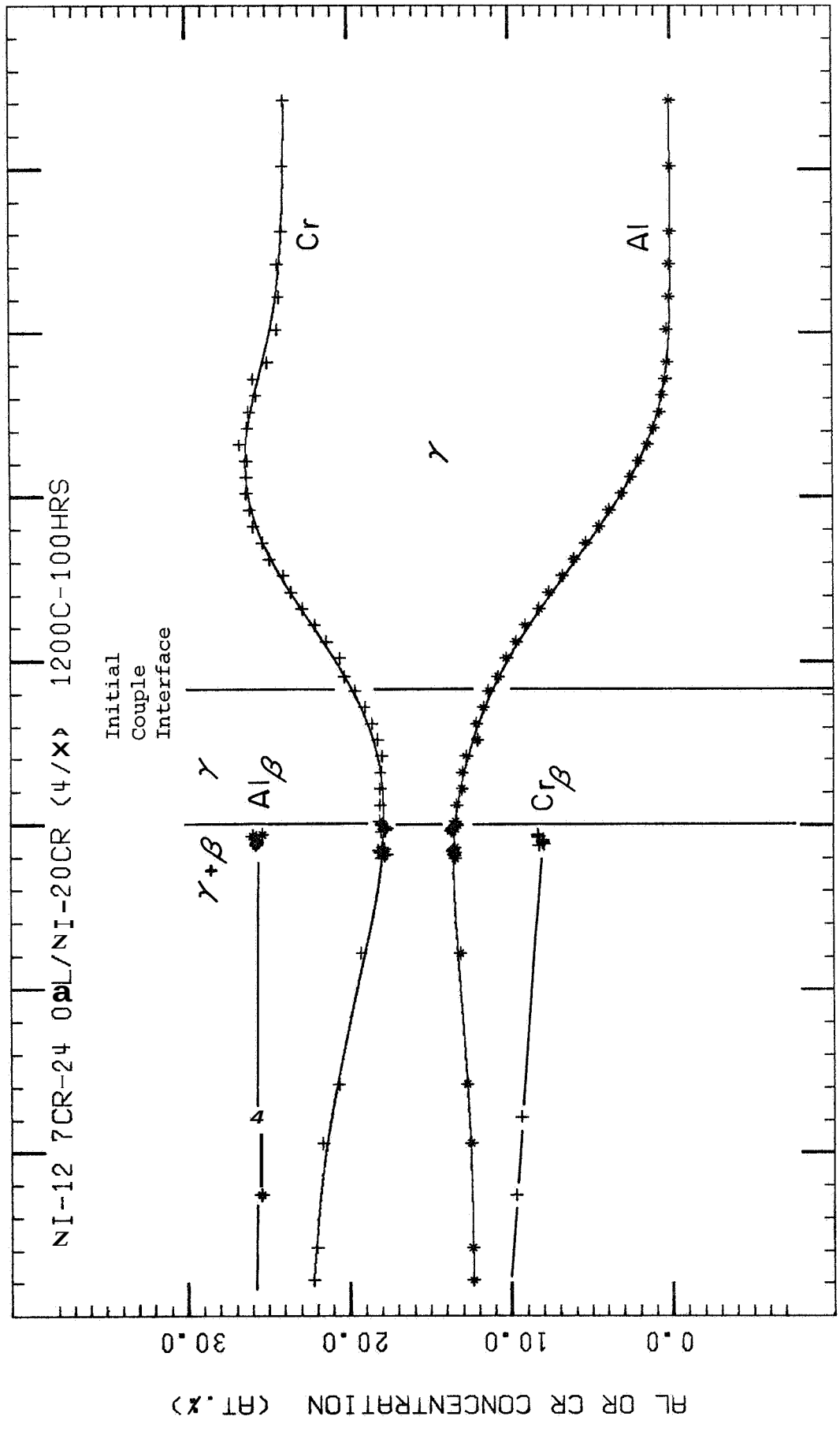

Figure 35 Concentration/distance profiles for the +β couple 4/X annealed for 100 hours at 1200°C.

Table C-2

β Recession in γ/γ + β Couples (1200°C)

Couple	β Recession (μm)
4/Ni	317 ± 21
4/X	205 ± 11
4/Y	143 ± 9
4/Z	123 ± 5
Bl/Ni	510 ± 26
Bl/W	363 ± 16
Bl/Y	222 ± 13
Bl/Z	155 ± 9
8/Ni-10Al	533 ± 13
8C/W	460 ± 10
8/Z	270 ± 9
B3/X	428 ± 17
B3/Y	314 ± 10
6C/W	140 ± 25
6/Y	129 ± 15
1C/W	150 ± 6
2C/W	313 ± 12
2C/3SL	114 ± 9
5C/W	33 ± 4
9C/W (γ' Recession)	503 ± 20

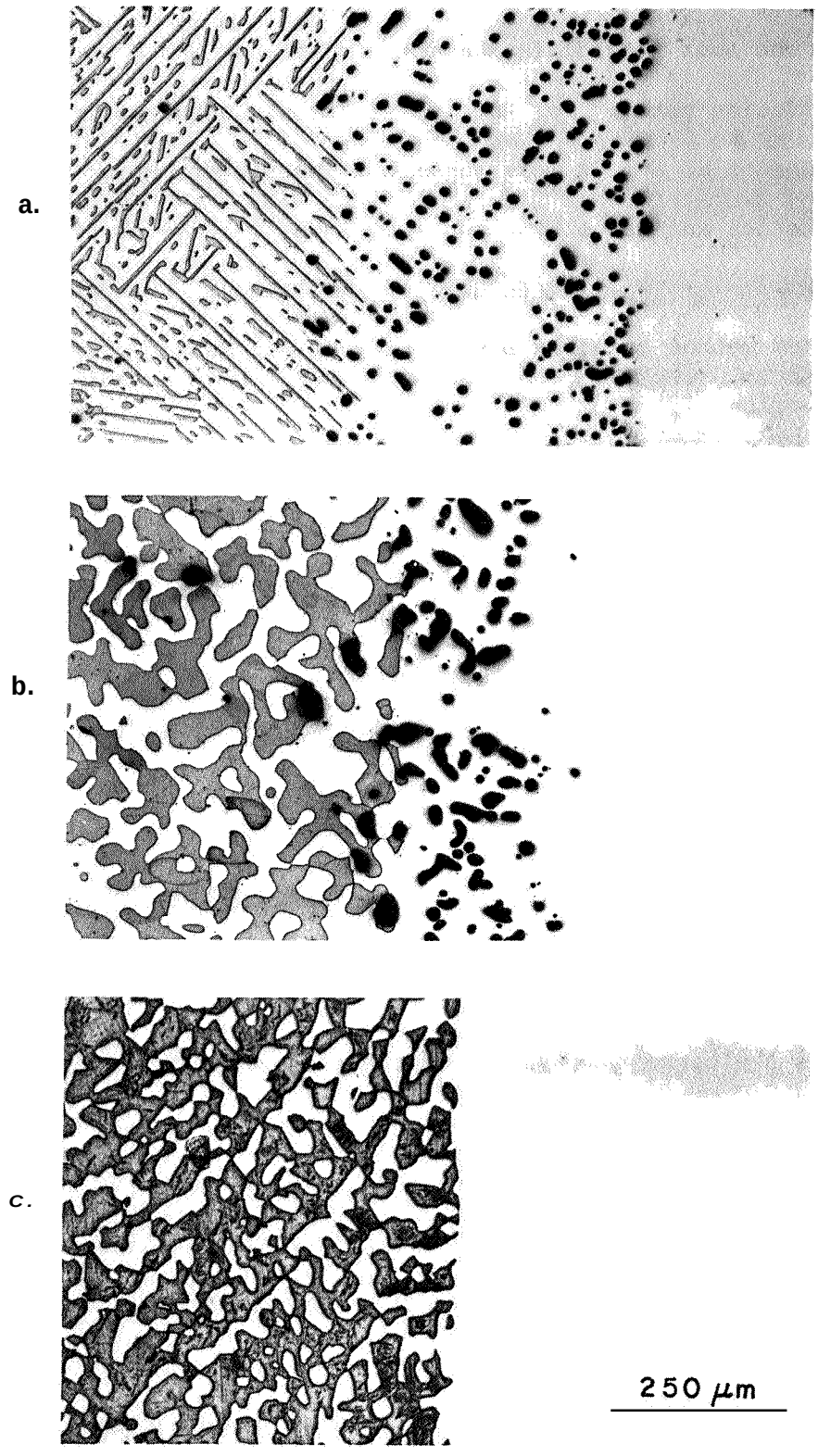

Figure C.6 $\gamma/\gamma+\beta$ **diffusion couples annealed at 1200°C for 100 hours. a.** Ni-10.2Cr-22.2Al/Ni-25.0Cr **(B3/X), b.** Ni-12.7Cr-24.0Al/Ni-25.0Cr **(4/X) and, c.** Ni-14.4Cr-23.7Al/Ni-12.0Cr **(1C/W).**

the second technique as WG (Whittle/Green [32]). Both techniques calculate the four interdiffusion coefficients at a common intersection of two diffusion paths. For the use of either technique, the partial molar volume of Al and Cr were assumed to be concentration independent. Characteristics and use of the two techniques will be briefly described separately.

The KBM method requires positioning of the Matano planes according to the Equation:

$$\int_{C_i^-}^{C_i^t} X\,dC = 0 \qquad i=Al,\ Cr \qquad [C.1]$$

where X is measured from the Matano plane and C_i^- and C_i^+ are the bulk concentrations at either end of the couple for both components Al and Cr. Splitting Equation [1] into two integrals yields:

$$\int_{C_i^-}^{C_i^*} X\,dC = \int_{C_i^+}^{C_i^*} X\,dC \qquad i=Al,Cr \qquad [C.2]$$

where C_i^* is the concentration of component i at the Matano plane. Positioning of the Matano plane for both components should ideally be identical. Coincidence of the Matano planes calculated by Equation [C.1] for each component can be used as an experimental check on the consistency of the concentration/distance measurements (33). One problem in positioning the Matano plane occurs in couples with a very small concentration difference of one component between the two bulk alloys. In this case, very small changes in the bulk concentration of one of the alloys can drastically affect the position of the Matano

plane. Couples 7S/1S and Ni-10Al/6S exhibit very Little change in the Al concentration across the diffusion zone, while couple 3SL/W (1100°C) exhibits very little Cr concentration change across the diffusion zone. For two of the couples, only the Cr Matano plane (7S/1S) or Al Matano plane (3SL/W, 1100°C) was used to calculate the interdiffusion coefficients. The Al and Cr Matano planes for each of the Y/Y couples are shown in the concentration/distance plots of Figures C.2, C.3 and Appendix C.2. Discrepancies between the Al and Cr Matano planes calculated on the basis of Equation [C.1] were used to help assess the accuracy of the measured diffusivities. If the Al and Cr Matano planes were not coincident, both Matano planes were used to calculate several sets of the four diffusion coefficients (see Appendix C.1). The range in the values of the diffusivities calculated for each Matano plane were taken as indicative of the accuracy of the diffusion coefficients.

All integrations involving the concentration/distance profiles for positioning the Matano plane and for subsequent calculation of the diffusivities were performed numerically using Simpsons 1/3 and 3/8 approximations (34). A smooth curve representative of the concentration/distance data was produced by a cubic spline curve smoothing routine (35). The cubic spline curve is shown as the solid line in each of the concentration/distance plots in Figures C.2, C.3 and Appendix C.2. Smoothing parameters for the Al and Cr curves are shown atop each plot to the right side. In general, a larger smoothing parameter is indicative of more random scatter in the experimental data, The smooth cubic spline curve was divided into 2500 segments to permit accurate numerical integration by Simpson's approximations. The

numerical integration was accurate to less than one percent relative error.

The possibility of misrepresenting the experimental data always exists when using curve smoothing routines. The cubic spline smoothing routine used in this study was desired to eliminate the obvious point to point fluctuations in the experimental data. The fluctuations were most obvious in the Cr concentrations. Small variation in the smoothing parameters did not strongly influence the numerical integrations. A significant benefit of the cubic spline smoothing routine was the ability to determine the concentration gradient at any position of a concentration profile. The concentration gradients for Al and Cr for both intersecting diffusion paths at the concentration of the intersection are required to calculate the four interdiffusion coefficients (17, see also Appendix C.1). Determination of the concentration gradients is often a source of considerable error (33) and discrepancies between diffusivities calculated by different authors. Tn this study, once the smoothing parameters for the cubic spline smoothing routine were chosen as most representative of the experimental data, the concentration gradients were fixed eliminating one subjective step of considerable sensitivity. The average and standard deviation of the four interdiffusion coefficients calculated at the intersections of the γ/γ diffusion paths are listed in Tables C-3 (1100°C) and C-4 (1200°C).

The WG technique eliminates the need to position the Matano plane by normalizing both the Al and Cr concentrations. Whittle and Green (32) have introduced the normalized concentration parameter Y_i defined as:

Table C-3

Ternary Interdiffusion Coefficients - 1100°C

	DIFFUSION COUPLE	INTERSECTION AT.%	DIFFUSION COEFFICIENTS X 10^{10} D-ALAL	STD DEV	D-ALCR	STD DEV	D-CRAL	STD DEV	D-CRCR	STD DEV
1	NI-10AL/W == NI-10CR-10AL/NI	NI- 6.74CR- 3.21AL	1.61	.16	.35	.03	1.02	.18	.89	.09
2	612/W == NI-10CR-10AL/NI	NI- 9.22CR- 3.77AL	1.67	.06	.44	.03	.94	.11	1.05	.08
3	3SL/W == 5SB/X	NI-13.54CR- 7.66AL	2.07	.36	.58	.19	.73	.06	.99	.03
4	3SL/W == 5SB/Y	NI-13.66CR- 8.46AL	2.47	.51	.81	.22	.90	.10	1.00	.29
5	4SL/W == NI-10CR/10AL/X	NI-16.70CR- 5.16AL	1.70	.16	.56	.08	.91	.12	.73	.06
6	4SL/W == 5SB/X	NI-17.21CR- 5.72AL	1.96	.19	.58	.10	.55	.15	.81	.08
7	4SL/W == 5SB/Y	NI-18.23CR- 6.71AL	2.58	.32	.80	.13	.73	.28	.97	.14
8	2S/W == NI-10CR-10AL/X	NI-19.90CR- 3.59AL	1.27	.06	.29	.01	1.46	.06	.89	.03
9	2S/W == 5SB/X	NI-20.83CR- 3.83AL	1.34	.03	.29	.02	1.12	.08	1.02	.01
10	2S/W == 5SB/Y	NI-24.05CR- 4.49AL	1.53	.07	.33	.02	1.14	.24	1.05	.03
11	2S/W == 4S/Y	NI-29.17CR- 5.33AL	1.92	.10	.43	.01	1.34	.09	1.15	.05

Table C-4

Ternary Interdiffusion Coefficients - 1200°C

	DIFFUSION COUPLE	INTERSECTION AT.%	DIFFUSION COEFFICIENTS X 10^{10} D-ALAL	STD DEV	D-ALCR	STD DEV	D-CRAL	STD DEV	D-CRCR	STD DEV
1	B69/X == 7S/1S	NI-18.00CR- 5.62AL	9.36	.19	2.57	.14	3.33	.21	3.86	.03
2	7S/1S == 3S/Y	NI-31.63CR- 4.40AL	11.41	.60	2.55	.16	4.62	.39	4.78	.03
3	NI-10AL/6S == 7S/1S*	NI- 9.05CR- 5.70AL	12.44	.97	2.91	.20	-.11	.84	3.01	.78
4	7S/1S == B69/Y	NI-24.68CR- 4.93AL	8.55	.22	2.02	.09	2.91	.17	3.71	.07
5	NI-10AL/X == 3SL/W	NI-13.05CR- 2.90AL	6.30	.53	1.13	.16	3.68	.17	3.71	.09
6	NI-10AL/X == B69/NI	NI- 3.32CR- 5.79AL	8.73	.96	2.37	.31	2.03	.72	3.20	.20
7	NI-10AL/W == B69/NI	NI- 2.48CR- 4.97AL	8.63	.80	1.89	.54	1.32	.66	3.59	.35
8	3SL/W == B69/X	NI-13.72CR- 8.33AL	11.60	.91	3.50	.52	6.43	.26	5.82	.15
9	B69/Y ==3SL/Y	NI-14.08CR- 9.55AL	11.40	1.54	3.50	.73	7.61	.43	6.71	.22
10	NI-10AL/6S == 3SL/W	NI-13.26CR- 4.90AL	7.64	.48	1.69	.13	3.85	.16	3.95	1.04
11	7S/1S == 3SL/Y	NI-13.39CR- 6.17AL	8.97	.57	2.78	.14	4.40	.16	3.60	.01
12	B69/NI == NI-10AL/6S	NI- 4.41CR- 6.74AL	9.16	1.11	2.89	.25	1.86	.82	3.80	.35
13	4/X == 6/W	NI-19.86CR-11.03AL	25.07	1.68	6.77	1.13	9.81	.91	6.17	.72
14	4/X == 8/NI-10AL	NI-20.41CR-10.53AL	23.50	1.51	7.07	.37	12.50	.50	8.84	.13
15	4/X == 8/W	NI-20.66CR-10.31AL	21.11	1.70	5.52	1.45	8.51	1.16	5.33	1.04
16	4/X == 5C/W	NI-20.80CR-10.18AL	21.80	1.30	6.45	.77	10.05	.72	6.77	.59
17	B69/Y == 4/X	NI-25.61CR- 4.55AL	8.63	.81	2.01	.33	8.44	.46	5.86	.18
18	4/X == 7S/1S	NI-25.46CR- 4.83AL	9.00	.67	2.16	.06	7.48	.16	4.24	.01
19	4/Z == 6/Y*	NI-29.05CR- 9.31AL	7.70	2.00	.16	1.06	7.41	1.80	6.61	1.39
20	4/Z == 5C/W*	NI-24.66CR-11.15AL	34.60	2.36	9.88	.84	14.21	3.15	9.91	.99
21	4/Z == B1/Y	NI-31.45CR- 8.32AL	15.95	2.01	3.93	.99	10.31	1.02	7.67	.98
22	B3/Y == 4/Y	NI-33.49CR- 2.96AL	7.16	.88	.39	.80	4.96	.32	4.81	.53
23	7S/1S == 4/Y	NI-32.36CR- 4.38AL	10.40	.62	2.85	.00	5.09	.25	4.96	.00
24	6/W == 4/Y	NI-21.42CR-11.59AL	29.14	2.08	7.93	1.80	6.91	1.78	7.68	.82
25	8/W == 4/Y	NI-21.86CR-11.34AL	26.11	3.48	7.95	2.00	9.33	2.93	8.75	1.74
26	8/NI-10AL == 4/Y	NI-22.02CR-11.24AL	24.91	.88	6.32	.82	11.52	.87	9.90	.60
27	3S/Y == 4/Y*	NI-27.40CR- 8.08AL	10.93	.43	1.31	.72	-1.20	.18	1.23	.43
28	3S/Y == 4/Y	NI-33.31CR- 3.23AL	7.50	1.21	.66	1.25	5.74	.67	5.94	.93
29	5C/W == 4/Y*	NI-22.84CR-10.76AL	25.70	1.53	7.52	.71	9.57	1.44	8.43	.67
30	5C/W == B3/Y	NI-21.60CR-10.43AL	21.83	1.46	7.04	.70	5.71	1.59	8.54	.68
31	8/NI-10AL == B3/Y	NI-21.10CR-10.76AL	23.50	1.34	7.88	.50	8.61	1.73	11.05	.65
32	6/W == B3/Y	NI-20.38CR-11.24AL	24.14	1.94	7.78	1.07	5.00	2.01	8.62	.94

Table C-4 (con't.)

	DIFFUSION COUPLE	INTERSECTION AT.%	DIFFUSION COEFFICIENTS x 10^{10} D-ALAL	STD DEV	D-ALCR	STD DEV	D-CRAL	STD DEV	D-CRCR	STD DEV
33	B1/N1 == B3/Y*	NI-ZO.W8CR-11.CSAL	31.51	2.92	13.20	1.21	-2.86	4.31	4.55	2.12
34	8/W == B3/Y	NI-21.18CR-10.70AL	21.82	2.33	6.95	1.57	5.34	2.09	8.80	1.45
35	NI-10AL/6S == 5/W	NI-13.80CR- 4.80AL	9.39	.48	1.89	.09	4.23	.22	3.43	.49
36	NI-10AL/6S == 5C/W	NI-15.38CR- 4.53AL	11.03	.67	2.26	.11	6.14	.42	3.84	.41
37	NI-10AL/6S == 6/W	NI-15.20CR- 4.36AL	12.73	.86	2.44	.14	6.04	.45	3.81	.43
38	NI-10AL/6S == 8/W	NI-14.70CR- C.04AL	8.41	.56	1.73	.10	3.98	.30	3.47	.41
39	9C/W == 8/NI-10AL	NI-10.02CR-1 56AL	19.44	3.22	5.69	.16	2.93	.57	5.77	.03
40	B69/NI == 8/NI-10AL*	NI- 8.05CR-10.65AL	12.33	.52	5.40	.26	3.46	.29	5.75	.54
41	5/W == 8/NI-10AL	NI-14.69CR-10.34AL	21.85	1.94	6.15	.09	5.64	.57	6.52	.03
42	6/W == 8/NI-10AL	NI-18.37CR-10.28AL	19.94	3.21	6.84	.13	5.04	1.87	8.13	.08
43	B69/Y == 8/NI-10AL*	NI-12.22CR-10.46AL	15.52	.64	5.88	.33	7.65	2.15	6.99	1.09
44	B69/Y == 5C/W	NI-17.15CR- 8.12AL	14.61	1.03	4.88	.47	6.76	.65	5.95	.30
45	B69/Y == 6/W	NI-16.54CR- 8.40AL	13.89	1.15	4.60	.52	5.97	.59	5.65	.27
46	B69/Y == 6/W	NI-17.21CR- 8.10AL	13.14	1.32	4.22	.59	4.95	.78	5.13	.35
47	B69/Y == 5/W	NI-14.34CR- 9.42AL	17.08	1.32	6.62	.64	5.20	.37	5.56	.18
48	B69/Y == 2C/W	NI-13.63CR- 9.76AL	16.10	1.84	5.97	.90	4.99	.21	5.52	.11
49	2C/W == 8/NI-10AL	NI-13.56CR-10.40AL	18.25	1.70	6.09	.30	5.54	.19	7.12	.96
50	2C/W == B69/X	NI-13.86CR- 8.24AL	12.75	1.07	4.10	.60	4.40	.15	4.62	.10
51	2C/W == NI-10AL/X	NI-14.04CR- 2.02AL	5.97	.33	.97	.09	3.63	.14	3.67	.08
52	2C/W == NI-10AL/6S	NI-14.19CR- 4.72AL	7.91	.54	1.64	.10	3.70	.23	3.37	.48
53	2C/W == 7S/1S	NI-14.14CR- 6.11AL	9.55	.83	2.86	.07	3.86	.21	3.71	.01
54	B69/Y == B3/X	NI-24.46CR- 5.01AL	11.77	1.09	3.31	.44	6.93	.23	5.33	.09
55	B3/X == 8/NI-10AL	NI-19.12CR-10.34AL	24.37	2.28	6.64	.22	8.30	.56	8.44	.05
56	B3/X == 8/W	NI-19.72CR- 9.75AL	20.01	1.47	4.31	1.20	5.89	.94	6.05	.82
57	B3/X == 5C/W	NI-19.70CR- 9.77AL	21.73	1.26	5.84	.80	7.4	.78	7.41	.54
58	B3/X == 6/W	NI-18.89CR-10.58AL	24.05	1.65	5.63	1.20	6.4	.90	7.31	.69
59	7S/1S == 6/W	NI-15.58CR- 5.97AL	10.83	1.48	3.42	.30	7.0	.68	4.12	.21
60	7S/1S == 8/W	NI-15.40CR- 5.89AL	9.60	.98	2.77	.11	4.3	.49	3.87	.05
61	7S/1S == 5/W	NI-13.9CLR- 0 13AL	11.20	.76	3.00	.06	4.5	.28	3.74	.02
62	7S/1S == B3/Y	NI-31.53CR- 4.40AL	10.94	.62	2.74	.02	4.0	.56	4.79	.02
63	7S/1S == B3/X	NI-24.55CR- 4.92AL	10.68	.83	2.37	.08	5.9	.03	4.09	.01
64	7S/1S == 5C/W	NI-15.92CR- 5.94AL	15.97	1.29	3.44	.14	8.19	.76	4.32	.06

Table C-4 (con't.)

	DIFFUSION COUPLE	INTERSECTION AT.%	DIFFUSION COEFFICIENTS × 10^{10} D-ALAL	STD DEV	D-ALCR	STD DEV	D-CRAL	STD DEV	D-CRCR	STD DEV
65	7S/1S == 6/Y	NI-34.31CR- 4.46AL	13.05	.88	2.81	.09	7.02	.03	4.63	.00
66	B69/X == 8/W	NI-16.11CR- 7.01AL	11.15	.79	3.25	.43	4.52	.42	4.55	.23
67	B69/X == 5C/W	NI-16.35CR- 6.89AL	11.31	.65	3.45	.28	5.47	.60	5.43	.46
68	B69/X == 6/W	NI-15.96CR- 7.10AL	11.15	.68	3.25	.37	5.17	.34	4.91	.19
69	B69/X == 8/NI-10AL*	NI-10.16CR-10.57AL	13.86	.36	5.62	.26	6.14	.94	6.40	.76
70	B69/X == 5/W	NI-14.10CR- 8.12AL	14.62	.84	5.14	.47	4.91	.25	4.91	.16
71	NI-10AL/X == 5C/W	NI-14.64CR- 2.45AL	7.61	.38	1.40	.11	4.66	.28	3.96	.09
72	NI-10AL/X == 8/W	NI-13.90CR- 2.65AL	6.75	.38	1.16	.11	3.61	.22	3.66	.09
73	NI-10AL/X == 6/W	NI-10.61CR- 2.46AL	8.21	.48	1.57	.13	4.58	.31	3.94	.10
74	NI-10AL/X == 5/W	NI-13.36CR- 2.80AL	7.13	.32	1.31	.09	3.70	.19	3.68	.08
75	5C/W == B1/NI*	NI-23.51CR-10.92AL	2.60	3.94	13.80	.80	25.20	6.91	5.59	1.49
76	5/W == B1/NI*	NI-14.88CR-10.74AL	20.58	2.16	2.02	.99	8.00	.88	3.35	1.19
77	4/Z == B1/NI*	NI-25.81CR-10.68AL	45.12	3.26	15.21	1.24	*****	7.69	-2.77	3.03
78	4/X == B1/NI*	NI-19.37CR-11.47AL	30.83	2.45	10.22	1.02	8.39	2.03	4.73	1.72
79	4/Y == B1/NI*	NI-22.15CR-11.18AL	54.76	5.92	23.29	1.81	-.81	0.61	2.84	3.54
80	2C/W == B1/NI*	NI-13.55CR-10.41AL	18.02	1.65	3.50	.80	5.21	.19	3.93	.86
81	B3/X == B1/NI*	NI-16.16CR-11.3EAL	29.11	2.61	6.39	.88	3.69	1.92	4.63	1.35
82	B69/Y == B1/NI*	NI-12.73CR-10.21AL	13.02	1.10	4.56	.55	2.80	1.37	4.52	.68
83	9C/W == B1/NI*	NI-10.89CR- 9.66AL	15.72	1.70	3.15	.77	2.69	.36	4.30	.66
84	6/W == B1/NI*	NI-20.81CR-11.39AL	9.60	4.04	13.44	.95	12.10	5.20	5.74	1.62
85	B69/X == B1/NI*	NI-11.31CR- 9.78AL	12.43	.68	4.27	.44	3.24	.79	4.22	.51
86	NI-10AL/X == B1/NI	NI- 2.70CR- 5.98AL	13.18	.75	3.78	.24	3.00	.40	3.36	.23
87	NI-10AL/W == B1/NI	NI- 1.98CR- 5.24AL	10.75	.53	3.19	.30	1.49	.24	3.56	.19
88	NI-10AL/6S == B1/NI	NI- 3.85CR- 6.86AL	15.94	1.11	4.28	.30	5.44	2.13	3.05	1.27
89	B69/NI == B1/NI*	NI- 5.65CR- 7.7EAL	2.73	2.19	8.84	1.50	2.30	1.57	4.39	1.08
90	4/NI == 6/NI-10AL	NI- 8.07CR-10.04AL	21.03	2.18	5.53	.25	5.88	1.93	5.78	.53
91	B69/NI == 4/NI*	NI- 8.05CR-10.64AL	10.17	.74	10.90	1.29	2.88	.42	7.25	.90
92	9C/W == 4/NI*	NI-10.51CR-11.78AL	26.90	5.15	8.14	2.77	1.70	.86	10.91	1.43
93	B69/X == 4/NI	NI- 9.34CR-11.25AL	17.15	.86	9.52	.80	6.08	.71	7.08	.67
94	B69/Y == 4/NI	NI-10.10CR-11.60AL	20.54	1.58	9.75	.93	7.43	1.38	7.59	.81
95	4/NI == NI-10AL/6S	NI- 2.88CR- 7.06AL	12.72	.79	3.66	.33	3.49	1.77	2.18	1.81
96	4/NI == NI-10AL/X	NI- 2.10CR- 6.18AL	11.66	.61	3.34	.20	1.88	.30	2.94	.28

Table C-4 (con't.)

	DIFFUSION COUPLE	INTERSECTION AT.%	DIFFUSION COEFFICIENTS x 10^{10} D-ALAL	STD DEV	D-ALCR	STD DEV	D-CRAL	STD DEV	D-CRCR	STD DEV
97	4/NI == NI-10AL/W	NI- 1.58CR- 5.46AL	10.76	.46	3.31	.28	1.08	.18	3.30	.22
98	7S/1S == B1/Y	NI-34.58CR- 4.49AL	10.87	.16	2.83	.23	8.35	.33	3.90	.47
99	9C/W == NI-10AL/X	NI-13.25CR- 2.64AL	6.40	.44	1.11	.12	2.97	.10	3.47	.08
100	9C/W == NI-10AL/6S	NI-12.77CR- 4.97AL	8.07	.67	1.68	.12	2.45	.18	3.05	.57
101	9C/W == 7S/1S	NI-12.33CR- 6.22AL	9.79	.99	3.06	.04	2.49	.01	3.40	.00
102	9C/W == B69/X	NI-10.73CR-10.17AL	19.08	2.82	9.04	2.01	2.46	.48	3.72	.33
103	9C/W == B69/Y	NI-10.50CR-11.38AL	23.97	4.79	11.22	2.69	2.42	.88	4.55	.49
104	9C/W CR MAX	NI-13.33CR- 1.79AL	5.65	.43	.00	.00	3.30	.21	.00	.00
105	B1/Y CR MAX	NI-35.73CR- 1.57AL	6.03	.40	.00	.00	11.71	.42	.00	.00
106	B69/X CR MAX*	NI-25.30CR- .51AL	3.84	.74	.00	.00	2.36	.99	.00	.00
107	B69/Y CR MAX*	NI-34.50CR- .19AL	3.01	.00	.00	.00	-2.79	.00	.00	.00
108	3S/Y CRMAX	NI-35.15CR- .93AL	4.77	1.75	.00	.00	1.92	1.64	.00	.00
109	B1/Z CR MAX	NI-46.96CR- 1.48AL	4.87	.37	.00	.00	2.60	.19	.00	.00
110	4/X CR MAX	NI-26.36CR- 2.02AL	5.67	.38	.00	.00	9.15	.40	.00	.00
111	4/Y CR MAX	NI-33.95CR- 1.48AL	6.09	.38	.00	.00	4.25	.26	.00	.00
112	B3/Y CR MAX	NI-35.43CR- .94AL	6.21	.40	.00	.00	5.65	.69	.00	.00
113	2C/W CR MAX	NI-14.19CR- 4.65AL	7.82	.63	.00	.00	3.65	.23	.00	.00
114	B3/X CR MAX	NI-25.74CR- 2.22AL	6.91	.47	.00	.00	6.04	.28	.00	.00
115	6/Y CR MAX	NI-35.92CR- 1.62AL	5.87	.42	.00	.00	6.35	.71	.00	.00
116	7S/1S AL MAX	NI-11.56CR- 6.24AL	.00	.00	3.18	.00	.00	.00	3.26	.00
117	7S/1S AL MIN	NI-32.61CR- 4.38AL	.00	.00	2.90	.00	.00	.00	5.01	.00
118	NI-10AL/6S AL MAX	NI- .87CR- 7.34AL	.00	.00	2.69	.00	.00	.00	3.48	.00
119	NI-10AL/6S AL MIN*	NI-19.52CR- 4.05AL	.00	.00	1.86	.00	.00	.00	2.82	.00
120	4/Z CR MAX	NI-46.37CR- .82AL	4.33	.30	.00	.00	4.67	.33	.00	.00
121	8/NI-10AL AL MAX	NI- 7.31CR-10.05AL	.00	.00	5.36	.31	.00	.00	5.54	.61

* - Questionable values (see text)

$$Y_i = \frac{C_i - C_i^-}{C_i^+ - C_i^-} \qquad i=1,2 \qquad [C.3]$$

where C_i is the concentration of Al or Cr, and C_i^- and C_i^+ are the concentrations of Al or Cr at either end of the diffusion couple. The necessary equations to calculate the four interdiffusion coefficients are fully described in References 32 and *36*. Since the Matano plane is not calculated by the WG method, only one set of diffusivities is determined. The four interdiffusion coefficients for each of the γ/γ couples at 1100° and 1200°C calculated using the WG technique were usually in the range of values and typically very close to the average calculated using the KBM technique. The diffusivities calculated by the WG technique were included in the average values listed in Tables C-3 and C-4.

Additionally, two of the four interdiffusion coefficients can be determined from a single diffusion couple by either the KBM or WG method when the Al or Cr concentration profiles exhibit a maximum or minimum. A discussion of the use of both techniques and a caution for using the KBM method, is given in Reference *36*. Both methods have been used to determine two of the four interdiffusion coefficients wherever a clearly discernible maximum or minimum in the Al or Cr concentration profile occurred in the γ/γ couples. (Only the diffusion couples annealed at 1200°C exhibited clearly discernible extrema.) Where the Al and Cr Matano planes were not coincident, the KBM method yielded two sets of diffusion coefficients. The diffusivities calculated at Al or Cr extrema are also listed in Table C-4.

$\gamma/\gamma+\beta$ Couples: The WG method for calculating interdiffusion coefficients can only be used with $\gamma/\gamma+\beta$ couples if diffusion in

the $\gamma + \beta$ region is insignificant or can be accurately measured. Measuring the diffusion in the $\gamma + \beta$ region requires determining the average concentration in the two-phase region as a function of the distance from some convenient reference point. The lack of accurate measurements of the β phase composition in this study precluded straightforward use of the WG method. As a result, this method was not utilized to calculate the diffusivities with the $\gamma/\gamma + \beta$ couples.

The KBM method has previously been used to calculate ternary interdiffusion coefficients in γ/β -type diffusion couples (37). The main difficulty in using the KBM method with $\gamma/\gamma + \beta$ couples comes with positioning the Matano plane. Accurate positioning of the Matano plane assumes a knowledge of the average Al and Cr concentration as a function of position in the $\gamma + \beta$ region when diffusion in the two-phase region has occurred. The lack of accurate β phase concentration data in the $\gamma + \beta$ region prevented the determination of the Matano plane directly from the concentration/distance profiles.

The position of the Matano plane was approximated as the present location of markers originally located at the initial couple interface. Because of the uncertainty in the position of the Matano plane, a range of ± 20 microns from the location of the markers was used. Review of Figures C.2,C.3 and Appendix C.2 show that the calculated Matano planes for Al and Cr in the γ/γ couples are almost always within 20 microns of the original interface markers. The range in the position of the Matano planes again gave several sets of diffusion coefficients when calculated using the KBM method. The average and standard deviation of the four interdiffusion coefficients calculated using the KBM method for each of the $\gamma/\gamma + \beta$ (and the $\gamma/\gamma + \gamma'$) couples are listed in

Table C-4. Two of the four interdiffusion coefficients were also calculated at Al and Cr maxima and minima and are also listed in Table c-4.

Discussion

Possible Errors

There are several possible sources of error associated with calculating the interdiffusion coefficients in this study. Some of the possible sources of error include:

1. Integration of the areas under the concentration/distance profiles and determination of the concentration gradient at specific concentrations.
2. The accuracy of the concentration measurements.
3. Ignoring an obvious vacancy flux imbalance which has resulted in significant porosity in many of the couples.
4. The assumption of a concentration/independent partial molar volume of Al and Cr.
5. The 5°C difference between the annealing temperature of the couples fabricated in this study and the previously fabricated and annealed couples (12).
6. Solution of the flux balance equations where the two diffusion paths cross at high angles or near the end points of one of the diffusion paths.
7. Positioning of the Matano plane.

Errors associated with the area integration and gradient determination have previously been discussed and are dependent on the

cubic spline represention of the experimental data. The cubic spline smoothing routines eliminate point-to-point concentration fluctuations associated with the electron microprobe measurements. In addition, use of the cubic spline curve smoothing routine is believed to improve the accuracy of the integration and concentration gradient determination over manual techniques to determine the areas and gradients. The accuracy of the concentration measurements has previously been discussed. Ignoring the vacancy flux imbalance should have no effect on the measurement of the interdiffusion coefficients, affecting mainly the relationship between the interdiffusion coefficients, the intrinsic diffusion coefficients, and marker motion due to the Kirkendall effect (38,391. The reduction in cross-sectional area in the diffusion zone of the couples containing significant porosity might be expected to reduce interdiffusion, but surface diffusion of Al and/or Cr on the inner surface of the pores may provide enhanced diffusion paths. Couples 4/Ni and B69/Ni both contain considerable Kirkendall porosity in the diffusion zone. Values of D_{AlAl} calculated at six diffusion path intersections with 1-5 at.% Cr show very good agreement with the binary interdiffusion coefficients at similar Al concentrations in the Ni-A1 system (15,19-22) suggesting that the porosity may have a limited effect on reducing interdiffusion. Errors introduced by the assumption of concentration-independent partial molar volumes is probably well within the accuracy of the diffusion coefficients (17). The effect on the diffusivities of the 5°C difference in the annealing temperature is probably well within the accuracy of the diffusion coefficients (see Tables C-3 and C-4). Solution of the flux balance equations to calculate the diffusivities are most sensitive when the diffusion paths

intersect at high angles or near the end point of one of the diffusion paths (14,33). Under these conditions, small errors in the area integrations or concentration gradients result in large discrepancies in the diffusion coefficients. Several intersecting diffusion paths in this study can be identified as exhibiting these characteristics (i.e. Ni-10Al/6S and 7S/1S, B69/Ni and 4/Ni). The diffusion coefficients at these intersections are of questionable value and exhibit diffusivities typically out of the range of diffusivities of close compositions. Each of the diffusivities of questionable value are starred in Tables C-3 and C-4. Positioning of the Matano plane has a significant effect on the calculation of the interdiffusion coefficients. The standard deviation of each diffusivity listed in Tables C-3 and C-4 is the result of two Matano planes being used to calculate the diffusivities. Therefore the error associated with the Matano planes is indicated by the standard deviations listed in Tables C-3 and C-4. The most significant test of the validity of the diffusivities is the ability to utilize the diffusivities to predict concentration/distance profiles in the Y phase resulting from interdiffusion, and is discussed in part II of this appendix.

Constraints on Ternary Diffusion Coefficients. Confidence in the validity of the diffusion coefficients can be increased by examining the diffusivities with respect to certain kinetic and thermodynamic constraints. Kirkaldy et. al (40) have derived the following thermodynamic constants for ternary diffusion coefficients:

1. $D_{AlAl} + D_{CrCr} > 0$

2. $D_{AlAl} \times D_{CrCr} - D_{AlCr} \times D_{CrAl} \geq 0$

3. $(D_{AlAl} + D_{CrCr})^2 \geq 4(D_{AlAl} \times D_{CrCr} - D_{AlCr} \times D_{CrAl})$

combining thermodynamic and kinetic constrants (17,40) results in the following conditions:

4. $D_{AlAl} > 0$ and $D_{CrCr} > 0$

5. $D_{AlCr} \times D_{CrAl} \geq 0$

6. $D_{AlAl} \times D_{CrCr} - D_{AlCr} \times D_{CrAl} \geq 0$

After eliminating the diffusivities of questionable value (starred concentrations in Tables C-3 and C-4), examination of Tables C-3 and C-4 shows that all of the 1100" and 1200°C diffusivities satisfy all six of the kinetic and thermodynamic constraints.

It is interesting to examine the concentration dependence of the four interdiffusion coefficients. The diffusion coefficients for Al, D_{AlAl} and D_{AlCr} both increase with increasing Al concentration but show little dependence on the Cr concentration. D_{AlAl} increases by a factor of 5-6 in the range 0-14 wt.% Al while D_{AlCr} shows a slightly larger relative increase. D_{AlAl} and D_{AlCr} (1200°C) are shown as functions of the Al concentration in Figures C.7a and b. Neither D_{CrAl} or D_{CrCr} exhibit a definite dependence on either the Cr or Al concentration. D_{CrAl} and D_{CrCr} (1200°C) are shown as functions of the Cr concentration in Figures C.7c and d.

Various authors have utilized dilute solution and regular solution approximations to describe the variation of ternary diffusion coefficients with composition, primarily in ternary systems involving an interstitial solute (28,41-43). Following the treatment of Bolze et.al. (41), the Wagner dilute solution model (44) predicts

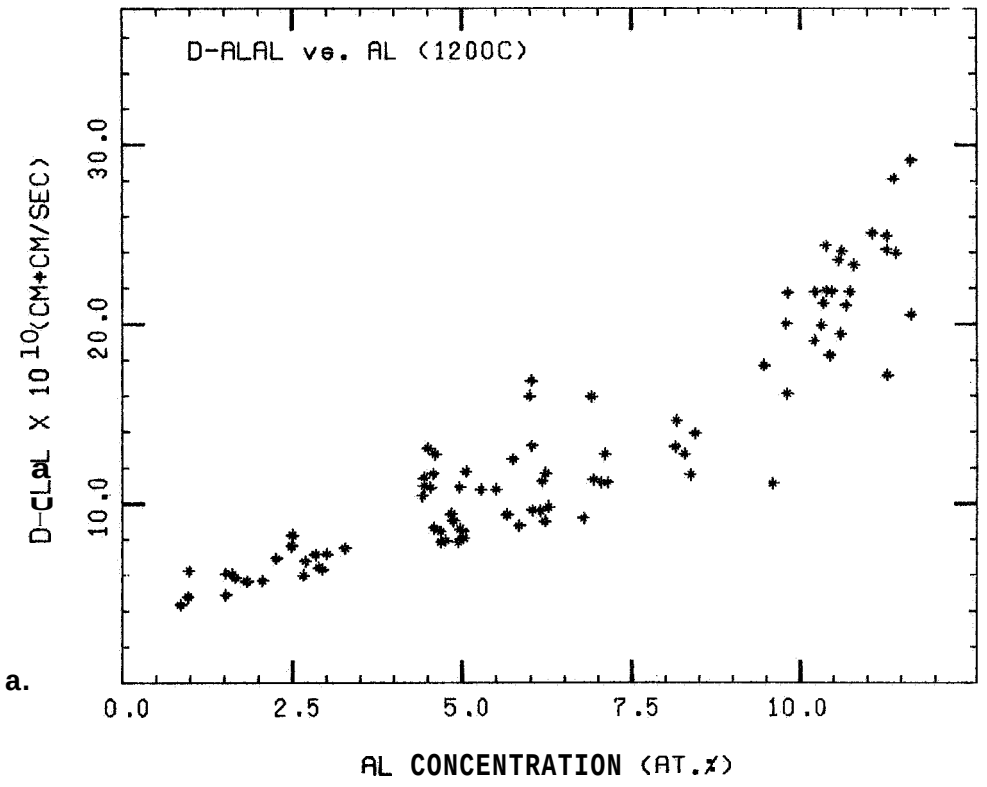

a.

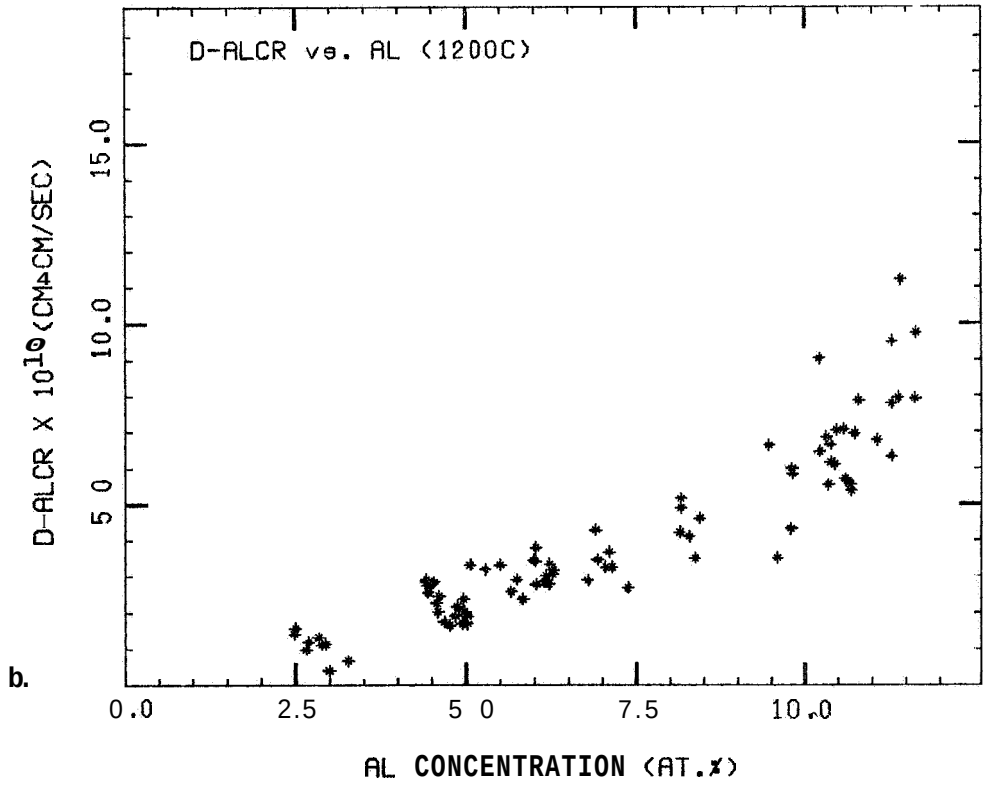

b.

Figure G.7 Variation of diffusivities with concentration (1200°C) a. D_{AlAl} **vs. Al,** b. D_{AlCr} **vs. Al.**

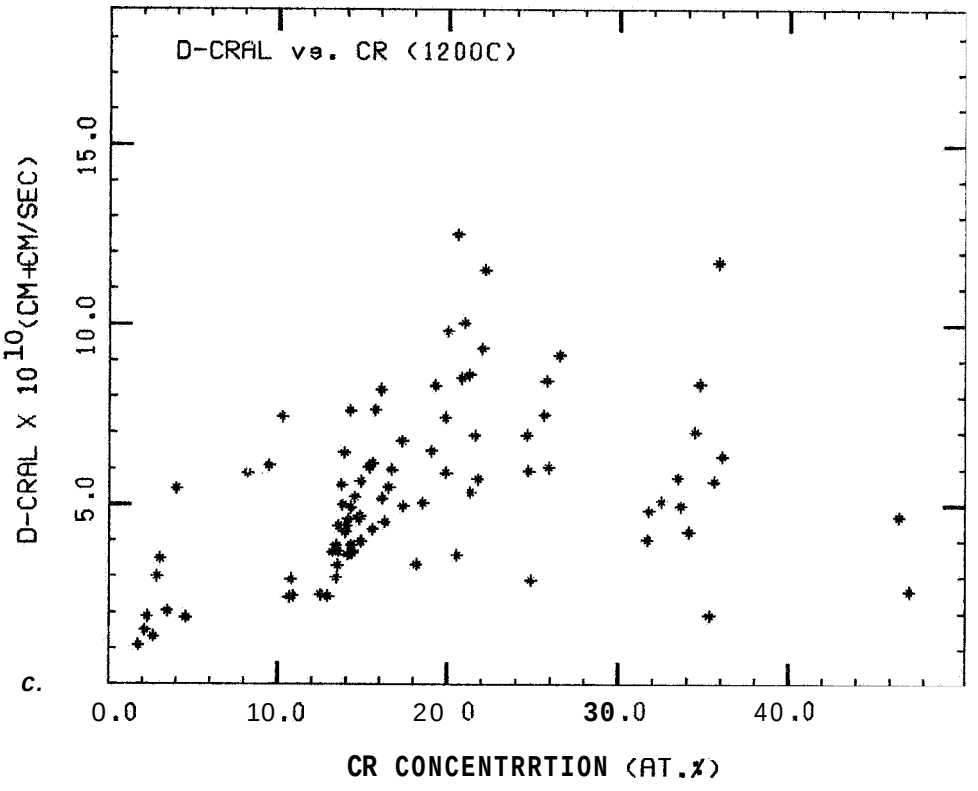

c.

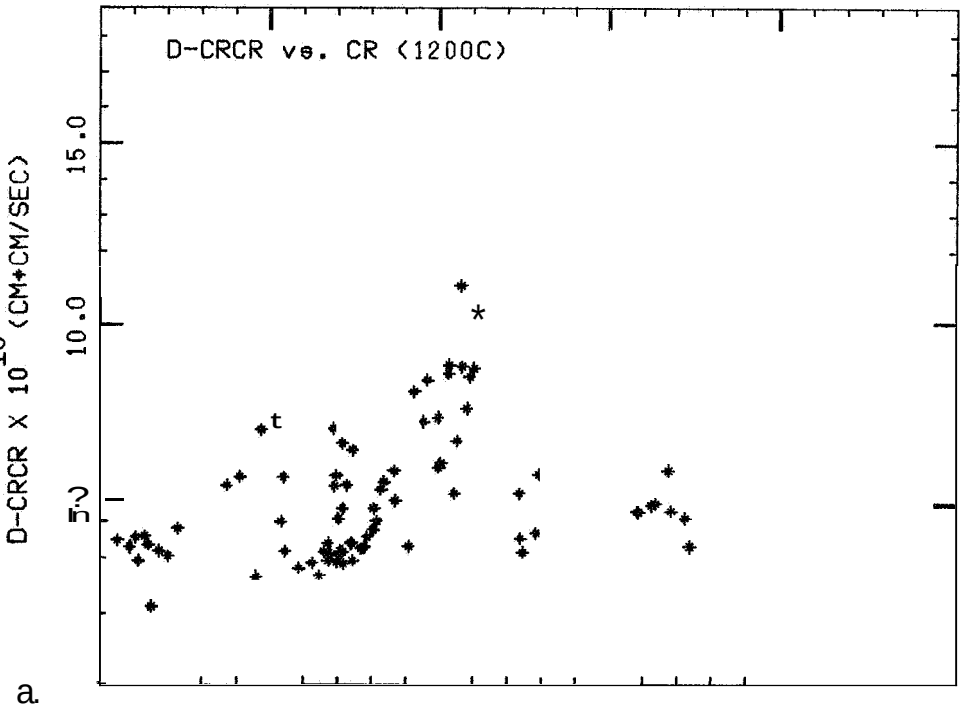

a.

Figure C.7 (con't.) Variation of diffusivities with concentration (1200°C). c. D_{CrAl} vs. Cr and, d. D_{CrCr} vs. Cr.

concentration-independent diagonal diffusion coefficients (D_{AlAl} and D_{CrCr}) and off-diagonal coefficients given as:

$$\frac{D_{AlCr}}{D_{AlAl}} \propto C_{Al} \qquad [C.4]$$

$$\frac{D_{CrAl}}{D_{CrCr}} \propto C_{Cr} \qquad [C.5]$$

D_{AlAl} and D_{CrCr} have previously been shown to be dependent on the concentration (Figures C.7a and d) although D_{CrCr} shows no specific dependence on the Al or Cr concentration taken separately. Figures C.8 a and b show that D_{AlCr}/D_{AlAl} increases slightly with increasing Al concentration, whereas D_{CrAl}/D_{CrCr} shows no clear relationship ta the Cr concentration. Clearly the Wagner dilute solution model does not apply for the concentrations examined in this study.

The Al concentration gradient has a much larger effect than the Cr concentration gradient on the diffusion of Al. This result is evident in Figure C.8a where it is shown that $D_{AlCr} \simeq$ 0.2-0.4 D_{AlAl} for most of the Al concentrations in the γ phase. That D_{AlCr} is much less than D_{AlAl} might be expected considering the NiCrAl phase diagram. The $\gamma / \gamma + \beta$ phase boundary is almost parallel to the Ni-Cr side of the ternary phase diagram (Appendix B) indicating a weak dependence of the Al chemical potential on the Cr concentration (45). D_{AlCr} is proportional to the derivative of the Al chemical potential with respect to the Cr concentration (16) and would therefore be expected to be small. The fact that the Al concentration gradient does have a significant effect on the diffusion of Cr is evident from Figure C.8b where DCrAl $\simeq$ 0.5-1.5

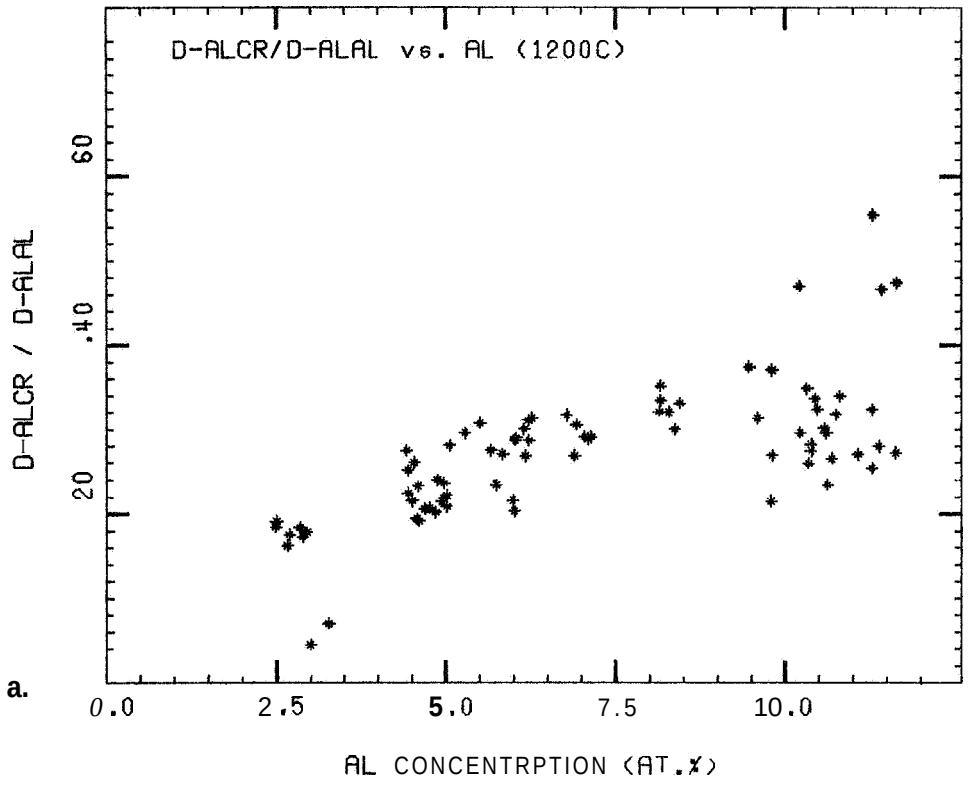

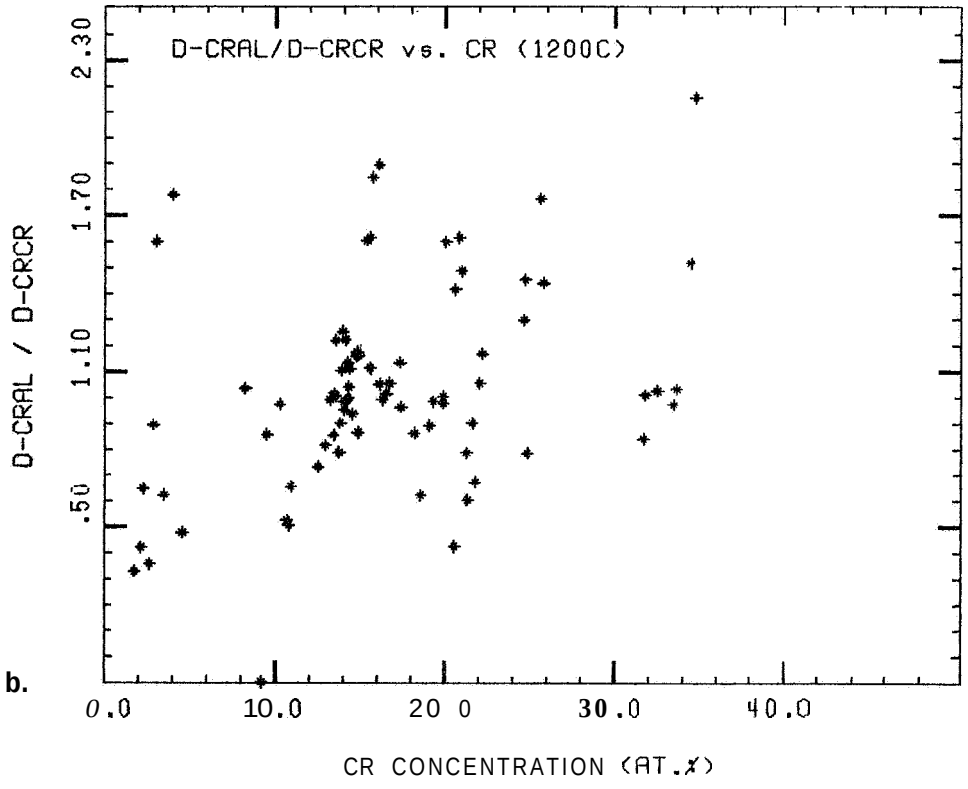

Figure C.8 Ratio of the diffusivities (1200°C) a. D_{AlCr}/D_{AlAl} vs. Al, b. D_{CrAl}/D_{CrCr} vs. Cr.

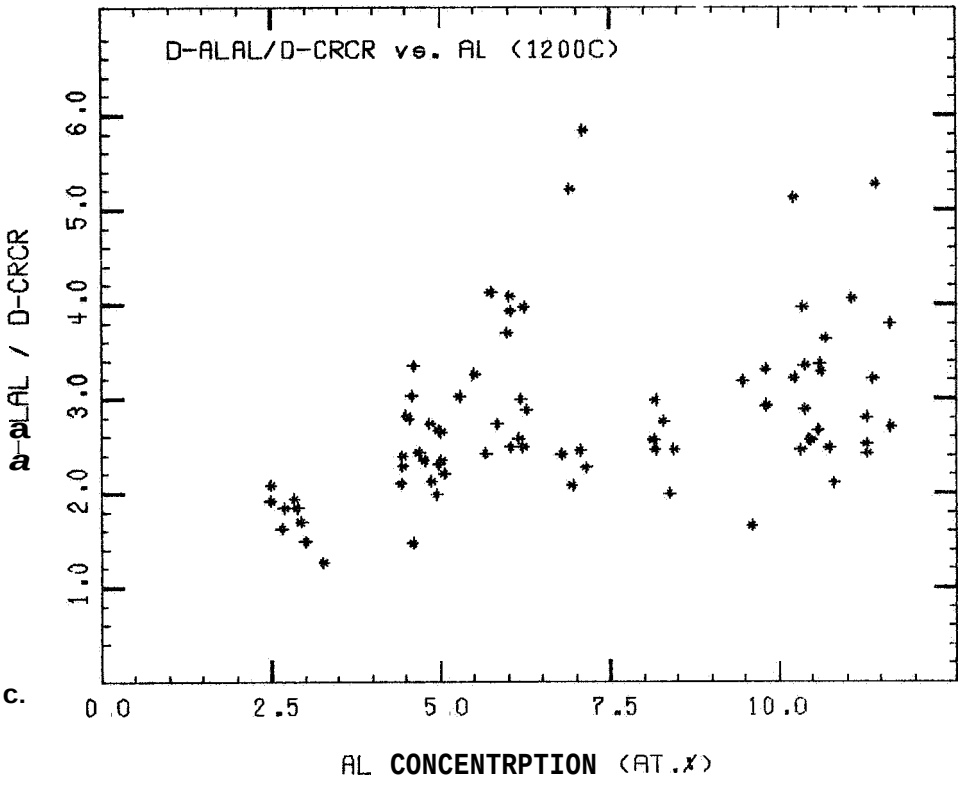

c.

Figure C.8 (con't) Ratio of the diffusivities (1200°C) c. D_{AlAl}/D_{CrCr} vs. Al.

D_{CrCr} for most of the Cr concentrations. In all cases, D_{AlAl} is greater than D_{CrCr}, generally by a factor of 2-4. The ratio D_{AlAl}/D_{CrCr} is shown as a function of the Al concentration in Figure C.8c. Similarly ratios for the diffusivities were reported for the NiCrAl system at 1025°C (15) and 1150°C (46). One exception (46) to the ratio D_{AlAl}/D_{CrCr} is discussed shortly.

It is much more helpful to view the diffusion coefficients as functions of both Al and Cr. To accomplish this task, the diffusivity data for each of the four interdiffusion coefficients for both 1100° and 1200°C were fit using a simple regression analysis (47) to second order polynomial equations with the independent variables being the Al and Cr concentration. Interdiffusion coefficients from the literature for binary Ni-Al (15,19-23) and Ni-Cr (15,24-26) alloys were also regression fit with a second order polynomial equation with one independent concentration variable, Al or Cr, respectively. Binary interdiffusion coefficients for the γ phase of the Ni-Al system (0-18 at.% Al) were calculated using the binary regression equation and added to the measured values of D_{AlAl} at 0.0 at.% Cr. Likewise, binary coefficients for the Ni-Cr system (0-44 at.% Cr) were added to the measured values of D_{CrCr} at 0.0 at.% Al. The concentration dependence of the binary interdiffusion coefficients and the regression fit to the binary data are shown in Figures C.9a (Ni-Al system) and C.9b (Ni-Cr system). In addition, since D_{AlCr} and D_{CrAl} go to zero as the Al concentration and as the Cr concentration go to zero (17), respectively, values of $D_{AlCr}=0$ for 0.0 at.% Al (0-40 at.% Cr) were added to the measured values of D_{AlCr} and $D_{CrAl}=0$ for 0.0 at.% Cr (0-20 at.% Al) were added to the measured values of D_{CrAl}. The ternary interdiffusion

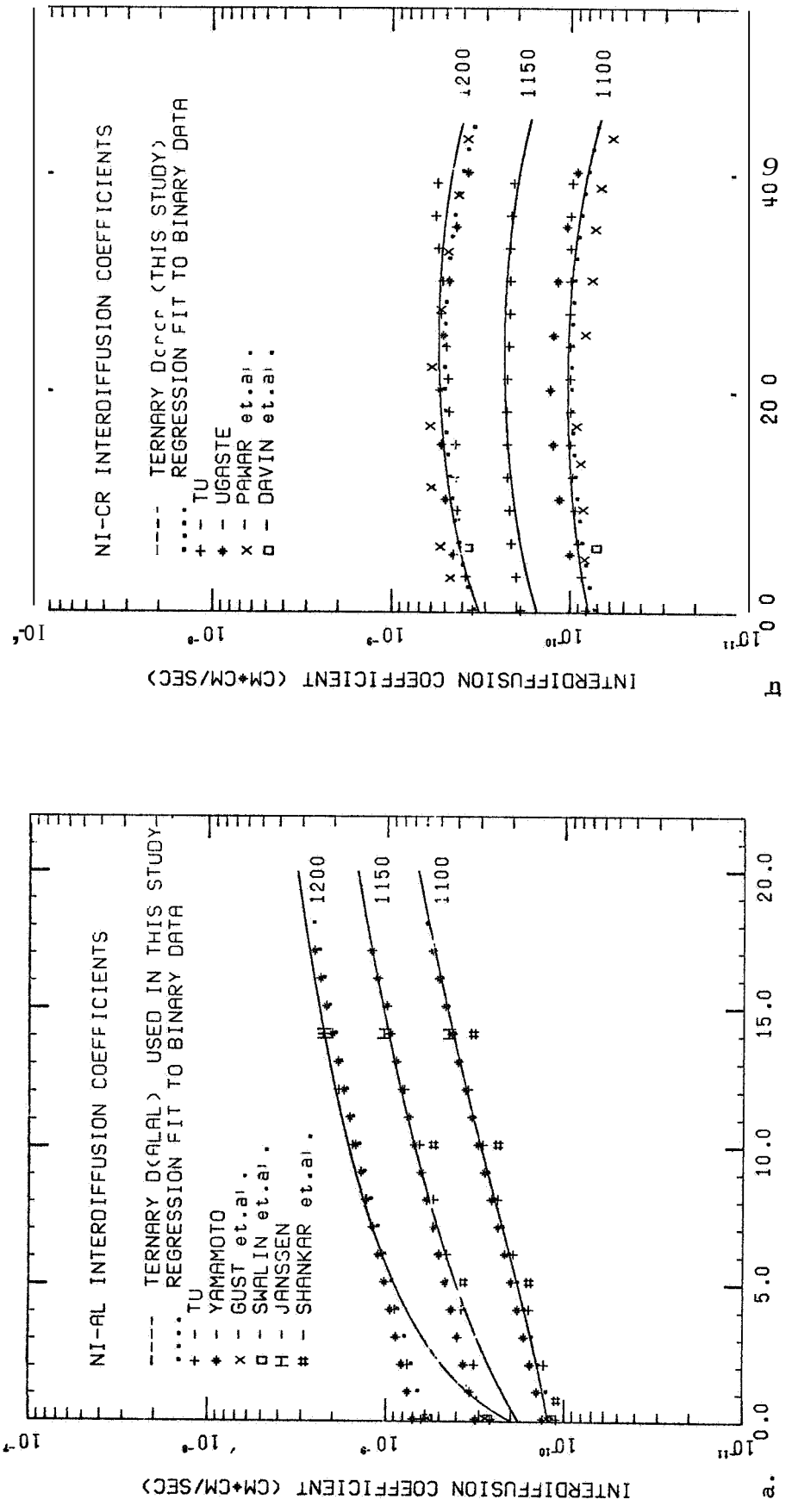

Figure 9 Binary interdiffusion coefficients and ternary diffusivities calculated with regression equations (Table C-5) for the a. Ni-Al and, b. Ni-Cr systems.

coefficients, with the added binary data, were fit to a second order polynomial equation by a regression analysis (47). The resulting equations and correlation coefficients for both 1100°C and 1200°C are given in Table C-5. The interdiffusion coefficients for 1200°C are shown plotted as functions of Al and Cr in Figures C.10a-d. In each of the plots, the flat areas at high Al contents represent the $\gamma + \beta$ region where the diffusivity in the γ phase is expected to be essentially equal to the diffusivity at the $\gamma/\gamma + \beta$ phase boundary. D_{AlAl} and D_{AlCr} increase with increasing Al concentration, in agreement with the data of Tu (NiCrAl-1025°C [15] and Roper and Whittle (CoCrAl-1100°C [14]), but show only a weak dependence on the Cr concentration. D_{CrAl} shows a strong Cr concentration dependence but weak Al concentration dependence, similar to that in the CoCrAl system (14). D_{CrCr} shows a very weak Cr dependence but increases with increasing Al concentration, especially for Al concentrations greater than 10 at.%.

As previously shown (Figure C.8c), D_{AlAl} in the NiCrAl system is always greater than D_{AlCr}, while D_{CrAl} is the same magnitude as D_{CrCr}. Green (46) has measured two sets of interdiffusion coefficients in the γ phase of the NiCrAl system at 1150°C. Roper and Whittle (14) have extrapolated the diffusion coefficients to 1100°C for comparison with diffusivities measured in the CoCrAl system. There is excellent agreement between the values measured in this study and the extrapolated (1100°C) values for D_{CrCr} and D_{CrAl}, while the extrapolated values for D_{AlAl} and D_{AlCr} are 3-10 times less than the values measured in this study. The diffusivities measured by Green exhibit similar characteristics to the diffusivities measured in this study ($D_{AlAl} > D_{AlCr}$, $D_{CrCr} \simeq D_{CrAl}$) except than Green has found that D_{CrCr} and D_{CrAl}

Table C-5

Concentration Dependence of Interdiffusion Coefficients

$D \times 10^{10}$ $cm^2/sec.$

1200°C

$$D_{AlAl} = 1.97 + 1.38 \times Al + 0.18 \times Cr + 0.0061 \times Al^2 - 0.0032 \times Cr^2$$

$$D_{AlCr} = 0.135 + 0.28 \times Al - 0.016 \times Cr + 0.035 \times Al^2 + 0.00040 \times Cr^2$$

$$D_{CrAl} = -1.41 + 0.33 \times Al + 0.47 \times Cr - 0.013 \times Al^2 - 0.0081 \times Cr^2$$

$$D_{CrCr} = 3.21 - 0.56 \times Al + 0.18 \times Cr + 0.070 \times Al^2 - 0.0037 \times Cr^2$$

1100°C

$$D_{AlAl} = 1.23 + 0.073 \times Al - 0.0083 \times Cr + 0.010 \times Al^2 = 0.00016 \times Cr^2$$

$$D_{AlCr} = 0.012 + 0.092 \times Al - 0.0010 \times Cr + 0.00016 \times Al^2 + 0.00002 \times Cr^2$$

$$D_{CrAl} = 0.0766 - 0.015 \times Al + 0.084 \times Cr + 0.000062 \times Al^2 - 0.0015 \times Cr^2$$

$$D_{CrCr} = 0.783 - 0.012 \times Al + 0.025 \times Cr \quad 0.00096 \times Al^2 - 0.00052 \times Cr^2$$

Al and Cr concentrations in atom per cent.

Coefficients of Determination (R^2)

	1100°C	1200°C
D_{AlAl}	0.99	0.85
D_{AlCr}	0.97	0.93
D_{CrAl}	0.91	0.75
D_{CrCr}	0.74	0.75

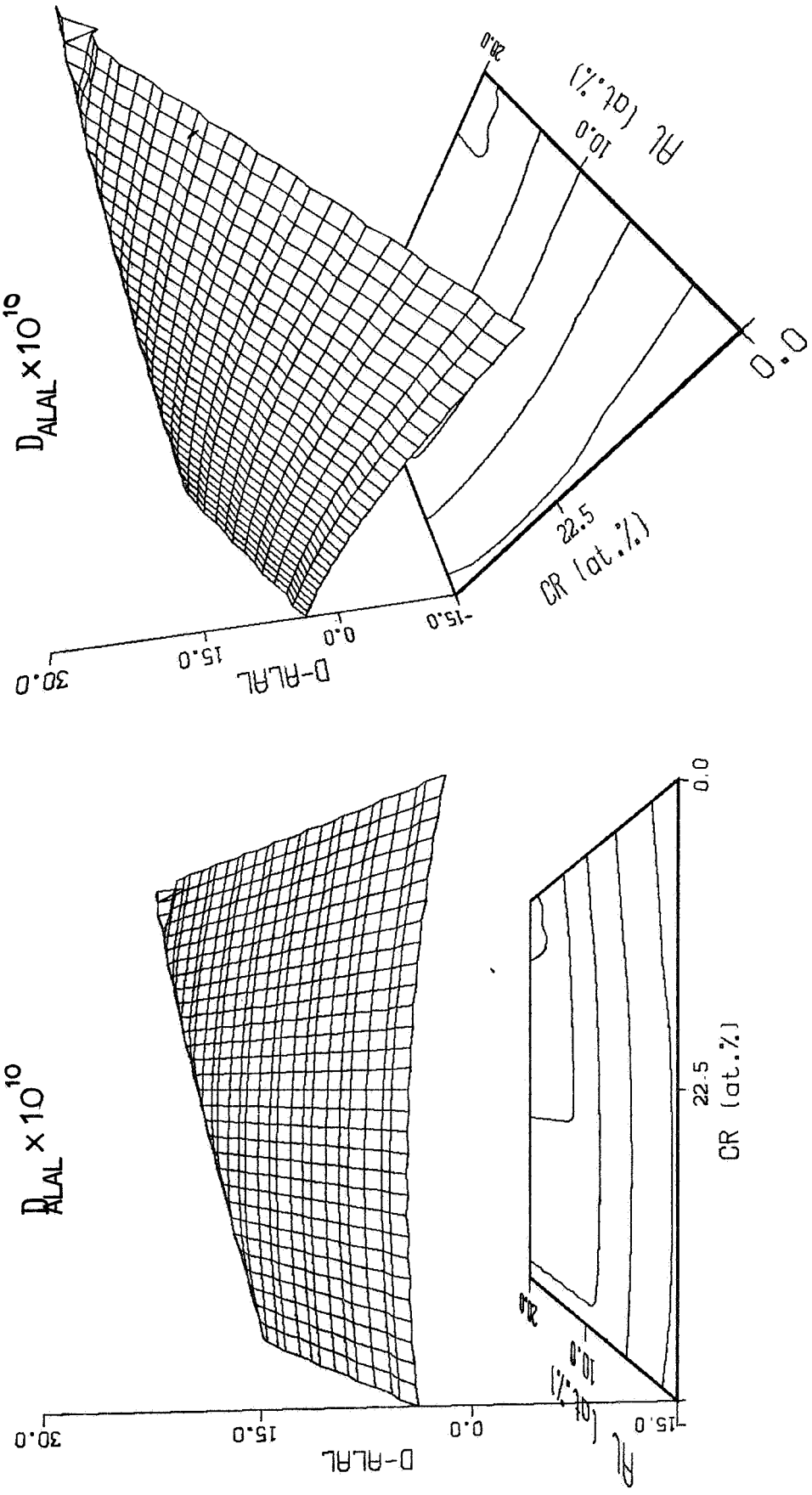

Figure C 10 Variation of the ternary diffusivities (1200°C) with Al and Cr concentration.

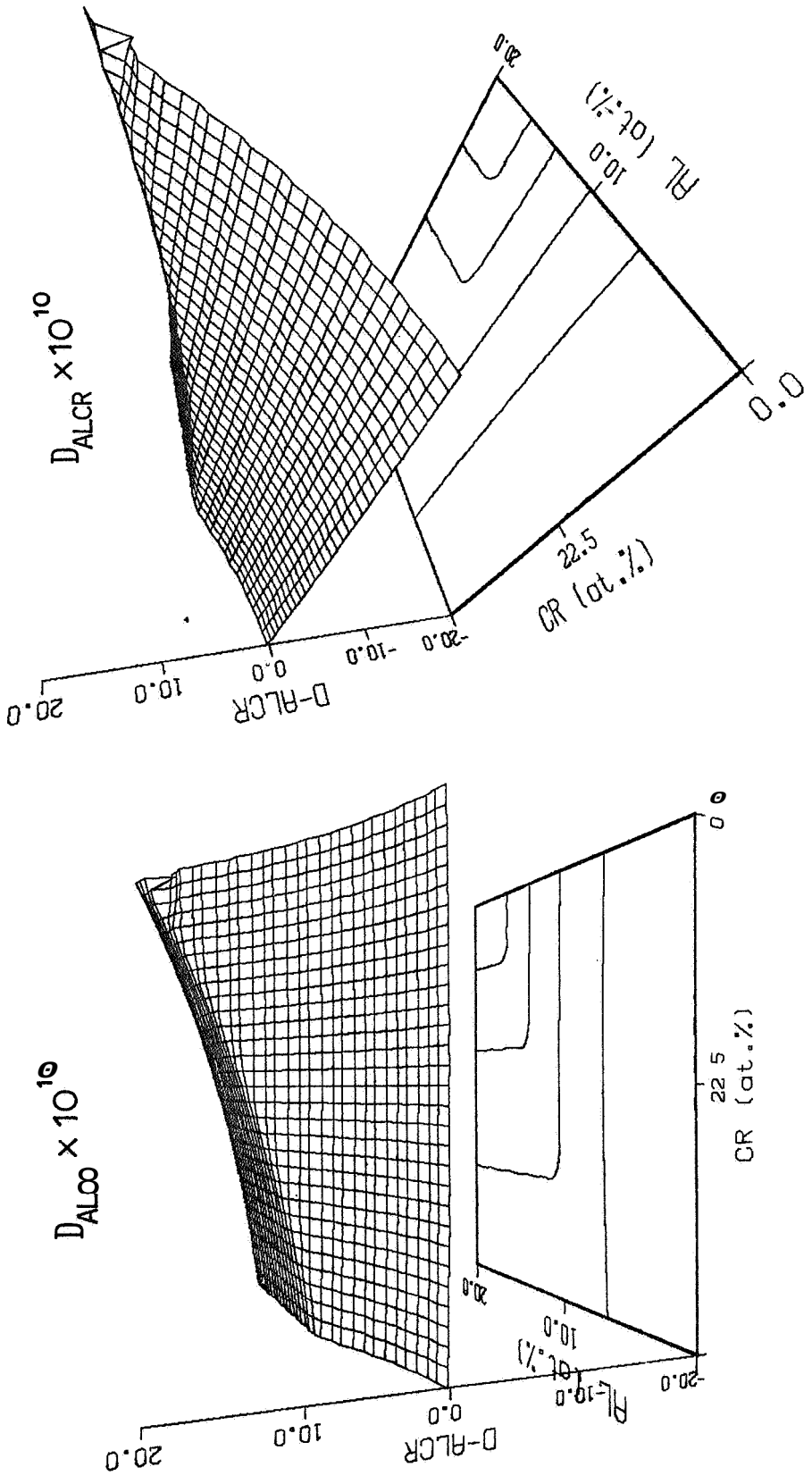

Figure C 4 (con't.) Variation of the ternary diffusivities (1200°C) with Al and Cr concentration.

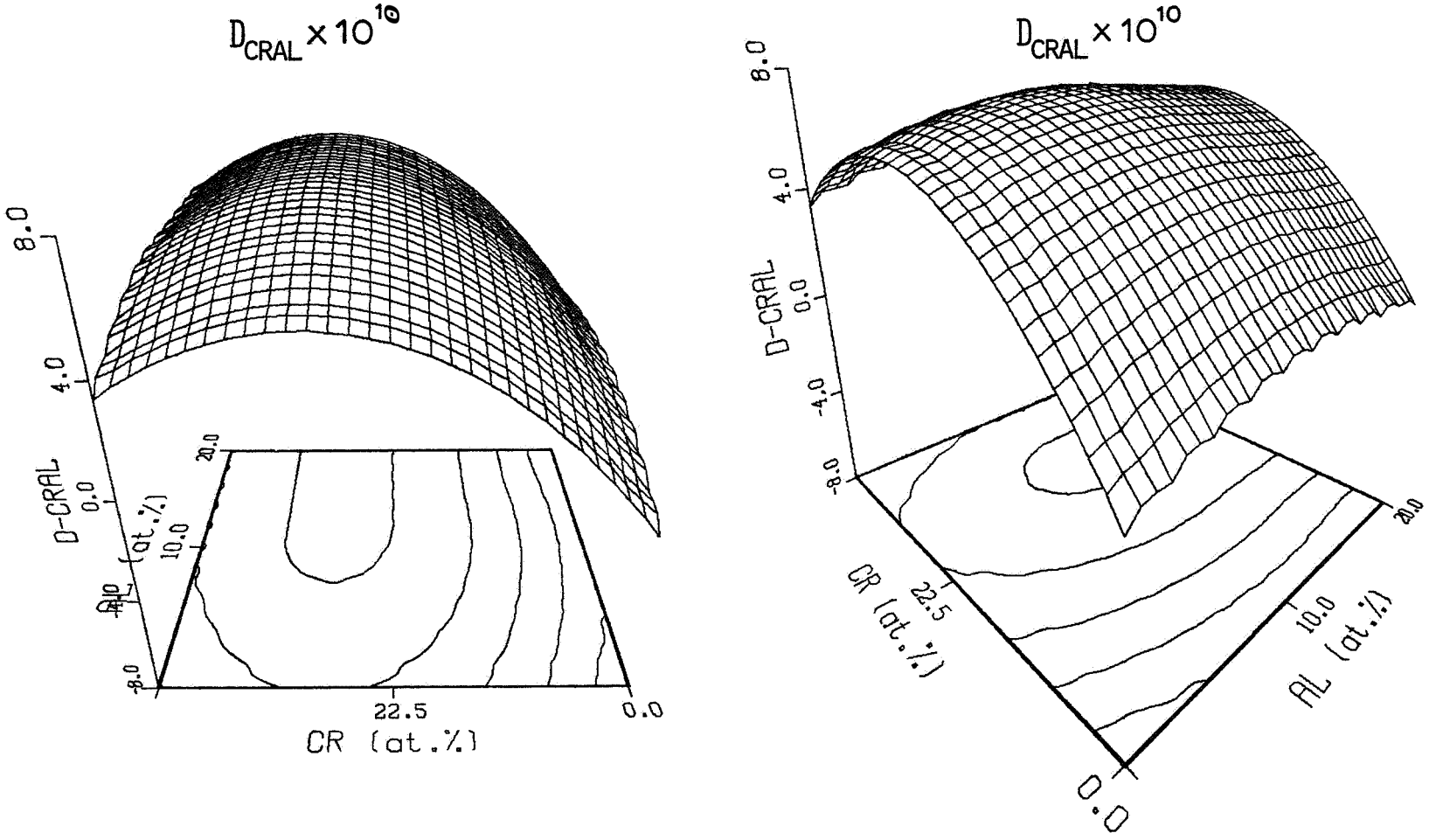

Figure C.10 (con't.) Variation of the ternary diffusivities (1200°C) with Al and Cr concentrations.

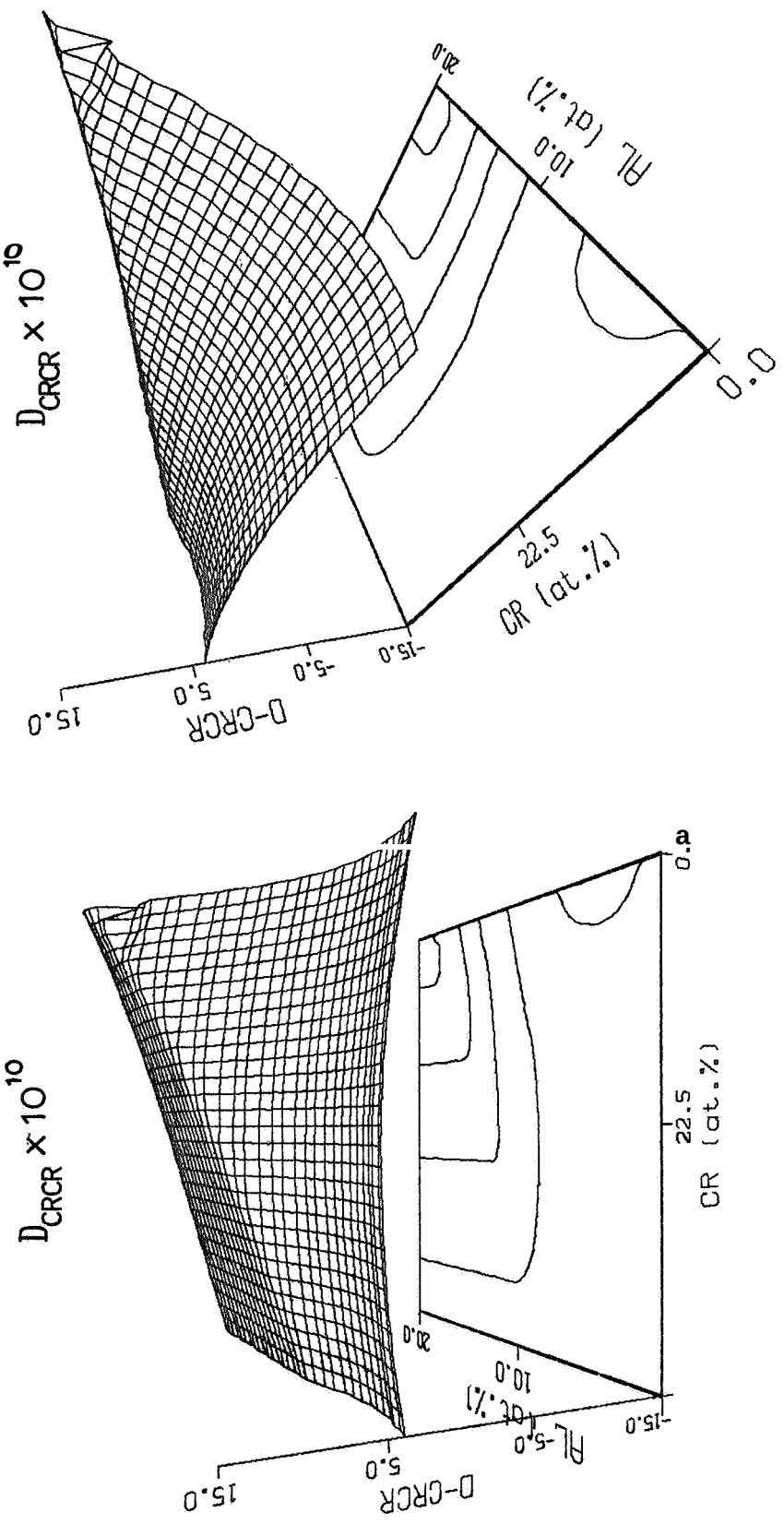

Figure C.10 (con't.) Variation of the ternary diffusivities (1200°C) with Al and Cr concentration.

are greater than D_{AlAl} and D_{AlCr} in obvious disagreement with the present study. The limited results of Green do not permit a satisfactory explanation for this disagreement.

The four interdiffusion coefficients can be calculated at various Al and Cr concentrations at temperatures other than 1100°C and 1200°C by use of the regression equations in Table C-5. The main diffusion coefficients (D_{AlAl} and D_{CrCr}) were calculated at 1025°C by assuming the temperature dependence of the diffusivities to be described by the Arrhenius equation (18). The 1025°C diffusivities were calculated at Al and Cr concentrations where the diffusivities were reported by Tu (15). Good agreement was found between the predicted values and the values measured by Tu. Comparing the values at each concentration shows the predicted D_{AlAl} to be an average of 1.4 times greater than those measured by Tu. The predicted values for D_{CrCr} were an average of 1.6 times greater than those of Tu. The average value for D_{AlAl} (cm^2/s) for each of the concentrations reported by Tu was $D_{AlAl}=3.4X10^{-11}$ compared to $4.4X10^{-11}$ predicted in this study, and the average value for D_{CrCr} (cm^2/s) measured by Tu was $D_{CrCr}=1.8X10^{-11}$ compared to $2.4X10^{-11}$ predicted in this study.

Activation energies for D_{AlAl} and D_{CrCr} were also calculated assuming an Arrhenius-type temperature dependence of the regression equations in Table C-5. The activation energy for D_{AlAl} was relatively constant for Al concentrations greater than $\sim$ 3 at.%Al. The average value of the activation energy for D_{AlAl} (excluding concentrations in the $\gamma + \beta$ region) was 69 kcal/mol (288 kJ/mol). This value compares very well with the activation energy in the binary Ni-Al system of 56-72 kcal/mol (234-301 kJ/mol) (15,19-21). The activation energy for D_{AlAl} is shown in Figure C.11a.

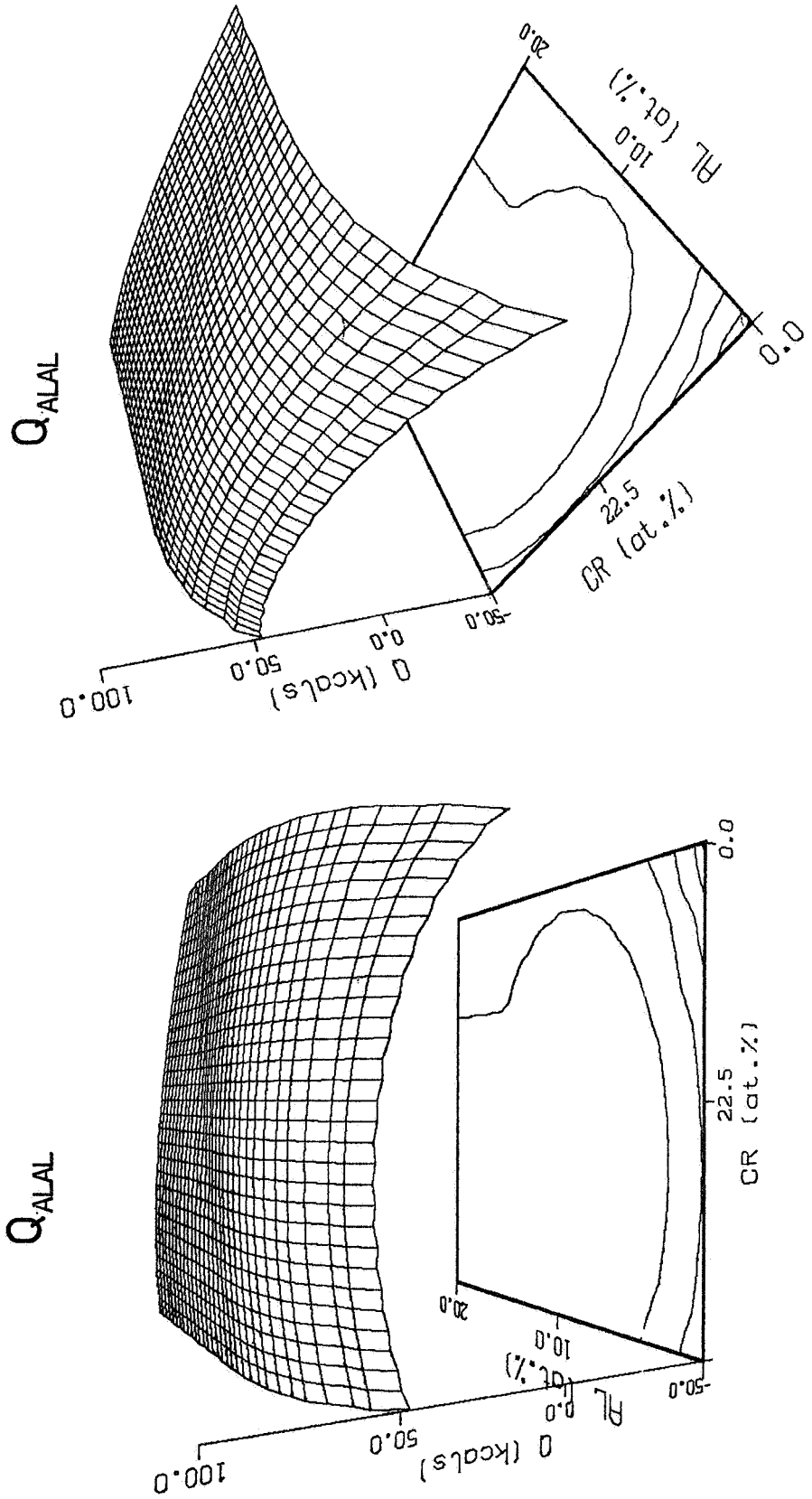

Figure C 11 Variation of the activation energy with Al and Cr concentration.

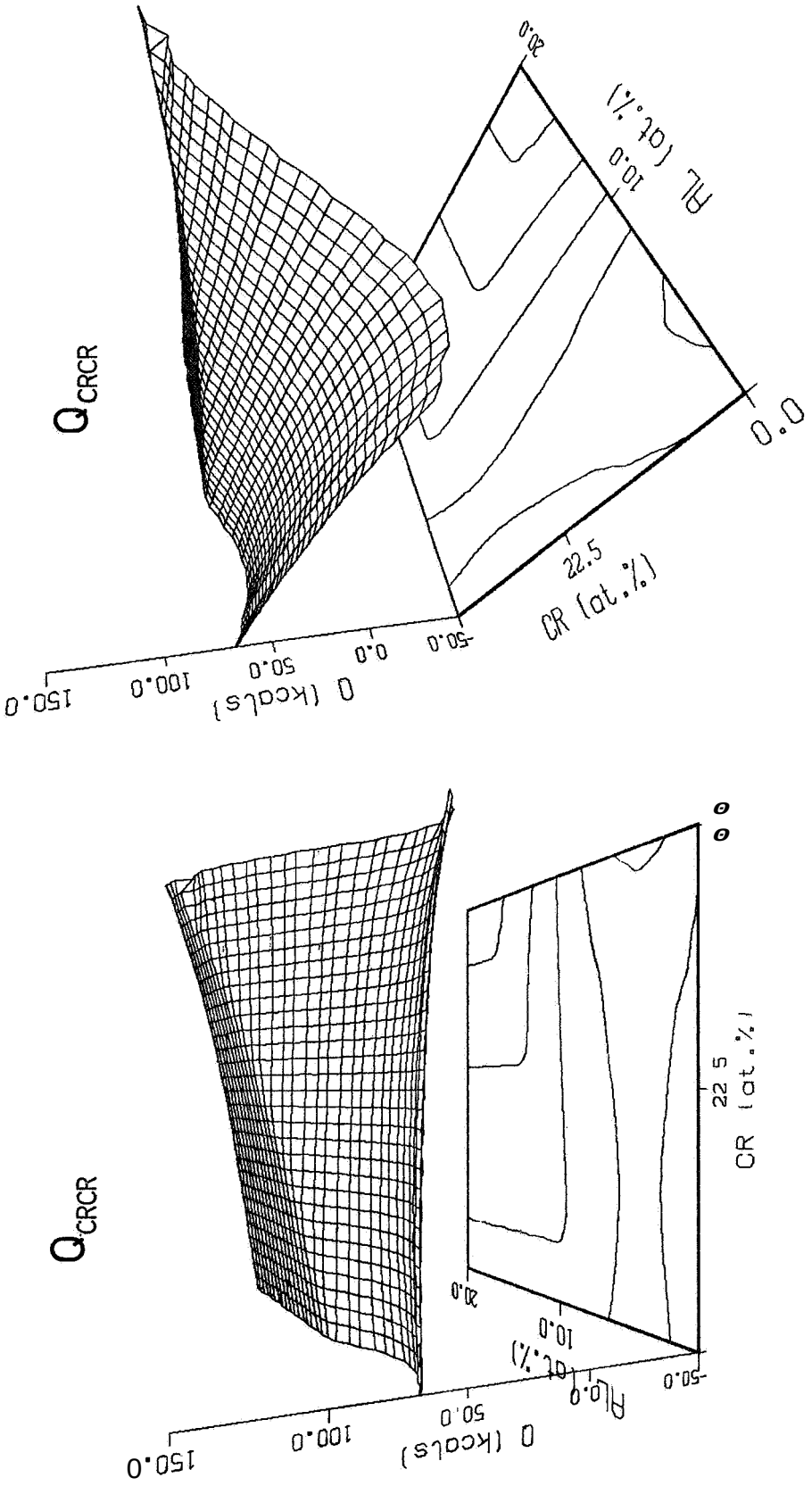

Figure C.11 (con't.) Variation of the activation energy with Al and Cr concentration.

The activation energy for D_{CrCr} (Figure C.11b) shows very little Cr concentration dependence in agreement with the activation energy in binary Ni-Cr alloys (24-26). The average value of the activation energy for D_{CrCr} was 67 kcal/mol (280 kJ/mol), consistent with values in the literature for the Ni-Cr system of 61-70 kcal/mol (255-293 kJ/mol) (24-26).

Examination of the location of the porosity and the Al and Cr concentration gradients suggest a relative ordering of the intrinsic diffusivities. Assuming the ratios between the intrinsic diffusivities to be similar to that in the interdiffusion coefficients (i.e. $D_{AlAl} \simeq 4D_{AlCr} \simeq 3D_{CrAl} \simeq 3D_{CrCr}$) and approximating concentration gradients as the difference in the bulk composition of the alloys in a couple allows prediction of a vacancy flux imbalance. Porosity would be expected in a couple where a large vacancy flux was predicted. The above crude approximations correctly predict the location (which side of the original interface) of the porosity observed in the γ/γ couples annealed at 1200°C. When both Al and Cr diffuse into pure Ni (i.e. B69/Ni), the porosity always appears on the high Al, high Cr side of the original interface indicating that Al and Cr atoms are diffusing more rapidly than those of Ni, implying $D_{AlAl} > D_{CrCr} > D_{NiNi}$. This ranking of the intrinsic diffusivities is supported by the findings of two authors (19,20) that $D_{Al}/D_{Ni} > 1$ in the Ni solid-solution phase of the Ni-Al system. In addition, the presence of Kirkendall porosity on the high-Cr side of NiCr couples (26) also indicates that $D_{Cr}/D_{Ni} > 1$ in the Ni solid-solution phase of the Ni-Cr system. The diffusion couples fabricated in the earlier study (12) exhibit no porosity or less porosity than those fabricated in the present study. The cause for the observed difference in the amount of porosity is not known.

II. Predicting Concentration/Distance Profiles and Interface Motion

Predicting Concentration/Distance Profiles

The most critical test of the validity of interdiffusion coefficients is the comparison of measured and predicted concentration/distance profiles. A computer model was developed to simulate interdiffusion in infinite γ/γ diffusion couples to test the validity of the diffusion coefficients determined in this study. The computer model was based on finite-difference techniques and took full account of the concentration dependence of the four interdiffusion coefficients. Details of the computer model are given in Appendix E. The γ / γ diffusion couples of this study were considered acceptable for comparison since each diffusion couple yielded diffusivities only at discrete concentrations. The diffusivities used to predict the concentration profiles were based on a regression fit (see Table C-5) of all the measured diffusion coefficients. The contribution of one diffusion couple on the final regression equation was usually limited. Excellent agreement was found between the predicted and measured concentration/distance profiles. The predicted profiles are shown in Figures C.2, C.3, and Appendix C.2 for each of the Y/Y couples at 1100°C and 1200°C. Couple 3SL/W (γ / γ + γ' at 1100°C) was modeled as a γ / γ couple with the Al concentration in the 3SL alloy equal to 10.0 at.% Al, the Al concentration of the γ phase in the $\gamma + \gamma'$ phase region. The close agreement between the measured and predicted profiles indicates that the recession of the γ' phase does not significantly influence the concentration profile in the γ phase, not surprising since alloy 3SL and alloy W have very close Cr contents and the γ and γ'

phases have similar Al contents. The interdiffusion of alloys 4SL and W at 1150°C after a 500 hour anneal was also predicted and compared to the measured concentration/distance profile. The diffusivities at 1150°C were determined from the 1100°C and 1200°C diffusivity equations assuming an Arrhenius temperature dependence. Again, the predicted concentration profile shows good agreement to the measured concentration profile, as shown in Figure C.12.

It is significant that the predicted and measured concentration/distance profiles exhibit such good agreement considering the earlier discussion of the possible errors. One of the main objections to the diffusivities measured in this study might be the amount of porosity in the diffusion zone of many of the diffusion couples. The porosity reduces the cross-sectional area of metal in the diffusion zone and might be expected to act as a diffusion barrier limiting interdiffusion. Yet, the excellent agreement between the measured profiles in the couples containing the most porosity (i.e. 7S/1S, Ni-10Al/6S), and the predicted concentration/distance profiles, in which no account is made for a vacancy flux imbalance or for the presence of porosity, strongly supports the validity of the measured diffusivities. In addition, the good agreement between the predicted and measured profiles for each of the γ/γ couples justifies the analysis procedure which yielded several diffusivities as a result of the uncertainty in the position of the Matano plane. Therefore, the diffusion coefficients measured in this study are regarded as adequate to describe diffusion in the γ phase of the NiCrAl system between 1100°C and 1200°C.

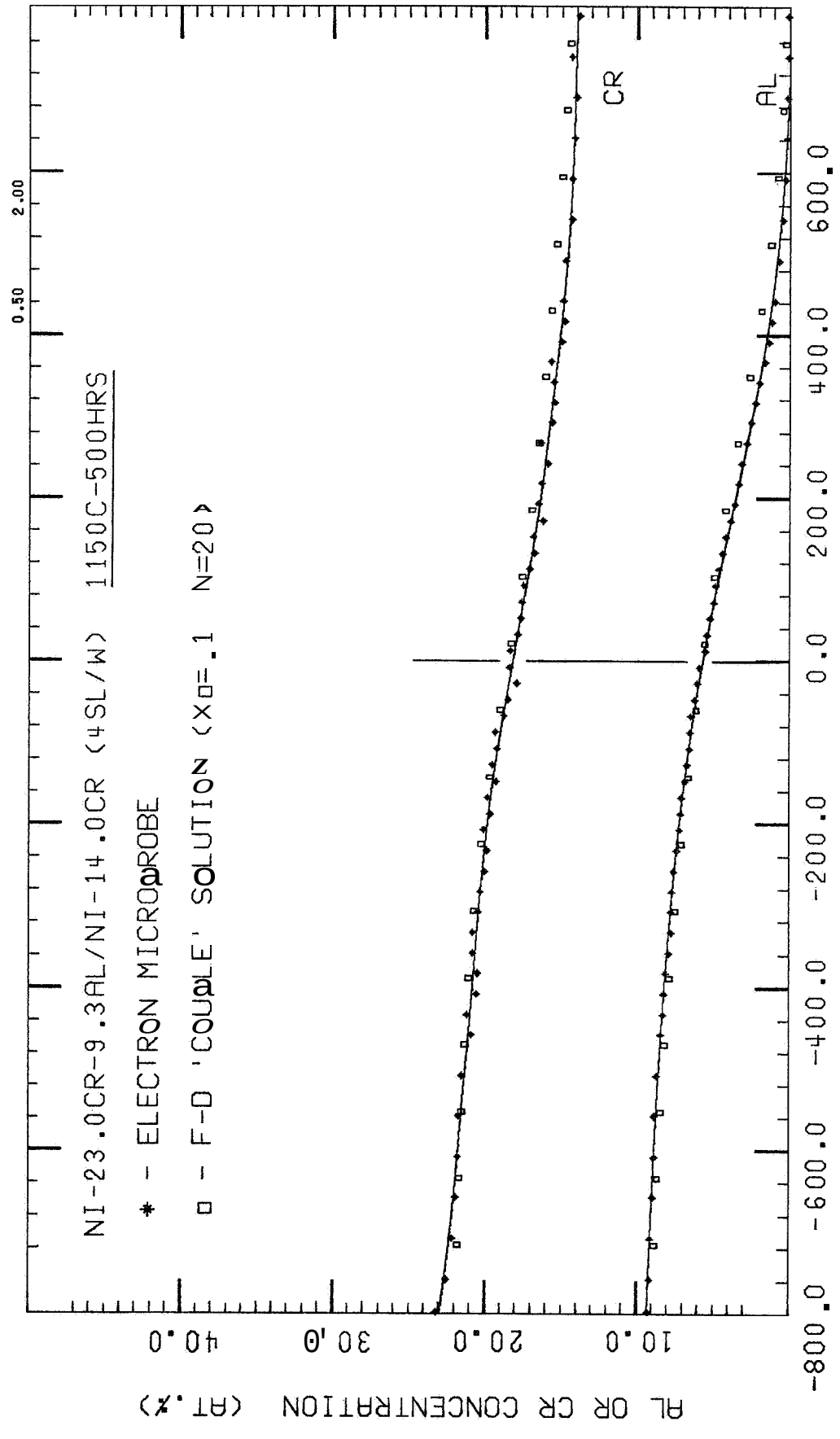

Figure C 12 Predicted and measured concentration/distance profile for the Ni-23.0Cr-9.3Al/Ni-14.0Cr (4SL/W) couple after 500 hours at 1150°C.

y/y +β Interface Motion

It is interesting to examine the $\gamma/\gamma + \beta$ interface motion with regard to the measured interdiffusion coefficients. Several authors (28,29,37,48-54) have previously studied multiphase diffusion in ternary alloys, typically examining diffusion paths and the complex phase morphologies which often result. Precipitation and phase transformations in Fe-C-X alloys have received particular attention (55-58). The theoretical basis for γ/β interface motion in ternary systems has previously been discussed (31,59-61) and there have been several modeling studies simulating precipitate growth in ternary alloys (52,53,59,62). In both the theoretical work and modeling studies, the γ/β interface is assumed to be either planar, or in the case of precipitation, cylindrical or spherical. Predicting concentration/distance profiles and the γ/β interface motion requires solution of Fick's second law in both the γ and β phases, constrained by a flux balance condition at the γ/β interface (52,53,59). A tie-line across the $\gamma+\beta$ phase field is chosen so as to satisfy the flux balance at the interface (52,53,62). During the early stages of precipitation of β in γ, the tie-line need not pass through the bulk composition in the $\gamma + \beta$ phase field, but may shift with time passing through the bulk composition only when the diffusion fields about the precipitates overlap and inpinge in the latter stages of precipitate growth (52,53,63,64).

There have been no known modeling studies of $\gamma/\gamma + \beta$ interdiffusion in ternary alloys. Kirkaldy and Brown (28) have introduced the concept of the "virtual path" which is useful for predicting isolated precipitation or a non-planar interface in γ/β couples. In brief, use of the virtual path requires determining a

diffusion path in the γ phase and also in the β phase subject to the flux balance condition at the γ/β interface. If the predicted diffusion path in one of the phases loops into the $\gamma+\beta$ field, isolated precipitation or a non-planar interface is predicted and the path is "virtual" and not real since the diffusion path was calculated on the basis of a simple γ/β couple with a planar γ/β interface. The concept of the virtual path is useful for predicting isolated precipitation, but fails to predict the width, or growth rate of the $\gamma/\gamma+\beta$ or $\beta/\gamma+\gamma$ interface. Roper and Whittle (45) have initiated the theoretical basis for $\gamma/\gamma+\beta$ diffusion by allowing for diffusion in two-phase regions. The concept of the virtual path was extended by introducing a "composite diffusion path". The composite diffusion path takes into account both changing concentrations and varying volume fractions in the two-phase region.

In binary $\gamma/\gamma+\beta$ couples, concentration/distance profiles and the $\gamma/\gamma+\beta$ interface velocity are easily calculated (65,661. For the binary case, the concentrations at the $\gamma/\gamma+\beta$ interface are constant and can be read directly from the phase diagram. In addition, the Gibbs phase rule prohibits any diffusion in the $\gamma+\beta$ region. In contrast, the extra degree of freedom afforded by the inclusion of a third element permits diffusion in the $\gamma+\beta$ region of the couple. Therefore, a possible diffusion path for a ternary $\gamma/\gamma+\beta$ couple might start at the bulk composition of the $\gamma+\beta$ alloy, cut across tie-lines in the $\gamma+\beta$ region exiting the two-phase region at a tie-line far removed from the ETL, then proceed through the γ phase to the bulk composition of the γ alloy. This latter diffusion behavior was observed in the $\gamma/\gamma+\beta$ couples examined in this study. For each of

the γ/γ t β couples examined, the diffusion path from the $\gamma+\beta$ alloy cut tie-lines in the $\gamma+\beta$ region, exiting the region at a higher Al, lower Cr concentration than that of the ETL. A partial explanation for this behavior can be given by considering the concentration/distance profiles and the flux balances for Al and Cr at the $\gamma/\gamma+\beta$ interface.

Consider first a $\gamma/\gamma+\beta$ couple where the Cr content of the alloy (C^{s}_{Cr1}) is greater than that in the $\gamma+\beta$ alloy (C^{o}_{Cr}). The diffusion path and concentration/distance profiles are shown schematically in Figures C.13a-c. Considering the Al concentration/distance profile (Figure C.13b), Al diffuses to the left (negative flux) from the $\gamma+\beta$ alloy into the γ-phase alloy resulting in motion of the $\gamma/\gamma+\beta$ interface to the right (positive). The flux balance at the $\gamma/\gamma+\beta$ interface for Al states:

$$(C^{o}_{Al} - C^{\gamma}_{Al})\frac{d\xi}{dt} = -J^{\gamma}_{Al}\Big|_{X=\xi} \qquad [C\text{-}6]$$

where the concentrations are as shown in Figure C.13b, $d\xi$ is the $\gamma/\gamma+\beta$ interface motion in time dt, and J^{γ}_{Al} is the Al flux in the γ phase evaluated at the $\gamma/\gamma+\beta$ interface. The Al flux is also defined as

$$J^{\gamma}_{Al} = -D_{AlAl}\frac{\partial C_{Al}}{\partial X} - D_{AlCr}\frac{\partial C_{Cr}}{\partial X} \qquad [C\text{-}7]$$

Since the Al concentration gradient is positive (as shown in Figure C.13b) and D_{AlAl} is always positive, the contribution of the first term containing D_{AlAl} in Equation [C-7] is negative. In contrast, the Cr

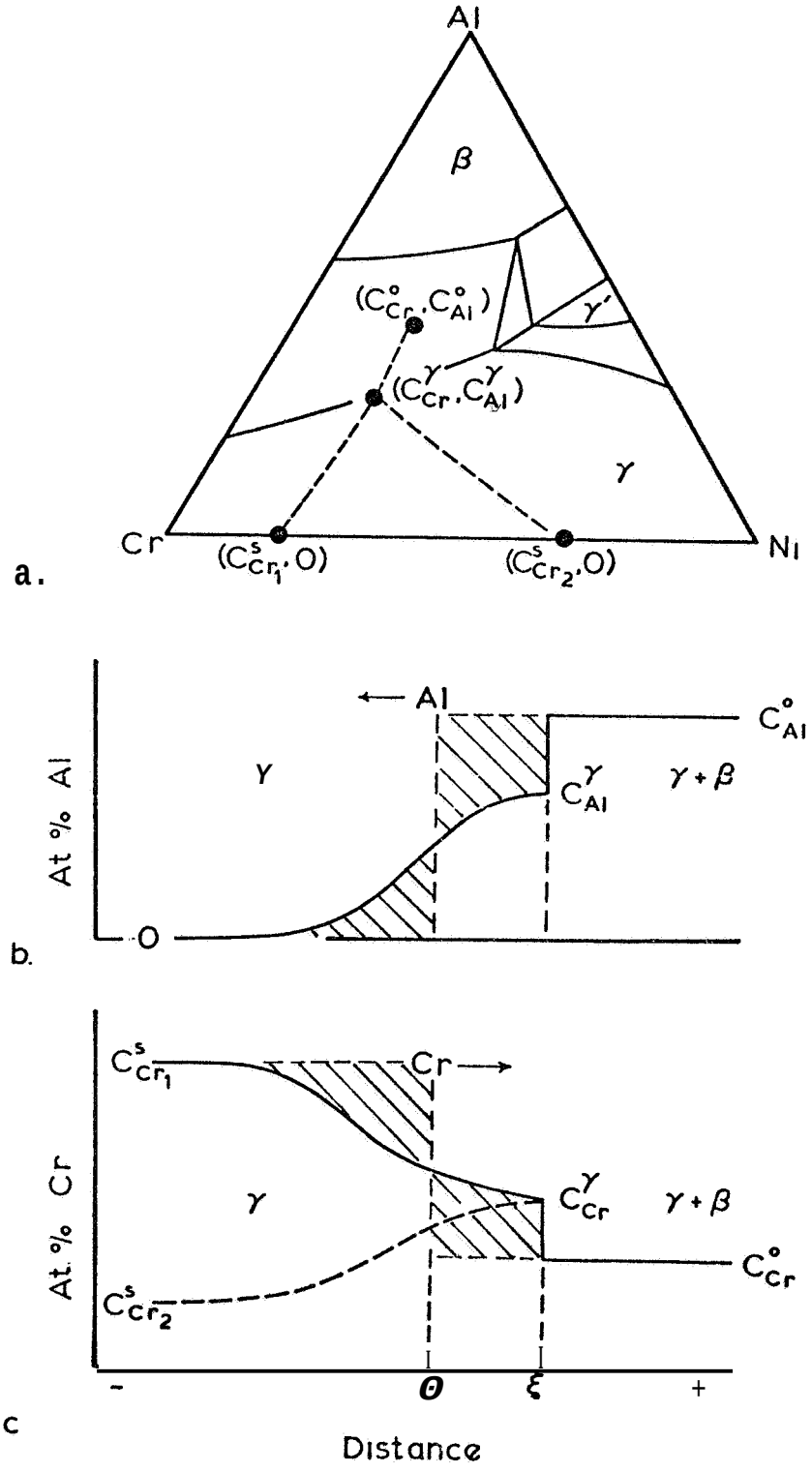

Figure C.13 γ/γ+β **Diffusion Couples**
a. Schematic diffusion paths for one γ+β alloy coupled to two Ni-Cr alloys.
b. Schematic Al concentration profile and, c. Cr concentration profile.

concentration gradient is negative, and since D_{AlCr} is always positive in the Y phase, the contribution of the second term containing D_{AlCr} in Equation [C-7] is positive. Since D_{AlAl} is always much greater than D_{AlCr}, the first term typically dominates and the overall Al flux is negative, into the Yphase. A mass balance for Al requires that the two cross-hatched areas in Figure C.13b be equal. The **flux** balance for Cr is given as:

$$(C^{\theta}_{Cr} - C^{\gamma}_{Cr}) \frac{d\xi}{dt} = -J^{\gamma}_{Cr}\Big|_{X=\xi} \qquad [C-8]$$

where all terms are the Cr equivalent to those in Equation IC-61, the interface motion $d\xi$ obviously being equal to that in Equation [C-61. For $\gamma/\gamma+\beta$ interface motion to the right (positive) in Figure C.13, the Cr flux must also be positive and is given as:

$$J^{\gamma}_{Cr} = -D_{CrAl} \frac{\partial C_{Al}}{\partial X} - D_{CrCr} \frac{\partial C_{Cr}}{dX} \qquad IC-91$$

Since D_{CrAl} and D_{CrCr} are both positive in the γ phase, the first term containing D_{CrAl} in Equation IC-91 is negative while the second term containing D_{CrCr} is positive. Since D_{CrAl} and D_{CrCr} are of the same magnitude, the Cr concentration gradient must be greater than the Al concentration gradient in order for the overall Cr flux at the $\gamma/\gamma+\beta$ interface to be positive. As shown in Figure C.13c, Cr must diffuse down the Cr gradient for the Cr flux to be positive. A mass balance for Cr requires that the cross-hatched areas in Figure C.13c to be equal.

It becomes much more interesting to examine a γ alloy with a Cr content lower than that in the $\gamma+\beta$ alloy. This case is also shown schematically in Figure C.13 for the γ alloy with the Cr concentration

C^{s}_{Cr2}. As a first choice, the Cr concentration profile might be assumed to be as the dashed curve in Figure C.13c. This choice is obviously in error for two reasons; for a positive Cr flux (required for the flux balance given in Equation [C-8]), Cr must diffuse up its own concentration gradient. But from Equation [C-9], this is clearly impossible since both the Al and Cr concentration gradients are positive and both D_{CrAl} and D_{CrCr} are always positive. The second error involves a mass balance between the initial and final Cr content of both alloys. There is clearly a higher Cr content in the γ alloy to the left of the original interface, and a higher Cr content to the right of the original interface (now in the β-depleted region) than what was in the original $\gamma + \beta$ alloy. The creation of the additional Cr is clearly in error.

The necessity for diffusion in the $\gamma+\beta$ region in $\gamma/\gamma+\beta$ couples can best be illustrated by considering a $\gamma+\beta$ alloy coupled to pure Ni. For this case, the initial Cr concentration profile is shown in Figure C.14a. The Al concentration profile is assumed to be approximately the same as that shown in Figure C.13b. For $\gamma/\gamma+\beta$ interface motion to the right into the $\gamma+\beta$ alloy, the Cr concentration in the β-depleted region must increase (see Figure C.13c). Obviously the Cr can not come from the Ni side of the couple but must be supplied from the $\gamma+\beta$ region. The only possibility for this to occur is by diffusion in the $\gamma+\beta$ region so that the diffusion path cuts tie-lines in the $\gamma+\beta$ field and exits the two-phase region at a lower Cr concentration. A diffusion path and associated concentration profile are shown in Figure C.14a and c. When diffusion occurs in the $\gamma+\beta$ region, the Cr flux balance at the $\gamma/\gamma+\beta$ interface becomes

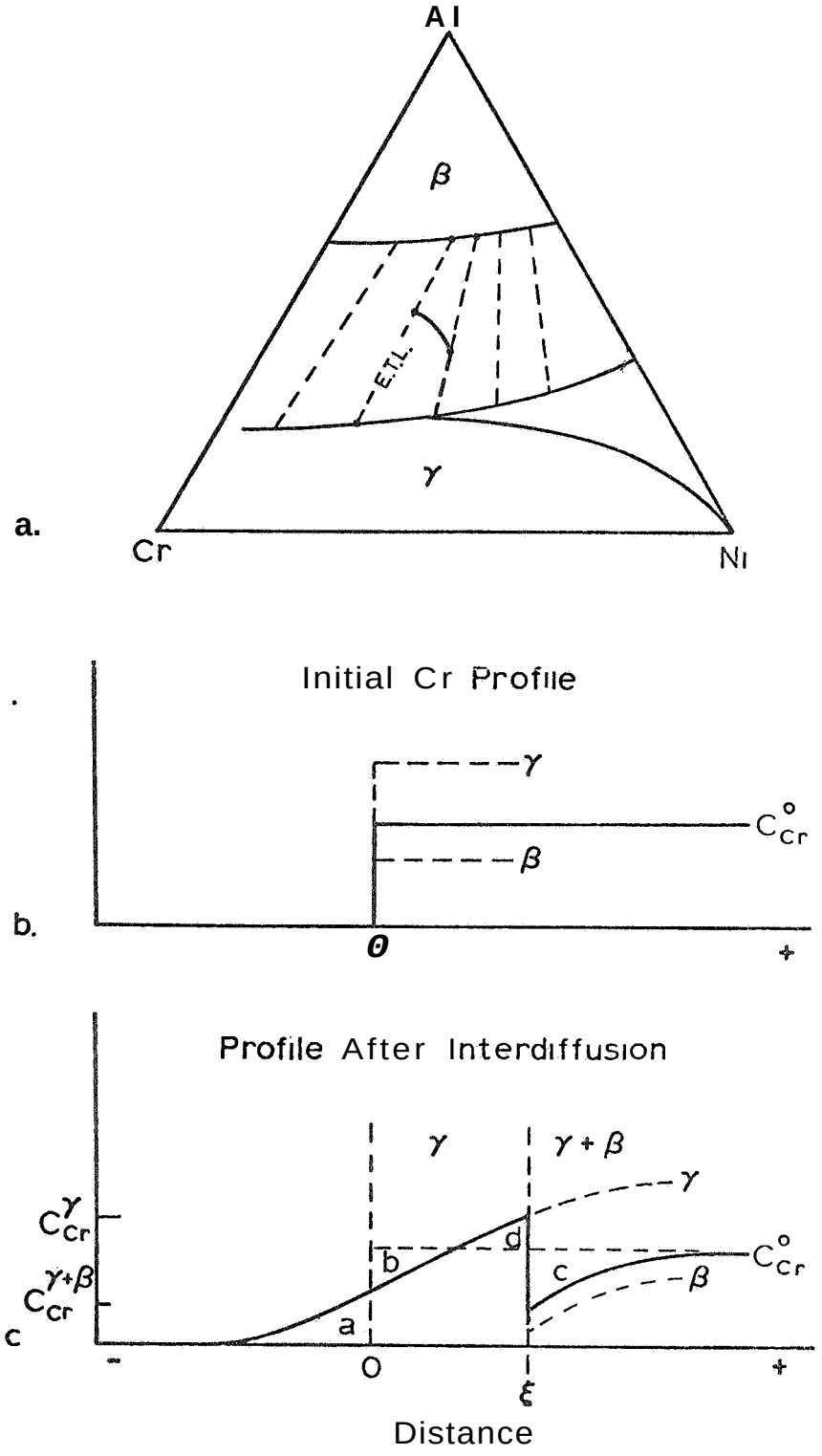

Figure C.14 Ni/γ+β Diffusion Couple
a. Schematic diffusion path, b. initial Cr concentration profile and, c. after interdiffusion.

$$(C_{Cr}^{\gamma+\beta} - C_{Cr}^{\gamma}) \frac{d\xi}{dt} = J_{Cr}^{\gamma+\beta} - J_{Cr}^{\gamma} \qquad [C.10]$$

where C_{Cr}^{γ} is the Cr concentration in the γ phase where the diffusion path exits the $\gamma+\beta$ region. The interface concentration $C_{Cr}^{\gamma+\beta}$ is an average Cr concentration in the $\gamma+\beta$ region containing contributions from both the γ and β phases. The depression of $C_{Cr}^{\gamma+\beta}$ below C_{Cr}^{o} is dependent on the diffusion path in the $\gamma+\beta$ region. The term $J_{Cr}^{\gamma+\beta}$ refers to the Cr flux in the $\gamma+\beta$ region towards the $\gamma/\gamma+\beta$ interface and consists of diffusion in both the γ and β phases. Since the left-hand side of Equation [C-10] is negative, and both Cr fluxes in Equation [C-10] are negative, the Cr flux in the $\gamma+\beta$ region towards the interface, $J_{Cr}^{\gamma+\beta}$, must be of greater magnitude (more negative) than the Cr flux in the γ phase away from the interface, J_{Cr}^{γ}, in order for the $\gamma/\gamma+\beta$ interface to move to the right into the $\gamma+\beta$ region. Additionally, Cr is conserved by having the areas which have lost Cr (area b+c in Figure C.14c) equal to the areas which have gained Cr (area a+d). Therefore, diffusion in the $\gamma+\beta$ region of $\gamma/\gamma+\beta$ couples is required when the Cr concentration in the γ alloy is less than that in the $\gamma+\beta$ alloy. Even when the Cr concentrations in the γ and $\gamma+\beta$ alloys are nearly equal, diffusion in the $\gamma+\beta$ region may be necessary because the influence of the Al concentration gradient is to drive Cr away from the $\gamma/\gamma+\beta$ interface into the γ alloy (see Equation [C-9]).

An analytical solution predicting concentration/distance profiles and the $\gamma/\gamma+\beta$ interface position can be derived if several simplifying assumptions are made. The solution is basically a modified form of the solution for γ/β couples (58) and assumes

concentration-independent diffusivities and planar interfaces. In applying the γ/β solution to $\gamma/\gamma+\beta$ couples, it is also assumed that no diffusion occurs in the $\gamma+\beta$ region. Cr and Al concentrations at the $\gamma/\gamma+\beta$ phase boundary (C^{γ}_{Cr}, C^{γ}_{Al}) are chosen which satisfy the flux balance at the $\gamma/\gamma+\beta$ interface (Equations [C-6] and [C-8]). The $\gamma/\gamma+\beta$ interface concentrations must also be consistent with a solution of Fick's second law in the γ phase. Therefore, the Al and Cr concentrations in the $\gamma+\beta$ region are constant (See Figure C.13b and c). Implicit in this simplified ,solution is a total disregard for the actual tie-lines, always assuming the equilibrium tie-line to pass through the bulk $\gamma+\beta$ composition (C^{o}_{Cr}, C^{o}_{Al}) and exit the $\gamma+\beta$ region at the concentrations C^{γ}_{Cr}, C^{γ}_{Al}. Diffusion paths and schematic Cr concentration profiles are shown in Figure C.15 for two hypothetical $\gamma/\gamma+\beta$ diffusion couples. Alloy S_1 has a Cr content greater than that of the $\gamma+\beta$ alloy. As in Figure C.13, Cr diffuses to the right down the Cr concentration gradient so that the cross-hatched areas in Figure C.15b are equal. The dashed lines passing through (C^{o}_{Cr}, C^{o}_{Al}) and (C^{γ}_{Cr}, C^{γ}_{Al}) in the $\gamma+\beta$ region (Figure C.15a) are assumed tie-lines. For alloy S_2 (pure Ni) , the Cr concentration at the $\gamma/\gamma+\beta$ interface, C^{γ}_{Cr2}, has shifted to a Cr concentration below C^{o}_{Cr}. A schematic Cr concentration profile is shown in Figure C.15c. The dashed line passing through (C^{o}_{Cr}, C^{o}_{Al}) and (C^{γ}_{Cr2}, C^{γ}_{A12}) in the $\gamma+\beta$ region (Figure C.15a) is again an assumed tie-line.

An analytical solution for this simplified case was applied to the 4/Ni, 4/X, 4/Y and 4/Z diffusion couples. The diffusivities calculated for the solution were appropriate for the concentrations at the $\gamma/\gamma+\beta$ interface. The $\gamma/\gamma+\beta$ phase boundary was assumed to extend across

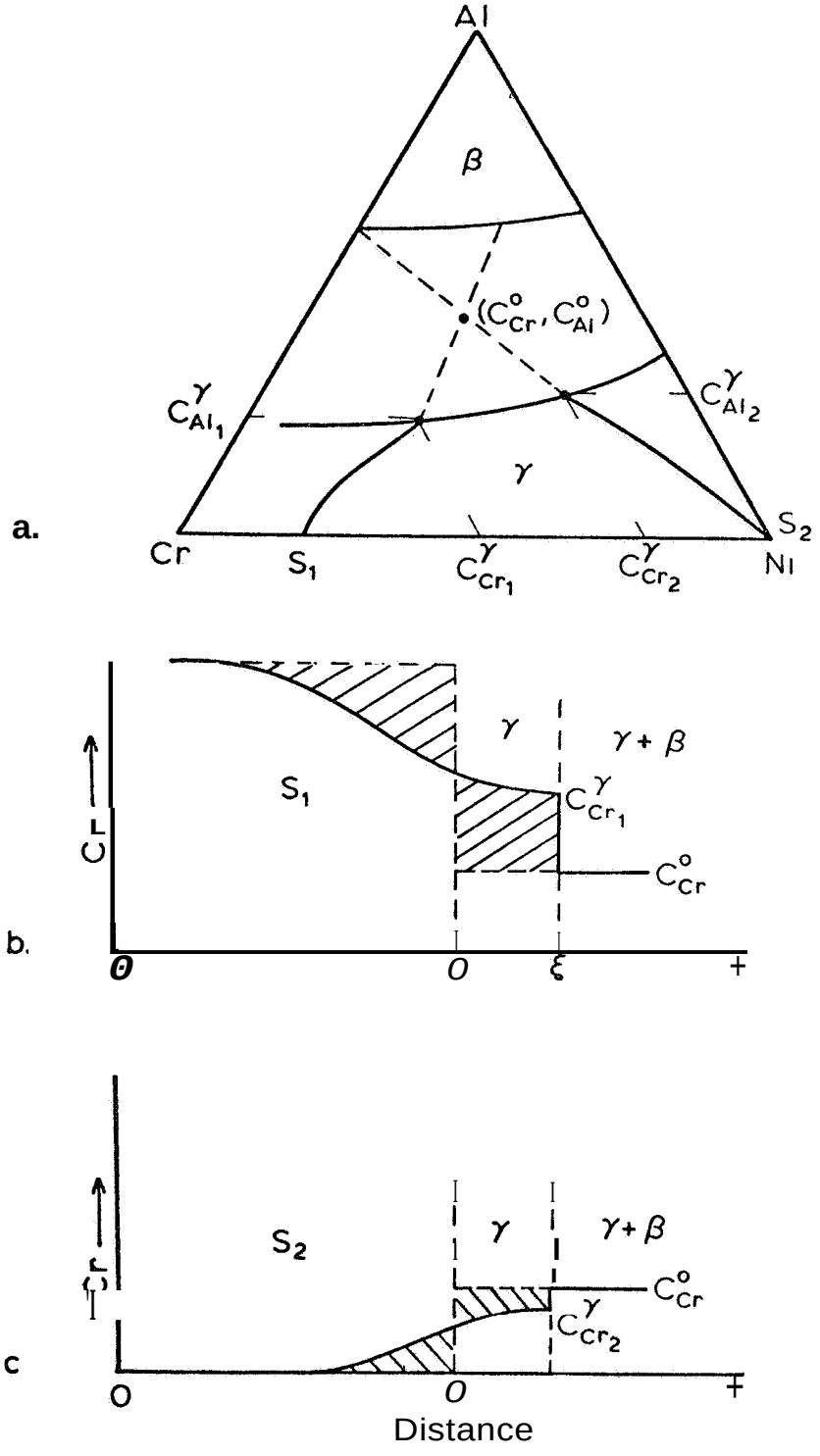

Figure C.15 γ/γ+β **Diffusion Couples**
a. Schematic diffusion paths for couples S_1/ γ+β **and** S_2/ γ+β. **b. Schematic Cr concentration profile for couple** S_1/ γ+β **and, c.** S_2/ γ+β.

the γ phase region to the Ni-Al axis (i.e. no γ' phase was considered). The analytical solution correctly predicted shifts in the concentration at the $\gamma/\gamma+\beta$ interface (C^{γ}_{Cr}, C^{γ}_{Al}) to lower Cr concentrations as the Cr content of the Yalloy decreased, but showed a much larger shift than was actually present in the annealed alloys. In addition, the solution predicted an increase in the Cr concentration at the $\gamma/\gamma+\beta$ interface for couple 4/Z, whereas in the actual couple there was little deviation from the ETL. The measured and predicted diffusion paths were previously shown in Figure C–4. The failure of the analytical solution to predict the correct concentrations at the $\gamma/\gamma+\beta$ interface result from neglect of the diffusion in the $\gamma+\beta$ region, which was previously shown to be significant in $\gamma/\gamma+\beta$ NiCrAl couples. Allowing Lor diffusion in the $\gamma+8$ region reduces the necessary shift in the $\gamma/\gamma+\beta$ interface concentrations. Prediction of the $\gamma/\gamma+\beta$ interface position by the analytical solution shows acceptable agreement with the measured interface positions for the alloy 4 couples. The predicted and measured interface positions are shown in Figure C.16. In summary, the analytical solution predicted shifts in the concentration at the $\gamma/\gamma+\beta$ interface typically much greater than those observed in the diffusion couples. The $\gamma/\gamma+\beta$ interface positions predicted by the analytical solution showed reasonable agreement with the interface positions measured on four $\gamma/\gamma+\beta$ couples. More accurate modeling of the diffusional interactions in $\gamma/\gamma+\beta$ diffusion couples must await further development and extension of the theoretical work initiated by Roper and Whittle (45).

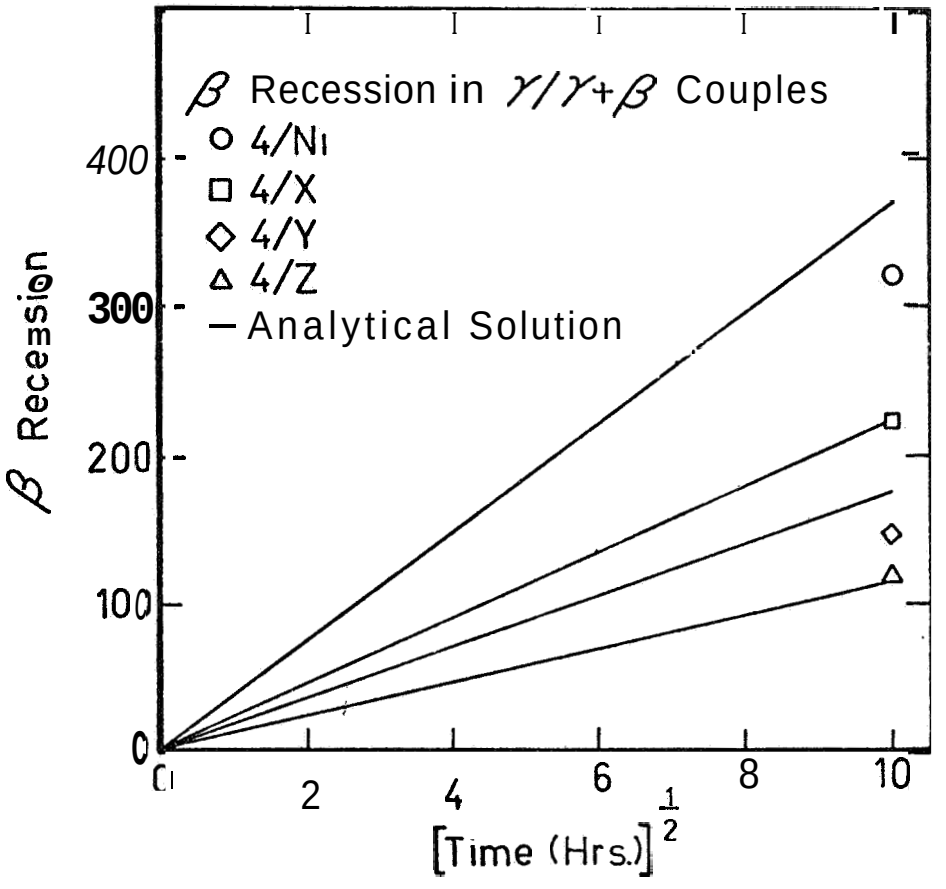

Figure C.16 Measured and predicted β recession in the alloy 4 couples.

Conclusions

1. Interdiffusion coefficients in the γ phase of the NiCrAl system have been measured at 1100°C and 1200°C. D_{AlAl} is approximately four times greater than D_{AlCr} while D_{CrAl} and D_{CrCr} are of the same magnitude. For all concentrations, D_{AlAl} is 2-3 times greater than D_{CrCr}.

2. The location of porosity in the couples suggests that the intrinsic diffusivities can be ranked as:

$$D_{AlAl} > D_{CrCr} > D_{NiNi}$$

3. The diffusion coefficients have been shown to describe adequately interdiffusion in γ / γ couples at 1100°-1200°C. Good agreement between predicted and measured γ / γ concentration profiles justifies the use of couples containing Kirkendall porosity, and the assumptions made in the analysis of $\gamma / \gamma + \beta$ couples.

4. The need for diffusion in the two-phase region of certain $\gamma / \gamma + \beta$ couples has been discussed and a simplified analytical solution for $\gamma / \gamma + \beta$ couples has been utilized with limited success.

References

1. G. W. Goward, "Protective Coatings for High Temperature Alloys - State of Technology", Source Book on Materials for Elevated Temperature Applications, pp. 369–386, ASM, 1979.

2. S. Shankar, D. E. Koning and L. E. Dardi, J. Met., 33, 13 (1981).

3. M. R. Jackson and J. R. Rairden, "Protective Coatings for Superalloys and the Use of Phase Diagrams", General Electric Corporate Research and Development, Rept. No. 77CRD029, March 1977.

4. W. K. Halnan and D. Lee, High Temperature Protective Coatings, S. C. Singhal, Editor, p. 3, TMS–AIME, 1982.

5. M. Nakamori, Y. Harada, and I. Hukue, High Temperature Protective Coatings, S. C. Singhal, Editor, p. 175, TMS–AIME, 1982.

6. C. J. Spengler, S. T. Scheirer, and D. C. Barksdale, High Temperature Protective Coatings, S. C. Singhal, Editor, p. 189, TMS–AIME, 1982.

7. W. F. Smith, Structures and Properties of Engineering Alloys, McGraw–Hill, 1981.

8. C. A. Barrett and C. E. Lowell, Oxid. of Met., 11, 199 (1977).

9. C. A. Barrett and C. E. Lowell, Oxid. of Met., 12, 293 (1978).

10. C. A. Barrett, A. S. Kahn, and C. E. Lowell, J. Electrochem. Soc., 128, 25 (1981).

11. G. W. Goward, J. of Metals, 22, 31 (1970).

12. S. R. Levine, Met. Trans. 9A, 1237 (1978);
see also S. R. Levine, "Reaction Diffusion in the Nickel–Chromium –Aluminum and Cobalt–Chromium–Aluminum Systems", NASA *TN.* D–8383, 1977.

13. J. L. Smialek and C. E. Lowell, J. Electrochem. Soc. 121, 800 (1974).

14. G. W. Roper and D. P. Whittle, Met. Sci., 14, 21 (1980).

15. D. Tu, "Diffusion and Pack Aluminizing Study in the Ni-Cr-Al System", Ph.D. Dissertation, SUNY, Stoneybrook, N.Y. 1982.

16. G. W. Roper and D. P. Whittle, "Multicomponent Diffusion", submitted to Int. Met. Rev., 1979.

17. J. S. Kirkaldy, Advances in Materials Research, 4, 55, (1970).

18. P. G. Shewmon, Diffusion in Solids, McGraw-Hill Book Co. Inc., N.Y 1963.

19. T. Yamamoto, T. Takashima and K. Nishida, Trans. JIM, 21, 61 (1980).

20. M. M. P. Janssen, Met. Trans., 4, 1623 (1973).

21. S. Shankar and L. L. Seigle, Met. Trans. 9A, 1467 (1978).

22. W. Gust, M. B. Hintz, A. Lodding, H. Odelius and B. Predel, Phys. Stat. Sol. 64, 187 (1981).

23. P. A. Swalin and A. Martin, Trans. AIME 206, 567 (1956).

24. Y. E. Ugaste, Fiz. Metal. Metalloved., 24, 442 (1967).

25. A. Davin, V. Leroy, D. Coutsouradis and L. Habraken, Memoires Scientifiques Rev. Metallurg., 60, 275 (1963).

26. A. V. Pawar and D. R. Tenney, Met. Trans. 5, 2139 (1974).

27. K. E. Heinrich, R. L. Myklebust, H. Yakowitz and S. D. Rasberry, "A Simple Correction Procedure for Quantitative Electron Probe Microanalysis", NBS Technical Note 719, 1972.

28. J. S. Kirkaldy and L. C. Brown, Can. Met. Quart. 2, 89 (1963).

29. J. S. Kirkaldy and D. G. Fedak, Trans. AIME, 224, 490 (1962).

30. A. D. Smigelskas and E. O. Kirkendall, Trans. AIME, 171, 130 (1947).

31. D. E. Coates, Met. Trans, 3, 1203 (1972).

32. D. P. Whittle and A. Green, Scripta Met., 8, 883 (1974).

33. T. O. Ziebold and R. E. Ogilvie, Trans. AIME, 239, 942 (1967).

34. W. S. Dorn and D. D. McCraken, Numerical Methods With Fortran IV Case Studies, John Wiley and Sons, Inc., N.Y., 1972.

35. IMSL Library Reference Manual, Chapter I, Vol. 2, 9th Edition, IMSL Inc., 1982.

36. G. W. Roper and D. P. Whittle, Scripta Met., 8, 1357 (1974).

37. G. H. Cheng and M. A. Dayananda, Met. Trans. 10A, 1415 (1979).

38. D. B. Butrymowicz and J. R. Manning, Met. Trans., 9A, 947 (1978).

39, J. R. Manning, Diffusion Kinetics for Atoms in Crystals, D. Van Nostrand Co., Princeton, N.J., 1968.

40. J. S. Kirkaldy, D. Weichert, and Zia-Ul-Hag, Can. J. Physics, 41, 2166 (1963).

41. G. Bolze, D. E. Coates and J. S. Kirkaldy, Trans. ASM, 62, 795 (1969).

42. J. S. Kirkaldy and G. R. Purdy, Can. J. Physics, 40, 208 (1962).

43. G. W. Roper and D. P. Whittle, Met. Sci. 14, 541 (1980).

44. C. Wagner, Thermodynamics of Alloys, Addison-Wesley, N.Y., 1952.

45. G. W. Roper and D. P. Whittle, Met. Sci., 15, 148 (1981).

46. A. Green, M. Eng. Thesis, Univ. of Liverpool, 1975.

47. T. A. Ryan, B. L. Joiner and B. F. Ryan, Minitab Reference Manual, Academic Computing Services, MTU, Houghton, MI, 1981.

48. J. B. Clark and F. N. Rhines, Trans. ASM, 51, 199 (1959).

49. L. E. Wirtz and M. A. Dayananda, Met. Trans., 8A, 567 (1977).

50. R. D. Sisson, Jr. and M. A. Dayanada, Met. Trans., 3, 647 (1972).

51. C. W. Taylor, Jr., M. A. Dayanada, and R. E. Grace, Met. Trans., 1, 127 (1970).

52. J. I. Goldstein and E. Randich, Met. Trans., 8A, 105 (1977).

53. E. Randich and J. I. Goldstein, Met. Trans., 6A, 1553 (1975).

54. A. S. Norkiewicz and J. I. Goldstein, Met. Trans., 6A, 891 (1975).

55. J. Chance and N. Ridley, Met. Trans., 12A, 1205 (1981).

56. R. C. Sharma, G. R. Purdy and J. S. Kirkaldy, Met. Trans., 10A, 1129 (1979).

57. J. B. Gilmour, G. R. Purdy and J. S. Kirkaldy, Met. Trans., 3, 3213 (1972).

58. G. R. Purdy, D. H. Weichert and J. S. Kirkaldy, Trans. AIME, 230, 1025 (1964).

59. J. S. Kirkaldy, Can. J. Physics, 36, 907 (1.958).

60. J. S. Kirkaldy, Can. J. Physics, 36, 917 (1958).

61. D. E. Coates, Met. Trans., 4, 1077 (1973).

62. A. Moren, E. Randich and J. I. Goldstein, Nuclear Metallurgy 20, 221 (1976).

63. A. D. Romig, Jr. and J. I. Goldstein, Met. Trans., 9A, 1599 (1978).

64. S. Widge and J. I. Goldstein, Met. Trans., 8A, 309 (1977).

65. W. Jost, Diffusion in Solids, Liquids, Gases, Academic Press, N.Y., 1952.

66. R. F. Sekerka, C. L. Jeanfils and R. W. Heckel, Lectures on the Theory of Phase Transformations, H. I. Aaronson, Editor, p. 117, TMS-AIME, N.Y. 1975.

Appendix C. 1

Calculation of Ternary Interdiffusion Coefficients When the Matano Planes Are Not Coincident

Four ternary interdiffusion coefficients can be determined by using a Boltzman/Matano analysis applied to ternary alloys. For semi-infinite γ/γ diffusion couples, Kirkaldy (17) has shown that integration of Fick's second law yields:

$$\int_{C^-}^{C_1^*} X dC_i = -2t\left[D_{i1}\frac{dC_1}{dX} + D_{i2}\frac{dC_2}{dX}\right] \qquad i=1,2 \qquad [C1.1]$$

The origin for X must be defined by the Matano plane given as:

$$\int_{C_i}^{C_i^t} X dC = 0 \qquad i=1,2 \qquad [C1.2]$$

From Equation [C1.2], the left hand integral in Equation [C1.1] can be written as either integral:

$$\int_{C_i}^{C_i^*} X dC_i = \int_{C_1}^{C_i^*} X dC_i \qquad i=1,2 \qquad [C1.3]$$

Simultaneous solution of four equations of the type shown above in Equation [C1.1] (for both components [i=1,2] of two intersecting diffusion paths) where C_i^* is the concentration at the intersection, yields the four interdiffusion coefficients. When the Matano planes for components 1 and 2 as (defined in Equation [C1.2]) are not coincident, several sets of diffusion coefficients can be calculated. Consider Figure C1.1 where the Matano planes for component 1 and 2 are indicated as Xm_1 and Xm_2 and the concentration and position representing a

diffusion path intersection is indicated by C_1^* and X^*. Based on the Matano plane for component 1, the left hand integral in Equation [C1.3] is equal to the area -(A+B) in Figure C1.1. The right hand integral in Equation [C1.3] is equal to the area -(E+F)+D. By definition of the Matano plane for component 1, areas E+F=A+B+D, and therefore, both integrals in Equation [C1.3] are equal when calculated on the basis of the Matano plane for component 1. But, if the same integrals are calculated on the basis of Xm_2, the integrals are not equal to one another or the previous calculated integrals based on $Xm_{1'}$ The left hand integral is now equal to -(A+B+C) while the right hand integral is equal to -F+D+G. These latter results are both less (more negative) and greater (less negative) than the areas previously determined [-(A+B) = -(E+F)+D] using $Xm_{1'}$ Therefore, for component 1 there are three values of the left integral in Equation [C1.1] when Xm_1 is not equal to Xm_2, one based on Xm_1 and two based on Xm_2. There are also three comparative values for the left hand integral for component 2 in Equation [C1.1]. If the Matano planes for the second intersecting diffusion path are not equal, there are a comparative number of values for the left hand integral in Equation [C1.1]. Simultaneous solution of the four equations of the type [C1.1] for various combinations of values for the integral in Equation [C1.1] results in numerous sets of the four interdiffusion coefficients at one diffusion path intersection. The differences between the various sets of diffusion coefficients are solely the result of non-coincident Matano planes.

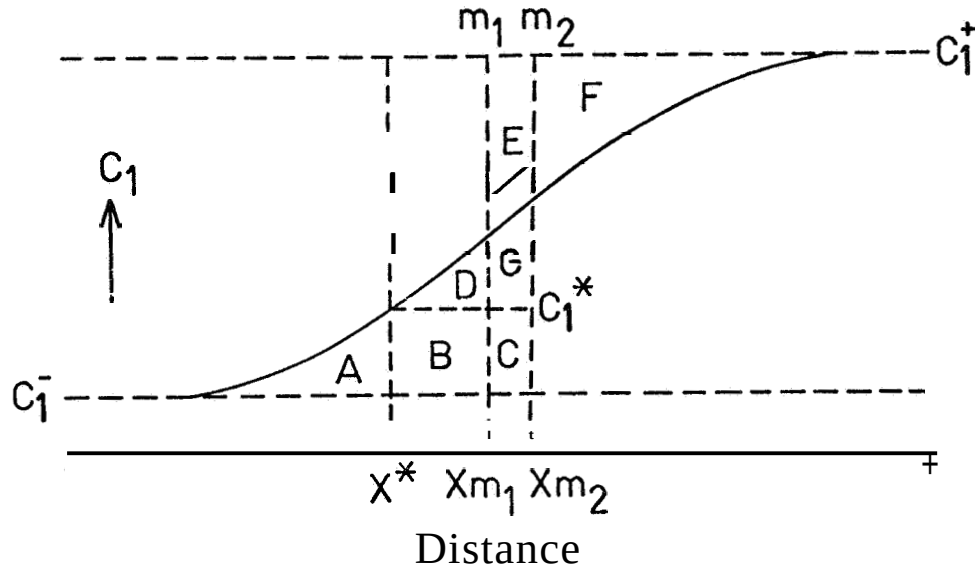

Figure C1.l Schematic concentration/distance profile for component 1.

Appendix C.2

Concentration/Distance Profiles for γ/γ Couples: 1100° and 1200°C

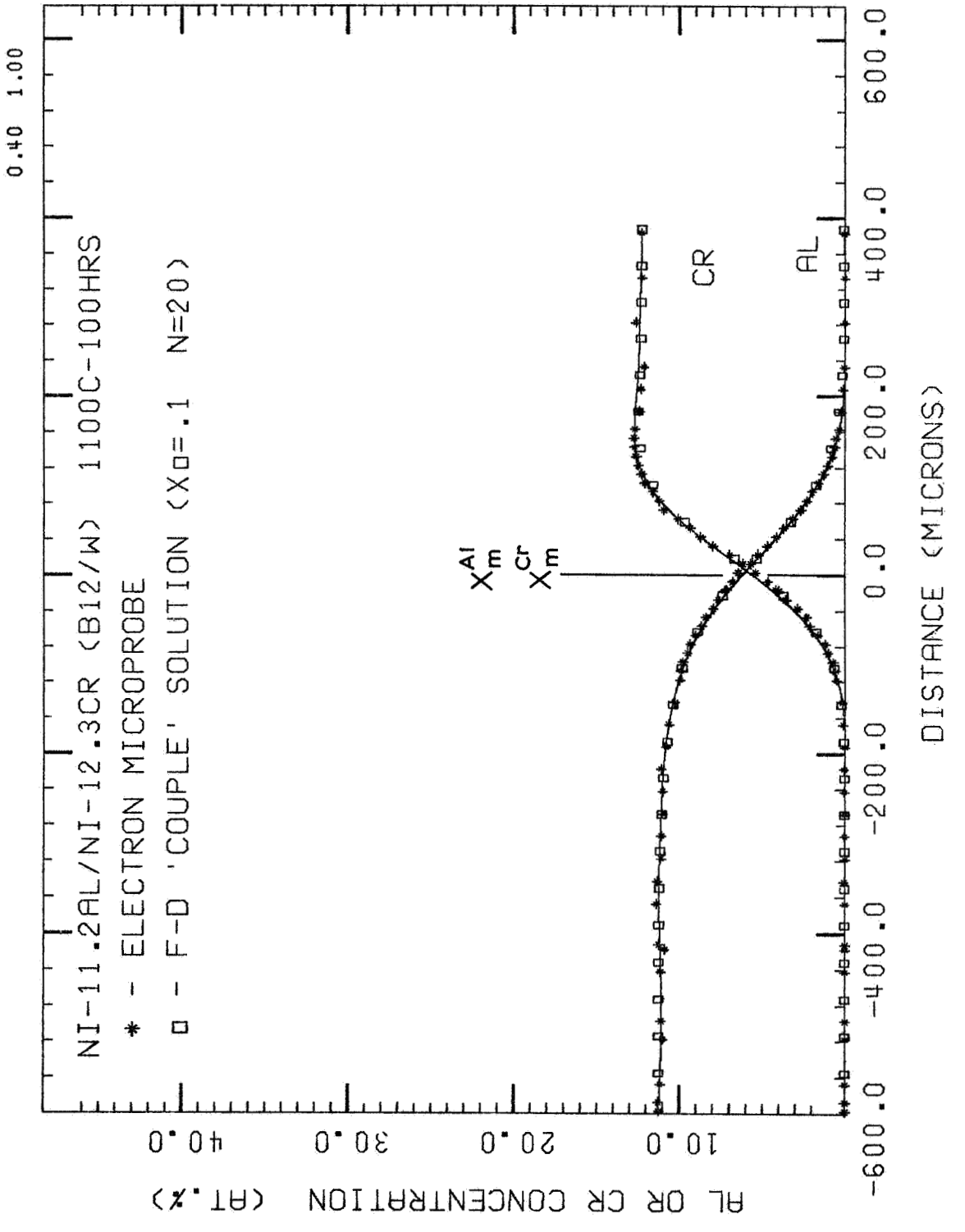

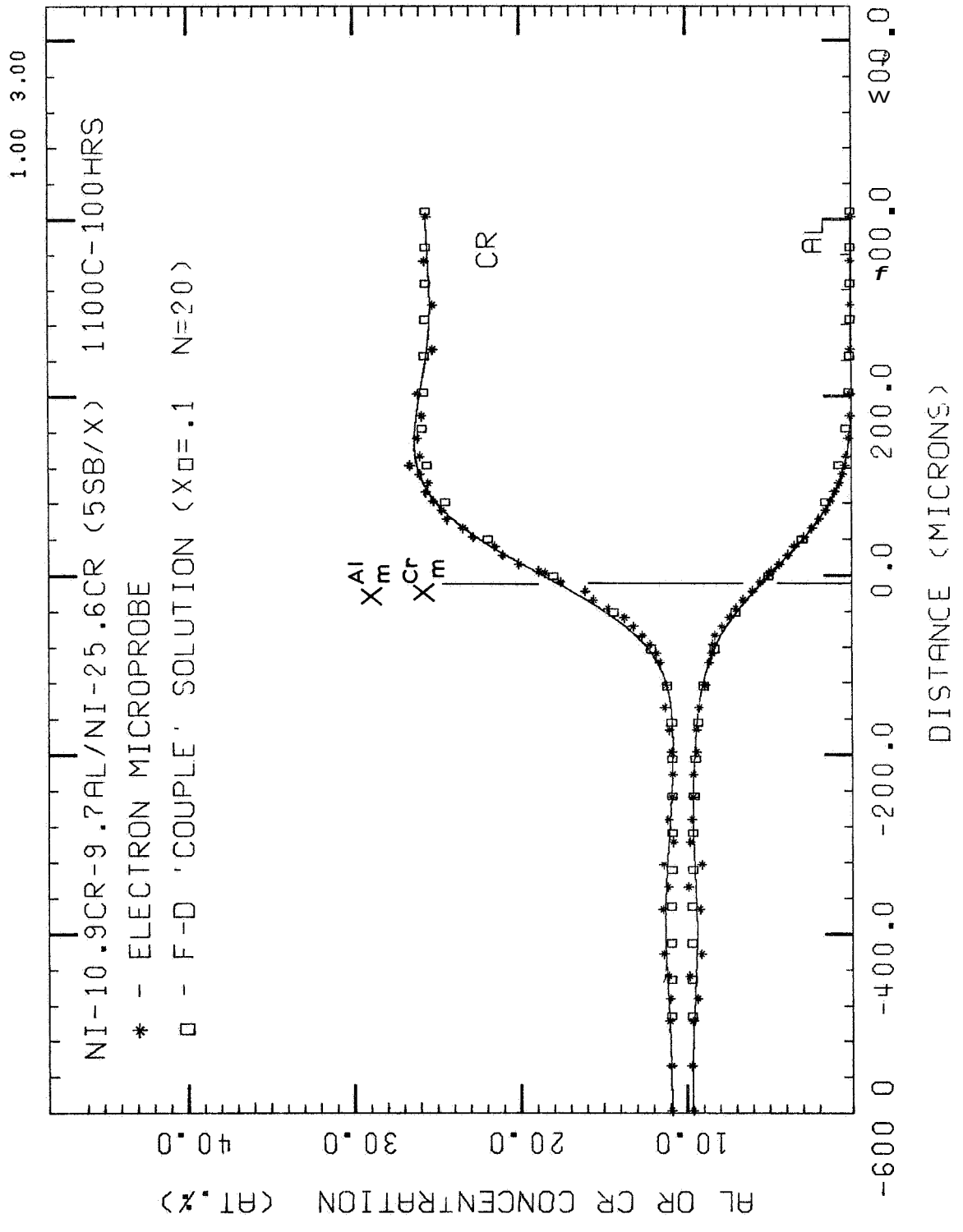
1.00 3.00
NI-10.9CR-9.7AL/NI-25.6CR (5SB/X) 1100C-100HRS
* - ELECTRON MICROPROBE
□ - F-D 'COUPLE' SOLUTION (X□=.1 N=20)
AL OR CR CONCENTRATION (AT.%)
10.0
20.0
30.0
40.0
-600.0
-400.0
-200.0
0.0
200.0
400.0
DISTANCE (MICRONS)
CR
AL
X_m^{Al}
X_m^{Cr}

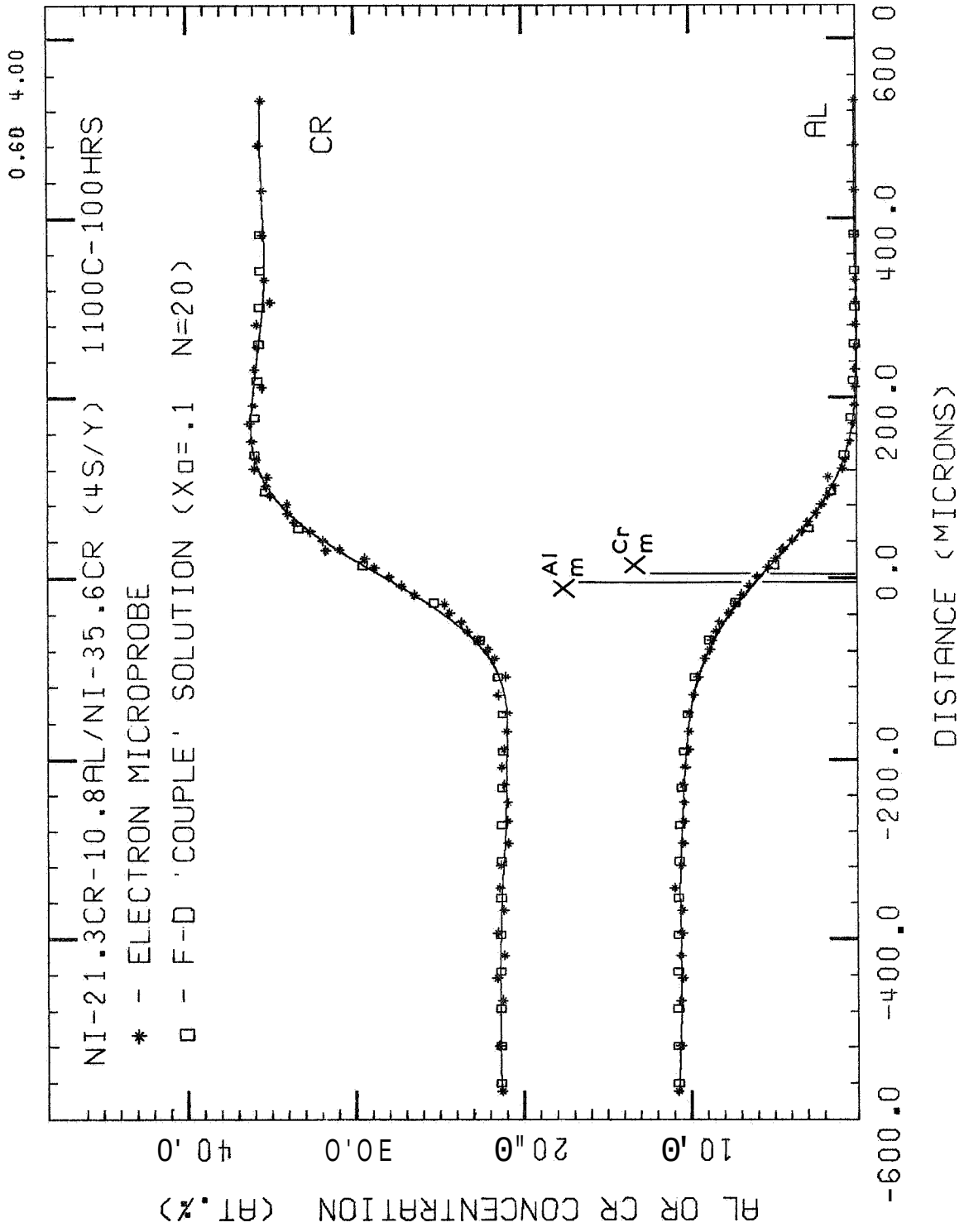
NI-21.3CR-10.8AL/NI-35.6CR (4S/Y) 1100C-100HRS
* - ELECTRON MICROPROBE
□ - F-D 'COUPLE' SOLUTION (X□=.1 N=20)
CR
AL
X_m^{Al}
X_m^{Cr}
AL OR CR CONCENTRATION (AT.%)
DISTANCE (MICRONS)
0.60 4.00
-600.0
-400.0
-200.0
0.0
200.0
400.0
600.0
10.0
20.0
30.0
40.0

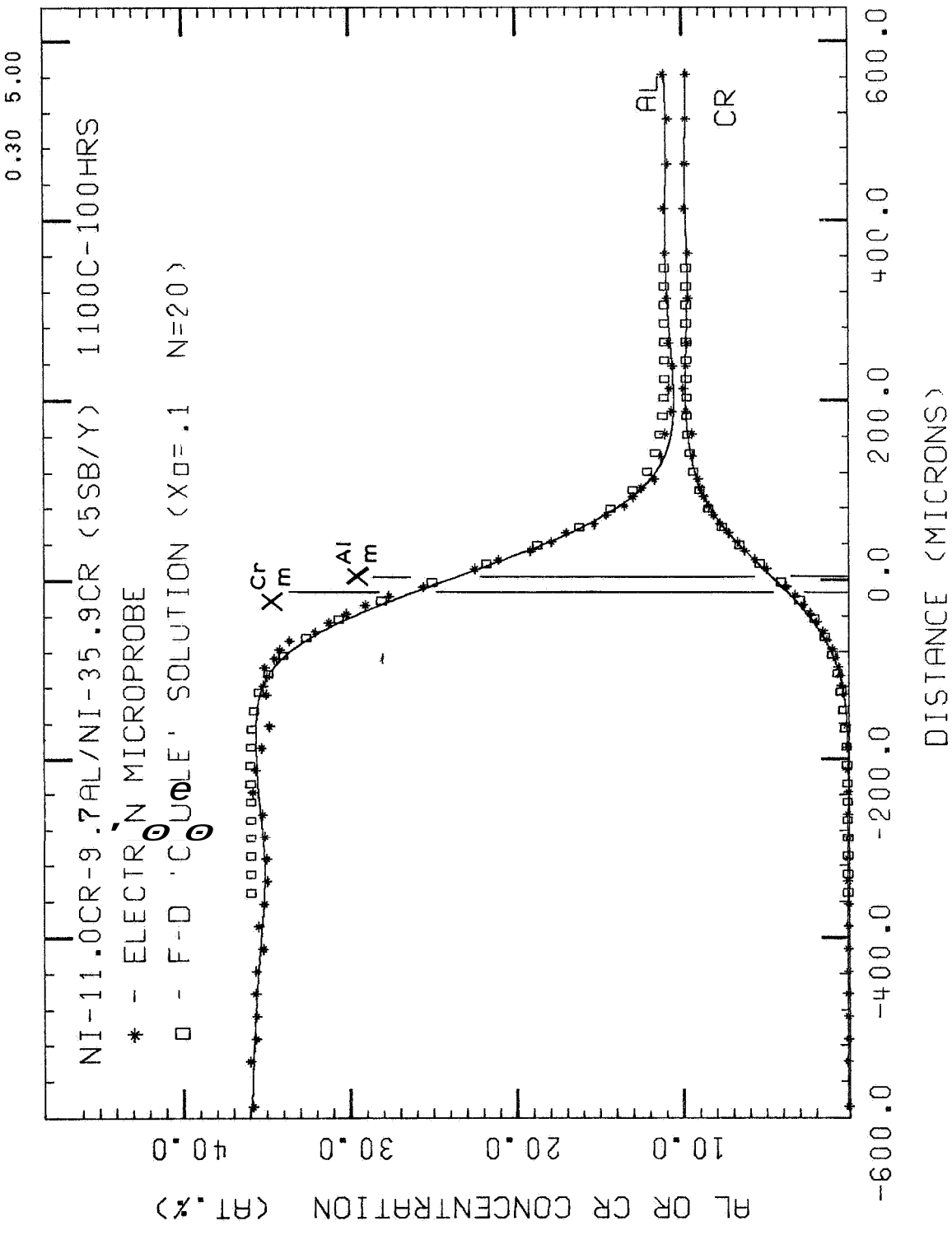
0.30 5.00
NI-11.0CR-9.7AL/NI-35.9CR (5SB/Y) 1100C-100HRS
* - ELECTRON MICROPROBE
□ - F-D 'CUBE' SOLUTION (X□=.1 N=20)
AL
CR
X_m^{Cr}
X_m^{Al}
AL OR CR CONCENTRATION (AT.%)
10.0
20.0
30.0
40.0
-600.0
-400.0
-200.0
0.0
200.0
400.0
600.0
DISTANCE (MICRONS)

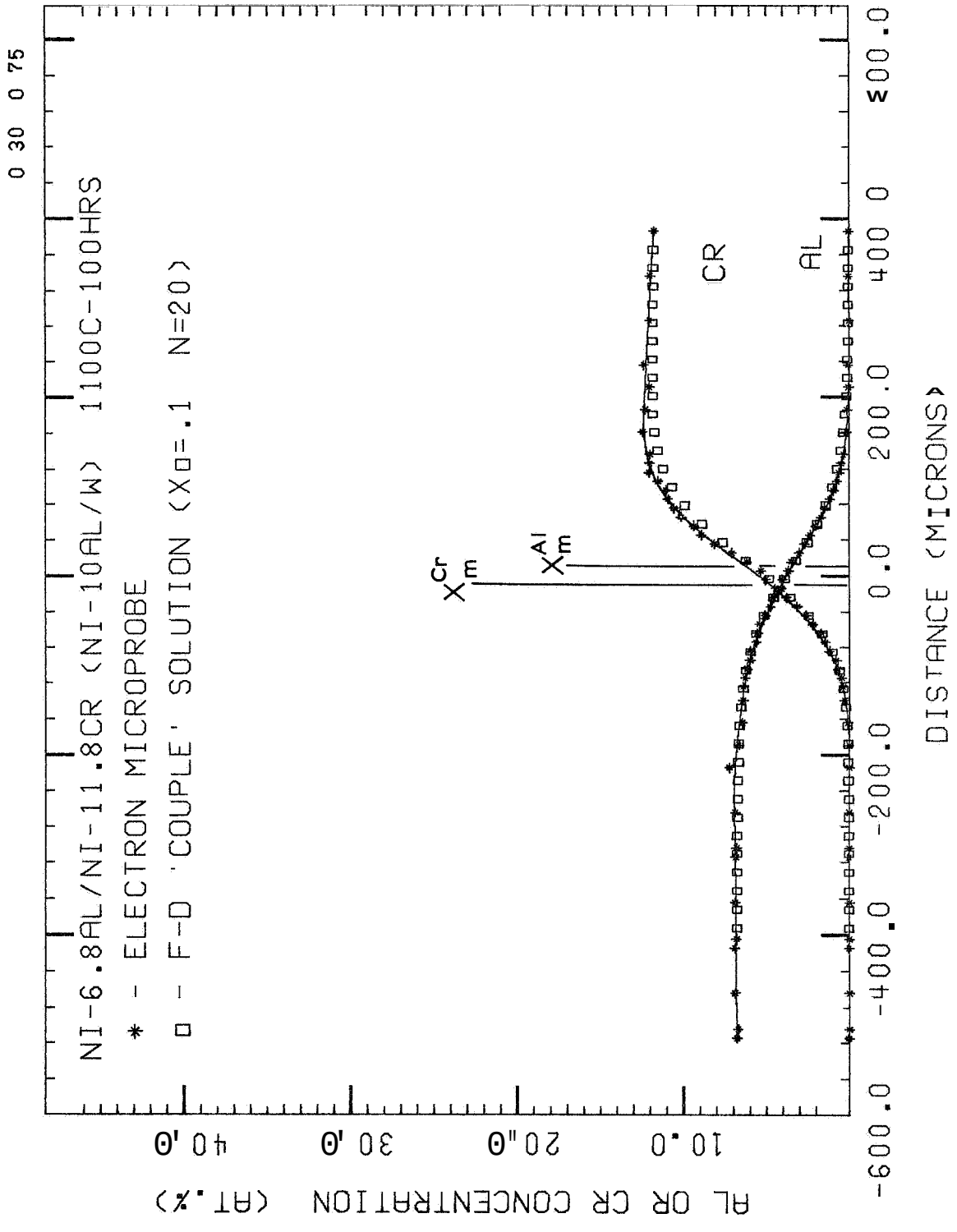
NI-6.8AL/NI-11.8CR (NI-10AL/W) 1100C-100HRS
* - ELECTRON MICROPROBE
□ - F-D 'COUPLE' SOLUTION (X□=.1 N=20)
AL OR CR CONCENTRATION (AT.%)
DISTANCE (MICRONS)
CR
AL
X_m^{Cr}
X_m^{Al}
-600.0
-400.0
-200.0
0.0
200.0
400.0
600.0
10.0
20.0
30.0
40.0

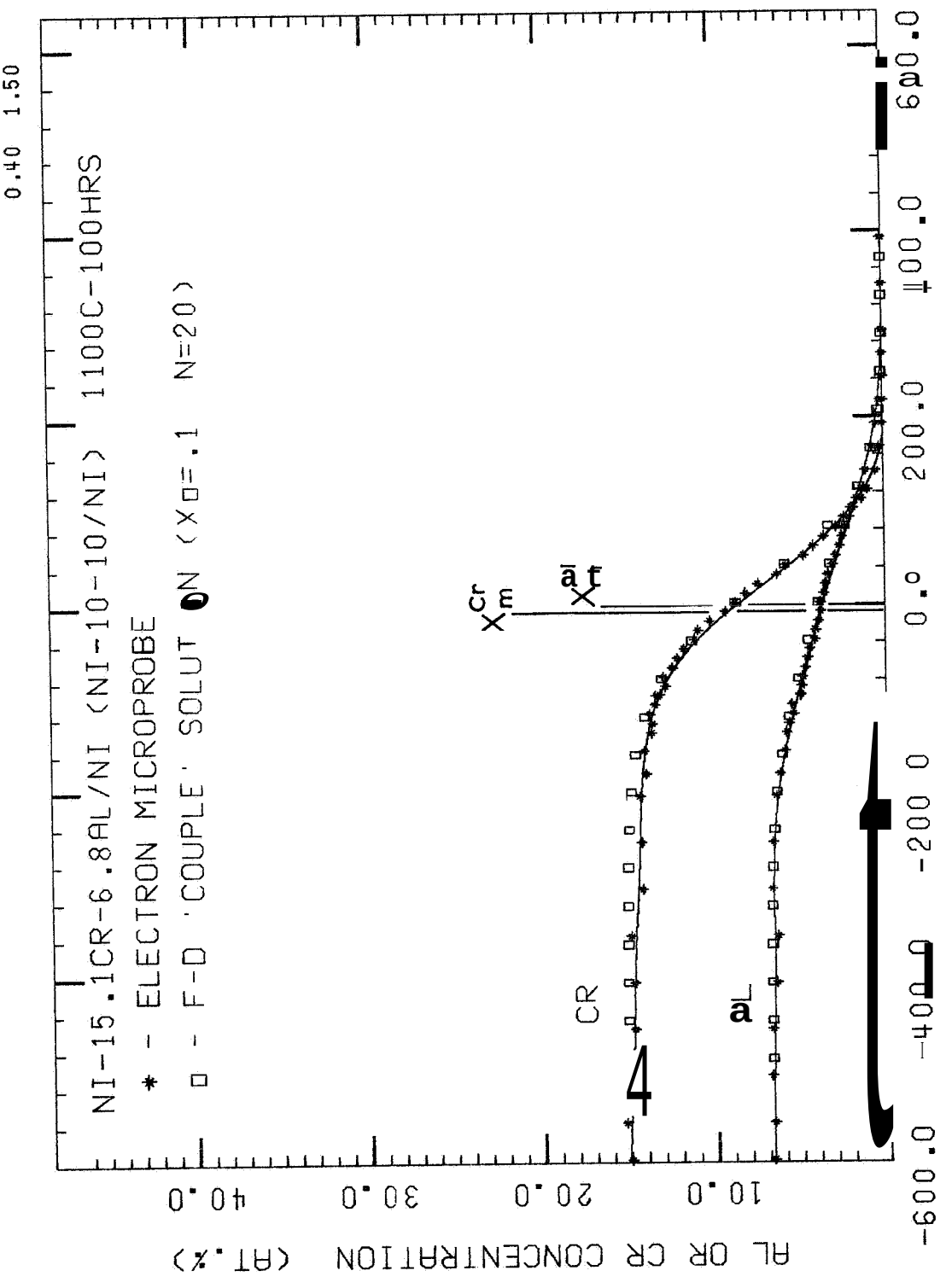
NI-15.1CR-6.8AL/NI (NI-10-10/NI) 1100C-100HRS
* - ELECTRON MICROPROBE
□ - F-D 'COUPLE' SOLUT ● N (Xo=.1 N=20)
AL OR CR CONCENTRATION (AT.%)
DISTANCE (MICRONS)
CR
AL
4
0.40 1.50
10.0
20.0
30.0
40.0
-600.0
-400.0
-200.0
0.0
200.0
400.0
600.0

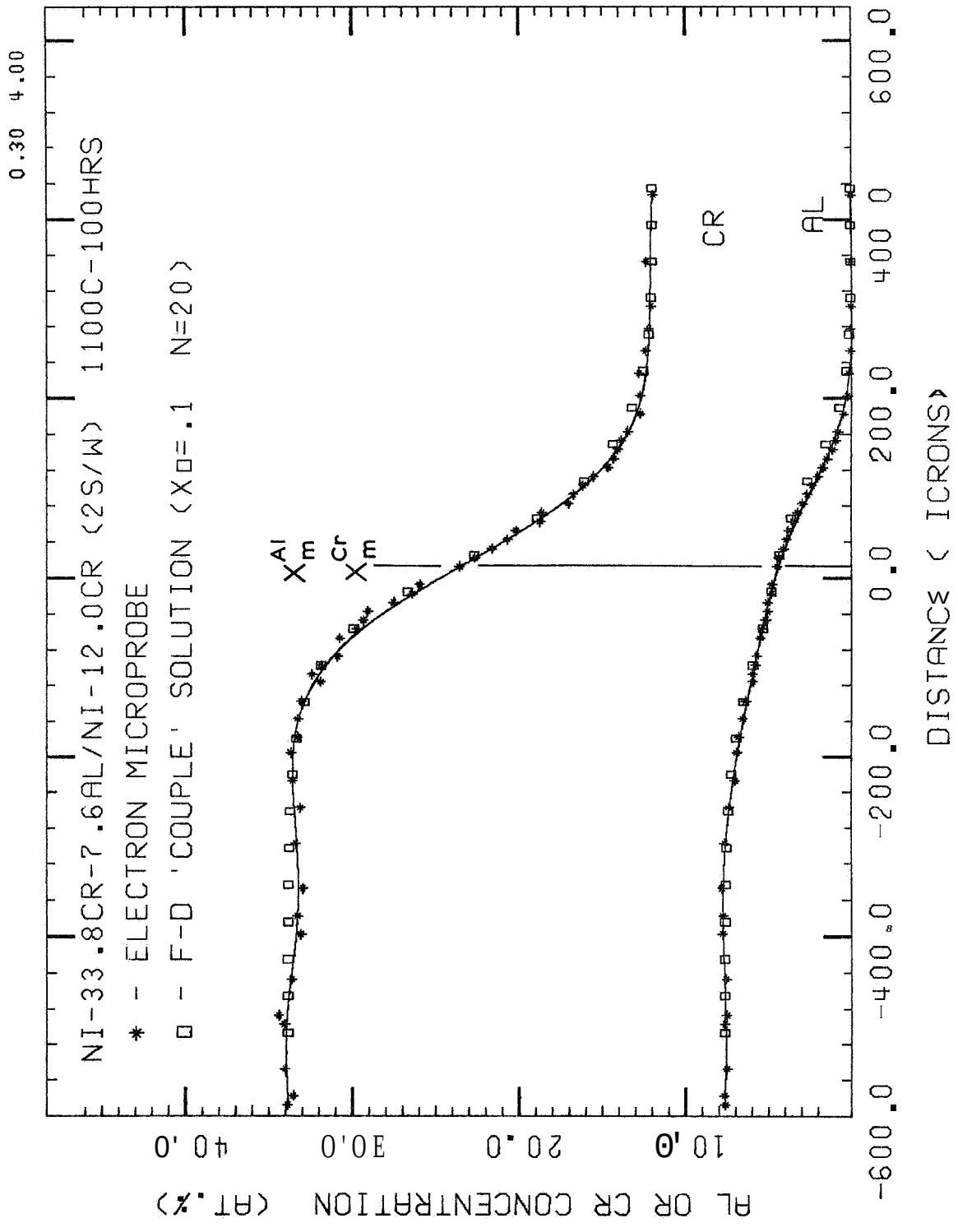
0.30 4.00
NI-33.8CR-7.6AL/NI-12.0CR (2S/W) 1100C-100HRS
* - ELECTRON MICROPROBE
□ - F-D 'COUPLE' SOLUTION (X□=.1 N=20)
AL OR CR CONCENTRATION (AT.%)
10.0
20.0
30.0
40.0
-600.0
-400.0
-200.0
0.0
200.0
400.0
600.0
DISTANCE (MICRONS)
AL
CR
Xm Al
Xm Cr

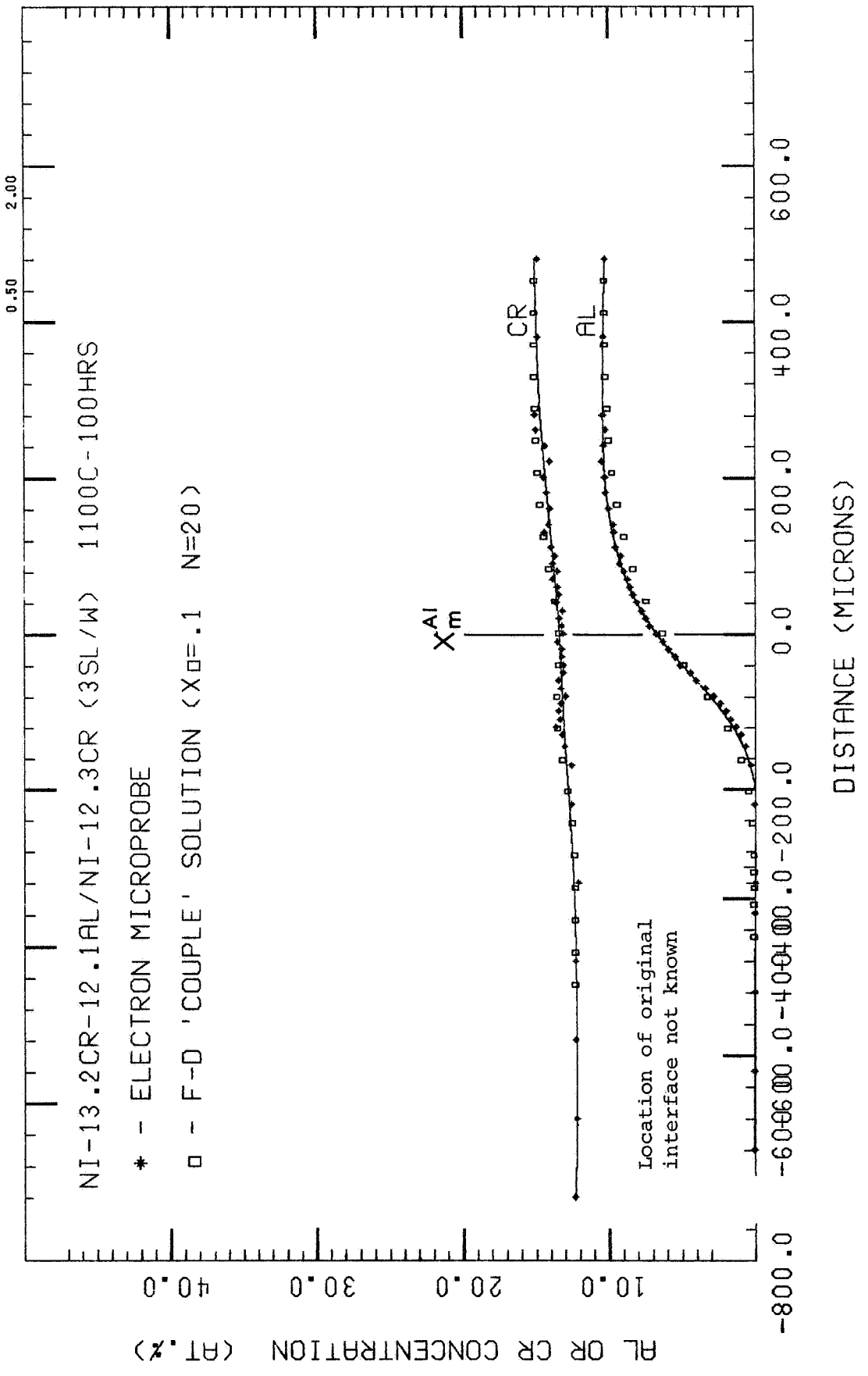
NI-13.2CR-12.1AL/NI-12.3CR (3SL/W) 1100C-100HRS
* - ELECTRON MICROPROBE
□ - F-D 'COUPLE' SOLUTION (X□=.1 N=20)
CR
AL
X_m^{Al}
Location of original interface not known
AL OR CR CONCENTRATION (AT.%)
DISTANCE (MICRONS)
10.0
20.0
30.0
40.0
-800.0
-600.0
-400.0
-200.0
0.0
200.0
400.0
600.0
0.50
2.00

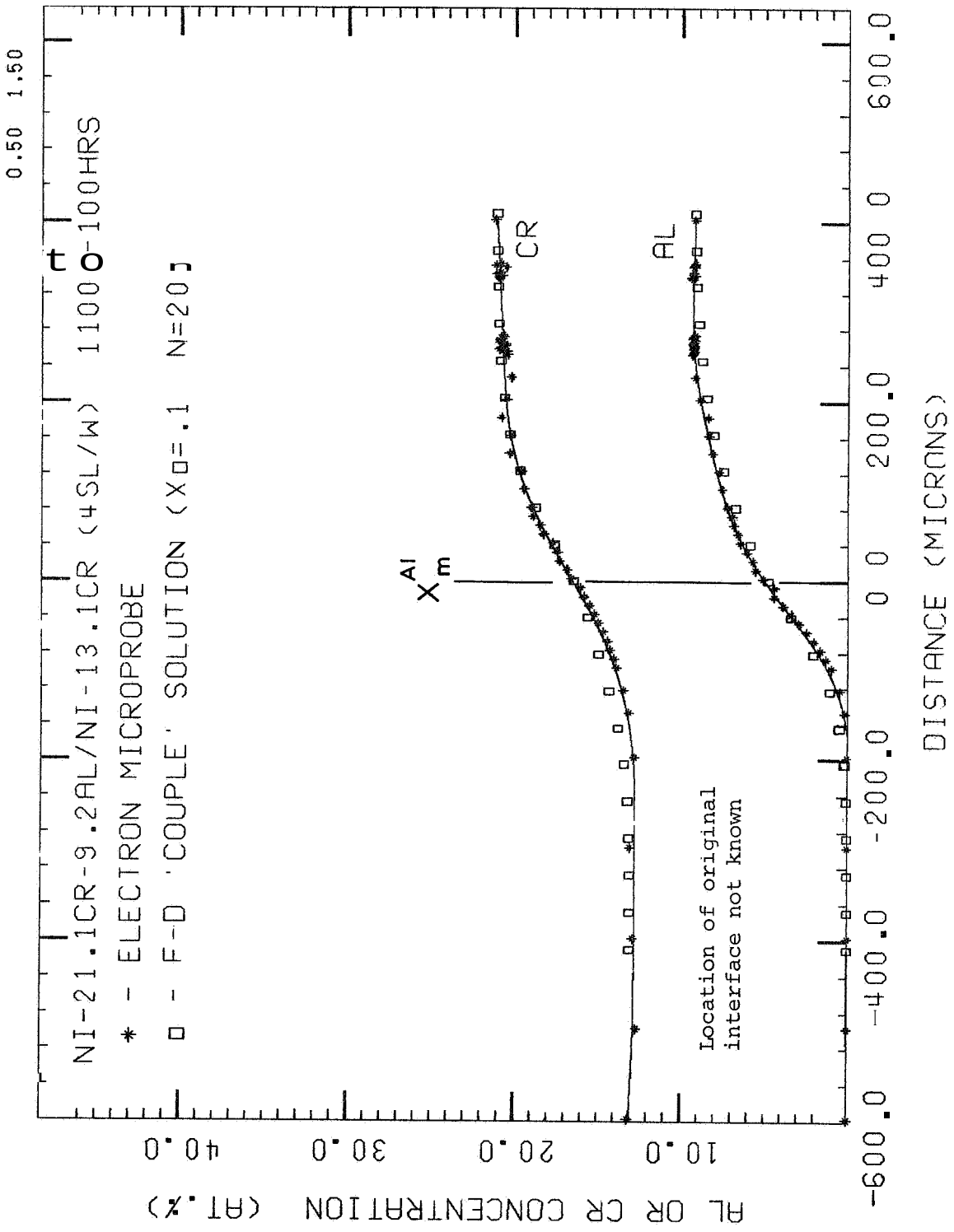
0.50 1.50
NI-21.1CR-9.2AL/NI-13.1CR (4SL/W) 1100 to 100HRS
* - ELECTRON MICROPROBE
□ - F-D 'COUPLE' SOLUTION (X□=.1 N=20)
CR
AL
X_m^{Al}
Location of original interface not known
AL OR CR CONCENTRATION (AT.%)
10.0
20.0
30.0
40.0
-600.0
-400.0
-200.0
0.0
200.0
400.0
600.0
DISTANCE (MICRONS)

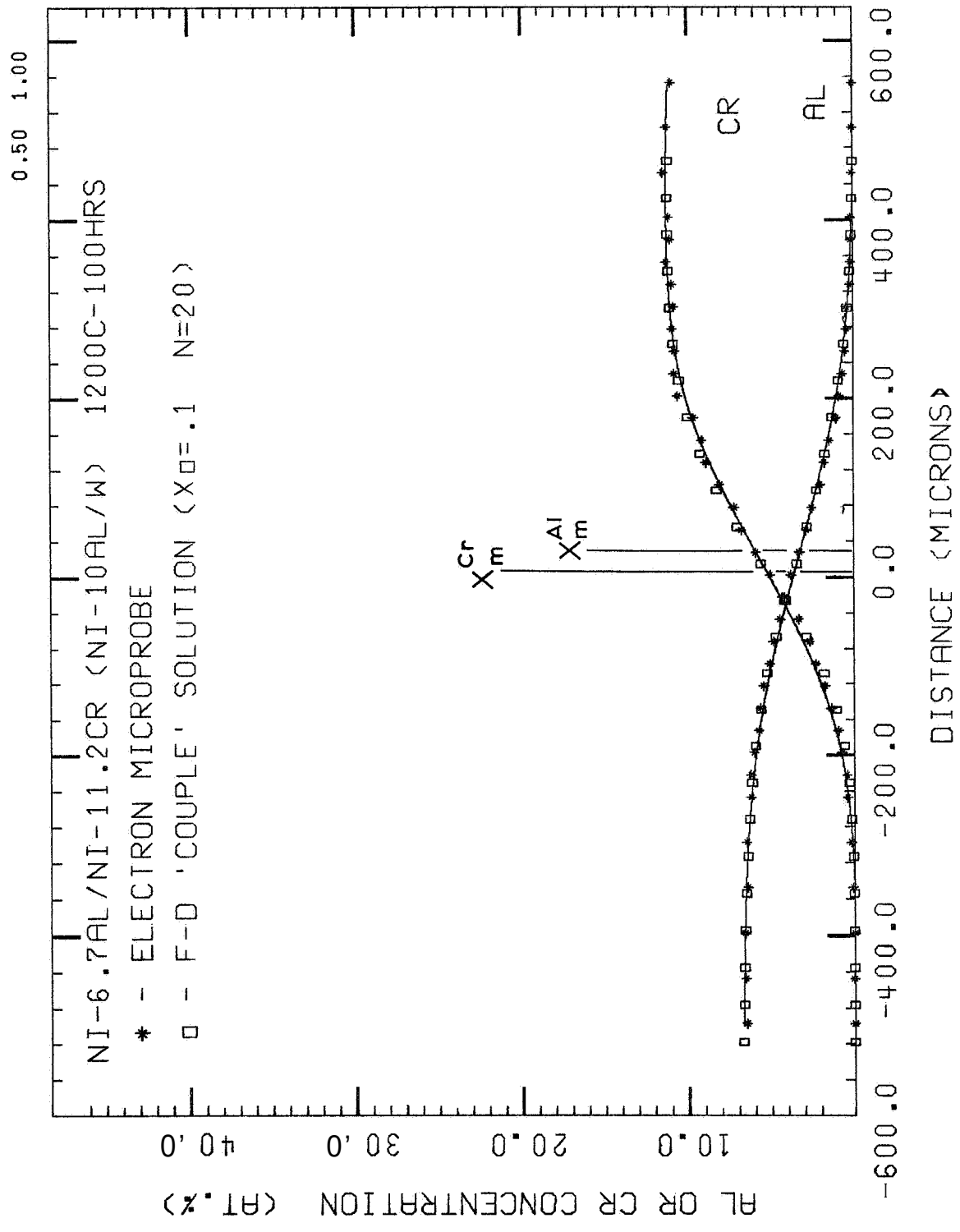
NI-6.7AL/NI-11.2CR (NI-10AL/W) 1200C-100HRS
* - ELECTRON MICROPROBE
□ - F-D 'COUPLE' SOLUTION (X□=.1 N=20)
AL OR CR CONCENTRATION (AT.%)
DISTANCE (MICRONS)
CR
AL
X_m^{Cr}
X_m^{Al}
0.50 1.00
10.0
20.0
30.0
40.0
-600.0
-400.0
-200.0
0.0
200.0
400.0
600.0

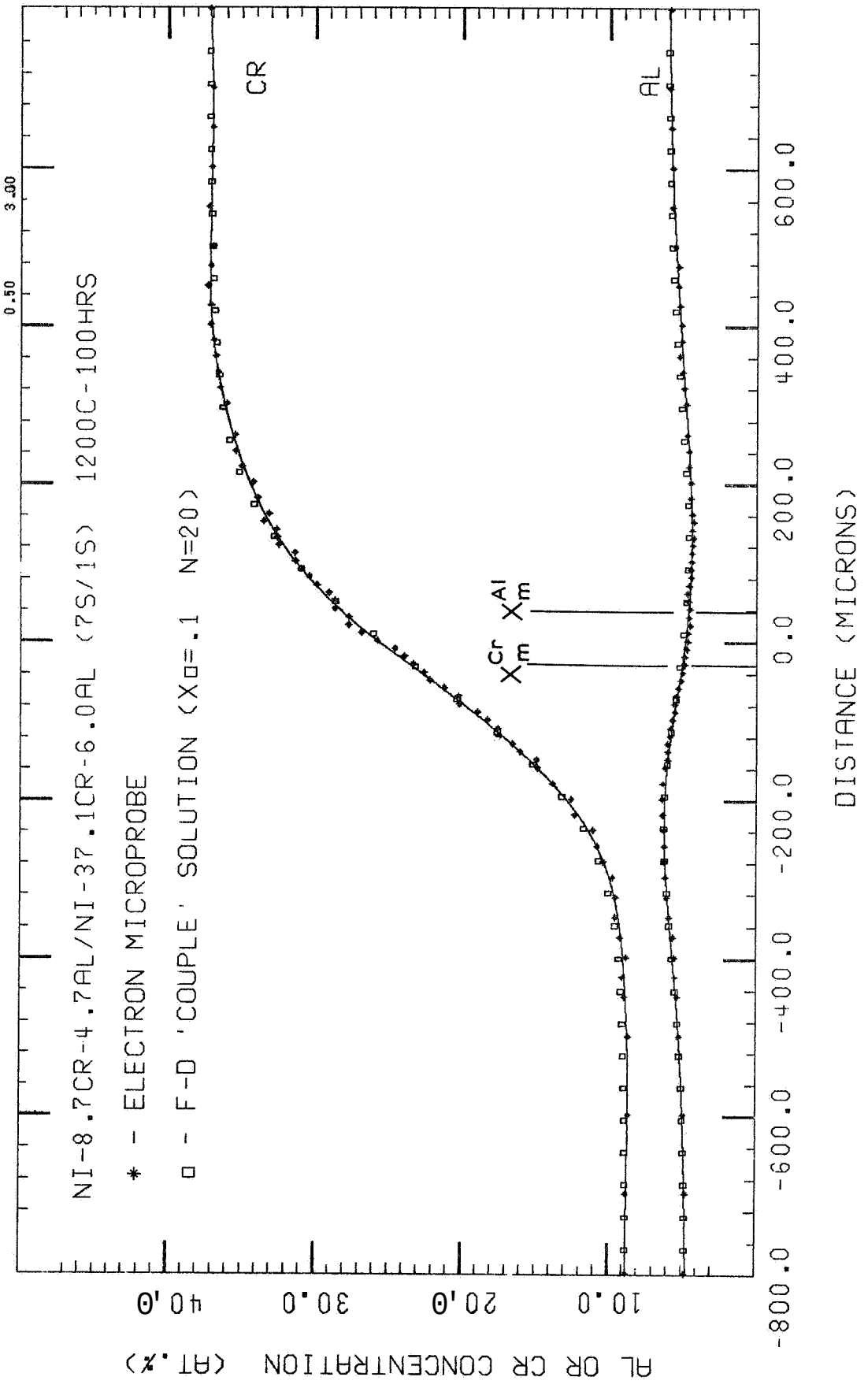
NI-8.7CR-4.7AL/NI-37.1CR-6.0AL (7S/1S) 1200C-100HRS
* - ELECTRON MICROPROBE
□ - F-D 'COUPLE' SOLUTION (X□=.1 N=20)
CR
AL
X_m^{Cr}
X_m^{Al}
AL OR CR CONCENTRATION (AT.%)
DISTANCE (MICRONS)
0.50
3.00
10.0
20.0
30.0
40.0
-800.0
-600.0
-400.0
-200.0
0.0
200.0
400.0
600.0

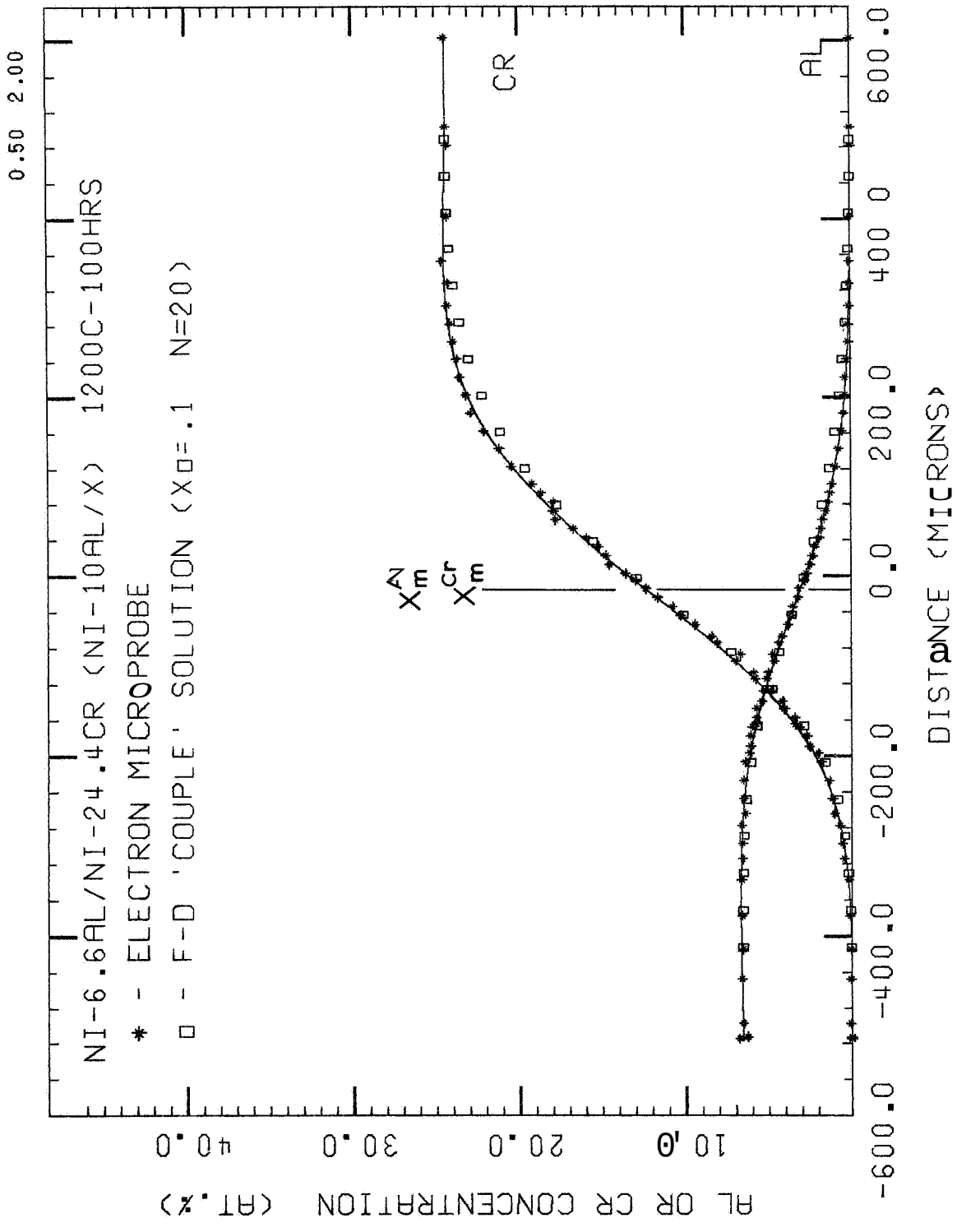
NI-6.6AL/NI-24.4CR (NI-10AL/X) 1200C-100HRS
* - ELECTRON MICROPROBE
□ - F-D 'COUPLE' SOLUTION (X□=.1 N=20)
AL OR CR CONCENTRATION (AT.%)
DISTANCE (MICRONS)
CR
AL
X_m^{Al}
X_m^{Cr}
0.50 2.00
40.0
30.0
20.0
10.0
-600.0
-400.0
-200.0
0.0
200.0
400.0
600.0

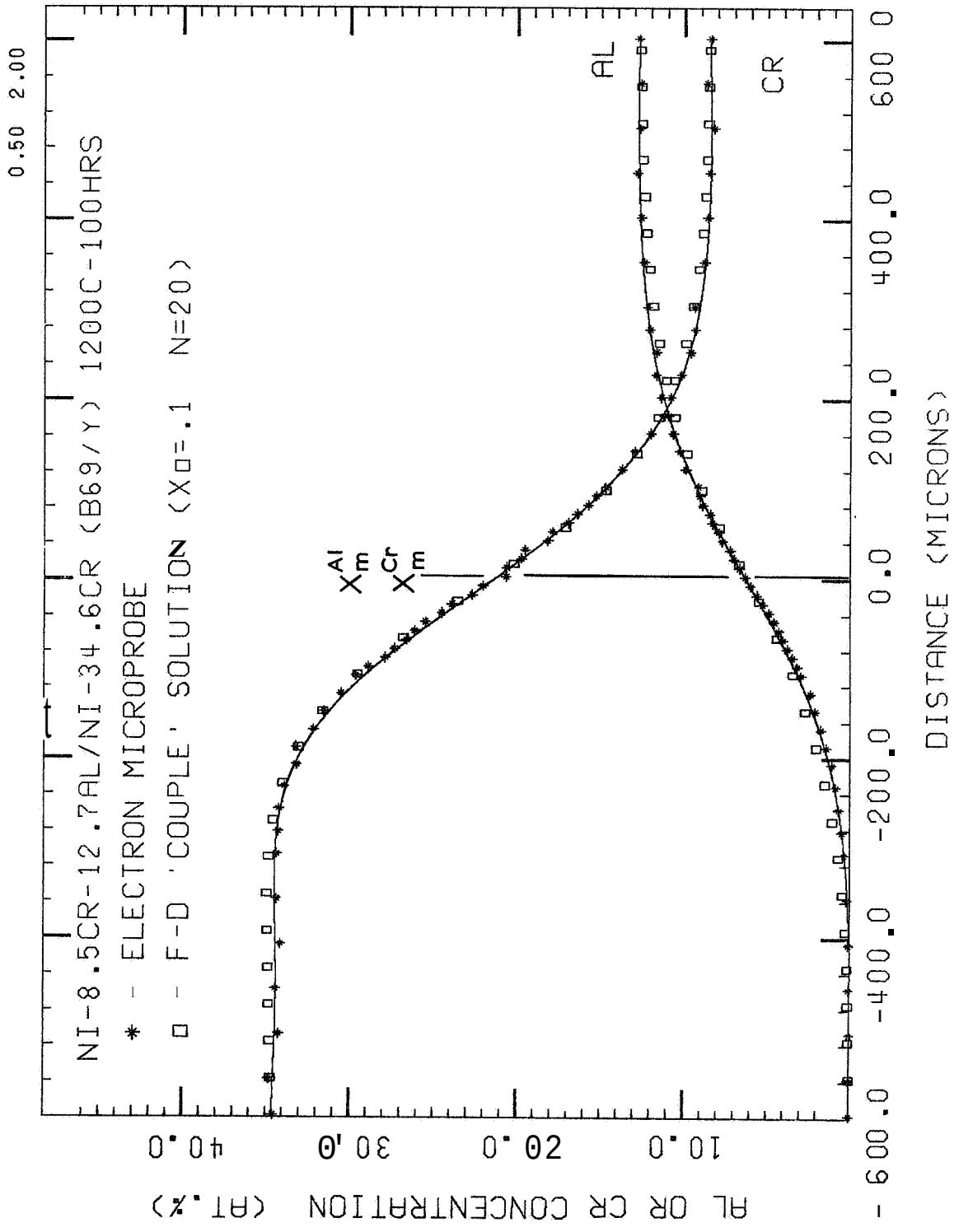
NI-8.5CR-12.7AL/NI-34.6CR (B69/Y) 1200C-100HRS
* - ELECTRON MICROPROBE
□ - F-D 'COUPLE' SOLUTION (X□=.1 N=20)
AL
CR
X_m^{Al}
X_m^{Cr}
AL OR CR CONCENTRATION (AT.%)
DISTANCE (MICRONS)
0.50 2.00
10.0
20.0
30.0
40.0
-600.0
-400.0
-200.0
0.0
200.0
400.0
600.0

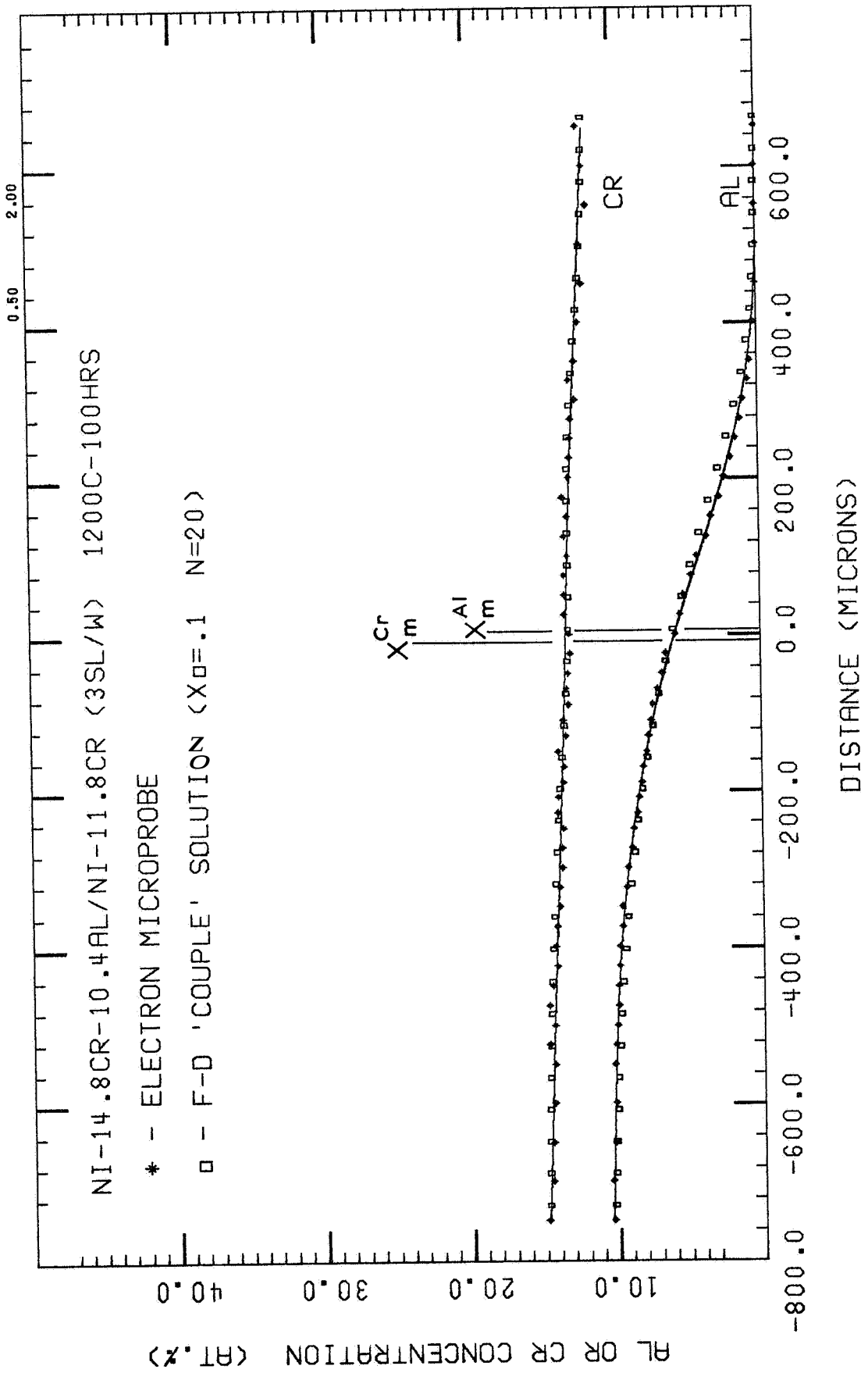
NI-14.8CR-10.4AL/NI-11.8CR (3SL/W) 1200C-100HRS
* - ELECTRON MICROPROBE
□ - F-D 'COUPLE' SOLUTION (X□=.1 N=20)
AL OR CR CONCENTRATION (AT.%)
DISTANCE (MICRONS)
CR
AL
X_m^{Cr}
X_m^{Al}
0.50
2.00
10.0
20.0
30.0
40.0
-800.0
-600.0
-400.0
-200.0
0.0
200.0
400.0
600.0

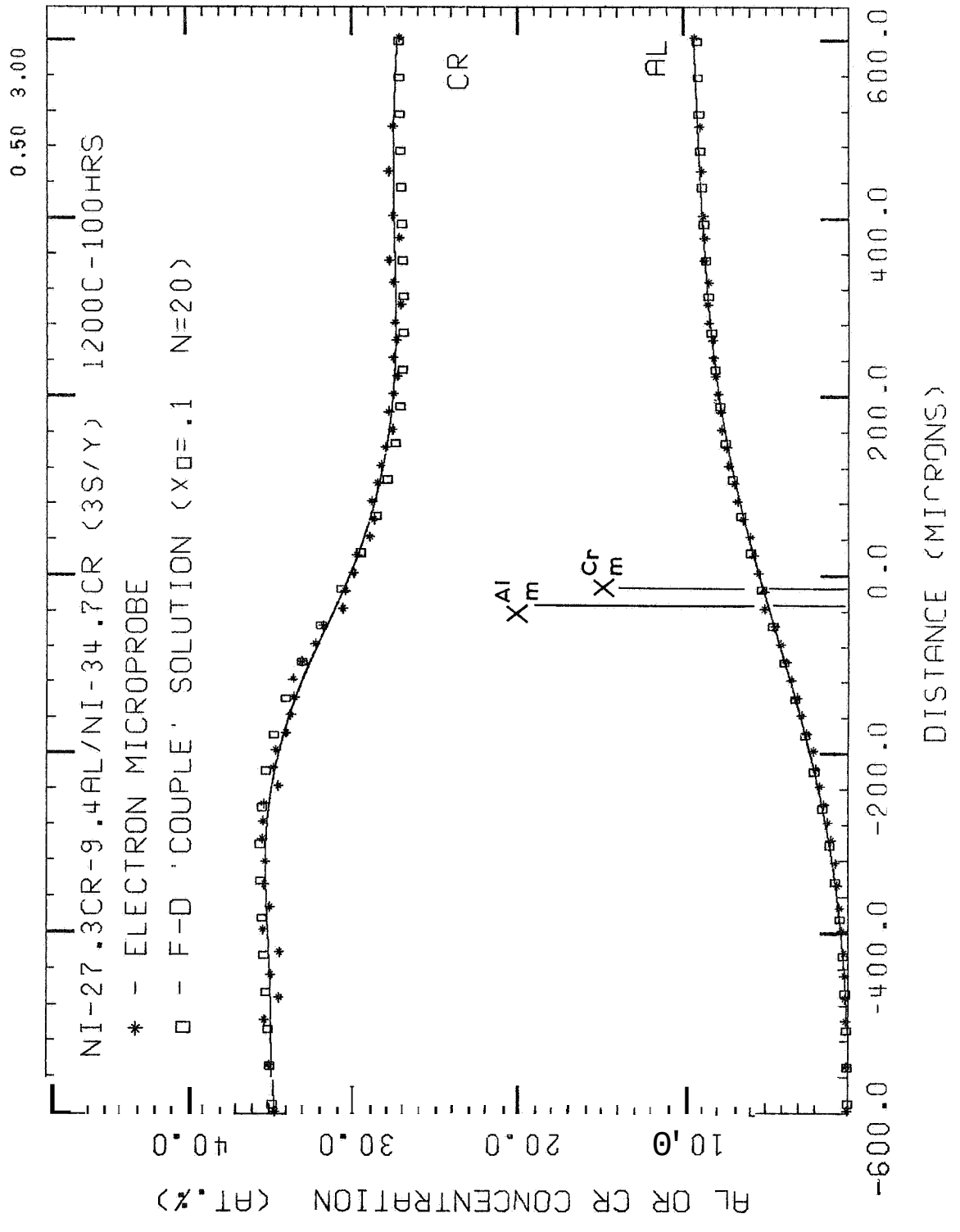
NI-27.3CR-9.4AL/NI-34.7CR (3S/Y) 1200C-100HRS
* - ELECTRON MICROPROBE
□ - F-D 'COUPLE' SOLUTION (X□=.1 N=20)
CR
AL
X_m^{Al}
X_m^{Cr}
AL OR CR CONCENTRATION (AT.%)
DISTANCE (MICRONS)
0.50 3.00
10.0
20.0
30.0
40.0
-600.0
-400.0
-200.0
0.0
200.0
400.0
600.0

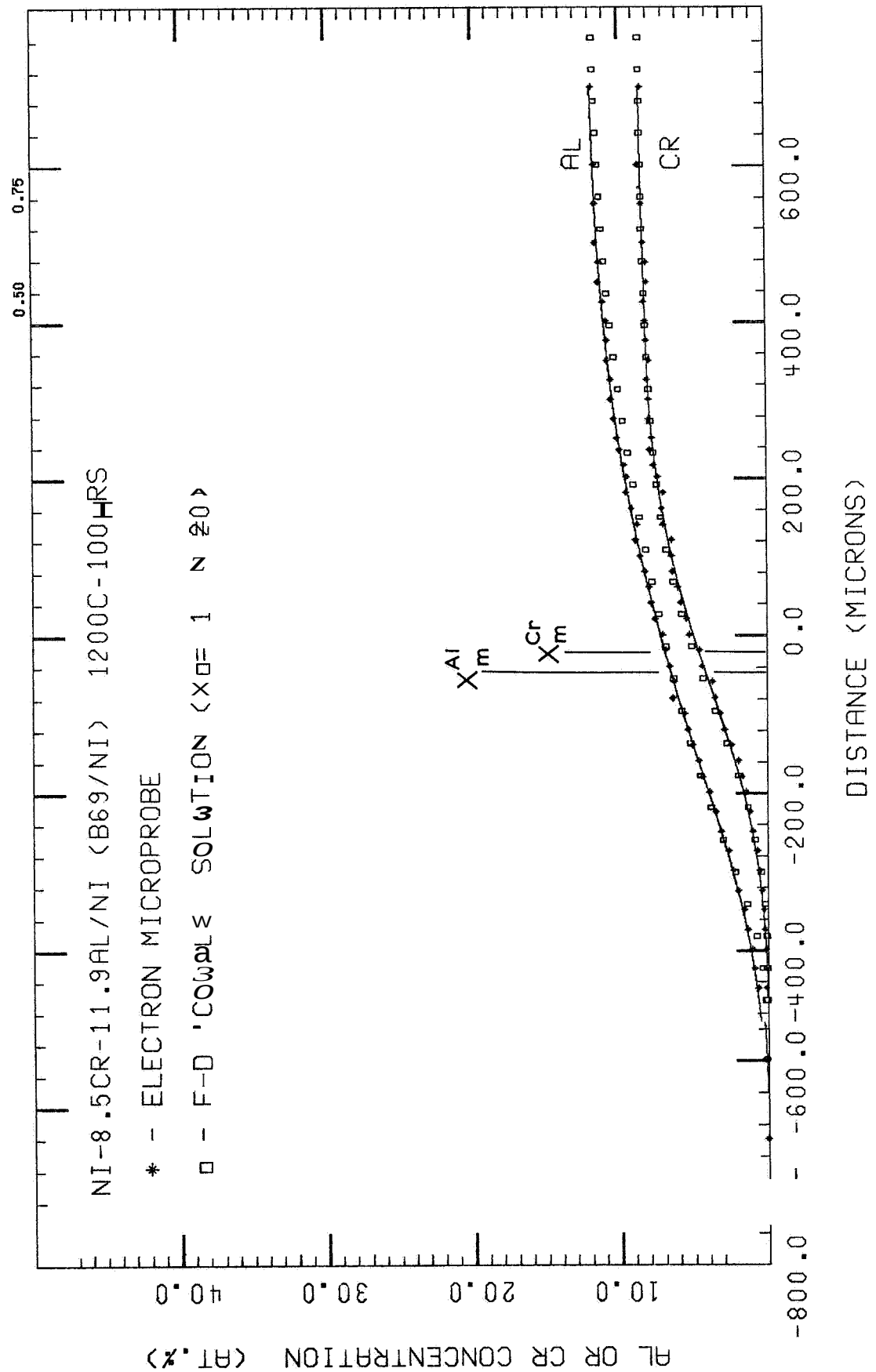
NI-8.5CR-11.9AL/NI (B69/NI) 1200C-100HRS
* - ELECTRON MICROPROBE
□ - F-D 'COωaLw SOLωTION (Xo= 1 N ≠0)
AL
CR
X^{Al}_m
X^{Cr}_m
AL OR CR CONCENTRATION (AT.%)
DISTANCE (MICRONS)
10.0
20.0
30.0
40.0
-800.0
-600.0
-400.0
-200.0
0.0
200.0
400.0
600.0
0.50
0.75

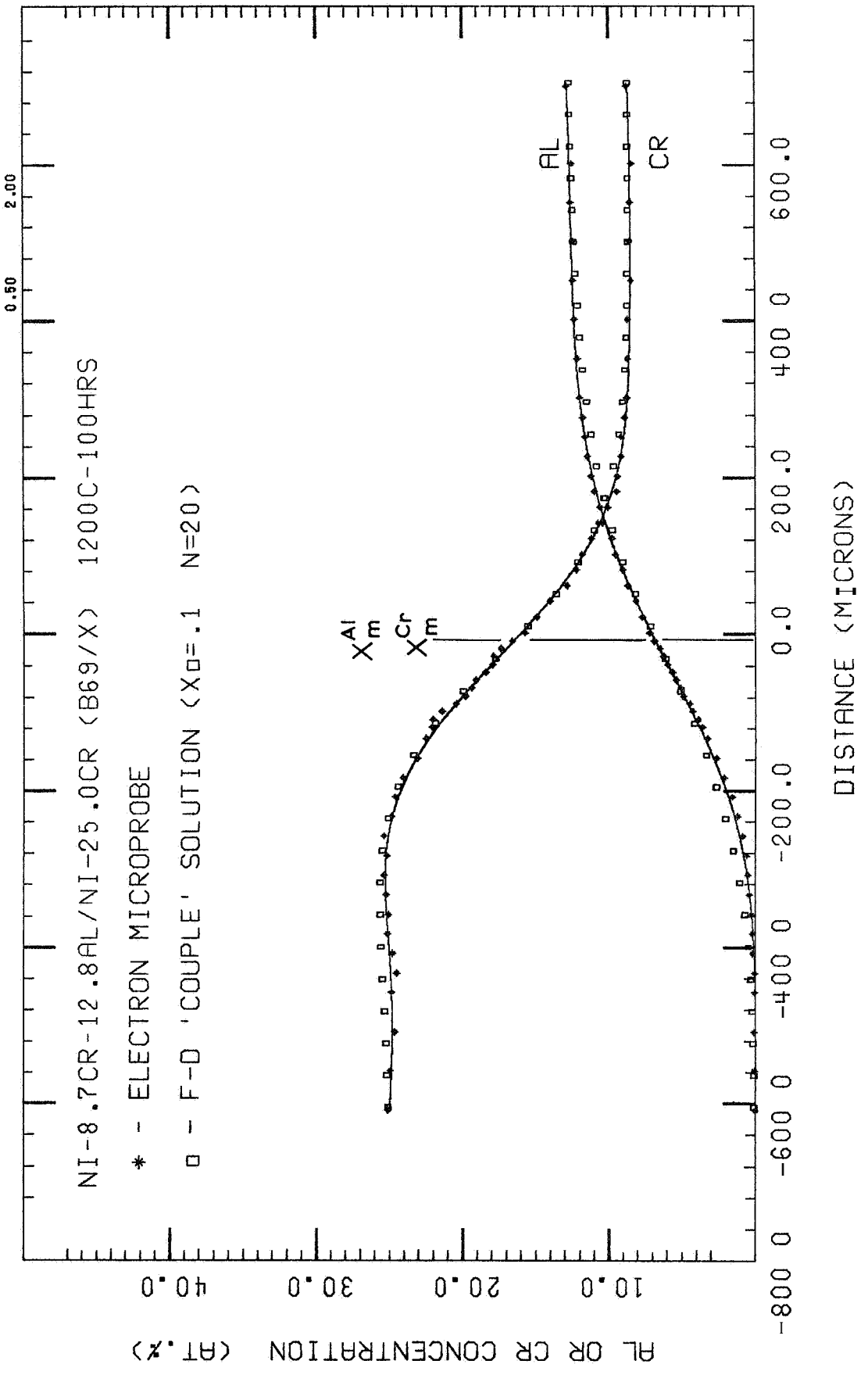
NI-8.7CR-12.8AL/NI-25.0CR (B69/X) 1200C-100HRS
* - ELECTRON MICROPROBE
□ - F-D 'COUPLE' SOLUTION (X□=.1 N=20)
AL
CR
X_m^{Al}
X_m^{Cr}
AL OR CR CONCENTRATION (AT.%)
DISTANCE (MICRONS)
10.0
20.0
30.0
40.0
-800 0
-600 0
-400 0
-200.0
0.0
200.0
400 0
600.0
0.50
2.00

Appendix D

γ' and β Recession in NiCrAlZr Overlay Coatings

The early stages of coating/substrate interdiffusicn were examined for several NiCrAl γ -phase substrates coated with a $\gamma + \beta$ NiCrAlZr overlay coating. The substrates were repeatedly arc melted (from pressed, elemental powders) and sectioned into 1.3 cm X 0.3 cm disks. The overlay coating was applied to one side of the disk by low-pressure plasma spray at the General Electric Research and Development Center, Schenectady, N.Y. The average particle size of the powder before spraying was less than 40 μm. The coating thickness varied between disks from 40-250 μm. The coated substrates were annealed at 1150°C in either still air or flowing Ar for 0.5-25 hours. Compositions of the substrates and coating are given in Table D-1. The as-sprayed coating is shown in Figure D.1a. The coating appears almost fully dense with no obvious porosity at the coating substrate interface. Two powder particles which were not melted in the plasma spraying process are obvious in Figure D.1a. The $\gamma + \beta$ structure of the coating is clear in Figure D.1b where the coated substrate has been annealed in still air at 1150°C for four hours. Porosity at the coating/substrate interface is visible. The coating contains approximately 70 % β phase.

Coating/substrate interdiffusion results in a complex diffusion path between the $\gamma + \beta$ coating and the γ substrate. Diffusion of Al from the coating into the substrate results in recession of the β phase. Formation of γ' occurs when the diffusion path from the $\gamma + \beta$ coating passes through the $\gamma+\gamma'$ region of the phase diagram. Oxidation also causes recession of the β phase in the outer half of the coating. Schematic diffusion paths for oxidation of the coating and coating/substrate interface are shown on the NiCrAl phase

Table D-1

Coating and Substrate Compositions

Substrate Designations	Composition (at.%) Cr	Al
Ni-10Cr	11.8	-
Ni-10Al	-	6.8
Ni-20Cr	22.8	-
Ni-10Cr-10Al	13.0	7.0
Coating Composition	13.5	24.85 (0.06Zr)
Alloy Compositions in Y/Y + β Couples shown in Figure D.3 (Ref. 1)		
1C	14.4	23.7
5c	17.1	28.2
6C	18.8	23.4
8C	20.8	16.9
W	11.0	-

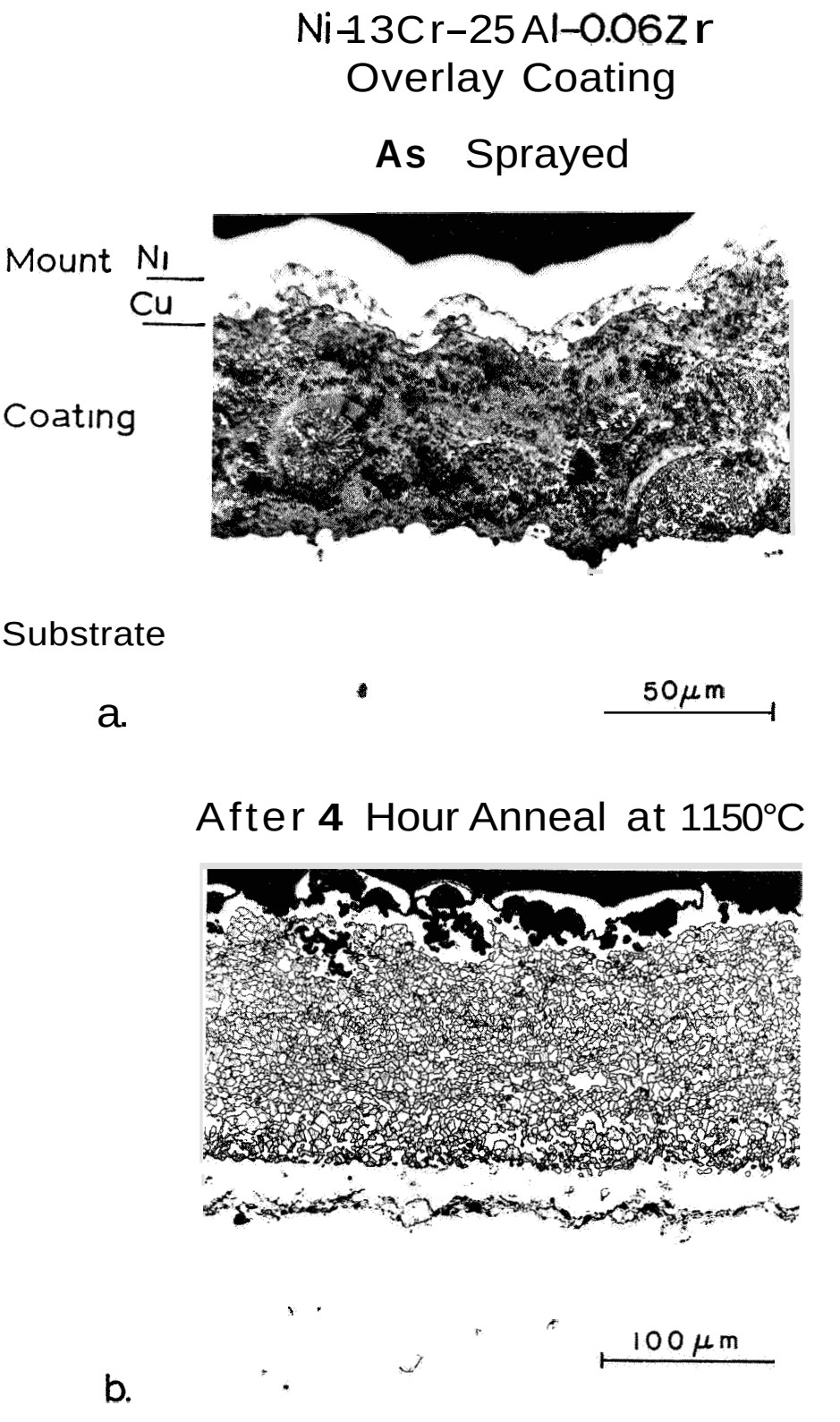

Figure D.1 NiCrAlZr overlay coating
a. as sprayed b. after 4 hour anneal at 1150°C.

diagram in Figure D.2a. The β recession and formation of γ' are shown in Figure D. 2b. Considerable oxidation and/or interdiffusion result in complete β depletion leaving only a γ + γ' region in the center of the coating (Figure D.2c). Further oxidation and interdiffusion deplete the coating of the γ' phase leaving only the Ni-solid-solution γ phase. Diffusion in the γ + β region of the coating sometimes caused the average composition in the center of the coating to shift into the γ + γ' + β region before total β depletion. Considerable porosity usually developed at the original coating/substrate interface as well as in the β-depleted region in the coating. The porosity appears to be located mainly in the inner half (nearest the substrate) of the coating (Figure D. 2c).

Precipitation of γ' was observed in the Ni-10Al substrate near the coating/substrate interface after very short anneals (Figure D.1b). The γ' dissolved with further annealing. The appearance of the γ' in the substrate indicates a very high Al flux from the coating into the substrate during the early stages of coating/substrate interdiffusion. A rapid influx of Al from the coating to the substrate is not surprising considering the fine microstructural scale of the as-sprayed coating. The as-sprayed coating presents several possible high-diffusivity paths, such as initial powder particle surfaces (possibly associated with an Al_2O_3 film) and numerous γ/β phase boundaries. There is also a considerable microstructural change in the as-sprayed coating in the first few hours of an anneal (Figures D.1a and b). The location of the porosity also supports the possibility of a high Al flux from the coating into the substrate. The work presented in Appendix C suggested a ranking of the intrinsic diffusivities as $D_{AlAl} > D_{CrCr} > D_{NiNi}$. A high Al flux from the coating to the substrate would result in a reverse flux of vacancies from the substrate towards the coating. Oxide particles in

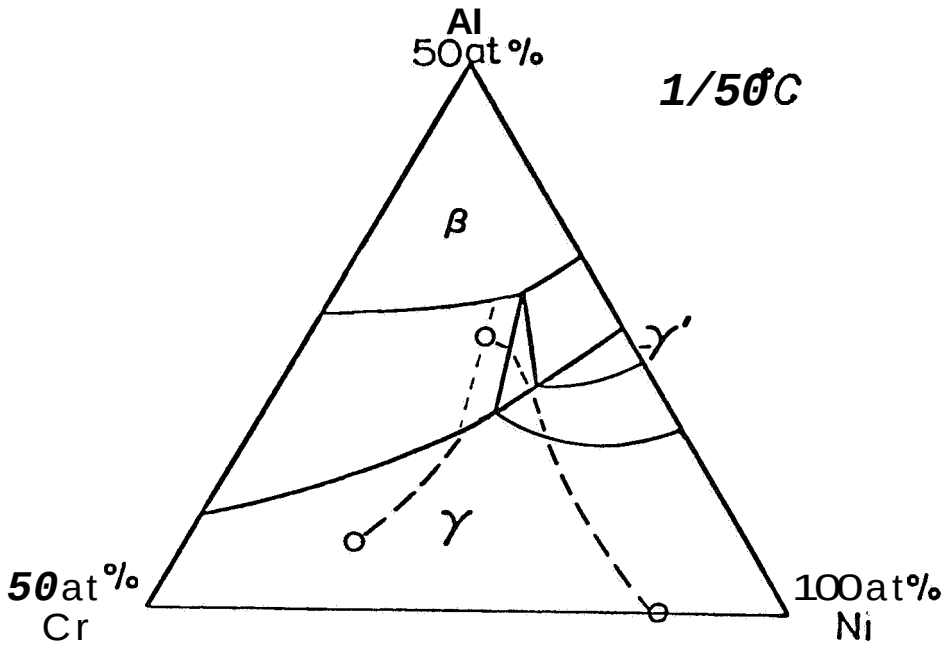

a.

Ni-13Cr-25Al-0.06Zr Overlay Coating

Ni-10Cr Substrate

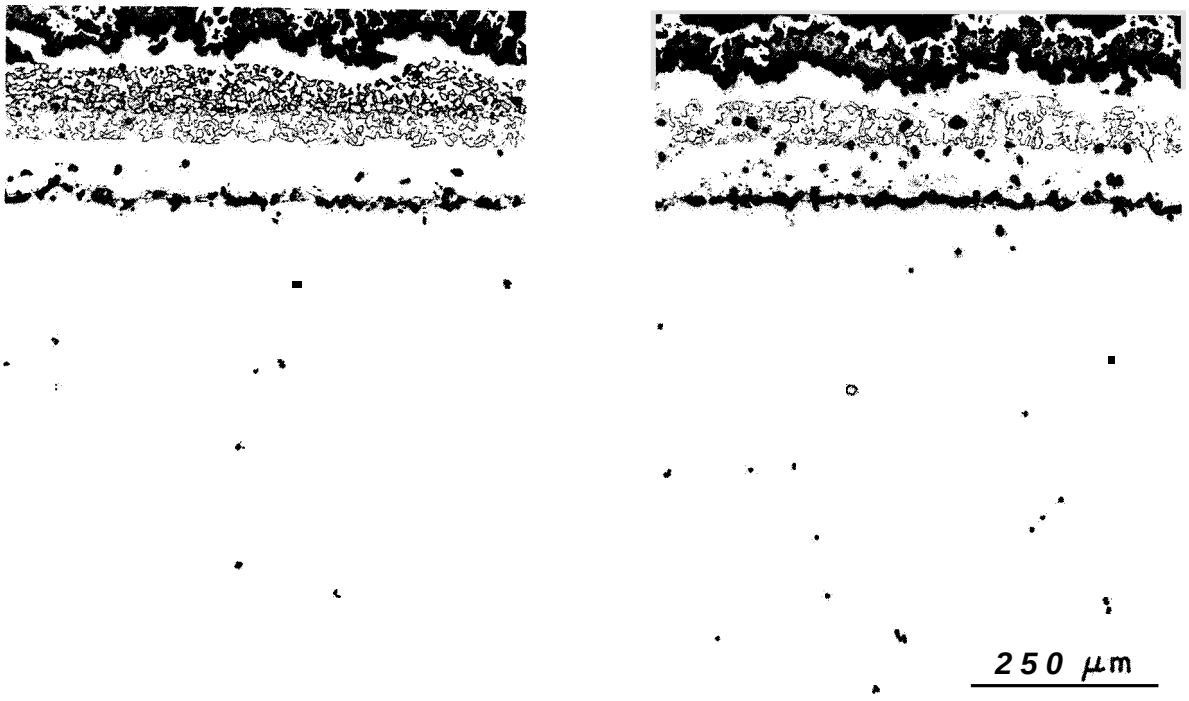

b. c.

Figure 0.2 Schematic diffusion paths (a) and microstructures of overlay coating after oxidation (b and c).

the coating or at the coating/substrate interface could easily act as preferred sites for vacancy coalescence.

The γ' and β phases exhibit accelerated recession during the first hour of an anneal and again when diffusion was affected by the finite width of the coating. The occurrence of diffusion in the $\gamma + \beta$ region in NiCrAl alloys has previously been observed (Appendix C). In finite overlay coatings, diffusion in the $\gamma + \beta$ region nearest the oxide/metal interface occurs due to oxidation and the transport of Al to the oxide scale, while diffusion in the $\gamma + \beta$ region nearest the substrate occurs as a result of interdiffusion. When the diffusion fields in the $\gamma + \beta$ region due to oxidation and interdiffusion overlap, the volume fraction of the β phase decreases resulting in accelerated β recession. Levine (1)* has previously shown that recession in "infinite" γ / $\gamma + \beta$ NiCrAl couples is parabolic with time. The and β recession in the present study appears parabolic after the first hour of the anneal until overlapping diffusion fields resulted in accelerated recession. Recession of the γ' and β phases is shown in Figure D.3. The onset of accelerated recession due to overlapping diffusion fields occurred at different times since the coating thickness on each of the substrates varied. Therefore, β recession after one hour was — 52 μm in a coating only 71 μm thick (Ni-10Cr substrate) while the β recession on the same substrate was only 48 μm after nine hours in a coating 190 μm thick. For parabolic recession, the γ' and β recession for each substrate in Figure D.3 should be described by a straight line passing through the origin. Although the amount of data presented in Figure D.3 is somewhat limited, examination of the recession for similar substrates indicates a very rapid recession rate for the first hour of

---

* The references for this appendix are listed on page D9.

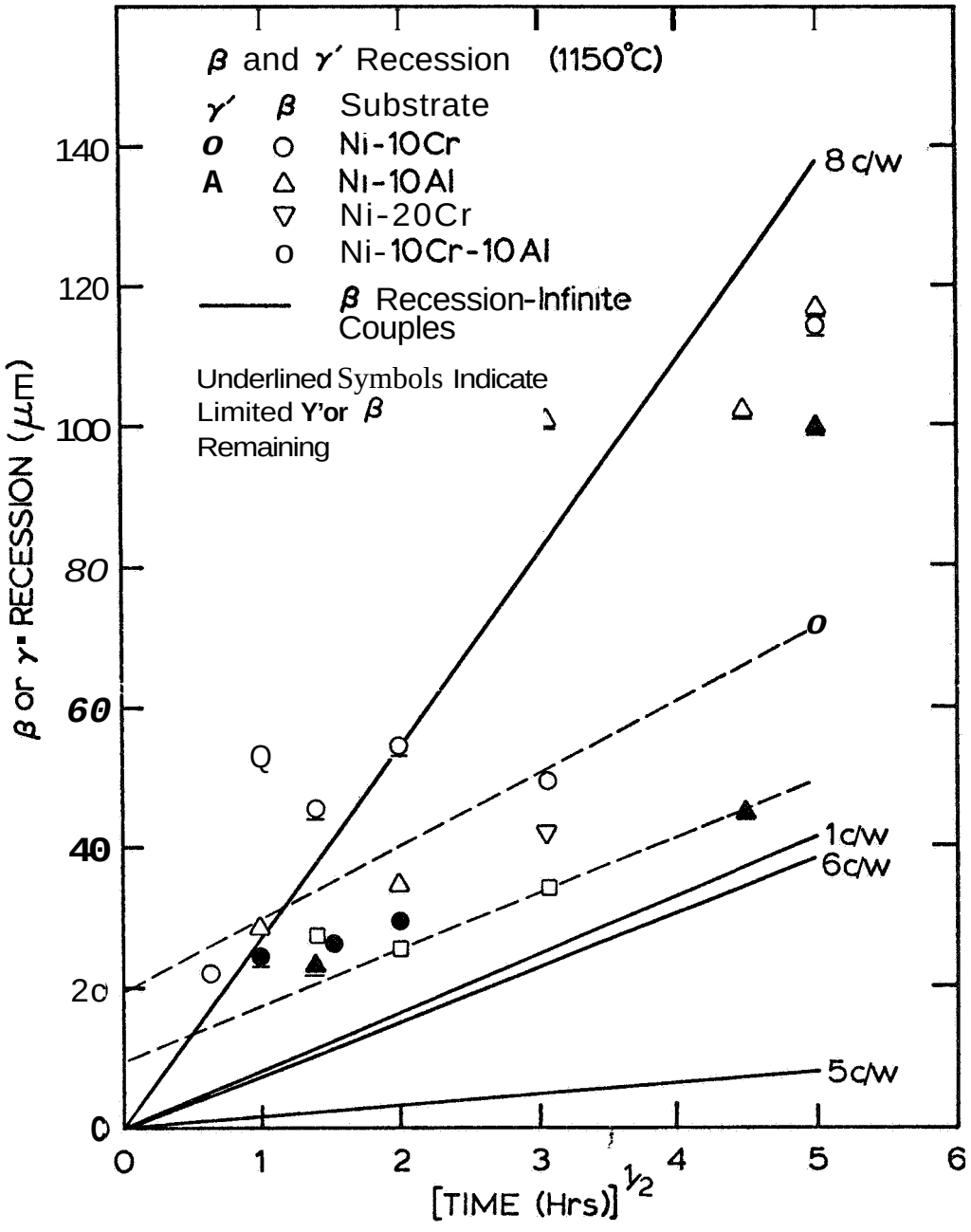

Figure D.3 β and γ' recession in NiCrAlZr overlay coatings and γ/γ+β diffusion couples.

annealing. This result is in agreement with the earlier discussion suggesting an unusually high Al flux from the coating to the substrate during the very early stages of coating/substrate interdiffusion. β recession assuming parabolic rates are shown in Figure D.3 for several γ/γ + β infinite couples annealed at 1150°C (1). Alloy compositions are listed in Table D-1. Alloy 1C is very similar in concentration and β volume fraction (~70%) to the overlay coating, while alloy 8C contains less Al and a lower β volume fraction (~25%) than the coating. The β recession rate in the thick overlay coatings is very close to that in the 1C/W couple. The β recession rates in the coating after the diffusion fields in the finite coating overlap appear very similar to that in the 8C/W couple.

The previous discussions can be summarized in a few statements:

1. β recession is very rapid during the early stages of coating/substrate interdiffusion. The location of porosity in the coating supports the suggestion that the rapid β recession is the result of a high Al flux from the coating to the substrate.
2. The β recession rate in thick coatings is approximately the same as that in γ/γ + β infinite couples with similar compositions (accounting for the rapid initial β recession).
3. Overlapping diffusion fields in the coating accelerate γ' and β recession.
4. Complete depletion of the γ' and β phases would be expected at 5-15 hours in a 60-100 μm thick coating on the four substrates examined in this study when exposed to both oxidation and interdiffusion at 1150°C.

References

1. S. R. Levine, Met. Trans., 9A, 1237 (1978).

Appendix E

COSIM - Coating Oxidation/Substrate Interdiffusion Model

A numerical model utilizing finite-difference techniques was developed to simulate diffusional interactions which occur during cyclic oxidation of coated substrates. The numerical model, entitled COSIM, simulates diffusional degradation of overlay coatings by oxidation and coating/substrate interdiffusion. When applied to NiCrAlZr coatings on various NiCrAl substrates, the numerical model predicts Al and Cr concentration/distance profiles in both the coating and substrate. In addition, the model predicts the time at which the coating becomes sufficiently depleted of Al so as to permit breakaway oxidation and formation of less protective oxides. Variables input to the model are the coating thickness, the Al and Cr content of the coating and substrate, and the concentration dependence of the ternary diffusion coefficients for the temperature of interest. In addition, various oxidation parameters (thermal cycle frequency, oxide growth rate, oxide spalling constants) were indirectly used by the model by coupling the COSP spalling model (1)* to the COSIM diffusion model. The COSP model predicts the rate of Al consumption (as Al_2O_3), which was used as a boundary condition at the oxide/metal interface in the COSIM model.

Several assumptions were made in the development of the numerical model. They were:

1. The two-phase coating could be approximated as a single

---

* The references for this appendix are listed on page E20.

phase of equivalent Al and Cr concentrations.

2. The ternary diffusivities appropriate for the γ phase could be extrapolated to the high Al concentration in the assumed, single-phase coating.
3. Only Al_2O_3 was formed.
4. The oxide/metal interface was planar.
5. Diffusion occurred only at the oxidizing temperature, i.e. negligible diffusion occurred during sample heat-up or cool down.
6. The partial molar volume of Al and Cr was independent of concentration.

The validity of each of these assumptions has been discussed in the numerical modeling section of this report.

The **COSIM** model has been embodied in two computer programs, COSIMl and **COSIM2. The COSIMI** program operates from the start of oxidation until the diffusion-affected zones caused by oxidation and coating/substrate interdiffusion first begin to overlap. Until the overlap occurs, the first program considers the oxidation of the coating, and the coating/substrate interdiffusion separately and independent of one another, Therefore, the **COSIMl** program operates while the coating "behaves" as a semi-infinite slab on an infinite substrate. The **COSIM2** program operates when the finite thickness of the coating becomes apparent, i.e. when the diffusional transport caused by oxidation at the outer coating surface affects the concentration profiles caused by coating/substrate interdiffusion, and likewise, when coating/substrate interdiffusion affects the ability of the coating to supply Al to the oxide scale. Once overlap of the diffusion-affected

zones in the coating occurs, the combined effect of coating/substrate interdiffusion and oxidation rapidly reduce the Al content in the coating.

All diffusion, whether that caused by oxidation or coating/substrate interdiffusion, must obey the ternary equivalent of Fick's second law. From Kirkaldy (2), for Al and Cr:

$$\frac{\partial C_{Al}}{\partial t} = \frac{\partial}{\partial X}\left(D_{AlAl}\frac{\partial C_{Al}}{\partial X}\right) + \frac{\partial}{\partial X}\left(D_{AlCr}\frac{\partial C_{Cr}}{\partial X}\right) \qquad \text{[E-1a]}$$

$$\frac{\partial C_{Cr}}{\partial t} = \frac{\partial}{\partial X}\left(D_{CrAl}\frac{\partial C_{Al}}{\partial X}\right) + \frac{\partial}{\partial X}\left(D_{CrCr}\frac{\partial C_{Cr}}{\partial X}\right) \qquad \text{[E-1b]}$$

Equations [E-1a and b] can be rewritten as:

$$\frac{\partial C_{Al}}{\partial t} = \frac{\partial D_{AlAl}}{\partial X}\frac{\partial C_{Al}}{\partial X} + D_{AlAl}\frac{\partial^2 C_{Al}}{\partial X^2} + \frac{\partial D_{AlCr}}{\partial X}\frac{\partial C_{Cr}}{\partial X} + D_{AlCr}\frac{\partial^2 C_{Cr}}{\partial X^2} \qquad \text{[E-2a]}$$

$$\frac{\partial C_{Cr}}{\partial t} = \frac{\partial D_{CrAl}}{\partial X}\frac{\partial C_{Al}}{\partial X} + D_{CrAl}\frac{\partial^2 C_{Al}}{\partial X^2} + \frac{\partial D_{CrAl}}{\partial X}\frac{\partial C_{Cr}}{\partial X} + D_{CrCr}\frac{\partial^2 C_{Cr}}{\partial X^2} \qquad \text{[E-2b]}$$

Since the diffusivities are known as functions of the Al and Cr concentration, the partial derivative of the diffusivity with respect to distance can be rewritten for each of the four diffusivities in Equations [E-2a and b] by use of the chain rule as

$$\frac{\partial D}{\partial X} = \frac{\partial D}{\partial Al}\frac{\partial Al}{\partial X} + \frac{\partial D}{\partial Cr}\frac{\partial Cr}{\partial X} \qquad \text{[E-3]}$$

Substituting the appropriate form of Equation [E-3] into Equations [E-2a and b] yields two, rather lengthy, second order partial differential equations describing the diffusion of Al and Cr in single-phase NiCrAl alloys. Solution of Equations [E-2a and b] requires certain initial and boundary conditions which are described in the sections below dealing separately with interdiffusion and oxidation.

Basic Operation of the COSIM Model

COSIM1

The COSIM1 program consists of two distinct parts dealing separately with coating/substrate interdiffusion and coating oxidation. Both parts of COSIM1 program will be briefly discussed below.

Interdiffusion. The finite-difference technique requires definition of a grid across the diffusion-affected zone. The initial diffusion zone for interdiffusion was chosen as 0.1 μm positioned at the coating/substrate interface. The initial diffusion zone was divided into 30 grid points. Initial Al and Cr Concentrations were assigned to each grid point using the error function *so* that the concentrations varied smoothly from the coating composition (Cr_0,Al_0) to the substrate composition (Cr_S,Al_S).

The basic operation of the COSIM model is a sequential interation of the finite-difference equivalents to Equations [E-2a and b] for successive increments of time. First central-difference equations were substituted for each of the concentration derivatives in Equations [E-2a and b]. (The finite-difference technique and the difference equations can be found in most basic texts dealing with numerical analysis [3,4]).

Since the concentration dependence for each of the diffusivities was described in analytic form (Appendix C), the derivatives of the diffusivities (Equation [E-3]) were calculated exactly. For each increment in time At, the change in concentration AC for each grid point could be determined. By repetitive iteration, the concentration/distance profile could be determined for the total accumulated time $i \Delta t$, where i is the number of iterations. For each iteration, the boundary conditions at grid 1 and grid 30 must be satisfied. The boundary conditions in the coating and in the substrate were of the same form for interdiffusion. For the boundary condition in the substrate (at grid 30) an addition grid point (31) was added with a concentration equal to the bulk concentration of the substrate (Cr_S or Al_S). The concentration of grid 30 was allowed to increase or decrease according to Equation [E-2]. When the concentration at grid 30 for either Al or Cr differed from the bulk composition by 0.005 at.%, an additional grid point (32) was added at a distance ΔX into the substrate with a concentration equal to the bulk substrate concentration. The number of grids in the coating (at grid 1) was also permitted to increase in the same manner. In this way, the number of grid points increased as the width of the diffusion-affected zone increased. When the number of grids in the diffusion zone had doubled to 60, the number was halved by using only every other grid. Cutting in half the number of grids effectively doubled the grid spacing Δx. Doubling ΔX permitted the increment in time per iteration At to be increased, thereby reducing the necessary computation time.

The accuracy of the interdiffusion portion of the COSIMl program was verified by comparison to a closed-form analytical solution valid

for concentration-independent diffusion coefficients(2). The parameters specific to the finite-difference technique, the number of grids (N), the initial diffusion zone width (X_0), and the concentration difference at the first and last grid point (DELC) controlling expansion of the diffusion zone, were each varied to determine the sensitivity of the finite-difference solution to these parameters. Figure E.la shows the excellent agreement between the analytical solution and the finite-difference solution 'INTER1' for several different parameter choices. The COSIMl program used an even more conservative set of parameters than shown in Figure E.l (viz., X_0–0.1 μm, N=30 and DELC=0.005 at.%).

Oxidation. An initial diffusion zone was defined in the coating at the oxide/coating interface with a starting width of 0.1 m. Twenty grid points were equally spaced across the initial diffusion zone. The coating was modeled as a single phase with the initial concentrations at each grid point equal to the bulk concentration of the coating (Cr_0, Al_0). The oxidation portion of the COSIMl model operated in an identical fashion to that previously described, that is, by a sequential iteration of the appropriate finite-difference equations. There are several important differences between the oxidation and interdiffusion portions of the COSIMl model. The boundary condition at; the oxide/coating interface was provided by the COSP spalling model(l). The COSP model predicted the rate of Al consumption (as Al_2O_3) as a function of time. Details of the COSP model are given in a later section. For each iteration of the COSIMl program, the COSP model predicted the rate of AL consumption for the accumulated oxidation time (based on the current oxide thickness). The rate of Al consumption

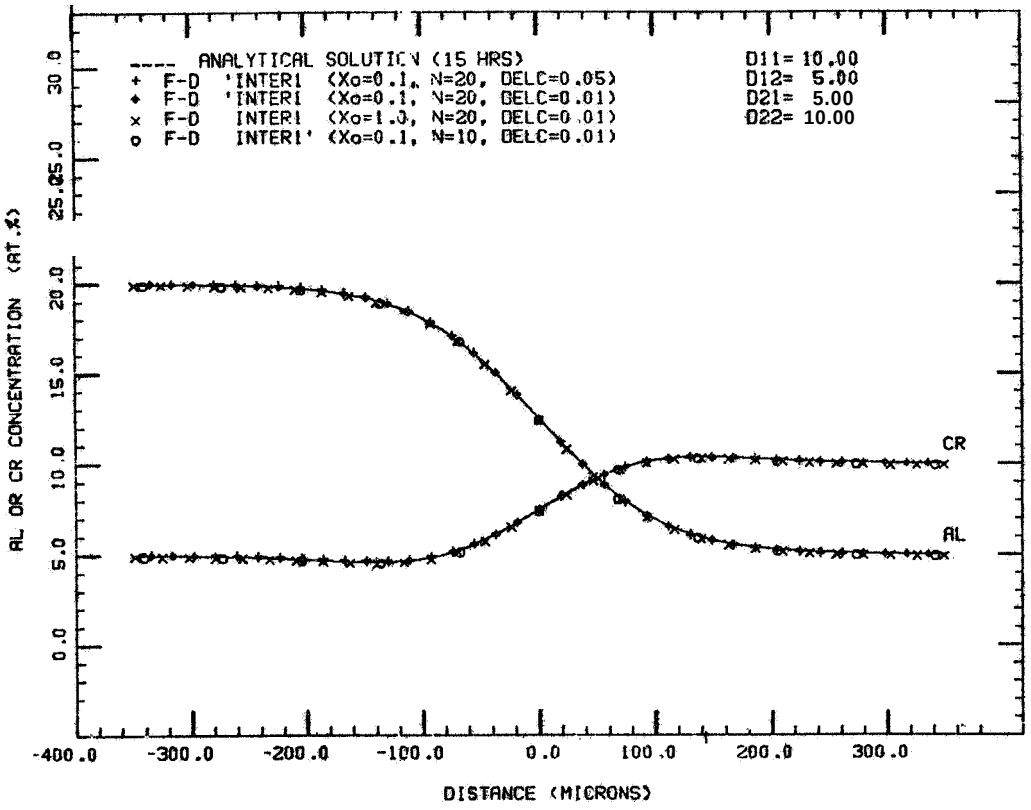

a.

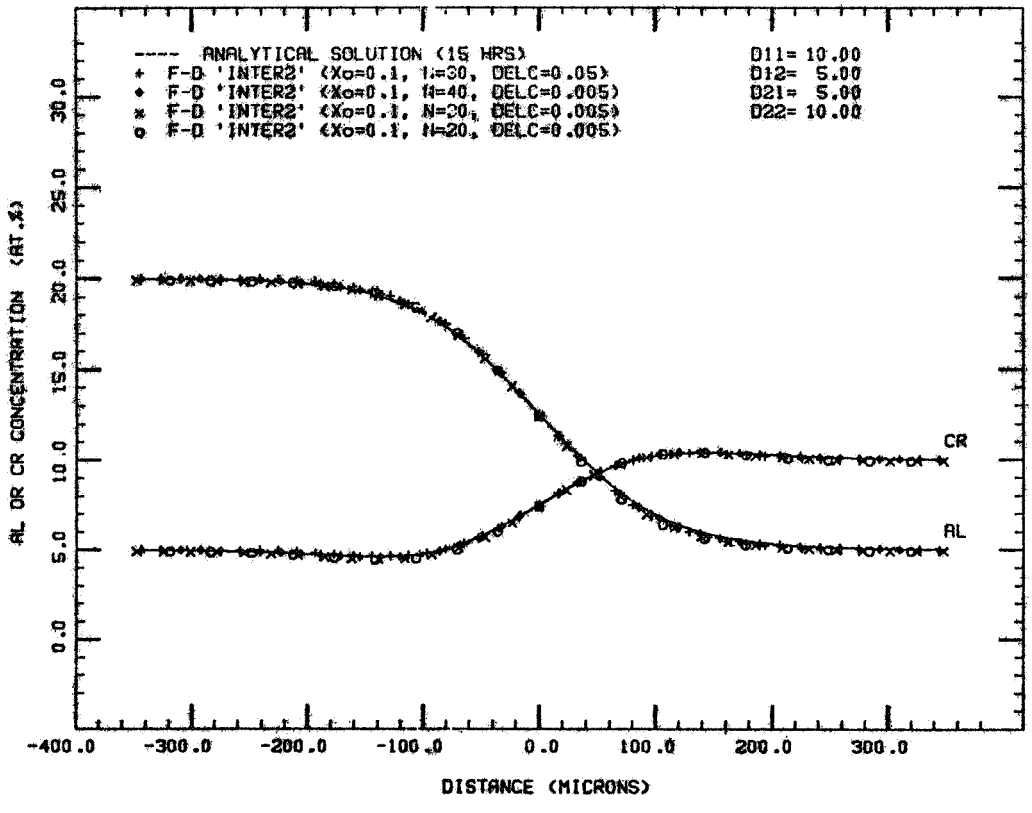

b.

Figure E.1 Comparison of finite-difference solution and analytical solution for "infinite" γ/γ diffusion couples, a. INTER1 program and, b. ENTER2 program. (The diffusivities, D_{ij}, above *have* the units $cm^2/s \times 10^{**}$.)

($mg/cm^2/s$) was converted into the appropriate units used in the **COSIMl** program to define the necessary flux of Al at the oxide/coating interface. The Al flux in the coating is defined as(2):

$$J_{Al}^{\gamma} = -D_{AlAl} \frac{\partial C_{Al}}{\partial X} - D_{AlCr} \frac{\partial C_{Cr}}{\partial X} \qquad [E\text{-}4]$$

The flux of Al entering the oxide is defined as(5):

$$J_{Al}^{OX} = \alpha J_{Al}^{\gamma} \qquad [E\text{-}5]$$

where α is defined as:

$$\alpha = \frac{1}{(1-\bar{V}_{Al} C_{Al}^{*})} \qquad [E\text{-}6]$$

where $\bar{V}_{Al}$ is the partial molar volume of Al in the coating and C_{Al}^{*} is the Al concentration in the coating at the oxide/coating interface. The Al flux in the oxide away from the oxide/metal interface is always greater than the Al flux in the coating towards the interface because of the motion of the interface into the coating. Using Equations [E-4 and 5], and J_{Al}^{ox} predicted by COSP allows determination of the Al concentration gradients in the coating at the oxide/coating interface. Using a first-order backwards difference equation for the Al gradient permits calculation of the Al concentration at the oxide/coating interface, C_{Al}^{*}. For each iteration, the COSIM model also predicts the recession of the oxide/coating interface resulting from the loss of Al from the coating. The equation relating the interface recession $\Delta\xi$, in the time interval Δt is(5):

$$\Delta\xi = -\bar{V}_{Al}\, J_{Al}^{ox}\, \Delta t \qquad [E-7]$$

where all terms are as previously defined. Since Cr is not permitted in the oxide scale, Cr atoms must diffuse away from the moving oxide/metal interface. Motion of the interface tends to "pile-up" Cr in the coating near the oxide/coating interface. The appropriate mass balance for Cr at the interface is given as:

$$(C_{Cr}^{*} - 0)\,\frac{\Delta\xi}{\Delta t} = J_{Cr}^{\gamma} = -D_{CrAl}\,\frac{\partial C_{Al}}{\partial X} - D_{CrCr}\,\frac{\partial C_{Cr}}{\partial X} \qquad [E-8]$$

where C_{Cr}^{*} is the Cr concentration at the oxide/coating interface and other terms are as previously defined. Since $\Delta\xi$ is fixed by Equation [E-7], Equation [E-8] can be used to calculate C_{Cr}^{*} for the current time $t+\Delta t$ (the Cr concentration gradient in Equation [E-8] is calculated at time t). Therefore, C_{Cr}^{*} is not fixed but allowed to vary with time. The greater the oxide/coating interface recession, and the slower the Cr diffusion away from the interface, the greater the value of C_{Cr}^{*}.

The concentrations at each grid point must be shifted to account for the recession of the oxide/coating interface. The grid spacing was also redetermined, The Al and Cr concentrations were shifted according to the usual Murray/Landis-type transformation(6). The final operation during each iteration of the COSIMl program was to force the Al and Cr concentration at each grid point to satisfy the finite-difference equivalent of Equations [E-2a and bl just as for the interdiffusion portion of the COSIMl program. When the concentrations at the inner-most grid point in the coating (nearest the substrate - grid 20) differed from the bulk concentration of the coating by 0.005 at.%, the

total width of the diffusion zone was increased by ΔX (the grid spacing was increased by $\Delta X/20$). The concentrations and positions of the grid points were shifted again by a Murray/Landis-type transformation. Therefore, in contrast to the interdiffusion portion of the COSIMl program where the number of grids varied from 30-60 and the grid spacing occasionally doubled, the number of grids in the diffusion-affected zone resulting from oxidation remained constant and the grid spacing increased gradually to accommodate the expanding diffusion affected zone.

The accuracy of the oxidation portion of the COSIMl program was verified by comparison to a closed-form analytical solution dervied by making several restrictive assumptions. The analytical solution requires that the diffusion coefficients be concentration independent and that the partial molar volume of Al ($\overline{V}_{Al}$) be equal to zero. Setting $\overline{V}_{Al}=0$ eliminates the recession of the oxide/metal interface. In addition, the boundary condition at the oxide/metal interface could not be supplied by the COSP spalling model. The Al and Cr concentrations at the oxide/metal interface, input to the analytical solution, remained constant with time. The last restriction results in concentration/distance profiles more indicative of isothermal oxidation. The parameters specific to the finite-difference technique were the number of grids (N), the initial diffusion zone width (X_0), and the concentration difference at the inner-most grid point controlling expansion of the diffusion zone (DELC). Figure E.2 shows the excellent agreement between the analytical solution and the finite-difference solution for 2–10 grid points in the diffusion zone. The other finite-difference parameters for the profiles in Figure E.2 were X_0 =1.0 μm

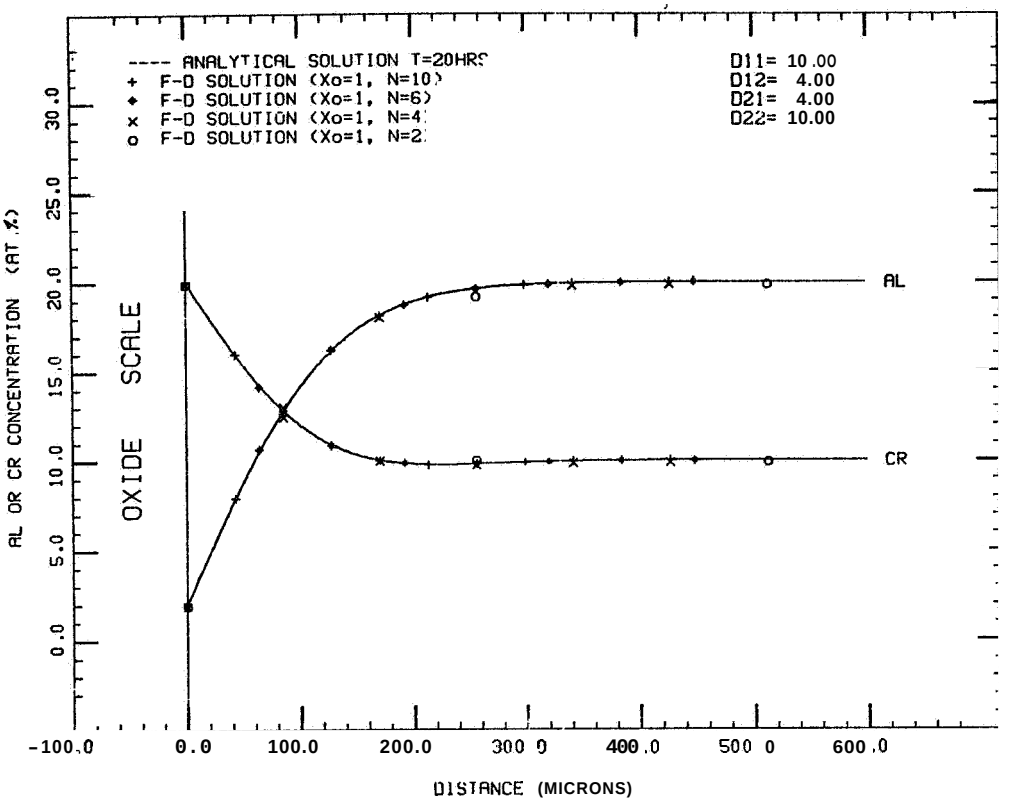

Figure E.2 Comparison of finite-difference solution and analytical solution for oxidation of a single phase alloy. (The diffusivities, D_{ij}, shown above have the units $cm^2/s \times 10^{10}$.)

and DELC=0.05 at.%. The more conservative values used in the COSIMl program were N=20, X_0=0.1 μm and DELC=0.005 at.%.

It should be pointed out that the accuracy of the COSIMl predictions were not sensitive to the choice of methods used to expand the width of the diffusion-affected zone. A constant number of grids and slowly increasing grid spacing were used in the interdiffusion program 'INTER2' and a comparison to the analytical solution for interdiffusion is shown in Figure E.1b. The excellent agreement is identical to that shown in Figure E.1 where the number of grids was allowed to increase to twice the initial value. The method using a constant number of grids and slowly increasing grid spacing was used with the oxidation portion of COSIMl to eliminate any possible "jolts" to the system caused by doubling the grid spacing (when the number of grids was cut in half) at the same time the Al flux rapidly increased due to oxide spallation.

COSIM2

Oxidation and Interdiffusion. The COSIM2 program used a single diffusion zone which extended across the coating and into the substrate to a depth where no diffusion had occurred. The COSIM2 program was initiated when the diffusion-affected zones in the COSIMl program first overlapped in the coating. Since the grid spacing for the oxidation and interdiffusion portions of the COSIMl program were usually different when the overlap occurred, a cubic spline equation (7) was fit to each concentration profile caused by oxidation and interdiffusion. The cubic spline equation was used to interpolate the Al and Cr concentrations at equally spaced grid points extending across the coating and into the

substrate. The COSIM2 program utilized 60 grid points. The COSIM2 program operated in an iterative fashion identical to that of COSIM1. The boundary condition at the oxide/metal interface was provided by the COSP spalling model as previously described for COSIM1. The boundary condition in the substrate was identical to that at the inner-most grid point in the oxidation portion of COSIM1. Equations [E-2a and b] were utilized in the same manner as previously described. Therefore, in the COSIM2 program, the number of grid points remained constant while the grid spacing gradually increased. The maximum time increment for each iteration of COSIM2 was 300 seconds.

There is no analytical solution with which to compare to the complete COSIM model. Increasing the number of grids in either COSIMl or COSIM2 produced equivalent results. Decreasing the time interval, At, also results in convirgance to a single value. Performing mass balance calculations by integrating under the concentration/distance profiles before and after simulated cyclic oxidation produced a relative error generally less than 5%. Based on the previous verifications of the separate portions of the COSIMl program, the COSIM model is considered as a valid solution to the diffusion equations for the given boundary conditions.

COSP Spalling Model

The COSP spalling model (1) simulates oxide growth and spallation during oxidation accompanied by thermal cycling. The COSP model predicts the weight of retained oxide (W_r) remaining on the sample surface, the overall weight change of a sample (ΔW), the weight of metal consumed (W_m), and the rate of metal consumption ($\dot{W}_m$), each as a

function of the time. The most important parameters input to the model are the oxide growth rate k_p, oxide spalling parameters Q_o and α (defined below), and the thermal cycle frequency Δt.

The basic operation of the COSP model is an iterative calculation of the amount of oxide growth and the amount of oxide spallation for each thermal cycle. During each thermal cycle, the rate of oxide growth is dependent on the current oxide thickness. The greater the oxide thickness, the lower the oxide growth rate. The COSP model is capable of dividing the sample surface into a grid of rectangular areas and calculating the oxide growth and random oxide spallation at each rectangular area on the surface. Use of the COSP model in this study assumed uniform oxide growth and spallation across the entire surface of the sample. Stated otherwise, the COSP model was used to predict the average oxide growth rate (averaged over the surface of the sample), average thickness, average weight of oxide spalled during each cycle, etc.

The COSP model can best be explained by examining the predictions from the model for several thermal cycles. Upon heating a sample, an oxide scale initially grows parabolically with time until the sample is removed from the furnace. The weight of oxide on the sample surface (W_r) before the first cooling period is given as:

$$W_r = b\sqrt{(k_p \Delta t)} \qquad [E\text{-}9]$$

where Δt is the length of the high-temperature exposure and b is a constant relating the weight of oxygen in the oxide to the weight of oxide (k_p as traditionally measured during isothermal oxidation reflects the weight of oxygen in the oxide). On cooling, the weight of oxide

which spalls (W_s) is related to the current amount of oxide on the surface and is given as:

$$W_s = Q_o W_r^{1+\alpha} \qquad \text{[E-10]}$$

where Q_o and α are spalling parameters and will be discussed again shortly. The increase in the weight of retained oxide, and the decrease resulting from oxide spallation is shown for one-hour thermal cycles in Figure E.3a. The oxide growth rate after spallation increases due to the reduced oxide thickness. Therefore, the oxide growth rate upon heating during the second cycle (time=1 hour) is initially equivalent to the growth rate at approximately 0.25 hours in the first one-hour exposure (see Figure E.3a). The rate of metal consumption, being proportional to the oxide growth rate, more clearly reveals the increase in the oxide growth rate after each thermal cycle. When the oxide scale is thin (time << 1 hour) the oxide growth rate and rate of metal consumption are very high, but decrease rapidly as the scale thickens. The rate of metal consumption before the first thermal cycle is given as:

$$\dot{W}_m = \frac{dW_m}{dt} = \frac{a}{2}\sqrt{(k_p/t)} \qquad \text{[E-11]}$$

where a is a constant similar to b in Equation [E-9] relating the weight of metal in the oxide to the weight of oxide. When the thickness of the oxide scale decreases due to spallation, the growth rate of the oxide and the rate of metal consumption both rapidly increase, but gradually decease again as the oxide scale thickens. This behavior is shown in Figure E.3b. The **COSP** model also predicts the total weight of metal consumed (W_m) and is shown in Figure E.3c. The W_m versus time curve is

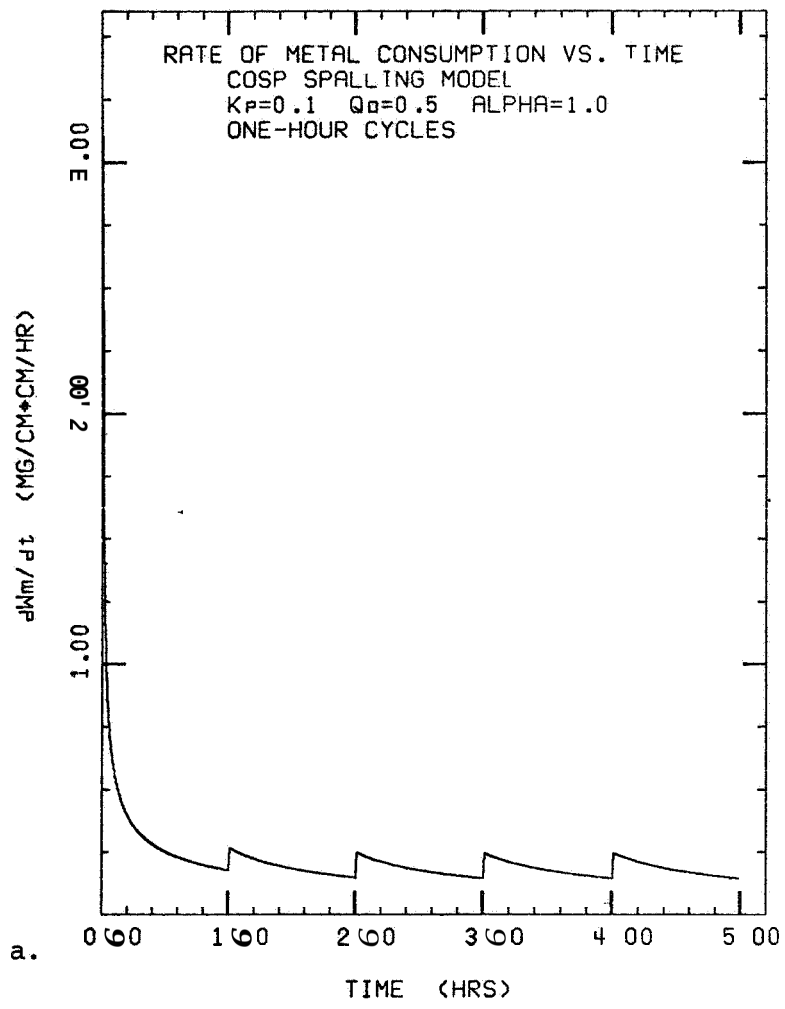

a.

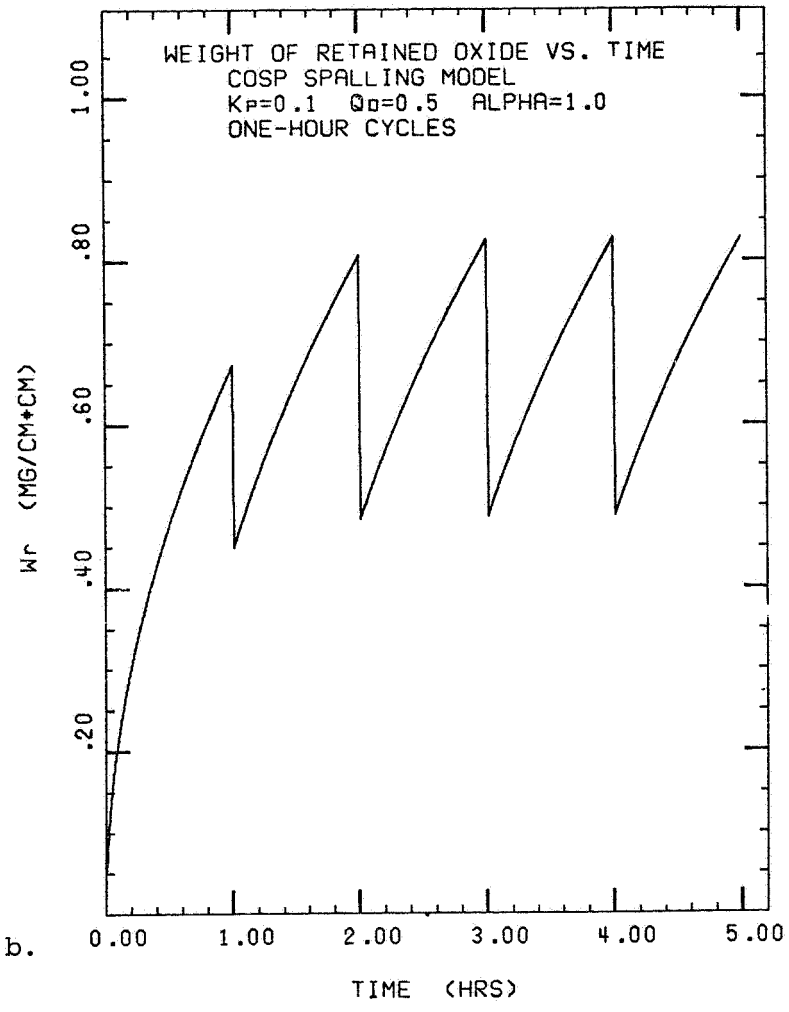

b.

Figure E.3 Output from the COSP spalling model,
a. rate of metal consumption, b. weight of retained oxide.

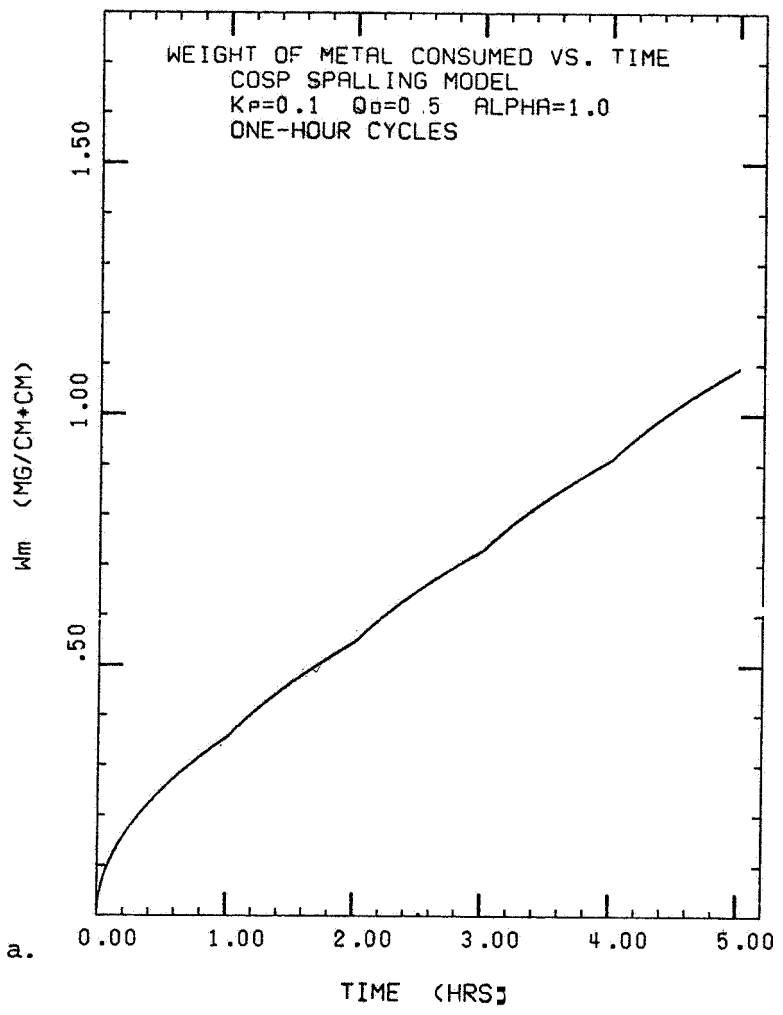

a.

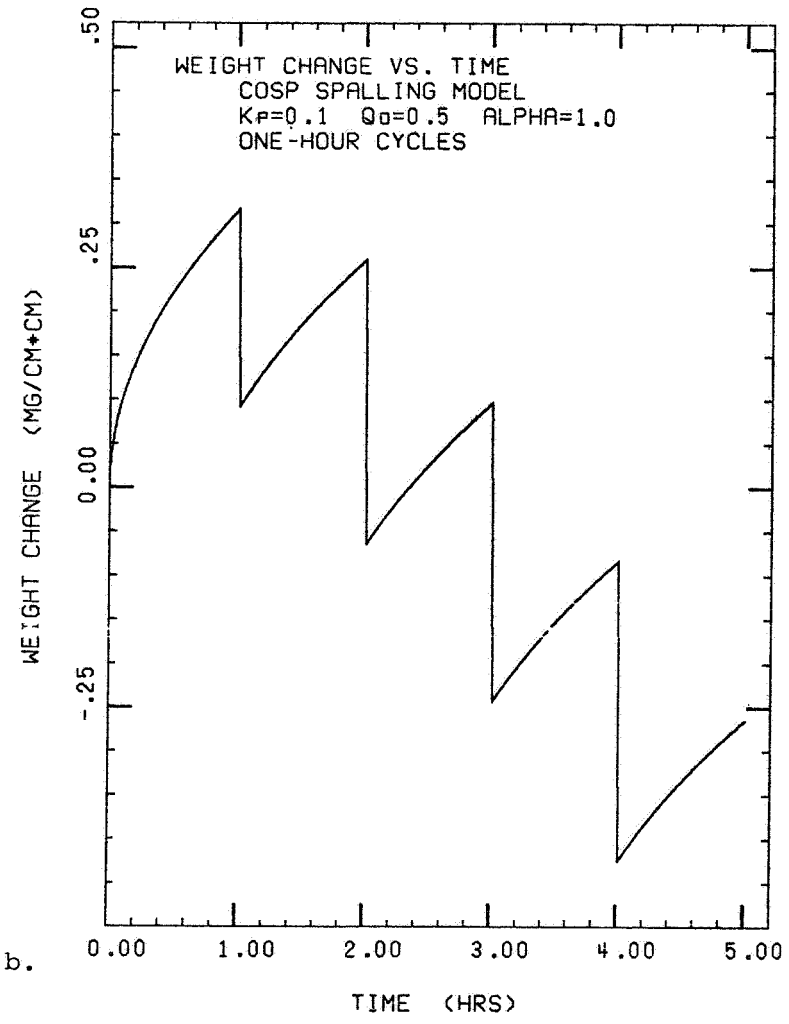

b.

Figure E 3 (con't) Output from COSP spalling model, c. weight of metal consumed, d. weight change.

slightly "scalloped" because of the increased rate of metal consumption following each thermal cycle. The COSP model also predicts the weight change of a sample (ΔW) during oxidation accompanied by thermal cycling. Weight increases are due to the addition of oxygen (in the oxide) to the sample, while weight losses are due to the loss of metal (in the oxide) during oxide spallation. The sample weight change is shown in Figure E.3d. The sample weight change is the most common variable measured during cyclic oxidation testing of alloys. Using k_P for a specific oxide at a given test temperature, the spalling parameters Q_σ and α are varied in the COSP model to yield the best fit to the experimentally determined weight change data. Experimental weight change data typically appear quite smooth when viewed on a scale of several hundred hours (see experimental section of this report),

The rate of Al consumption predicted by the COSP model is used as a boundary condition to the COSIM model. The effect of a changing rate of Al consumption, shown by the COSIM model, is a cyclic decrease in the Al concentration at the oxide metal interface. The rapid increase in the growth rate of the oxide results in a rapid decrease in the Al concentration at the interface. Conversely, for each drop in the Al concentration at the interface is a similar jump in the Cr concentration at the same interface. The Al and Cr concentrations at the oxide/metal interface as predicted by the COSIM model are shown in Figures E.4a and b for a Ni-20Cr-10Al alloy undergoing cyclic oxidation.

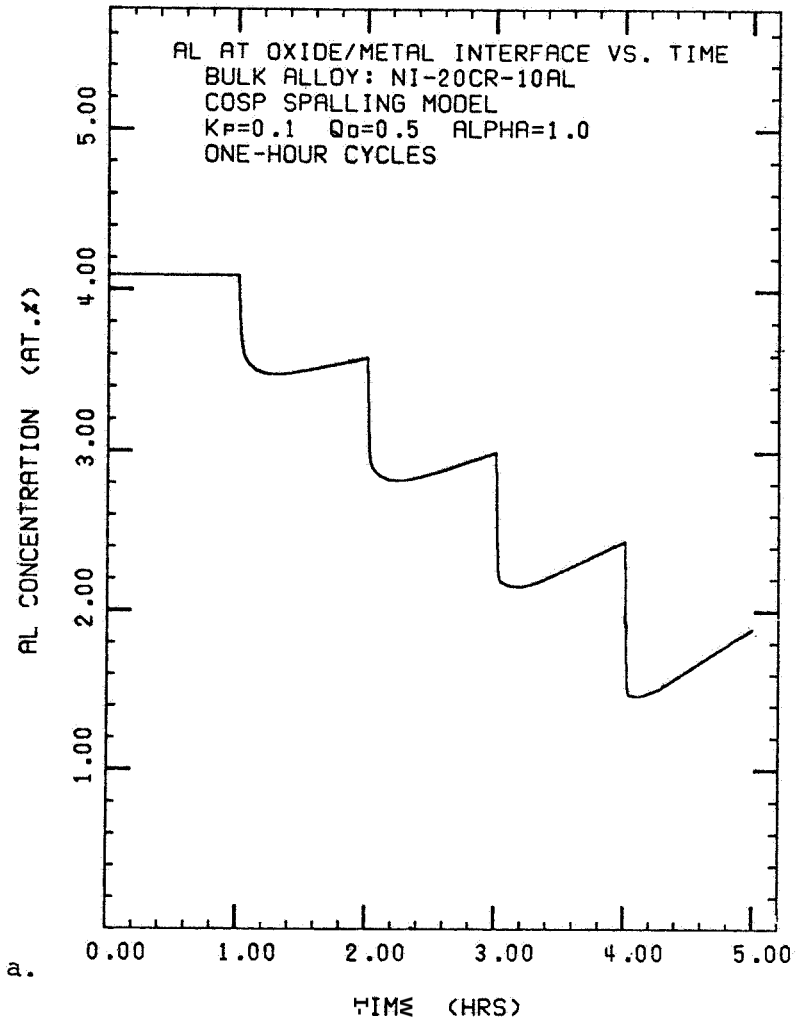

a.

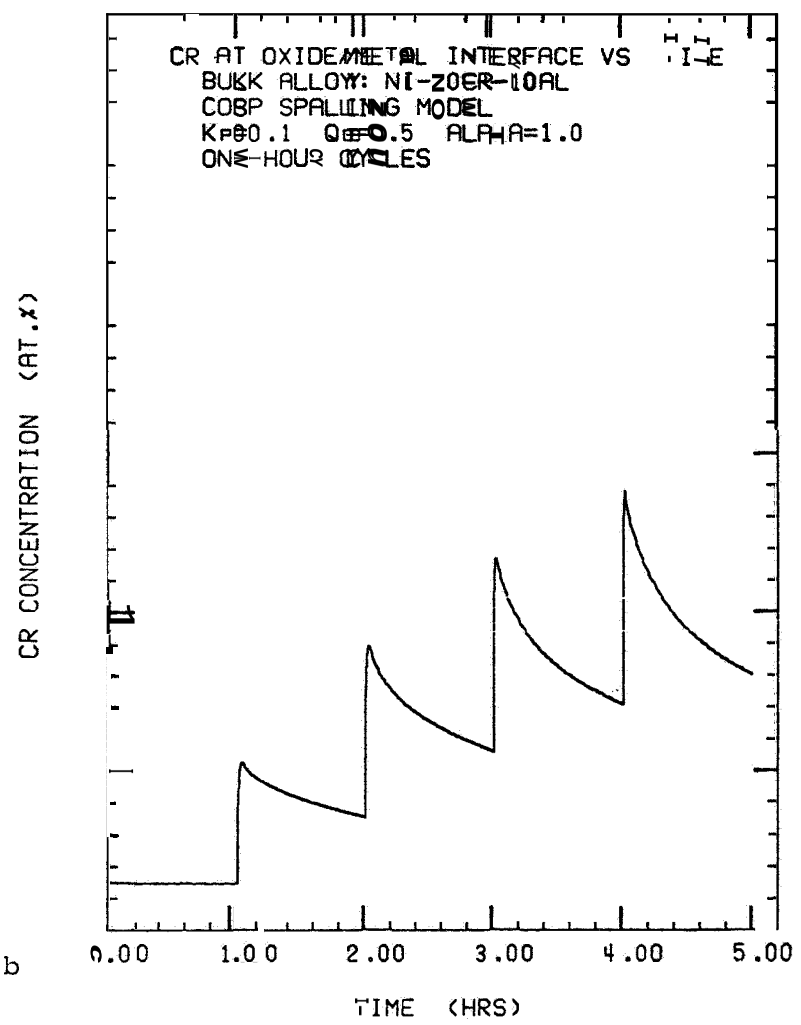

b

Figure E.4 Output from the COSIM model,
a. Al at oxide/metal interface and b. Cr at oxide/metal interface.

References

1. C.E. Lowell, C.A. Barrett, and R.N. Palmer, "Development of a Cyclic Oxidation Spall Model", Presented at the Oxidation, Deposition and Hot Corrosion in Combustion Turbine Engines Conference, NASA Lewis Research Center, Cleveland, OH, April 27-28, 1983.

2. J.S. Kirkaldy, "Isothermal Diffusion in Multicomponent Systems", Advances in Materials Research, 4, 55 (1970).

3. R. Hornbeck, Numerical Methods, Quantum Publishers Inc., N.Y., 1975,

4. M.L. James, G.M. Smith, and J.C. Wolford, Analog and Digital Computer Methods, International Textbook Co., Scranton, N.Y., 1964.

5. R.E. Sekerka, C.L. Jeanfils, and R.W. Heckel, Lectures on the Theory of Phase Transformations, H.I. Aaronson, Editor, pp. 117-169, TMS-AIME, N.Y., 1975.

6. D. Murray and F. Landis, Trans. ASME, Series D, 81, 106 (1959).

7. IMSL Library Reference Manual, Chapter I, Vol. 2, 9th Edition, IMSL Inc., 1982.

1. Report No.	2 Government Accession No.	3. Recipient's Catalog No.
NASA TM-83738		

4. Title and Subtitle

Overlay Coating Degradation by Simultaneous Oxidation and Coating/Substrate Interdiffusion

5. Report Date	6. Performing Organization Code
August 1984	533-04-1E

7 Author(s)

James A, Nesbitt

8. Performing organization Report No.	10. Work Unit No.
E-2223	

9. Performing Organization Name and Address

National Aeronautics and Space Administration
Lewis Research Center
Cleveland, Ohio 44135

11 Contract or Grant No.	13. Type of Report and Period Covered
	Technical Memorandum

12. Sponsoring Agency Name and Address

National Aeronautics and Space Administration
Washington, D.C. 20546

14. Sponsoring Agency Code

17 Key Words (Suggested by Author(s))	18. Distribution Statement
NiCrAl ; Coating degradation; Overlay coatings; Interdiffusion; Oxidation; NiCrAl diffusion coefficients; Life prediction	Unclassified - unlimited STAR Category 26

19. Security Classif. (of this report)	20. Security Classif (of this page)	21 No. of pages	22. Price'
Unclassified	Unclassified		